UNIVERSITAT POLITÈCNICA DE CATALUNYA BARCELONATECH

Investigations of topological phases for quasi-1D systems

Emanuele Tirrito

The Institute of Photonic Sciences

QUANTUM OPTICS THEORY DIVISION

Ph.D. degree in Theoretical Physics

Investigations of topological phases for quasi-1D systems

PhD thesis

Candidate:
Emanuele Tirrito

Thesis advisor:
Prof. M. Lewenstein

Research supervisor:
Dr. A. Bermudez

Thesis submitted in January 2020

Abstract

For a long time, quantum states of matter have been successfully characterized by the Ginzburg-Landau formalism that was able to classify all different types of phase transitions. This view changed with the discovery of the quantum Hall effect and topological insulators. The latter are materials that host metallic edge states in an insulating bulk, some of which are protected by the existing symmetries.

Complementary to the search of topological phases in condensed matter, great efforts have been made in quantum simulations based on cold atomic gases. Sophisticated laser schemes provide optical lattices with different geometries and allow to tune interactions and the realization of artificial gauge fields.

At the same time, new concepts coming from quantum information, based on entanglement, are pushing the frontier of our understanding of quantum phases as a whole. The concept of entanglement has revolutionized the description of quantum many-body states by describing wave functions with tensor networks (TN) that are exploited for numerical simulations based on the variational principle.

This thesis falls within the framework of the studies in condensed matter physics: it focuses indeed on the so-called synthetic realization of quantum states of matter, more specifically, of topological ones, which may have on the long-run outfalls towards robust quantum computers. We propose a theoretical investigation of cold atoms in optical lattice pierced by effective (magnetic) gauge fields and subjected to experimentally relevant interactions, by adding a modern numerical approach based on TN algorithms. More specifically, this work will focus on (i) interacting topological phases in quasi-1D systems and, in particular, the Creutz-Hubbard model, (ii) the connection between condensed matter and high energy physics studying the Gross-Neveu model and the discretization of Wilson-Hubbard model, (iii) implementing tensor network-based algorithms.

Resumen

Tras varias décadas de investigación, los estados cuánticos de la materia se han caracterizado con éxito por el formalismo de Ginzburg-Landau que permitió la clasificación de todos los diferentes tipos de transiciones de fase.

Esta visión cambió con el descubrimiento del efecto Hall cuántico y los aislantes topológicos. Estos últimos son materiales que albergan estados de borde metálicos en una masa aislante, algunos de los cuales están protegidos por las simetrías existentes.

Conjuntamente a la búsqueda de fases topológicas en materia condensada, se han hecho grandes esfuerzos en simulaciones cuánticas basadas en gases atómicos fríos. Los sofisticados esquemas láser proporcionan redes ópticas con diferentes geometrías y permiten ajustar las interacciones y la realización de campos de gauge artificial.

Al mismo tiempo, los nuevos conceptos que provienen de la información cuántica, basados en el entanglement, están empujando la frontera de nuestra comprensión de las fases cuánticas en su conjunto. El concepto de entanglement ha revolucionado la descripción de los estados cuánticos de muchos cuerpos al describir las funciones de onda con redes tensoriales (TN) que se explotan para simulaciones numéricas basadas en el principio variacional.

Esta tesis se enmarca en los estudios de física de la materia condensada: en particular, se centra en la llamada realización sintética de los estados cuánticos de la materia, más específicamente, de los topológicos, que pueden tener en las salidas a largo plazo hacia computadoras cuánticas robustas. Se propone una investigación teórica de los átomos fríos en la red óptica con campos de gauge efectivos y sometidos a interacciones relevantes experimentalmente, agregando un enfoque numérico moderno basado en algoritmos TN. Más específicamente, este trabajo se centrará en (i) fases topológicas en los sistemas cuasi-1D y, en particular, el modelo Creutz-Hubbard, (ii) la conexión entre la materia condensada y la física de alta energía estudiando el modelo Gross-Neveu y el discretización del modelo Wilson-Hubbard, (iii) implementación de algoritmos basados en redes tensoras.

Acknowledgements

I am very grateful to Maciej Lewenstein for his great scientific support, for the many things he has taught me, but also for the fatherly way he leads his group. I also would like to thank Alejandro Bermudez, who has been a great co-supervisor. His cheerful personality has always been motivating and I have learned a lot from him, not only scientifically. A particular thanks also goes to Matteo Rizzi and Luca Tagliacozzo for the scientific discussions, but more important are the friendships I gained. Special thanks also goes to the rest of the QOT group for stimulating discussions.

Finally, I want to express my deep gratitude to my family, especially my parents, my brother, and Stefania. Your support and love have been a great source of motivation and happiness during these past years.

Contents

Chapter 1

Introduction

Quantum states of matter have been successfully characterized by the concept of spontaneous symmetry breaking [1]. Indeed, in condensed matter theory the phase transitions have been described using Landau-Ginzburg theory [2–4]. This theory invokes the existence of a local order parameter that distinguishes between two different phases and at the phase transition point, the symmetry of the system spontaneously breaks.

With the discovery of topological insulators [5–7], a new family of quantum states was found which did not fit into this simple classification of condensed matter systems.

The topological insulators are materials with an insulating bulk and metallic edges, which are protected by topology. This mechanism is called the *bulk-edge correspondence*. The topological phases are richer than usual quantum phases because the topology of the system comes into play together with quantum effects.

An example of a topological insulator is the quantum Hall effect (QHE) [8, 9] observed in $2D$ semi-conductors at a very low temperature. The charged particles move around in the perpendicular magnetic field. Due to the Lorentz force, these particles will be deflected. For stronger magnetic fields the trajectory of the electrons is deflected so heavily that they start moving in small circular trajectories whose radii are quantized. For electrons in the bulk, this means that they cannot transport charge through the system anymore and the bulk becomes insulating. However, at the edges, the electrons cannot make full circles but they start bouncing off the edges in semicircles, the so-called skipping orbits, winding in a clockwise or anti-clockwise sense depending on the direction of the external magnetic field. Due to their left or right-handedness, these states have a certain chirality. The chiral edge states are capable of carrying current and cause the transverse conductivity to still be present in the system. Each of these states contributes to quantum conductance e^2/h which gives rise to the robustly quantized Hall conductance discovered in 1980 [10–12]. The number of edge states is determined by the value of an integer topological invariant,the so-called Chern number [10, 11], such that the quantization is topologically protected against small perturbations of the system.

The origins of topological insulators can be understood in a single-particle framework. A complete classification of topological insulators and superconductors has been carried out in terms of discrete symmetries that are protected in the systems: time-reversal, particle-hole and, sublattice symmetry [13–15]. Two models in the same discrete symmetry class may posses groundstates with different values of a topological invariant and may be topologically inequivalent [13–15].

Complementary to the search of topological phases in condensed matter, great efforts have been made in quantum simulation. The concept of quantum simulation was introduced by Feynman at the beginning of the 80s [16, 17]. His idea was to use more controllable setups of quantum particles to encode the relevant degrees of freedom of complex real materials for which the isolated control of single ingredients is usually complicated. Exploiting these quantum setups, he envisioned controlling their dynamics to reproduce a particular model under study, and address difficult questions by directly measuring on the quantum simulator. When Feynman put forward this revolutionary idea of quantum simulations, he did not specify a particular setup. Then several proposals have emerged comprising diverse setups as ultracold atoms [18–20], trapped ions [21], superconducting circuits with Josephson junctions [22] and photonic technologies [23].

Here, we are interested in ultracold atoms in optical lattices [18–20] because they have proven to be well-suited to simulate condensed-matter Hamiltonians [19,20]. Neutral atoms are routinely cooled and trapped in periodic potentials created by interfering laser beams [24,25]. Using these techniques various lattice geometries can be engineered with a high degree of experimental control [26–28]. The physics of interacting atoms in such periodic potential can be described by the Hubbard model [29–31] which is an essential model to characterize strongly-correlated electrons in condensed matter systems.

With ultra-cold atoms in an optical lattice, the Hubbard parameters can be tuned individually in a very clean, defect-free realization by changing the lattice depth, which changes the kinetic energy, or by controlling the interaction strength via Feshbach resonances [32].

Moreover, the simulation of the artificial gauge fields is also feasible [33–38]. Indeed cold atoms are neutral atoms and do not feel the magnetic field like charged particles. There are, however, several proposals to engineer artificial magnetic fields such as laser-assisted tunneling [39–41], shaking [42], rotations of the atomic cloud [35] which enable to reach very high effective magnetic fields. Using such methods, several experiments have recently simulated the physics of the Hall effect, the spin Hall effect [43–47], the integer quantum Hall effect for bosons [48] and the Haldane model for fermions [49].

In the light of the synthetic quantum matter, analytical and numerical approaches assist the experimental progress. The theoretical calculations allow us to predict physical behavior and can, therefore, guide the experimental efforts into promising directions. Likewise, the numerical calculations are very useful to study the quantum many-body systems whose properties are governed by the interactions between their constituents that are computationally difficult to handle.

These systems are notoriously hard to be studied analytically. Exact solutions are extremely rare for such kind of systems. For these reasons, an intense research effort has been devoted to the development of new powerful numerical methods. These new methods naturally have to face great challenges, primarily that the dimension of Hilbert space of the systems considered increases exponentially with the number of particles.

One of the most important numerical tools in low-dimensional quantum many-body systems developed in the last decades is the method based on tensor networks (TN) [50–55] . They are based on the concept of entanglement entropy and area-law [56–58]. The TN states represent quantum states in terms of networks of interconnected tensors, which in turn capture the relevant entanglement of a system. This way of describing quantum states is radically different from the usual approach, where one just gives the coefficients of a wave-function in a given basis. The most relevant properties

of TN methods are: (i) the possibility to access the entanglement spectrum which carries important information about the topological nature of system phase, (ii) their flexibility. For instance, one can study a variety of systems in different dimensions of finite or infinite size, with different boundary conditions, symmetries as well as systems of bosons, fermions, and frustrated spins. Different types of phase transitions have also been studied in this context. Moreover, these methods are also now finding important applications in the context of quantum chemistry and lattice gauge theory.

Within this framework, the main goal of this thesis is to find a combination of interactions and synthetic gauge fields to study topological insulators, focusing on a two-leg ladder for fermions. To access the strongly-correlated physics and to account for different microscopic ingredients, we employ tensor network methods as a versatile and powerful technique.

This thesis is divided into two parts: in the first one we will investigate the symmetry topological phases in condensed matter and high-energy physics, while in the second part we will describe the properties of the TN algorithm that we used.

More specifically, this thesis is organized as follows:

- In Chapter 2, we present the general concepts that play a role in the study of one-dimensional synthetic quantum matter. We introduce these components pedagogically and contextualize them concerning each other, making connections to current research. The ideas shown here represent the building blocks that we combine in the following chapters. This Chapter has a review character and does not contain original results.

- In Chapter 3, we study the Creutz-Hubbard ladder. This fermionic lattice model combines aspects of lattice geometry and artificial gauge fields to display flat band physics with topological features. We study the stability of the topological phase with respect to interactions and layout the full phase diagram using MPS methods, shining new light on the mechanisms that work in topological phase transitions. This Chapter has a review character and it is based on original results presented by J. Jünemann et al. in [59].

- In Chapter 4, we will investigate the connection between topological phases in condensed matter and high energy physics. In particular, we present a complete analysis of continuum long-wavelength description of a generic class of topological insulators: Wilson-Hubbard topological matter. We show that a Wilsonian renormalization group approach, combined with the so-called topological Hamiltonian, provides a quantitative route to understand interaction-induced topological phase transitions that occur in Wilson-Hubbard matter. Moreover, we will benchmark two-loop RG predictions for a quasi 1D Wilson-Hubbard model using exhaustive numerical simulations based on MPS. This Chapter is based on original results presented in the paper [60].

- In Chapter 5, we show that a Wilson-type discretization of the Gross-Neveu model can serve as a playground to explore correlated symmetry-protected phases of matter using techniques borrowed from high-energy physics. A large N study, both in the Hamiltonian and Euclidean formalism, yields a phase diagram with trivial, topological and symmetry-broken phases separated by critical lines that meet at a tricritical point. This Chapter is based on original results presented in the paper [61].

Although the focus of the main body of this thesis is on one-dimensional fermionic models and the physics arising in these models, the numerical techniques involved in our studies are highly relevant aspects that also deserve their place in this thesis.

- In Chapter 6, we introduce some basic definitions and concepts of TN's. We will show that the TN can be used to represent quantum many-body states where we explain MPS in $1D$ and PEPS in $2D$ systems, as well as the generalizations to thermal states and operators. The quantum entanglement properties of the TN states including the area law of entanglement entropy will be discussed. Finally, we will present several special TN's that can be exactly contracted and demonstrate the difficulty of contracting TN's in general cases. This Chapter is based on original results presented in the book [55].

- In Chapter 7, we will introduce several paradigmatic tensor network-based algorithms, including DMRG, TEBD, and CTMRG. Moreover, we will present an optimization of DMRG called PT-DMRG to largely increase its accuracy in an extremely simple and efficient way. This Chapter is based on original results presented in the book [55] and in the paper [62].

- In Chapter 8, we will discuss the continuous limit of MPS. In particular, we construct the continuous MPS representation of the vacuum of the field corresponding to the continuous limit of the Ising model. This Chapter is based on original results presented in the paper [63].

- In Chapter 9, we will present some conclusions and discuss possible directions for future research.

Publications

The following articles have been published in the context of this thesis.

- E. Tirrito, S.-J. Ran, A. J. Ferris, I. P. McCulloch, and M. Lewenstein, An efficient perturbation theory of density matrix renormalization group, *Phys. Rev. B* **95**, 064110 (2017).

- Authors: S.-J. Ran, E. Tirrito, C. Peng, X. Chen, L. Tagliacozzo, G. Su, M. Lewenstein, Tensor Network Contractions, *Lecture notes in Physics*, Springer (2020).

- A. Bermudez, E. Tirrito, M. Rizzi, M. Lewenstein, and S. Hands, Gross-Neveu-Wilson model and correlated symmetry-protected topological phases, *Ann. of Phys.* **399**, 149-180 (2018).

- E. Tirrito, M. Rizzi, G. Sierra, M. Lewenstein, and A. Bermudez, Renormalization group flows for Wilson-Hubbard matter and the topological Hamiltonian, *Phys. Rev. B* **99**, 125106 (2019).

- E. Tirrito, N. Robinson, A. Peter, Maciej Lewenstein, Shi-Ju Ran, and L. Tagliacozzo, Characterizing the quantum field theory vacuum using temporal Matrix Product states, *arXiv:* 1810.08050.

Part I

Quasi-1D interacting fermionic systems

Chapter 2

Recurring topological concepts

2.1 General framework

For a long time, classical and quantum phases have been characterized through the Ginzburg-Landau theory of spontaneous symmetry breaking where the free energy of a system is described as a function of external parameters and order parameters [1–3]. If the system displays a symmetry, the free energy is symmetric with respect to the corresponding order parameter and, for vanishing external parameters it has a unique minimum. When the external parameter is tuned, a phase transition can occur and the system changes from a disordered phase to an ordered phase. In the latter, the minima of the free energy lie at finite values of the order parameter. To minimize the energy the systems chooses one of such finite values of the order parameter, such that the symmetry of the state is then spontaneously broken.

With the discovery of the integer quantum Hall effect, a new family of quantum states was found which did not fit into this simple classification of condensed matter systems described by symmetry breaking.

The quantum Hall effect is observed in two dimensional materials in which the charged particles move around in a region subjected to a strong perpendicular magnetic field [8, 9]. Due to the Lorentz force $\overline{F}_L = q\left(\overline{E} + \overline{v} \times \overline{B}\right)$ these particles will be deflected.

For weak magnetic fields, we can treat the problem classically and the transverse conductivity is proportional to the strength of the magnetic field: $\sigma_{xy} = |\overline{B}|$. In this case, it is possible to observe only quantum oscillations such as the Shubnikov–de Haas oscillations [64] and the de Haas–van Alphen effect [65].

For strong magnetic fields, the trajectory of the electrons is deflected so heavily that they start moving in small circular trajectories. These orbits are quantized. The energy levels of these quantized orbitals are know as *Landau levels* and they take only discrete values $E_n = \hbar\omega_c\,(n + 1/2)$ where ω_c is the cyclotron frequency and n is an integer number. For strong magnetic fields, these Landau levels form highly-degenerated bands that are fully filled and have a non-zero energy gap with respect to each other. Therefore, the electrons in the bulk cannot transport charge through the system anymore: the bulk becomes insulating. At the edges, the electrons start moving in semi-circles with certain chirality depending on their left or right-handedness. These chiral edge states are capable of carrying current and cause the transverse conductivity to still be present in the system. In 1975, Ando *et al.* predicted this phenomenon as a quantum effect and proposed that the transverse conductivity is described by the

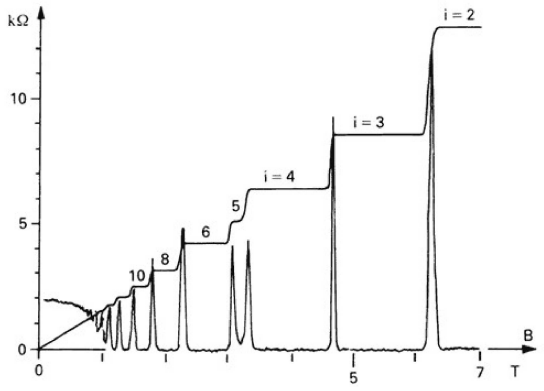

Figure 2.1: **Integer Quantum Hall Effect.** For stronger magnetic fields, the linear proportionality of the transverse conductivity to the strength of the magnetic fields displays plateaux proportional to integer multiples of e^2/h. Also the longitudinal conductivity is plotted, exhibiting spikes whenever the transverse conductivity changes plateau showing that in between the bulk becomes conducting. (Figure taken from [8].)

relation to

$$\sigma_{xy} = \frac{e^2}{h} N, \tag{2.1}$$

where $N \in \mathcal{N}$ is the number of edge states [66]. In 1980 this relation was probed in an experiment by von Klitzing *et al.* [8,9]. The quantized of conductivity are visible in Fig. 2.1.

The presence of edge states that transport charge permits us to understand the QHE in terms of the boundary of the system. Moreover, it is also valuable to understand it in terms of the bulk properties of the interior of the system. This was observed by Thouless, Kohmoto, Nightingale and den Nijs in the paper [11] in which they derived the famous formula that connects the conductivity to a bulk topological invariant.

Thouless *et al.* were inspired by the Hofstadter butterfly spectrum [67]. The Hofstadter model describes a spinless fermion model on a two-dimensional square lattice subjected to a uniform perpendicular magnetic field. In the tight-biding approximation, the model is described by the Hamiltonian

$$\hat{H} = J \sum_{\langle jk \rangle} \left(e^{i\theta_{jk}} \hat{c}_k^\dagger \hat{c}_j + H.c. \right), \tag{2.2}$$

$e^{i\theta_{jk}}$ refers to the Peierls phase factor due to the magnetic field associated to the vector potential A

$$\theta_{jk} = \frac{e}{\hbar} \int_{r_j}^{r_k} A \cdot dl. \tag{2.3}$$

The Peierls phase factor has a periodicity of q sites in the x-direction and p sites in the y-direction. Therefore, the Bloch theorem remains valid and the electronic wavefunctions can be written as

$$\Psi_{nk}(r) = e^{ik \cdot r} u_k(r), \tag{2.4}$$

where u_{nk} is a periodic function defined in a magnetic unit cell and k is the quasi-momentum.

Fig 2.2 shows the celebrated Hofstadter butterfly. The energy spectrum is presented in terms of the number of magnetic flux quanta $\phi = \Phi/\phi_0 = p/q$, where Φ is the magnetic flux and $\phi_0 = h/e$ is the flux quantum. Fig. 2.2 also depicts a fractal

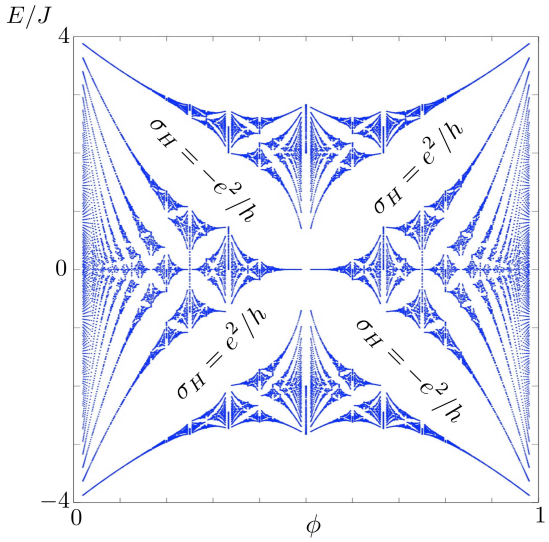

Figure 2.2: **The Hofstadter butterfly spectrum.** Energy spectrum of the Hofstadter model in terms of the magnetic flux $\phi = p/q$. The figure displays a fractal structure with energy gaps. The Hall conductivity σ_{xy} is quantized in the energy gaps. The value of the Hall conductivity in the principal wings is presented. (Figure taken from [67].)

structure displaying several energy gaps. If the Fermi energy E_F lies in an energy gap, the Hall conductivity is quantized and remains constant as long as the gap is open.

Using the Kubo formula of linear response theory, Thouless, Kohmoto, Nightingale, and den Nijs found that the transverse conductivity can be written in terms of the occupied states using the closure relation:

$$\sigma_{xy} = \frac{e^2}{h} \sum \int \frac{1}{2\pi i} \int_{BZ} \left[\left\langle \frac{\partial u_k^n}{\partial k_x} | \frac{\partial u_k^n}{\partial k_y} \right\rangle - \left\langle \frac{\partial u_k^n}{\partial k_y} | \frac{\partial u_k^n}{\partial k_x} \right\rangle \right] \tag{2.5}$$

The last equation highlights the proportionality between the Hall conductivity and the sum over the occupied bands of a quantity, called the Chern number C. The Chern number is expressed as the surface integral over the whole Brillouin zone of a function of the eigenvectors of the band α. Interestingly, the Chern number is defined as

$$C^\alpha = \frac{1}{2\pi i} \int_{BZ} \left[\left\langle \frac{\partial u_k^n}{\partial k_x} | \frac{\partial u_k^n}{\partial k_y} \right\rangle - \left\langle \frac{\partial u_k^n}{\partial k_y} | \frac{\partial u_k^n}{\partial k_x} \right\rangle \right] \tag{2.6}$$

Therefore, from the Eqs. (2.5) and (2.6), the number of edge states is mathematically determined by the value of an integer topological invariant C^α. This topological invariant is an integer that cannot change unless the filled energy bands touch, closing the gap of the system. Therefore, for small perturbations/disorder, the transverse conductivity remains unaltered, and one says that there is topological protection.

Topology is the branch of mathematics, introduced by J. B. Listing, originally used to classify shapes of $3D$ objects [68]. He observed that different objects are topologically equivalent if they can be smoothly transformed into each other, and he established a new language to describe the quantitative shape of geometric objects without making use of ordinary quantities that are usually employed to define the shape of an object. He observed that different topologies are classified by whole numbers, like the number of holes, that cannot change gradually. Mathematically these numbers can be described as integrals over the local curvature of the corresponding surface.

In condensed matter systems the concept of topology is more abstract and it can be applied to determine the topological properties of some phases of matter. A topological property of a phase is described by a set of quantized numbers related to the so-called topological invariants of the phase.

Topological properties are usually defined for spectrally gapped ground states that can be described through a certain manifold without the boundary of local Hamiltonian at zero temperature. Therefore, two systems belong to the same topological class if they can be transformed into each other such that the gap and the locality are preserved.

Moreover, an alternative characterization of topological classes uses the entanglement between disconnected parts of the system, typically referred to as subsystems. In this case, a quantum state has topologically trivial entanglement if it can be smoothly transformed into a state where each subsystem is an independent state where a measurement on that part has no effect on other parts of the system. The categorization distinguishes two classes of states: long-range entangled (LRE) states and short-range entangled (SRE) states [69, 70]. A state is called long-range entangled if it cannot be transformed under local-unitary transformation

$$U = \mathcal{T}\left[e^{-i\int_0^1 dg\tilde{H}(g)}\right], \tag{2.7}$$

where $\tilde{H}$ contains only local hermitian terms, to a fully unentangled state. States that are no product state but neither connectable through such a time evolution have different topologies and are so-called intrinsic topological states. All other states are called short-range entangled. They can be further distinguished by asking whether they are still connectable through a transformation like the above if $\tilde{H}$ displays some symmetry. States which under this constraint are unconnectable are considered different symmetry-protected topological states (SPT).

Quantum Hall insulators are examples of SPT phases. Since their experimental discovery [8,9,12], the field of topological insulators has been rapidly growing. Initially, it was believed that topological quantum states can only exist in $2D$ and if the time-reversal symmetry is broken applying the magnetic field. In 1988 Haldane realized that the necessary condition for a quantum Hall effect was not a magnetic field but just the broken time-reversal invariance [49]. He proposed a model based on two-dimensional graphene. The tight-binding approximation of this model can be seen as honeycomb lattice for the electrons that can hop along nearest-neighbor bonds with real matrix element and along the second-neighbor bonds with a complex matrix element. This model is also called the anomalous Hall effect or Chern insulator.

A generalization of Haldane's model was put forward by Kane and Mele [43] and Bernevig and Zhang [44] who predicted TR symmetric topological insulators due to spin-orbit interaction. This kind of topological insulators are called quantum spin Hall insulators and were observed experimentally in HgTe/CdTe quantum structures [45–47]. QSH materials are closely related to QH insulators; they are characterized by a charge excitation gap in the 2D bulk and gapless helical edge states that lie in the bulk gap and are protected by TR symmetry. The edge states appear in pairs at the surface and their propagation direction depends on the spin of the particle.

2.2 Discrete symmetries

Symmetries are very important in quantum mechanics. They are represented by operators that have to preserve the absolute value of the scalar product of any two

vectors in the Hilbert space. They can thus be either unitary operators, preserving the scalar product, or anti-unitary operators turning the scalar product into its complex conjugate. Normal unitary (anti-unitary) symmetries of a Hamiltonian do not have particularly interesting consequences for topological classification. One may always make the Hamiltonian block diagonal reducing the problem to the study of a single block, or a few degenerate blocks leading to the concept of spontaneous symmetry breaking.

In this section, following Refs. [14, 15], we will deal with the discrete symmetries: time-reversal (TR) $\mathcal{T}$, particle-hole (PH) $\mathcal{C}$ and chiral, also called sub-lattice, $\mathcal{S}$ symmetry. These discrete symmetries impose certain constraints on an irreducible Hamiltonian, for instance, by forcing it to be a real matrix or to be block off-diagonal.

The basic properties of $\mathcal{T}$, $\mathcal{P}$, $\mathcal{C}$ symmetries are:

- $\mathcal{T}$ is an anti-unitary operator that commutes with the Hamiltonian $\hat{H}$.
- $\mathcal{C}$ is an anti-unitary operator that anti-commutes with the Hamiltonian $\hat{H}$.
- $\mathcal{S}$ is a unitary operator that anti-commutes with $\hat{H}$.

In the following, we review how different symmetries are implemented in fermionic systems. Let us consider a general non-interacting system described by the following Hamiltonian:

$$\hat{H} = \sum_{i,j} \hat{\Psi}_i^\dagger \hat{\mathcal{H}}_{i,j} \hat{\Psi}_j = \hat{\Psi}^\dagger \hat{\mathcal{H}} \hat{\Psi}, \tag{2.8}$$

where $\hat{\mathcal{H}}_{i,j}$ is a $N \times N$ Hamiltonian. For our purposes, it is convenient to introduce the symmetry transformations in terms of their action on the fermionic operators. That is a linear transformation:

$$\hat{\Psi}_i \to \hat{\Psi}'_i = \mathcal{U} \hat{\Psi}_i \mathcal{U}^{-1} = U_i^j \hat{\Psi}_i, \tag{2.9}$$

where $\mathcal{U}$ and $\hat{\Psi}_i$ are second quantized operators that act on states in the fermionic Fock space.

Now the system is invariant under $\mathcal{U}$ if the canonical anti-commutation relation and $\hat{H}$ are preserved

$$\left\{\hat{\Psi}_i, \hat{\Psi}_j^\dagger\right\} = \mathcal{U} \left\{\hat{\Psi}_i, \hat{\Psi}_j^\dagger\right\} \mathcal{U}^{-1} \qquad \text{and} \qquad \mathcal{U} \hat{H} \mathcal{U}^{-1} = \hat{H}. \tag{2.10}$$

The former condition implies that U_i^j is a unitary matrix while the latter leads to $(U^\star)_k^i \, \hat{\mathcal{H}}^{k,l} U_l^j = \hat{\mathcal{H}}^{i,j}$, or $U^\dagger \hat{\mathcal{H}} U = H$ in matrix notation. A similar definition also applies to anti-unitary symmetry operations.

Time-Reversal symmetry

Let us now consider TRS. It is an anti-unitary operator that acts on the fermion creation and annihilation operators as

$$\hat{\mathcal{T}} \hat{\Psi}_i \hat{\mathcal{T}}^{-1} = (U_T)_i^j \, \hat{\Psi}_j, \qquad \hat{\mathcal{T}} i \hat{\mathcal{T}}^{-1} = -i. \tag{2.11}$$

A system is TR invariant if $\hat{\mathcal{T}}$ preserves the canonical anti-commutator and if the Hamiltonian satisfies:

$$\hat{\mathcal{T}} \hat{H} \hat{\mathcal{T}}^{-1} = \hat{H}. \tag{2.12}$$

In the non-interacting systems, this condition leads to

$$\hat{\mathcal{T}}: \qquad U_T^\dagger \hat{\mathcal{H}}^\star U_T = +\hat{\mathcal{H}}. \tag{2.13}$$

It can be represented as $\hat{\mathcal{T}} = U_T\hat{\mathcal{K}}$ where $\hat{\mathcal{K}}$ denotes complex conjugation and U_T is a unitary operator. Applying the TRS condition in eq. (2.12) twice one obtains $(U_T^\star U_T)^\dagger \hat{\mathcal{H}} (U_T^\star U_T)$. This means that $U_T^\star U_T$ should be a multiple of the identity matrix I due to the Shur's lemma, i.e., $U_T^\star U_T = e^{i\alpha} I$. Since U_T is a unitary matrix, it follows that $U_T^\star = e^{i\alpha} U_T^\dagger$. Hence we find $e^{2i\alpha} = 1$, which leads to the two possibilities $U_T^\star U_T = \pm I$. Thus acting on a fermion operator $\hat{\Psi}_I$ we obtain

$$\mathcal{T}^2 \hat{\Psi}_i \mathcal{T}^{-2} = (U_T^\star U_T)_i = \pm \hat{\Psi}_i. \tag{2.14}$$

To summarize, TR operation $\mathcal{T}$ satisfies

$$\mathcal{T}^2 = (\pm I)^N \qquad \text{when} \qquad U_T^\star U_T = \pm I. \tag{2.15}$$

Particle-hole symmetry

Particle-hole is a unitary transformation that mixes fermion creation and annihilation operators:

$$\hat{\mathcal{C}} \Psi_i \hat{\mathcal{C}}^{-1} = (U_C^\star)_i^j \, \hat{\Psi}_j^\dagger. \tag{2.16}$$

It flips the sign of the $U(1)$ charge, $\hat{\mathcal{C}}\hat{Q}\hat{\mathcal{C}}^{-1} = -\hat{Q}$ where $\hat{Q} = \hat{N} - N/2$ and $\hat{N}$ the total number of particle. Requiring that the canonical anti-commutation relation is invariant under $\hat{\mathcal{C}}$ one finds that U_C is a unitary matrix. For the case of a non-interacting Hamiltonian $\hat{H}$, we have $\hat{H} = \mathcal{C}\hat{H}\mathcal{C}^{-1}$,

$$\hat{\mathcal{C}} : \qquad U_C^\dagger \hat{\mathcal{H}}^T U_C = -\hat{\mathcal{H}}. \tag{2.17}$$

By repeating the same arguments as in the case of TRS, we find that there are two kinds of charge conjugation transformations:

$$\mathcal{C}^2 = (\pm I)^N \qquad \text{when} \qquad U_C^\star U_C = \pm I. \tag{2.18}$$

In conclusion, $\mathcal{C}$ is indeed an anti-unitary operator that can be decomposed as $\hat{\mathcal{C}} = \hat{U_C}\hat{\mathcal{K}}$ where $\hat{U_C}$ is a unitary operator.

Chiral symmetry

The combination of $\mathcal{T}$ with $\mathcal{C}$ leads to a third symmetry: the so-called chiral or sublattice symmetry. That is, one can have a situation where both $\mathcal{T}$ and $\mathcal{C}$ are broken, but their combination is satisfied by

$$\mathcal{S} = \hat{\mathcal{T}} \cdot \hat{\mathcal{C}}. \tag{2.19}$$

The chiral symmetry $\hat{\mathcal{S}}$ acts on fermion operators as:

$$\hat{\mathcal{S}} \hat{\Psi}_i \hat{\mathcal{S}}^{-1} = (U_c U_T)_i^j \, \hat{\Psi}_j. \tag{2.20}$$

It follows from $\hat{H} = \hat{\mathcal{S}}\hat{H}\hat{\mathcal{S}}^{-1}$ that the invariance of a quadratic Hamiltonian $\hat{H}$ under $\hat{\mathcal{S}}$ is described by:

$$\hat{\mathcal{S}} : \qquad U_S^\dagger \hat{\mathcal{H}} U_S = -\hat{\mathcal{H}} \qquad \text{where} \qquad U_S = U_C^\star U_T^\star. \tag{2.21}$$

Note that $\mathrm{Tr}\hat{\mathrm{H}} = 0$ follows immediately from condition in Eq. (2.21). Applying the same reasoning that we used to derive $\hat{\mathcal{S}}^2 = \hat{\mathcal{C}}^2 = (\pm I)^N$, we find that $U_S^2 = e^{i\alpha} I$. By redefining $U_s \to e^{i\alpha/2} U_S$, the chiral symmetry condition for single-particle Hamiltonian simplifies to:

$$\hat{\mathcal{S}} : \left\{ \hat{\mathcal{H}}, U_S \right\} = 0, \qquad U_S^2 = U_S^\dagger U_S = I. \tag{2.22}$$

Class	T	C	S	$d=0$	$d=1$	$d=2$	$d=3$
AI	+1	0	0	$\mathcal{Z}$	0	0	0
CI	+1	-1	1	0	0	0	$2\mathcal{Z}$
AII	-1	0	0	$2\mathcal{Z}$	0	$\mathcal{Z}_2$	$\mathcal{Z}_2$
D	0	+1	0	$\mathcal{Z}_2$	$\mathcal{Z}_2$	$\mathcal{Z}$	0
A	0	0	0	$\mathcal{Z}$	0	$\mathcal{Z}$	0
BDI	+1	+1	1	$\mathcal{Z}_2$	$\mathcal{Z}$	0	0
AIII	0	0	1	0	$\mathcal{Z}$	0	$\mathcal{Z}$
CII	-1	-1	1	0	$2\mathcal{Z}$	0	$\mathcal{Z}_2$
C	0	-1	0	0	0	$2\mathcal{Z}$	0
DIII	-1	+1	1	0	$\mathcal{Z}_2$	$\mathcal{Z}_2$	$\mathcal{Z}$

Table 2.1: **Periodic table of topological insulators and superconductors.** Here d is the space dimension. The left-most column (AI, CI,..., DIII) denotes the ten symmetry classes of fermionic Hamiltonians, which are characterized by the presence/ absence of time-reversal (T), particle-hole (C), and chiral (S) symmetry. The entries $\mathcal{Z}$, $\mathcal{Z}_2$, $2\mathcal{Z}$, and 0 represent the presence/absence of non-trivial topological insulators/superconductors.

2.3 Ten fold way

Let us now discuss a general symmetry classification of single particle Hamiltonians in terms of discrete symmetries [71]. So far we have considered the following set of discrete symmetries (see sec. 2.2):

$$\begin{aligned} T^{-1}\hat{\mathcal{H}}T &= \mathcal{H}, \qquad T = U_T\mathcal{K} \qquad U_T U_T^\star = \pm I \\ C^{-1}\hat{\mathcal{H}}C &= -\mathcal{H}, \qquad C = U_C\mathcal{K} \qquad U_C U_C^\star = \pm I \\ S^{-1}\hat{\mathcal{H}}S &= -\mathcal{H}, \qquad S = U_S\mathcal{K} \qquad U_S^2 = \pm I \end{aligned} \tag{2.23}$$

where $\hat{\mathcal{K}}$ is the complex conjugation operator. As it turns out, this set of global symmetries is exhaustive. That is, without loss of generality, we may assume that there is only a single TRS with operator $\hat{\mathcal{T}}$ and a single PHS with operator $\hat{\mathcal{C}}$. Now it is easy to see that there are only ten possible ways in which a Hamiltonian can transform under the general non-unitary symmetries in eq. (2.23). First, we observe that there are three different possibilities in which $\hat{H}$ can transform under TRS ($\hat{\mathcal{T}}$)

- $\hat{H}$ is not TR invariant which we denote by $\mathcal{T} = 0$ (cf. Table 2.1).
- $\hat{H}$ is TR invariant and $\hat{\mathcal{T}}^2 = +I$ in which case we write $\mathcal{T} = +1$ (cf. Table 2.1).
- $\hat{H}$ is symmetric under TR and $\hat{\mathcal{T}}^2 = -I$ which we denotes by $\hat{\mathcal{T}} = -1$ (cf. Table 2.1).

Similarly, there are three possible ways under which the Hamiltonian can transform under the PHS with PH operator $\hat{\mathcal{C}}$. For those three possibilities we write $C = 0, \pm 1$. Hence, there are $3 \times 3 = 9$ possibilities in which $\hat{H}$ can transform under both TRS and PHS.

These are not all the ten cases, since it is also necessary to consider the behaviour of the Hamiltonian under the product of $\hat{\mathcal{S}} = \hat{\mathcal{T}} \cdot \hat{\mathcal{C}}$. For 8 out of 9 possibilities, the presence or absence of $\hat{\mathcal{S}} = \hat{\mathcal{T}} \cdot \hat{\mathcal{C}}$ is fully determined by how $\hat{H}$ transforms under TRS and PHS, but in the case where both TRS and PHS are absent, there exist the extra

possibility that $\hat{\mathcal{S}}$ is still conserved, i.e., either $S = 0$ or $S = 1$ is possible. This then yields 10 possible behaviours of Hamiltonian which are listed in Table 2.1 that is the so-called A-Z classification.

Moreover in Table 2.1 each entry gives the topological classification of a system with a given combination of symmetries and dimensionality. In other words, it gives us the possible values the topological invariant Q that such systems can take. A $\mathcal{Z}$ entry tells us the topological invariant is an integer number $Q = 0, \pm 1, \pm 2, \cdots$. An example of such system is the quantum Hall effect, for which the topological invariant is the Chern number. The value of Q specifies the number of chiral edge states and their chirality, which is opposite for opposite signs of Q. Finally, a $\mathcal{Z}_2$ entry means that there are only two distinct topological phases with $Q = \pm 1$.

2.4 Topological invariants

In this section, we briefly introduce the topological invariants that characterize the topological phases. In particular, we will deal with the Berry phase and Berry curvature following the approach suggested by Bernevig in [13] and then we will define the Chern number and the winding number as discussed in [14].

2.4.1 Berry phase and Berry Curvature

The Berry phase appears in the adiabatic motion of a particle. Let us consider a Hamiltonian $\hat{H}(\overline{r})$ depending of the parameters $r_i(t)$, $1 \leq i \leq N_{parameter}$. At each time t, the Hamiltonian has N instantaneous eigenvectors $|n(\overline{r})\rangle$ labeled by n and satisfying

$$\hat{H}(\overline{r})\,|n(\overline{r})\rangle = E_n(\overline{r})\rangle |n(\overline{r})\rangle. \tag{2.24}$$

Now we consider the time evolution of the state $|n(\overline{r})\rangle$.

$$|\psi(t)\rangle = e^{i\gamma(t)} e^{-i\int_0^t E_n(\overline{r}(t))} |n(\overline{r})\rangle \tag{2.25}$$

where the second factor is the dynamical phase factor. To find the Berry phase, we insert the expression of $|\psi(t)\rangle$ defined in eq. (2.25) in the Schrödinger equation

$$\frac{\partial}{\partial_t}|\psi(t)\rangle = \hat{H}(\overline{r})\,|\psi(t)\rangle \tag{2.26}$$

and project it on the state $|n(\overline{r})\rangle$ to find

$$\gamma = \mathrm{Im}\int_\Gamma i\langle n(\overline{r})\,|\partial_{\overline{r}}|n(\overline{r})\rangle \tag{2.27}$$

where Γ is the path followed by $\overline{r}$ the parameter space. We define the Berry connection as

$$\mathcal{A}^n(\overline{r}) = \langle n(\overline{r})\,|\partial_{\overline{r}}|n(\overline{r})\rangle \tag{2.28}$$

One notes that $\mathcal{A}^n$ is not a gauge-invariant quantity. One can thus argue that the phase can be canceled by a suitable gauge transformation. However, in the case of a closed path, γ^n is gauge invariant and cannot be removed by a gauge transformation. In this case, one calls it the Berry phase or the geometric phase. We finally apply Stokes theorem:

$$\gamma^n = \mathrm{Im}\int_\Gamma \left(\overline{\nabla}_r \wedge \mathcal{A}^n\right) dS, \tag{2.29}$$

where the integral is performed on the surface encircled by the closed path Γ, and we define the Berry curvature:

$$\mathcal{F}^n(\overline{r}) = \overline{\nabla}_r \wedge \mathcal{A}^n, \tag{2.30}$$

which is a gauge invariant quantity.

2.4.2 Chern Number and winding number

We consider a translationally invariant system with periodic boundary conditions, described by the following Hamiltonian in Bloch representation

$$\hat{H} = \sum_k \Psi^\dagger_\alpha(\overline{k})\mathcal{H}_{\alpha,\alpha'}(\overline{k})\Psi_{\alpha'}, \tag{2.31}$$

where $\Psi^\dagger_\alpha$ creates a fermion of flavour $\alpha = 1, \cdots, N$ at momentum $\overline{k}$ in the Brillouin zone (BZ) and the summation over α and α' is implicit. Energy bands are obtained by diagonalizing the $N \times N$ matrices $\mathcal{H}(k) = \sum_{\alpha,\alpha'} \mathcal{H}_{\alpha,\alpha'}(\overline{k})$ at every momentum in BZ with the aid of a unitary transformation $U(\overline{k})$.

$$U(\overline{k})\mathcal{H}(k)U^\dagger(\overline{k}) = \mathrm{diag}\left(\epsilon_{\mathrm{m+n}}, \cdots \epsilon_{\mathrm{n}+1}, \epsilon_{\mathrm{n}}, \cdots \epsilon_1\right), \tag{2.32}$$

with $m, n \in \mathcal{Z}$, such that $m + n = N$.

We assume that a gap exists between the n-th and $(n+1)$-th eigenenergies. This allows to adiabatically deform the Bloch Hamiltonian $\mathcal{H}(k)$ to the flat band Hamiltonian:

$$\mathcal{Q}(k) = U(k)\begin{bmatrix} I_m & 0 \\ 0 & -I_n \end{bmatrix} U^\dagger(k) \tag{2.33}$$

and assigns the energy -1 and $+1$ to all states in the bands below and above the gap, respectively. This deformation preserves the eigenstates, but removes the non-universal information about energy band from the Hamiltonian: the degeneracy of its eigenspace equips the flat-band Hamiltonian $\mathcal{Q}(k)$ with an extra $U(n) \times U(m)$ gauge symmetry. $U(\overline{k})$ that diagonalizes $\mathcal{Q}(k)$ is an element of $U(n+m)$ for every $k \in BZ$, therefore we are free to change the basis for its lower and upper bands by a $U(n)$ and $U(m)$ transformation, respectively. Hence $\mathcal{Q}(k)$ is an element of the space $C_0 = U(m+n)/U(n) \times U(m)$ and it defines the map

$$\mathcal{Q} : BZ \to C_0. \tag{2.34}$$

The group of topologically distinct maps Q or equivalently, the number of topologically distinct Hamiltonians $\mathcal{H}$ is given by the homotopy map:

$$\pi_d\left(C_0\right), \tag{2.35}$$

which gives us the value of the topological invariant.

To verify that a given system is in a topological phase, one computes topological invariants or topological quantum numbers of the ground state. Such invariants are automatically numbers in the group of possible topological phases. We have two kinds of topological invariants: the Chern number and the winding number.

In the physical systems that we want to describe the manifold, M is the BZ and the analog of the tangent plane on M is a space spanned by the Bloch states of the occupied bands at given momentum $\overline{k} \in BZ$. The Gaussian curvature of different geometry is now generalized to a curvature form called Berry curvature $\mathcal{F}$ defined in eq. (2.30).

Using the unitary transformation $\hat{U}$, we can generalize the definition of the Berry connection presented in eq. (2.28) as:

$$\mathcal{A}_i = \sum_\alpha U_\alpha^\dagger \partial_i U_\alpha. \tag{2.36}$$

Now we can define the Chern number and the winding number:

- **Chern number**: It represents the generalization of Gauss-Bonnet theorem:

$$2C^{(1)} = \frac{1}{2\pi}\int_{BZ} \mathrm{Tr}\mathcal{F} = \frac{i}{\pi}\int_{BZ} d^2k \mathrm{Tr}\mathcal{F}_{12}, \tag{2.37}$$

  this defines a gauge-invariant quantity, the first Chern number defined in Eq. 2.6. For any dimensional space, we obtain that:

$$2C^{(s)} = \frac{1}{s!}\left(\frac{1}{2\pi}\right)^s \int_{BZ} \mathrm{Tr}\left[\mathrm{F}^{\mathrm{s}}\right], \tag{2.38}$$

- **Winding number**: We consider a different representation of the Chern number $C^{(s)}$. In terms of flat band projector Hamiltonian $\mathcal{Q}(k)$, it can be written as

$$C^{(s)} \propto \epsilon_{i_1\cdots i_d}\int_{BZ} d^dk \mathrm{Tr}\left(\mathcal{Q}(\mathrm{k})\partial_{\mathrm{i_1}}\mathcal{Q}(\mathrm{k})\cdots\partial_{\mathrm{i_d}}\mathcal{Q}(\mathrm{k})\right). \tag{2.39}$$

  The form of $C^{(s)}$ in Eq. (2.39) allows to interpret it as the winding number of the unitary transformation $\mathcal{Q}(k)$ over the compact BZ. In the odd dimension of space, we can define an alternative topological invariant. If we consider a system with chiral symmetry by modifying Eq. (2.39) and using the chiral operator S we obtain that:

$$W^{(s)} = \frac{(-1)^s s!}{2(2s+1)!}\left(\frac{i}{2\pi}\right)^{s+1}\epsilon_{i_1\cdots i_d}\int_{BZ} d^dk \mathrm{Tr}\left(\mathrm{S}\mathcal{Q}(\mathrm{k})\partial_{\mathrm{i_1}}\mathcal{Q}(\mathrm{k})\cdots\mathrm{S}\mathcal{Q}(\mathrm{k})\partial_{\mathrm{i_d}}\mathcal{Q}(\mathrm{k})\right) \tag{2.40}$$

2.5 Examples of topological phases

2.5.1 SSH model

The SSH model was first introduced by W. P. Su *et al* in 1979 to describe solitons in polyacetylene [72,73]. In recent times, it attracted the attention of many researchers because of its interesting topological properties, non-trivial edge states, and fractional charge [74, 75]. We consider spinless fermions on a one-dimensional lattice with alternating hopping strengths at half-filling. This staggered hopping in the SSH model is found naturally in various condensed matter systems as a consequence of the so-called Peierls instability [76].

The Hamiltonian of the model is the following:

$$\hat{H} = -J_v\sum_{n=1}^{L}\hat{c}_{A,n}^\dagger\hat{c}_{B,n} - J_w\sum_{n=1}^{L}\hat{c}_{B,n}^\dagger\hat{c}_{A,n+1} + H.c.. \tag{2.41}$$

This is depicted in Fig. 2.3(a). It is easy to diagonalize the Hamiltonian $\hat{H}$ and find the state energy and wave function by converting Eq. (2.41) into Fourier space and using Bloch theorem.

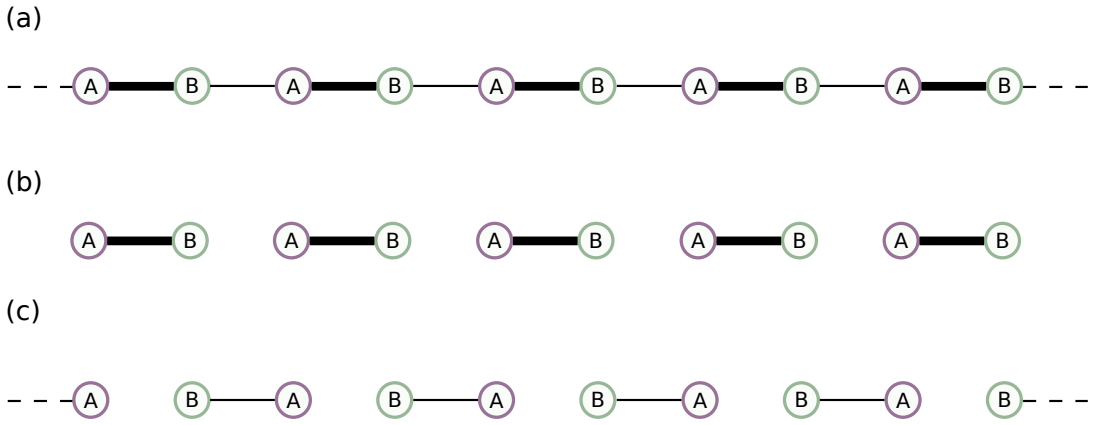

Figure 2.3: **Representation of SSH chain.** (a) Open SSH chain with intra cell hopping J_v and extra cell hopping J_ω. (b) Open SSH chain in the limit $J_w = 0$ and $J_v \neq 0$. (c) Open SSH chain in the limit $J_v = 0$ and $J_w \neq 0$.

The Fourier transformation of the creation (annihilation) operator can be written as

$$\hat{c}_{n,\alpha} = \frac{1}{\sqrt{L}} \sum_{k=-\pi}^{\pi} e^{-ikn} \hat{c}_{k,\alpha} \qquad \hat{c}^\dagger_{n,\alpha} = \frac{1}{\sqrt{L}} \sum_{k=-\pi}^{\pi} e^{ikn} \hat{c}^\dagger_{k,\alpha}, \tag{2.42}$$

where k is the wave vector. When $J_v = J_w$ the lattice is periodic with a unit cell of one site per cell so k is well-defined in the region $[-\pi, \pi]$. For $J_v \neq J_w$ the periodicity becomes two sites per unit cell which makes the k vector defined in the region $[-\pi, \pi]$. The complete Hamiltonian in Fourier space becomes:

$$H = \sum_k \begin{bmatrix} \hat{c}^\dagger_{A,k} & \hat{c}^\dagger_{B,k} \end{bmatrix} \begin{bmatrix} 0 & -J_v - J_w e^{-ik} \\ -J_v - J_w e^{ik} & 0 \end{bmatrix} \begin{bmatrix} \hat{c}_{A,k} \\ \hat{c}^\dagger_{B,k} \end{bmatrix} \tag{2.43}$$

Using the Pauli matrices, this two-level system can be represented as:

$$\mathcal{H}(k) = \overline{h}(k) \cdot \overline{\sigma} \qquad \text{where} \qquad \overline{h}(k) = (-(J_v + J_w \cos k), -J_w \sin k, 0)\,, \tag{2.44}$$

with $\overline{h}(k)$ a pseudo-spin vector. The eigenstates of any system written in the form expressed in eq. (2.44) are:

$$|E_-\rangle = \begin{bmatrix} \sin\left(\frac{\theta}{2}\right) \\ e^{-i\phi} \cos\left(\frac{\theta}{2}\right) \end{bmatrix}, \qquad |E_+\rangle = \begin{bmatrix} \cos\left(\frac{\theta}{2}\right) \\ e^{-i\phi} \sin\left(\frac{\theta}{2}\right) \end{bmatrix}. \tag{2.45}$$

Here $|E_-\rangle$ is the ground state for 1 fermion, θ and ϕ are defined as:

$$\cos\theta = \frac{h_z}{|\overline{h}(k)|}, \qquad e^{i\phi} = \frac{h_x + ih_y}{\sqrt{h_x^2 + h_y^2}}, \tag{2.46}$$

where $|\overline{h}(k)|$ is the norm of the pseudo-spin vector $\langle(k)$. Putting the definition of h_z, h_y, h_x in the eq.(2.44), we obtain

$$\theta = \frac{\pi}{2} \qquad \phi = \tan^{-1}\left[\frac{J_w \sin k}{J_v + J_w \cos k}\right]. \tag{2.47}$$

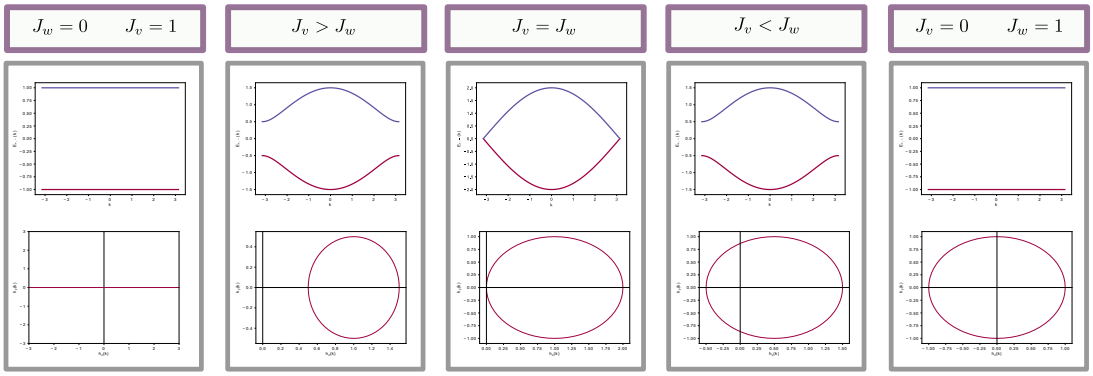

Figure 2.4: **Band structure and pseudo-spin representation of SSH chain.** We plotted the bands of $\hat{H}(k)$ and the pseudo-spin $\overline{h}(k)$ on h_x and h_y plane for different values of J_v and J_ω. We show the phase transition between the trivial topological phase to topological phase. The phase transition point occurs at $J_v = J_\omega$ where the gap between the two bands closes and $\overline{h}(k)$ passes through the origin.

The SSH model has chiral symmetry and it is metallic when $J_v = J_w$ and insulator otherwise. The energy dispersion relation of the SSH model can be derived from eq. (2.44)

$$E(k) = \sqrt{J_v^2 + J_w^2 + 2J_v J_w \cos k}. \tag{2.48}$$

For different values of J_v and J_w dispersion relation is plotted in Fig. 2.4. It can be seen that a gap closes at one point and then it reopens. For $J_v > J_w$ and $J_v < J_w$, dispersion plots are the same but they have different topology.

To understand this, we plot also the trajectory of $\overline{h}(k)$ for these two different cases (see Fig. 2.4). These trajectories on the h_x-h_y plane look very different. For one of the insulating cases, $J_v < J_w$, the vector $\overline{h}(k)$ winds around the origin and for the other case $J_v > J_w$ it does not. Notice that the origin is the point where $\overline{h}(k) = 0$, which follows from the gapless condition. Therefore a loop plotted for the $J_v = J_w$ case would pass through the origin indicating a metallic state. We can see this as a winding number ν (see sec. 2.4.2) that tells whether the trajectory of $\overline{h}(k)$ winds about the origin or not.

It is well known that the analytical expression for ν is given by

$$\nu = -\frac{i}{2\pi}\int_0^{2\pi} dk \frac{\partial \overline{h}(k)}{|\overline{h}(k)|}, \tag{2.49}$$

when $J_v < J_w$, the contour will encircle the origin so that $\nu = 1$, and the system is in the topological phase. In contrast, when $J_v > J_w$, the origin will not be enclosed by the contour so that $\nu = 0$, and the system is in the trivial phase. Therefore, the winding number distinguishes the two apparently equivalent cases. In particular, it is different from zero only in the topological phase.

In the literature, there is another physical quantity that is used to characterize the topological property of $1D$ system, the Zak phase [135] defined as:

$$\gamma = \frac{i}{2\pi}\int_0^{2\pi} dk \mathcal{A}_-, \tag{2.50}$$

where $\mathcal{A}_-$ is the Berry phase defined in sec. 2.4.1. Using the eq. (2.45), the Berry

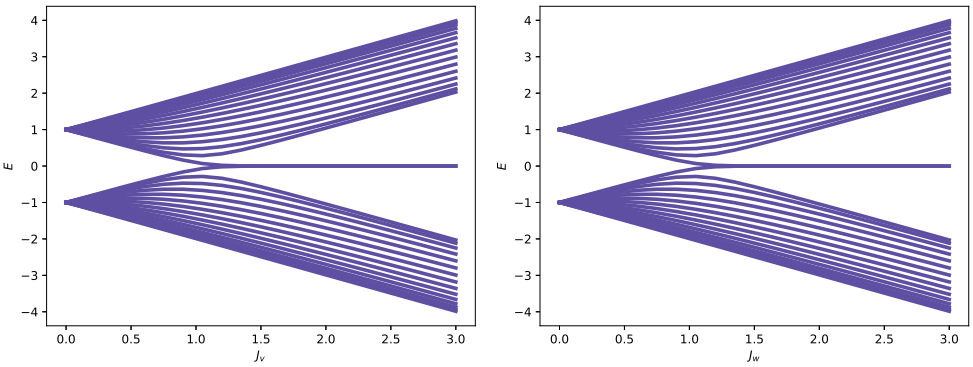

Figure 2.5: **Energy spectrum for open SSH chain.** (a) Energy spectrum as a function of model parameter J_v with $J_w = 1$. (b) Energy spectrum as as a function of J_w with $J_v = 1$.

phase for the lowest energy band is

$$\mathcal{A}_-(k) = i\langle E_-(k)|\frac{d}{dk}|E_-(k)\rangle = -\frac{1}{2}\frac{d\phi}{dk}. \tag{2.51}$$

Now if we integrate this quantity in the Brillouin zone we get

$$\frac{-1}{\pi}\int \mathcal{A}_-(k) = \begin{cases} 1 & J_v < J_w \\ 0 & J_v > J_w \\ \text{undefined} & J_v = J_w \end{cases} \tag{2.52}$$

this quantity determines the features of the two different phases, obtaining a topological phase for $J_v < J_w$ and a trivial insulator for $J_v > J_w$.

SSH model with one site potential

The SSH model with alternating on-site potential is known as the Rice-Mele model [77]. This term breaks the chiral symmetry of the SSH model. The on-site potential is described by the following Hamiltonian:

$$\hat{H}_\Delta = \Delta \sum_{n=1}^{L} \left(\hat{c}^\dagger_{A,n}\hat{c}_{A,n} - \hat{c}^\dagger_{B,n}\hat{c}_{B,n}\right), \tag{2.53}$$

where Δ is the strength of an on-site potential. In Fourier space, we obtain that:

$$H = \sum_k \begin{bmatrix} \hat{c}^\dagger_{A,k} & \hat{c}^\dagger_{B,k} \end{bmatrix} \begin{bmatrix} \Delta & -J_v - J_w e^{-ik} \\ -J_v - J_w e^{ik} & -\Delta \end{bmatrix} \begin{bmatrix} \hat{c}_{A,k} \\ \hat{c}^\dagger_{B,k} \end{bmatrix}, \tag{2.54}$$

where $\mathcal{H}(k) = h_x(k)\sigma_x + h_y(k)\sigma_y + h_z(k)\sigma_z$ with h_x, h_y given by eq. (2.44) and $h_z = \Delta$. The ground state wave function is given by eq. (2.45) with ϕ given by eq. (2.46) and θ given by

$$\theta = \tan^{-1}\left[\frac{\left|J_v + J_w e^{-ik}\right|}{\Delta}\right]. \tag{2.55}$$

Now the Zak phase is no longer quantized, can vary between $[-\pi, \pi]$ for different values of Δ.

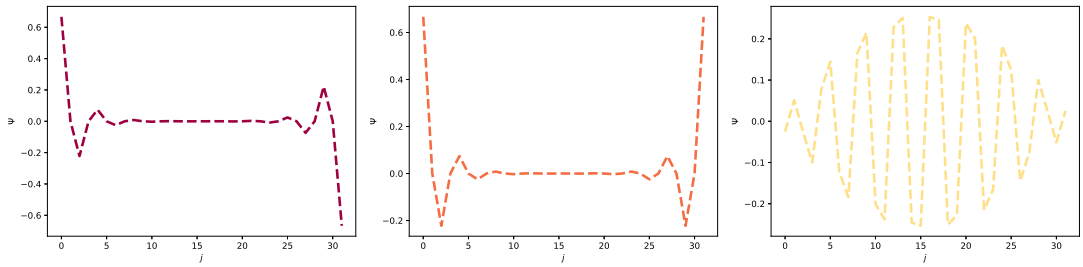

Figure 2.6: **Edgemodes for SSh chain.** Here we plot the amplitude $|\Psi|$ with respect to the position in the chain with 32 sites. (a)-(b) we show the zero energy edge states and (c) non-zero energy eigenstate.

SSH model with open boundary condition

Until now, we have looked into the solutions of a 1D SSH chain with periodic boundaries (i.e. on a ring). In this section, we focus on the physical consequence of the winding number and to do so let us look at the version of the SSH chain with open boundaries (i.e. open chain). The problem is slightly more involved, as there is no translational invariance one cannot make use of the Fourier transformation to diagonalize the Hamiltonian. Therefore we will use the exact diagonalization algorithm to solve the model. Before doing that we consider two cases:

- $J_w = 0$**,** $J_v \neq 0$**.** See Fig.2.3 (b). This case represents a trivial dimer case. The solutions should be the superposition of the A site and B site for each dimer. We can even guess that this should correspond to an insulating state as the chain is now broken and no particle can hop from one end of the chain to the other.

- $J_w \neq 0$**,** $J_v = 0$**.** See Fig. 2.3 (c). In this case, we obtain two isolated sites at the end of the chain. If these two sites carry an electron the energy should be zero because in the SSH model there is no energy contribution for an electron to be held fixed at one site. Consequently, we should expect two zero-energy modes in the system localized at the edges of the chain. Using the same argument as in the previous case we expect this case to describe an insulator.

Let us now solve the Hamiltonian for an open SSH chain and try to see what are the solutions for different parameter values. The plots in Fig.2.5 show the energy spectrum of the eigenstates as we vary the parameter J_v and J_w. One interesting feature we see here is that the zero energy states not only exist in the extreme limit but even for non-zero J_v, although the zero energy states are not quite zero energy states but are very close to zero. Intuitively a dimerized chain should not be conducting and also the zero energy states should be localized at the boundary. Therefore, let us look at the corresponding wave functions of these energy eigenstates in Fig.2.6. We see that the non-zero energy state is de-localized throughout the chain. On the contrary, the zero energy states are exponentially localized at the edges of the chain which we expected from the dimerized limit. These states are called the edge states because they live on the edges of the chain. Also, notice that these edge states only remain zero-energy edge states as long as $J_v < J_w$. Once $J_v > J_w$ there are no zero energy states and all states are de-localized throughout the lattice. The existence of these edge states in the $J_v < J_w$ case makes this case different from the case when $J_v > J_w$. Otherwise, in the bulk, for both these cases, the system behaves like an insulator.

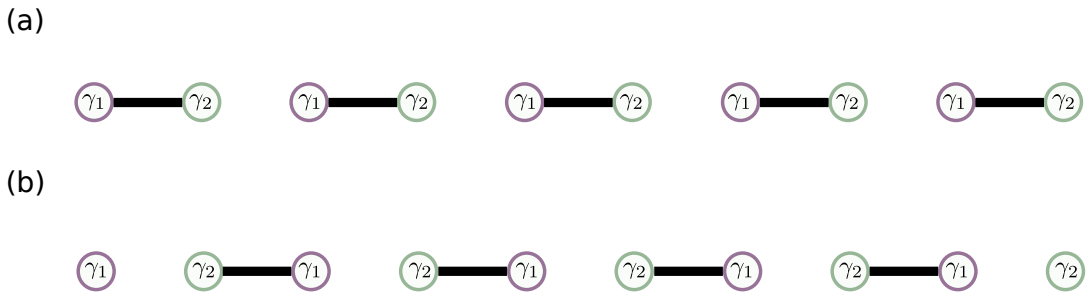

Figure 2.7: **Sketch of the Kitaev Chain.** In (a) the trivial pairing between the Majoranas is shown. In (b) the non-trivial pairing is shown. Here two unpaired Majoranas appear at the edges of the chain.

2.5.2 Kitaev chain

The Kitaev chain was proposed by A. Kitaev, and it is the simplest model that shows unpaired Majorana zero modes [78]. It is a toy model that can be exactly solved, providing a very useful paradigm for Majorana zero modes at the two ends of a quantum wire of a p-wave superconductor. The Kitaev chain is a spinless fermion model with nearest-neighbor hopping and pairing between the sites of a 1D lattice described by the Hamiltonian:

$$\hat{H} = \sum_j \left\{ -J\left(\hat{c}_j^\dagger \hat{c}_{j+1} + \hat{c}_{j+1}^\dagger \hat{c}_j\right) - \mu\left(\hat{c}_j^\dagger \hat{c}_j - \frac{1}{2}\right) + \Delta \hat{c}_j \hat{c}_{j+1} + \Delta^\star \hat{c}_{j+1}^\dagger \hat{c}_j^\dagger \right\}, \tag{2.56}$$

where μ is chemical potential, and $\Delta = \Delta e^{i\theta}$ is a superconducting gap. Consider a chain with L sites and open boundary conditions, we can rewrite the Hamiltonian in the Majorana representation [78, 79] by using Majorana operators $\gamma_{j,\alpha}$:

$$\hat{H} = \frac{i}{2} \sum_j \left\{ -\mu \hat{\gamma}_{j,1}\hat{\gamma}_{j,2} + (J + |\Delta|)\, \hat{\gamma}_{j,2}\hat{\gamma}_{j+1,1} + (-J + |\Delta|)\, \hat{\gamma}_{j,1}\hat{\gamma}_{j+1,2} \right\}. \tag{2.57}$$

Here the Majorana operators are defined as:

$$\gamma_{j,1} = e^{i\frac{\theta}{2}} \hat{c}_j + e^{-i\frac{\theta}{2}} \hat{c}_j^\dagger, \qquad \gamma_{j,2} = -i\left(e^{i\frac{\theta}{2}} \hat{c}_j - e^{-i\frac{\theta}{2}} \hat{c}_j^\dagger\right), \tag{2.58}$$

which satisfy the relations $\hat{\gamma}_{j,\alpha}^\dagger = \hat{\gamma}_{j,\alpha}$ and $\{\hat{\gamma}_{j,\alpha}, \hat{\gamma}_{k,\beta}\} = 2\delta_{j,k}\delta_{\alpha,\beta}$. Now we discuss two specific cases:

First case: $|\Delta| = J = 0$ **and** $\mu \neq 0$. This represents the topological trivial case. The Hamiltonian becomes:

$$\hat{H} = -\mu \sum_j \left(\hat{c}_j^\dagger \hat{c}_j - \frac{1}{2}\right) = \frac{-i}{2} \mu \sum_j \hat{\gamma}_{j,1}\hat{\gamma}_{j,2}. \tag{2.59}$$

The Majorana operators $\hat{\gamma}_{j,1}$ $\hat{\gamma}_{j,2}$ from the same site j are paired together, to form a ground state with the occupation number zero (see Fig. 2.7 (a)).

Second case $|\Delta| = J > 0$ **and** $\mu = 0$**.** In this case the Hamiltonian reads as

$$\hat{H} = iJ \sum_j^{L-1} \hat{\gamma}_{j,2}\hat{\gamma}_{j+1,1}. \tag{2.60}$$

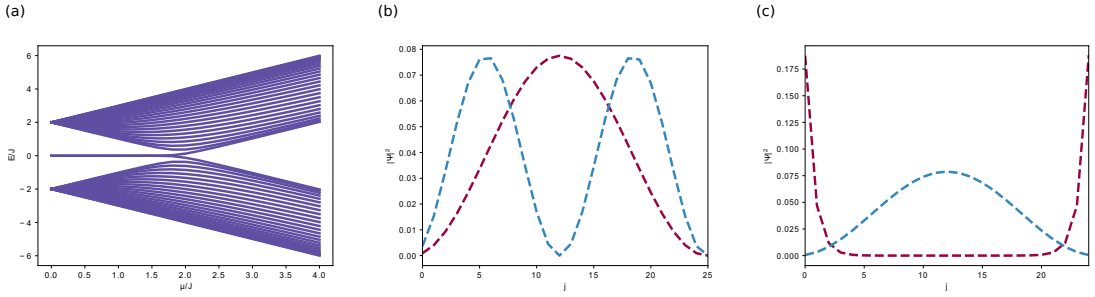

Figure 2.8: **Energy spectrum and eigenmodes for the Kitaev chain.** (a)The energy spectrum plotted in terms of μ. Both energies are rescaled in terms of t. Two zero-energy modes appear for μ smaller than $2t$. (b-c) Probability density of the two modes with the lowest energy with respect to the position. The blue curve corresponds to the lowest energy mode and the red curve to the next higher energy mode. (b) The probability density for $\mu/J = 4.0$. (c) Probability density for $\mu/J = 0$.

Now the Majorana operators $\hat{\gamma}_{j,2}$ and $\hat{\gamma}_{j+1,1}$ from different sites are paired together (see Fig. 2.7 (b)). The ground state of Hamiltonian in eq. (2.60) is easy found by defining new annihilation and creation operators

$$\hat{a}_j = \frac{1}{2}\left(\hat{\gamma}_{j,2} + i\hat{\gamma}_{j+1,1}\right) \qquad \hat{a}_j^\dagger = \frac{1}{2}\left(\hat{\gamma}_{j,2} - i\hat{\gamma}_{j+1,1}\right), \tag{2.61}$$

with $\hat{\gamma}_{j,2}\hat{\gamma}_{j+1,1} = 2\hat{a}_j^\dagger\hat{a}_j$ for $j = 1, 2, \cdots, L$. Subsequently, the Hamiltonian (2.60) can be rewritten in canonical form:

$$\hat{H} = 2J\sum_{j=1}^{L-1}\hat{a}_j^\dagger\hat{a}_j - J(L-1). \tag{2.62}$$

It can be noted that the Hamiltonian does not contain operators $\gamma_{j,1}$ and $\gamma_{L,2}$, i.e. $\left[\gamma_{1,1}, \hat{H}\right] = \left[\gamma_{L,2}, \hat{H}\right] = 0$, while all pairs $(\gamma_{j,2}, \gamma_{j+1,1})$ for $j = 1, 2, \cdots L-1$ form new fermions. The ground states with twofold degeneracy for $J > 0$ satisfy the condition $\hat{a}_j|g\rangle = 0$ for all j and

$$\hat{H}|g\rangle = -J(L-1)|g\rangle. \tag{2.63}$$

These represent zero energy Majorana modes localized at the two ends of the chain. Since $\left[\gamma_{1,1}, \hat{H}\right] = \left[\gamma_{L,2}, \hat{H}\right] = 0$, the two orthogonal ground states of the Kitaev chain model can be constructed as $|g\rangle$ and $\hat{a}^\dagger|g\rangle$ where $\hat{a} = 1/2(\hat{\gamma}_{1,1} + \gamma_{L,2})$ is an ordinary zero-energy fermion operator. These states have different fermionic parities: one is even and the other is odd. To understand this we study the eigenvalues of $\hat{H}$ in function of μ. In Fig.2.8 (a) we show the spectrum of the Hamiltonian (2.56) for different values of μ, which is mirrored at $E/t = 0$ due to the particle-hole symmetry. Considering this, one can see that there are two phases: the topological phase where we have the Majorna edge modes and the trivial phase. In order to be in the first phase, μ has to be smaller than $2t$. To be in the second phase however, μ is required to be bigger than $2t$.

To check if the zero energy states are localized at the edges, we look at the probability density varying position in the chain as shown in Fig. 2.8. The probability density is given by $|\Psi|^2 = |u|^2 + |v|^2$, where u are the eigenvectors corresponding to the electrons and v the eigenvectors corresponding to the holes. For the zero-energy states, we indeed observe that they are localized at the edge in the topological phase

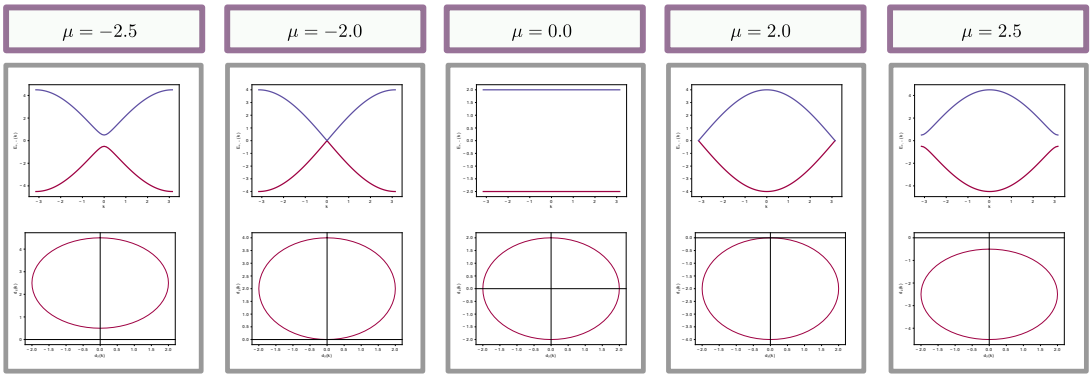

Figure 2.9: **Band structure and pseudo spin representation of Kitaev chain.** In upper panel we plot the band structure of the Kitaev chain in momentum space for $\Delta/J = 1$. Instead in lower panel we plot the Bloch vector $d(k)$ in the plane d_y-d_z . (a) Trivial phase, $\nu = 0$ $\mu = -2.5J$ (b) in between the two phases, $\nu = undifined$, $\mu = -2.0J$ (c) topological phase, $\nu = 1$, $\mu = 0$ (d) in between the two phases, $\nu = undifined$, $\mu = -2.0J$ (e) trivial phase, $\nu = 0$, $\mu = 2.5J$. Here ν is an integer which describes how many times the loop winds around the origin and ν corresponds to the chemical potential. Hence, with ν we can control if the system is topological or not.

and de-localized in a trivial phase. It should still be mentioned that this localization decays the closer one gets to the transition between the phases.

To study the general properties of the Kitaev chain we apply the Fourier transformation. The Hamiltonian in momentum space can be written in Bogoliubov de Gennes (BdG) form:

$$\hat{H} = \frac{1}{2}\sum_k \begin{bmatrix} \hat{c}_k^\dagger & \hat{c}_{-k} \end{bmatrix} \mathcal{H}_{BdG} \begin{bmatrix} \hat{c}_k^\dagger \\ \hat{c}_{-k} \end{bmatrix}, \tag{2.64}$$

where the BdG Hamiltonian is written in terms of Pauli matrices $\overline{\sigma}$ as

$$\mathcal{H}_{BdG}(k) = \overline{d}(k) \cdot \overline{\sigma} = \epsilon(k)\sigma_z + \Delta(k)\cos\theta\sigma_y + \Delta(k)\sin\theta\sigma_y, \tag{2.65}$$

with $\epsilon(k) = -2J\cos k - \mu$, $\Delta(k) = 2\,|\Delta|\sin k$. The energy spectrum is given by:

$$E(k) = \pm\sqrt{\epsilon^2(k) + |\Delta|^2}. \tag{2.66}$$

For $\Delta \neq 0$, the system is in superconducting state. The energy spectrum is always fully gapped except when $2J = +\mu$. In Fig. 2.9 the two lines representing the gap closing are defined. It marks the phase transition between the two distinct phases of the model. We can identify that the system in the region $|J| > \mu/2$ is a topological superconductor. In the other region, the system is a normal superconductor. Another way to calculate these two phases is by measuring the topological invariants. Here we calculate the winding number and the number of Majorana fermions.

In Fig. 2.9, we also show the vector $\overline{d}(k)$ in the d_z-d_y plane. It traces out an ellipse of radious 2 in z-direction and radious 2Δ in y-direction with center at $(\mu, 0)$. The topology of this loop can be characterized by an integer, the winding number ν. This counts the number of times the loop winds around the origin of the d_z-d_y plane. The behavior of the bands can be directly connected to topology since objects with the same topology can be deformed continuously into each other.

As regards the Majorana numbers, we analyze the properties of $\mathcal{H}_{BdG}(k)$. It preserves intrinsic particle-hole symmetry:

$$\mathcal{C}\mathcal{H}_{BdG}(k)\mathcal{C}^{-1} = -\mathcal{H}_{BdG}(-k), \tag{2.67}$$

where $\mathcal{C}$ is the particle-hole operator defined as

$$\mathcal{C} = \sigma_x\mathcal{K} \qquad \text{and} \qquad \mathcal{C}^2 = \pm I. \tag{2.68}$$

According to the topological classification, the Hamiltonian $\mathcal{H}_{BdG}$ belongs to the symmetry class D ($d = 1$) and thus has a $\mathcal{Z}_2$-type topological number. The relevant topological invariant of the system described by the Hamiltonian $\mathcal{H}_{BdG}$ is the so-called Majorana number $\mathcal{M} = \pm 1$, which is the Z_2 index, first formulated by Kitaev [78].

The fermionic systems with superconducting order fall into two categories distinguished by $\mathcal{M}$. One is topologically trivial with $\mathcal{M} = +1$ and the other is non-trivial with $\mathcal{M} = -1$ and the existence of unpaired Majorana zero modes.

To calculate $\mathcal{M}$ we consider the Hamiltonian that can be written in the Majorana representation as:

$$\hat{H} = \frac{i}{4}\sum_{lm\alpha\beta}\mathcal{B}_{\alpha\beta}(l-m)\hat{\gamma}_{l\alpha}\hat{\gamma}_{l\beta} \tag{2.69}$$

where l and m label the lattice sites while α and β denote all other numbers. Then $\mathcal{M}$ is defined as

$$\mathcal{M} = \operatorname{sgn}\left\{\mathrm{P_f}\left[\tilde{\mathrm{B}}(0)\right]\right\}\operatorname{sgn}\left\{\mathrm{P_f}\left[\tilde{\mathrm{B}}(\pi)\right]\right\}, \tag{2.70}$$

where $\tilde{B}(k)$ denotes the Fourier transformation of $B(l-m)$ regarded as a matrix in indices, α, β and $P_f[A]$ denotes the Pfaffian's number where $(P_f[A])^2 = \det[A]$ with A being an anti-symmetric matrix. Applying the Fourier transformation in the Hamiltonian (2.69) we obtain that:

$$\hat{H} = \frac{i}{4}\sum_{k}\begin{bmatrix}\hat{\gamma}_{k,1} & \hat{\gamma}_{k,2}\end{bmatrix}\begin{bmatrix}0 & D(k)\\ -D^{\star}(k) & 0\end{bmatrix}\begin{bmatrix}\hat{\gamma}_{-k,1}\\ \hat{\gamma}_{-k,2}\end{bmatrix} \tag{2.71}$$

with $D(k) = -2J\cos k - 2|\Delta| - \Delta$. The operators $\hat{\gamma_{k,1}}$ and $\hat{\gamma_{k,2}}$ are defined as

$$\hat{\gamma_{k,1}} = \hat{c}^{\dagger}_{-k} + \hat{c}_k \qquad \hat{\gamma_{k,2}} = i\left(\hat{c}^{\dagger}_{-k} - \hat{c}_k\right), \tag{2.72}$$

which satisfy relations

$$\left\{\gamma^{\dagger}_{k,\alpha}, \gamma_{k',\beta}\right\} = 2\delta_{k,k'}\delta_{\alpha,\beta} \qquad \gamma^{\dagger}_{k,\alpha} = \gamma_{-k,\alpha}. \tag{2.73}$$

Note that $\gamma_{k,1}$ and $\gamma_{k,2}$ are not the Majorana operators except when $k = 0$. The matrix $\tilde{B}(k)$ here for $k = 0, \pi$ is anti-symmetric so that the Pfaffian can be given by the upper off-diagonal component $D(k)$ in eq. (2.71). It yields the Majorana number

$$\mathcal{M} = \operatorname{sgn}\{\mathrm{P_f}[\mathrm{D}(0)]\}\operatorname{sgn}\{\mathrm{P_f}[\mathrm{D}(\pi)]\} = \operatorname{sgn}\left(\mu^2 - 4\mathrm{J}^2\right). \tag{2.74}$$

One can check that the topological superconducting phase occurs when $\mathcal{M} = -1$ for $|\mu| < 2J$, the other phase is trivial with $\mathcal{M} = +1$ for $|\mu| > 2J$.

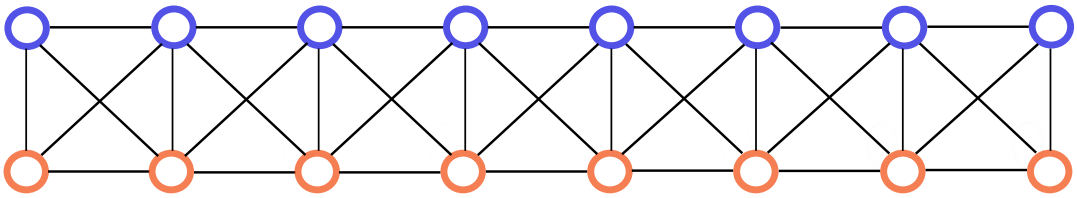

Figure 2.10: **General topological ladder representation.** A model for a quasi 1D topological insulator can be represented as a ladder. The sites of two-leg ladder are represented by blue and orange dots that represent a unit cell. Particles can hop from one site to another along the black lines.

2.5.3 Ladder models

General properties

In this section, following the Ref. [80], we will discuss the topological properties of ladder models described in Fig.2.10. In particular, we will show that depending on the parameters of Hamiltonian, we can identify different types of topological insulators in BDI and AIII symmetry classes. The most general ladder model corresponds to the following Hamiltonian

$$\hat{H} = -\sum_j \left(\hat{\Psi}_j^\dagger C \hat{\Psi}_j + \hat{\Psi}_{j+1}^\dagger T \hat{\Psi}_j + \hat{\Psi}_j^\dagger T^\dagger \hat{\Psi}_{j+1} \right), \tag{2.75}$$

where $\Psi_j^\dagger = \left(\hat{a}_j^\dagger, \hat{b}_j^\dagger\right)^t$, C and T are 2×2 matrices. Both matrices have no dependence on the lattice index j. In momentum space the Hamiltonian reads:

$$\hat{H} = -\sum_k \hat{\Psi}_k^\dagger M(k) \hat{\Psi}_k, \qquad M(k) = C + e^{-ik} T + e^{ik} T^\dagger. \tag{2.76}$$

As any 2×2 Hermitian matrix, it can be written as

$$M(k) = \lambda(k) I + \overline{n}(k) \times \overline{\sigma}, \tag{2.77}$$

where I the identity and $\overline{\sigma}$ a vector of Pauli matrices. Here $\lambda(k)$ is a real function and $\overline{n}(k)$ is a real unit vector in $3D$ space, defined as

$$\overline{n}(k) = \overline{n}_0 + \overline{n}_1 \cos(k) + \overline{n}_2 \sin(k), \tag{2.78}$$

where $\overline{n}_0$, $\overline{n}_1$ and $\overline{n}_2$ are three constant vectors that identify the Bloch sphere.

To have a non-trivial topological ladder we need to impose the chiral symmetry. This means that $\lambda(k) = 0$ and $\overline{n}_0$, $\overline{n}_1$ and $\overline{n}_2$ lie in the same plane. Therefore, we can rewrite $M(k)$ choosing a particular orthonormal basis within that plane made by just two vectors $\overline{n}_1$ and $\overline{n}_2$. In this way we can rewrite the Hamiltonian as a combination of $\sigma_1 = \overline{n}_1 \cdot \overline{\sigma}$ and $\sigma_2 = \overline{n}_2 \cdot \overline{\sigma}$, being $\{\sigma_1, \sigma_2\} = 0$. In conclusion, the most general ladder model for a topological insulator corresponds to a Hamiltonian matrix of the form

$$M(k) = f_1(k)\sigma_1 + f_2(k)\sigma_2, \tag{2.79}$$

where $f_1(k)$ and $f_2(k)$ are two real functions that depend on the momentum through the sine and cosine. Defining

$$\sigma_3 = -\frac{i}{2} \left[\sigma_1, \sigma_2\right], \tag{2.80}$$

it follows that

$$\sigma_3 M(k)\sigma_3 = -M(k). \tag{2.81}$$

Therefore, we can identify the orthogonal direction to the plane where $\overline{n}(k)$ lives with the unitary operator that fulfills the chiral condition that is $U_S = \sigma_3$.

The Hamiltonian matrix $M(k)$ can be related by defining the complex function $z(k)$ and the real function $\varphi(k)$ as

$$z(k) = \rho(k)e^{i\varphi(k)} = f_1(k) + if_2(k), \tag{2.82}$$

so that $\overline{n}(k) = \cos\varphi(k)\overline{n}_1 + \sin\varphi(k)\overline{n}_2$. In this way $\varphi(k)$ is the azimuth angle of the vector $\overline{n}(k)$ when using spherical coordinates if we choose the three Cartesian coordinates x, y, and z in the directions of $\overline{n}_1$, $\overline{n}_2$ and $\overline{n}_3$. Hence the eigenvectors of the Hamiltonian matrix are easy to obtain, as they correspond to vectors $\pm\overline{n}(k)$ in the Bloch sphere representation. That is:

$$\pm\,\overline{n}(k) \to \begin{bmatrix} 1 \\ \pm e^{i\varphi(k)} \end{bmatrix}. \tag{2.83}$$

The eigenstates of Hamiltonian under periodic boundary conditions are therefore:

$$|E(k)\rangle_\pm = \begin{bmatrix} \hat{a}_k^\dagger & \hat{b}_k^\dagger \end{bmatrix} \frac{1}{\sqrt{2}} \begin{bmatrix} 1 \\ \pm e^{i\varphi(k)} \end{bmatrix} |0\rangle, \tag{2.84}$$

whose corresponding energies are

$$E_\pm(k) = \mp\sqrt{f_1^2(k) + f_2^2(k)} = \mp\rho(k). \tag{2.85}$$

Now we can compute the Zak phase which characterizes the topological nature of the system. For the ladder model we obtain that

$$Z = -i\int_{BZ} dk \langle E_\pm(k)|\partial_k|E_\pm(k)\rangle = \frac{\varphi(\pi) - \varphi(0)}{2} = \frac{\Delta\varphi}{2}. \tag{2.86}$$

As we see, the Zak phase is quantized according to the winding number around the origin of $z(k)$ in the complex plane and equivalently, to the winding number of the vector $\overline{n}(k)$ around the origin in the plane generated by $\overline{n}_1$ and $\overline{n}_2$.

In the next section we analyze different types of energy bands that a topological ladder model can exhibit. In particular, we will show that the topological ladder models belong to the BDI or AIII classes.

BDI topological ladder

We consider a general Hamiltonian matrix with chiral symmetry as in Eq. (2.79). Imposing the chiral and time-reversal symmetry, the functions $f_1(k)$ and $f_2(k)$ are defined as:

$$f_1(k) = \alpha + \beta\cos k, \qquad f_2(k) = \gamma\sin k, \tag{2.87}$$

where α, β and γ are real parameters. Therefore the most general Hamiltonian for a ladder model in the BDI symmetry class corresponds to a matrix of the form:

$$M(k) = (\alpha + \beta\cos k)\,\sigma_1 + \gamma\sin k\sigma_2. \tag{2.88}$$

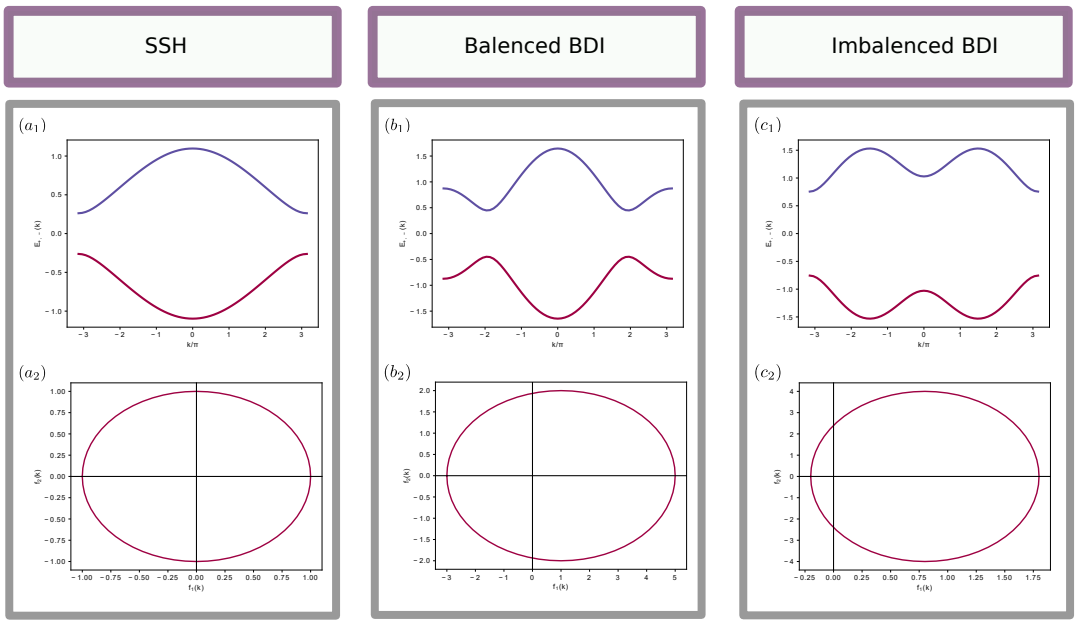

Figure 2.11: **Band structure and pseudo-spin vector for topological ladder in BDI class.** We show that there are three types of topological ladder models in the BDI symmetry class, which are distinguished and characterized by their energy gap configurations. (a) For $|\alpha\beta| \geq |\beta^2 - \gamma^2|$ the model corresponds to the SSH model. The energy gap is different from zero and the pseudo-spin vector in the f_1-f_2 correspond to a circumference. (b) For $|\alpha\beta| \leq |\beta^2 - \gamma^2|$ and $|\beta| > |\gamma|$ the lowest energy band show a single minimum at $k = 0$ and the model has two gaps. The pseudo-spin vector in f_1-f_2 plane correspond to an ellipse whose horizontal axis is bigger than the vertical one. (c) For $|\alpha\beta| \leq |\beta^2 - \gamma^2|$ and $|\beta| < |\gamma|$ the lowest energy band has two minima and the model presents two gaps with different width. Instead the Bloch vector represent an ellipse in f_1-f_2 plane.

This local Hamiltonian has chiral symmetry with $U_S = \sigma_3$ and time reversal symmetry identified by the operator $U_T = \sigma_2\sigma_y$

$$\sigma_2\sigma_y M^\star(-k)\sigma_y\sigma_2 = M(k). \tag{2.89}$$

Chiral and time reversal symmetries imply charge conjugation symmetry $U_C = \sigma_1\sigma_y$, therefore the condition for charge conjugation symmetry is also fulfilled. To understand the topological features of this model we study the curve drawn by the Hamiltonian matrix defined in the Eq. (2.82) in the complex plane and the energy gaps. It is easy to see that $z(k)$ is an ellipse with its center located at point $(\alpha, 0)$ and whose horizontal and vertical axes are given by $|\beta|$ and $|\gamma|$ respectively:

$$\left[\frac{f_1(k) - \alpha}{\beta}\right]^2 + \left[\frac{f_2(k)}{\gamma}\right]^2 = 1. \tag{2.90}$$

As regards the energy spectrum, we obtain the

$$E_\pm(k) = \mp\sqrt{\alpha^2\gamma^2 + 2\alpha\gamma\cos k + (\beta^2 - \gamma^2)\cos k} = \mp\rho(k). \tag{2.91}$$

Therefore the energy gaps will be located at the minima of the function $\rho(k)$. Taking into account the minima of $\rho(k)$ and the ellipse in Eq. (2.90) we can distinguish three different BDI models:

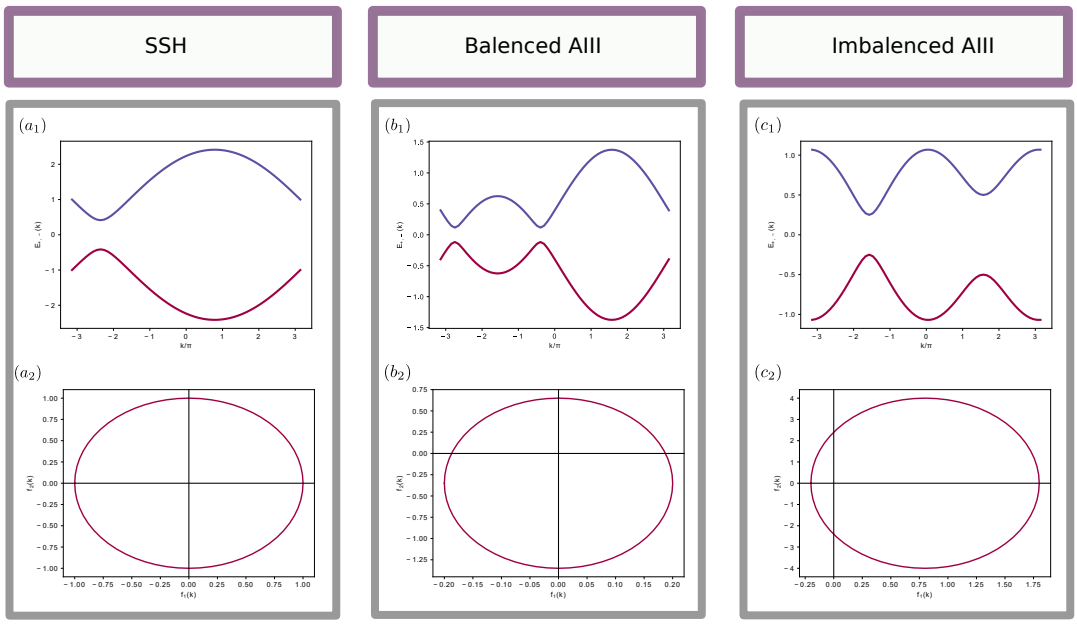

Figure 2.12: **Band structure and pseudo-spin vector for topological ladder in AIII class.** We show that there are three types of topological ladder models in the AIII symmetry class, which are distinguished and characterized by their energy gap configurations. (a) For $\beta = \gamma$ the model corresponds to the SSH model. The energy gap is different from zero and the pseudo-spin vector in the f_1-f_2 correspond to a circumference. (b) For $\beta < \gamma$ the lowest energy band shows a single minimum at $k \neq 0$ and the model has two gaps. The pseudo-spin vector in f_1-f_2 plane corresponds to an ellipse whose horizontal axis is bigger than the vertical one. (c) For $\beta > \gamma$ and $|\beta| < |\gamma|$ the lowest energy band has two minima in $k = 0$ and k_1 the model presents two gaps with different width.

- **SSH-like model**: In the case in which $|\alpha\beta| \geq |\beta^2 - \gamma^2|$ we obtain that the model is equivalent to the SSH model. In Fig. 2.11 (a_1) we show the energy bands and that the energy gaps can be located at the momentum $q = -\pi$ or $q = \pi$. In Fig.2.11 (a_2) we show that the ellipse that characterizes the Hamiltonian has a very low eccentricity and for $|\beta| = |\gamma|$ it collapses into a circle.

- **Balanced BDI model**: This model corresponds to the situation in which $|\alpha\beta| < |\beta^2 - \gamma^2|$, that implies that the upper band has two maxima and two minima, and $|\beta| > |\gamma|$, so that the horizontal axis of the ellipse is bigger than the vertical one (see Fig.(2.11) (b_2)). In this situation, the minima are located at $q_1 = q$ and $q_1 = -q$ with $\cos q = \alpha\beta/(\alpha^2 - \gamma^2)$ and the maxima are found at $q = 0$ and $q = \pi$. In this way, the energy gaps between the two bands are located at opposite momenta $\pm q$ as a consequence of time-reversal symmetry (see Fig.(2.11) (b_1)).

- **Imbalanced BDI model**: This model corresponds to the last possibility $|\alpha\beta| < |\beta^2 - \gamma^2|$ and $|\beta| < |\gamma|$ so that the ellipse has a vertical axis bigger than its horizontal axis (see Fig.(2.11) (c_2)). As in the previous case, this kind of BDI model is characterized by two minima and two maxima in its energy bands. However, the gaps are located at $q_1 = 0$ and $q_2 = \pi$ (see Fig.(2.11) (c_1)).

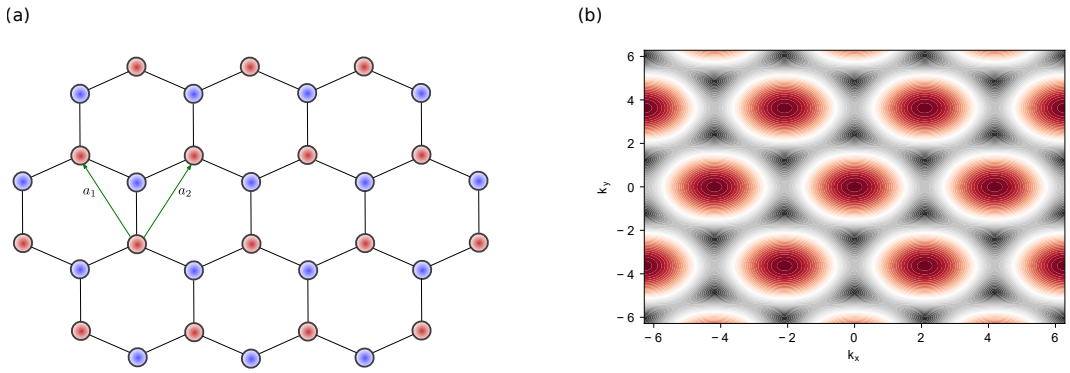

Figure 2.13: **Graphene structure.** (a) Two sites per unit cell (two sublattices) a and b (red and blue respectively). The green arrow indicates the lattice vectors $\overline{a}_1$ and $\overline{a}_2$. If we shift the lattices by $m\overline{a}_1 + n\overline{a}_2$ with m and n being integers, the lattice is invariant. (b) The contour plot of the energy dispersion for the lower band (as a function of k_x and k_y). The black region marks the first BZ, which is a hexagon.

AIII topological ladder

For the ladder model in the AIII classes we have only the chiral symmetry. The most general Hamiltonian $M(k)$ is

$$M(k) = (\alpha + \beta \cos k)\, \sigma_1 + (\eta + \gamma \sin k)\, \sigma_2 = f_1(k)\sigma_1 + f_2(k)\sigma_2. \tag{2.92}$$

As we have seen in the previous section, $f_1(k)$ and $f_2(k)$ describe an ellipse such that, in contrast to the BDI case, its center can be located anywhere in the plane and its axes can be rotated with respect to the x and y axes. One particular case of AIII topological ladder is the Creutz-Hubbard model that will be studied in the Chap. 3.

In this class we can distinguish other 3 cases:

- **SSH-like model:** For $|\beta| = |\gamma|$ the energy bands give rise to a single energy gap that can vary modifying β (see Fig. 2.12 (a_1)). Moreover, the curve described by the Hamiltonian matrix in the complex plane is a circle (see Fig. 2.12 (a_2)).

- **Balanced AIII model:** This model corresponds to the case in which the points associated to the minima of the upper band are at the same distance from the origin and, thus, there are two energy gaps of the same width between the two energy bands (see Fig 2.12 (b_1)). Moreover, the Hamiltonian matrix ellipse is such that one of its axes crosses the origin (see Fig 2.12 (b_2)).

- **Imbalanced AIII model:** Finally, the imbalanced AIII model consists of the more general case (see Fig 2.12 (c)). In this case, the energy bands show a pair of energy gaps with different widths and located at any momenta.

2.5.4 2D topological Insulator: Kane-Male model

In this section, we discuss a topological insulator that had a great impact in the past years: the Kane-Mele (KM) model for graphene [81] which was mentioned when we discussed the quantum Hall effect. Here, we will show how the model looks like and why it indeed gives the required result of two copies of the quantum Hall effect, one for spin up and one for spin down.

Before discussing the KM model we introduce the model that describes graphene [49]. Graphene has a honeycomb lattice structure, which must be described as a Bravais lattice, hence has two primitive vectors which may be chosen, e.g., as

$$\overline{a}_1 = \frac{a}{2}\left(1, \sqrt{3}\right), \qquad \overline{a}_2 = \frac{a}{2}\left(-1, \sqrt{3}\right), \tag{2.93}$$

where a is the lattice spacing. The tight-binding Hamiltonian is

$$\hat{H} = -t \sum_{\langle i\alpha j\beta \rangle} \left(\hat{c}^{\dagger}_{i\alpha} \hat{c}_{j\beta} + H.c. \right) + \sum_{i\alpha} m_{\alpha} \hat{c}^{\dagger}_{i\alpha} \hat{c}_{i\alpha}, \tag{2.94}$$

where i and j label different unit cells, while $\alpha, \beta = 1, 2$ label the basis sites within each cell. m_{α} is an on-site energy which can be different on the two sites within the unit cell. In particular we will consider that $m_{\alpha} = (-1)^{\alpha} m$. Note that $\langle i\alpha, j\beta \rangle$ means that the hopping only connects sub-lattices A and B (as shown in Fig. 2.13 (a)), so the Hamiltonian (2.94) becomes

$$\hat{H}_G = -t \sum_{i} \left(\hat{c}^{\dagger}_{iA} \hat{c}_{iB} + \hat{c}^{\dagger}_{i,A} \hat{c}_{i-\overline{a}_1,B} + \hat{c}^{\dagger}_{i,A} \hat{c}_{i-\overline{a}_2,B} + H.c. \right) + \sum_{i\alpha} m_{\alpha} \hat{c}^{\dagger}_{i\alpha} \hat{c}_{i\alpha}. \tag{2.95}$$

Going in momentum space and identifying the sublattice degree of freedom A, B as a pseudo-spin $\uparrow\downarrow$, we obtain the following Hamiltonian:

$$\hat{H}_G = -\frac{t}{2} \sum_{\overline{k}\alpha\beta} \left\{ \sigma^{+}_{\alpha\beta} \hat{c}^{\dagger}_{\overline{k}\alpha} \hat{c}_{\overline{k}\beta} \left(1 + e^{-i\overline{k}\cdot\overline{a}_1} + e^{-i\overline{k}\cdot\overline{a}_2} \right) + \sigma^{-}_{\alpha\beta} \hat{c}^{\dagger}_{\overline{k}\alpha} \hat{c}_{\overline{k}\beta} \left(1 + e^{i\overline{k}\cdot\overline{a}_1} + e^{i\overline{k}\cdot\overline{a}_2} \right) \right\} + \sum_{\overline{k}\alpha} \sigma^{z}_{\alpha\alpha} \hat{c}^{\dagger}_{\overline{k}\alpha} \hat{c}_{\overline{k}\alpha}, \tag{2.96}$$

where $\sigma^{\pm} = \sigma^x \pm \sigma^y$. Introducing the pseudo-spin vector $\overline{d}$ we can rewrite the Hamiltonian as follows:

$$\hat{H}_G = \sum_{\overline{k}} \left(\overline{d}(k) \cdot \overline{\sigma} \right) \hat{c}^{\dagger}_{\overline{k}} \hat{c}_{\overline{k}}, \tag{2.97}$$

where $\overline{d}(k)$ is defined as:

$$d^z(k) = m \tag{2.98}$$

$$d^x(k) = -t \left(1 + \cos\left(\overline{k} \cdot \overline{a}_1 \right) + \cos\left(\overline{k} \cdot \overline{a}_2 \right) \right) \tag{2.99}$$

$$d^y(k) = -t \left(1 + \sin\left(\overline{k} \cdot \overline{a}_1 \right) + \sin\left(\overline{k} \cdot \overline{a}_2 \right) \right). \tag{2.100}$$

Now we can easily find the eigenvalues and eigenvectors of $\hat{H}$ by using the properties of the Pauli matrices, obtaining that

$$E_{\pm}(\overline{k}) = \pm \sqrt{\overline{d}(k) \cdot \overline{d}(k)} \tag{2.101}$$

(see Fig. 2.13 (b)). If the mass $m = 0$, $d^z = 0$ and both $d^x(k)$ and $d^y(k)$ vanish at two distinct wave vectors in the Brillouin zone:

$$\overline{k} \cdot \overline{a}_1 = k_1 = \frac{2\pi}{3} \qquad \overline{k} \cdot \overline{a}_2 = k_2 = -\frac{2\pi}{3}, \tag{2.102}$$

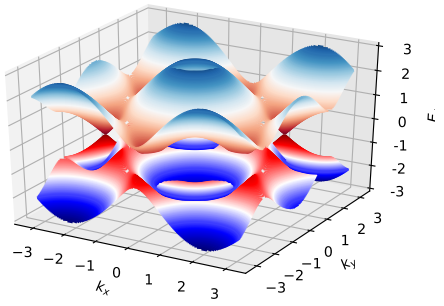

Figure 2.14: **Dirac Cone.** The energy dispersion for both bands ($E_\pm$ as a function of k_x and k_y) in the first BZ.

so that we can define $k_x = (k_1 - k_2)/a$ and$k_y = (k_1 + k_2)/\sqrt{3}a$. Now we can rewrite the vector $\overline{d}(k)$ in the following way:

$$d^x(k) = -t\left(1 + 2\cos\left(\frac{k_x a}{2}\right)\cos\left(\frac{\sqrt{3}k_y a}{2}\right)\right) \tag{2.103}$$

$$d^y(k) = -2t\cos\left(\frac{k_x a}{2}\right)\sin\left(\frac{\sqrt{3}k_y a}{2}\right), \tag{2.104}$$

which vanish at

$$k_x = \frac{4\pi}{3a} \qquad k_y = 0, \tag{2.105}$$

$$k_x = -\frac{4\pi}{3a} \qquad k_y = 0. \tag{2.106}$$

$$\tag{2.107}$$

Now let us expand the Hamiltonian around the 2 Dirac points we have picked. Let $k_x = k_x^0 + \delta k_x$, $k_y = \delta k_y$ and expand the cos and sin we obtain that

$$d_\pm^x = \pm\frac{\sqrt{3}}{2}ta\delta k_x \tag{2.108}$$

$$d_\pm^y = \frac{\sqrt{3}}{2}ta\delta k_y. \tag{2.109}$$

The Hamiltonian around the Dirac points has the following expression:

$$\hat{H}_+(k) = v\left(k_x\sigma_x + k_y\sigma_y\right), \qquad \hat{H}_-(k) = v\left(-k_x\sigma_x + k_y\sigma_y\right), \tag{2.110}$$

with $v = \sqrt{3}ta/2$. Adding the mass term we obtain:

$$\hat{H}_+(k) = v\left(k_x\sigma_x + k_y\sigma_y\right) + m\sigma_z, \qquad \hat{H}_-(k) = v\left(-k_x\sigma_x + k_y\sigma_y\right) + m\sigma_z. \tag{2.111}$$

When $m = 0$ the Dirac fermion has a linear spectrum; this correspond to graphene. Until now we have seen the Dirac cones in graphene (see Fig. 2.14). By calculating the energy bands for this term, one obtains a linear dispersion at points $k_x = \pm 4\pi/3a$. This dispersion is the same as the one obtained for a massless relativistic fermion in a $2D$ Dirac equation, hence the name Dirac cone.

In 1988 Handane introduced a more general model to describe the graphene

$$\hat{H}_{\text{Haldane}} = \hat{H}_G + \hat{H}_{NNN} = \hat{H}_G + t_2\sum_{\langle\langle ij\rangle\rangle} e^{-i\nu_{ij}\phi}\hat{c}_{i\alpha}^\dagger\hat{c}_{j\alpha}, \tag{2.112}$$

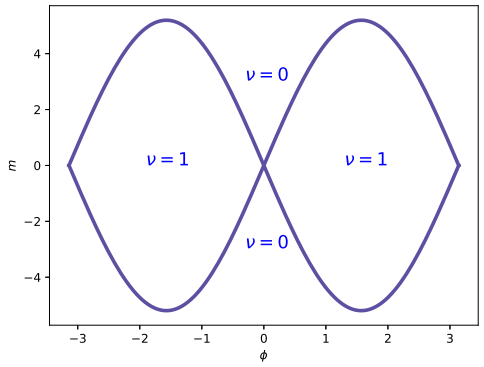

Figure 2.15: **Haldane mass.** We show the Haldane mass respect the flux ϕ. We distinguish two regions in which the Chern number is $\nu = \pm 1$ (topological phase) and the region where $\nu = \pm 0$. The phase transition occur at $m = \pm 3\sqrt{3}t_2 \sin\phi$.

where the second term describes the next-nearest hopping, where $\nu_{ij} = -\nu_{ji} = \pm 1$ are clock or counter-clockwise electron hopping and a flux ϕ which sums up to zero over each unit cell. This model was designed to describe a quantum Hall effect without the Landau level structure in graphene. Especially the last term is important for the quantum spin Hall effect, the NNN-hopping since it breaks the time-reversal symmetric without using a real magnetic field.

The NNN hopping is from an A-site to an A-site (and from B-site to B-site). For A-to-A hopping, there are three different types of NNN bonds. So the Hamiltonian is

$$\hat{H}^{(A)}_{NNN} = -t_2 e^{i\phi} \sum_i \left(\hat{c}^\dagger_{i,A} \hat{c}_{i+\nu_1,A} + \hat{c}^\dagger_{i+\nu_1,A} \hat{c}_{i-\nu_3,A} + + \hat{c}^\dagger_{i+\nu_1,A} \hat{c}_{i,A} + H.c \right) \tag{2.113}$$

($A \to B$ and $\phi \to -\phi$). Here ν_1, ν_2 and ν_3 are:

$$\nu_1 = (\sqrt{3}a, 0) \qquad \nu_2 = (-\frac{\sqrt{3}}{2}a, 0) \qquad \nu_3 = (-\frac{\sqrt{3}}{2}a, -\frac{3}{2}a). \tag{2.114}$$

In momentum space we obtain that:

$$\begin{aligned} \hat{H}_{NNN} = -2t_2 \sum_k \left[\cos\left(\overline{k} \cdot \overline{\nu}_1 - \phi\right) + \cos\left(\overline{k} \cdot \overline{\nu}_2 - \phi\right) + \cos\left(\overline{k} \cdot \overline{\nu}_3 - \phi\right) \right] \hat{c}^\dagger_{k,A} \hat{c}_{k,A} + \\ + 2t_2 \sum_k \left[\cos\left(\overline{k} \cdot \overline{\nu}_1 + \phi\right) + \cos\left(\overline{k} \cdot \overline{\nu}_2 + \phi\right) + \cos\left(\overline{k} \cdot \overline{\nu}_3 + \phi\right) \right] \hat{c}^\dagger_{k,B} \hat{c}_{k,B}. \end{aligned} \tag{2.115}$$

Using the Pauli matrices, we can rewrite the Hamiltonian in the Bloch form $H(k) = \overline{h}(k) \cdot \overline{\sigma}$:

$$H(k) = H_0(k) I + H_x(k)\sigma_x + H_y(k)\sigma_y + H_z(k)\sigma_z, \tag{2.116}$$

where

$$h_0(k) = -2t_2 \cos(\phi) \left\{ \cos\left(\overline{k} \cdot \overline{\nu}_1\right) + \cos\left(\overline{k} \cdot \overline{\nu}_2\right) + \cos\left(\overline{k} \cdot \overline{\nu}_3\right) \right\} \tag{2.117}$$

$$h_x(k) = -t \left\{ \cos\left(k_x\right) + \cos\left(\overline{k} \cdot \overline{a}_1\right) + \cos\left(\overline{k} \cdot \overline{a}_2\right) \right\} \tag{2.118}$$

$$h_y(k) = -t \left\{ \sin\left(k_x\right) + \sin\left(\overline{k} \cdot \overline{a}_1\right) + \sin\left(\overline{k} \cdot \overline{a}_2\right) \right\}. \tag{2.119}$$

Haldane showed that the σ_z contribution breaks the time-reversal symmetry and opens a gap in the energy spectrum. A phase transition between a trivial phase and topological

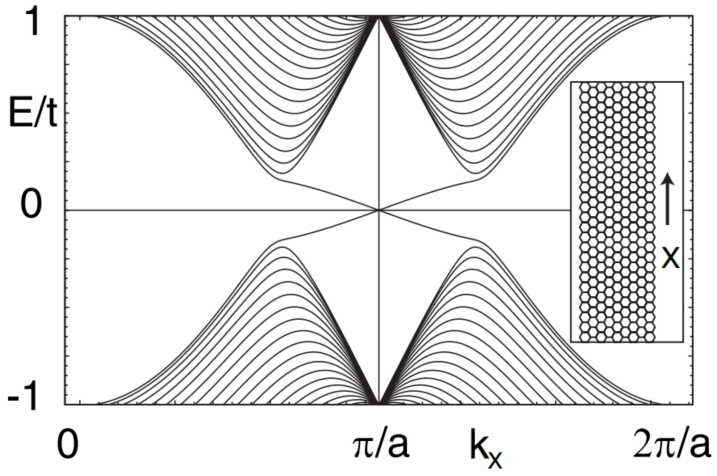

Figure 2.16: **Energy spectrum of Kane-Mele model.** The energy spectrum of the Kane-Mele model for a strip of graphene for $t_2/t = 0.3$. One can easily observe the counter-propagating edge states that cross at $k_x = \pi/a$ and zero energy. At $E = 0$, the edge states have a linear dispersion, making these electrons behave as Dirac fermions. This Fig. is taken from [81].

phase occurs at the Haldane mass $m = \pm 3\sqrt{3}\sin\phi$ by calculating the Chern number (see Fig. 2.15). The Chern number for this kind of systems can be seen as a winding number

$$Ch = \frac{1}{4\pi}\int d^2k\hat{h}\cdot\left[\frac{\partial\hat{h}}{\partial k_x}\times\frac{\partial\hat{h}}{\partial k_y}\right] \tag{2.120}$$

where Ch is the Chern number and $\hat{h} = h(k)/|h(k)|$ is a unit vector. In the insulating state, the sum of the winding number cancels and therefore there is no quantized current, but in the quantum Hall state, the winding numbers add and contribute to the conductivity $\sigma_{xy} = e^2/h$.

Kane and Mele took inspiration from this work to make a double copy of the model, by introducing spin in the system, eventually leading to the spin quantum Hall effect. The quantum spin Hall effect differs from the quantum Hall effect by Haldane because it is invariant under time-reversal symmetry and gives rise to helical, counter-propagating spin currents at the edge. The Hamiltonian of KM model is the following

$$\hat{H}_{KM} = \sum_{\langle ij\rangle\alpha}\hat{c}^\dagger_{i\alpha}\hat{c}_{j\alpha} + \sum_{i\alpha} m_i\hat{c}^\dagger_{i\alpha}\hat{c}_{i\alpha} + it_2\sum_{\langle\langle ij\rangle\rangle\alpha\beta}\nu_{ij}\sigma^z_{\alpha\beta}\hat{c}^\dagger_{i\alpha}\hat{c}_{j\beta}, \tag{2.121}$$

where the third term now describes the intrinsic spin-orbit coupling (SOC), with t_2 the SOC parameter, σ_z a Pauli matrix representing the electron's spin.

Whereas the quantum Hall effect gives rise to chiral edge states, here we will get two copies of these chiral edge states for different spins, leading towards a so-called helical edge state.

The spectrum of Eq. (2.121) can be calculated by considering a cylinder of graphene, periodic in the x direction and open in the y direction, as shown in Fig. 2.16. We see the normal energy bands, but also a crossing of two bands at $k_x = \pi/a$. These crossing bands are the spin up and spin down electrons at the edge of the system, and are propagating in opposite direction.

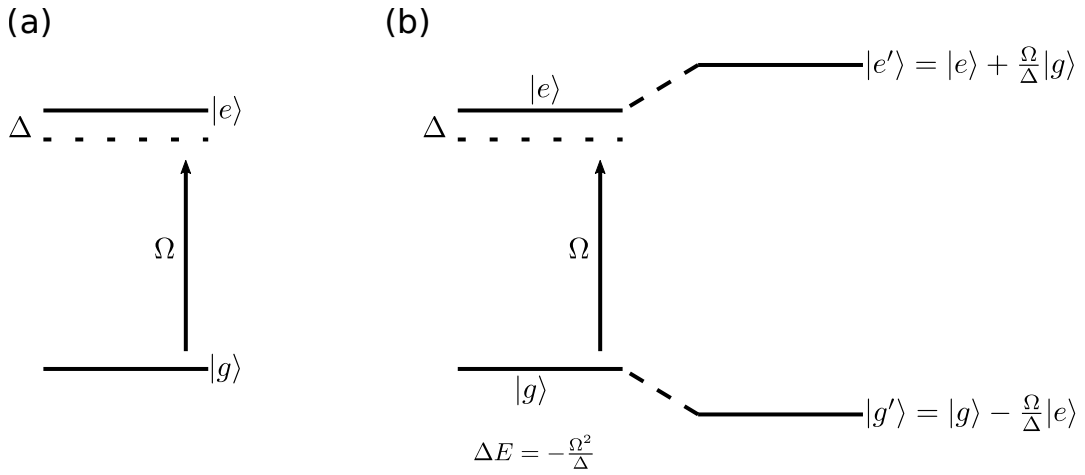

Figure 2.17: (a) Coupling between the internal states $|g\rangle$ and $|e\rangle$. Ω is the Rabi frequency and Δ is the detuning. (b) For $\Omega << \Delta$, the ground and excited states are coupled far off-resonantly. As a consequence, the ground state undergoes an energy shift of $\Delta E = -\Omega^2/\Delta$.

2.6 Engineering topological Hamiltonian with cold atoms

The systems investigated in this thesis have the properties of being simulatable in cold atoms experiments. Reviews of techniques needed to realize such setups have been presented in [20]. Here we revise shortly the technical ingredients for the experimental realization of fermionic systems.

We consider a system of N interacting spinless particles of mass m with positions $\{\overline{r}_1 \cdots \overline{r}_n\}$, momenta $\{\overline{p}_1 \cdots \overline{p}_n\}$, charge q and magnetic momentum μ_B. In first quantization, the Hamiltonian that describes the system in a fixed non-dynamical electromagnetic field by the vector potential $\overline{A} = (A_x, A_y, A_z)$ is the following:

$$\hat{H} = \sum_j \left\{ \frac{1}{2m} \left(\overline{p}_j - q\overline{A} \right)^2 + \hat{V}_{latt}(\overline{r}_i) + \hat{V}(\overline{r}_i) - \mu \cdot \overline{B}(\overline{r}_i) \right\} + \hat{U}_{int}, \tag{2.122}$$

where $\overline{p}_i = -i\hbar\overline{\nabla}$, is the momentum operator, $\overline{B}$ is the magnetic field, $\hat{V}_{latt}(\overline{r}_i)$ is the lattice potential, $\hat{V}(\overline{r}_i)$ is an external potential and U_{int} is the Hamiltonian caused by the interaction between particles.

The term U_{int} in Eq. (2.122) is induced by interaction between particles:

$$U_{int} = \frac{1}{2} \sum_{i \neq j} U_{int} \left(\overline{r}_j - \overline{r}_i \right). \tag{2.123}$$

Let us study the Hamiltonian in Eq. (2.122) in absence of gauge potential and Zeeman effect. The Hamiltonian for interacting particles becomes:

$$\hat{H} = -\frac{\hbar^2}{2m} \sum_i \left(\nabla_i^2 + V_{latt}(\overline{r}_i) + V(\overline{r}_i) + U_{int}(\overline{r}_i) \right). \tag{2.124}$$

In the following sections we explain how to design this Hamiltonian with cold atoms.

2.6.1 Optical lattices

In this section, we introduce the physics of ultracold atoms trapped in crystals of light: optical lattices. When atoms are illuminated by laser beams with a frequency

far off-resonance, the electric field of laser induces a dipole moment in the atoms which interacts with the electric field. This interaction modifies the energy of internal states of the atoms in a way that depends both on the light intensity and on the laser frequency. A spatially-dependent intensity induces spatially-dependent potential energy which can be used to trap the atoms.

Let us first start by explaining how optical lattice potentials are generated. In particular, we will discuss about the ac-Stark shift.

Consider a two level atom with internal ground state $|g\rangle$ and excited state $|e\rangle$ separated by an energy $\hbar\omega_0$. The atom is illuminated with an electromagnetic field $\overline{E} = \overline{\epsilon}(x)e^{-i\omega t} + \overline{\epsilon}^{\star}(x)e^{i\omega t}$ with amplitude $\overline{\epsilon}(k)$ and frequency $\nu = \omega/2\pi$ (as showed in Fig.2.17). The electromagnetic field induces a dipole moment in the atom, $\overline{d}$, which interacts with it in the usual way:

$$V = -\hat{d} \cdot \overline{E}. \tag{2.125}$$

Quantum mechanically the dipole moment is an operator and can be written in the two-level atom basis:

$$\hat{d} = \sum_{\alpha,\beta=g,e} \langle\alpha|\hat{d}|\beta\rangle|\alpha\rangle\langle\beta|. \tag{2.126}$$

Since atoms do not have a permanent dipole moment, $\langle\alpha|\hat{d}|\alpha\rangle = 0$ and only the out diagonal terms are non zero $\mu_{eg} = \langle e|\hat{d}|g\rangle \neq 0$:

$$\hat{d} = \mu_{eg}|e\rangle\langle g| + \mu_{eg}^{\star}|g\rangle\langle e|, \tag{2.127}$$

and the total Hamiltonian of the system can be written as

$$\hat{H} = \hbar\omega_0|e\rangle\langle e| - \left(\mu_{eg}|e\rangle\langle g| + \mu_{eg}^{\star}|g\rangle\langle e|\right) \cdot \left(\overline{\epsilon}(x)e^{-i\omega t} + \overline{\epsilon}^{\star}(x)e^{i\omega t}\right). \tag{2.128}$$

When the laser detuning is $\Delta = \omega - \omega_0$, the Hamiltonian becomes:

$$\hat{H} = -\frac{\hbar\Delta}{2}\sigma_z - \left(\frac{\hbar\Omega(\overline{x})}{2}|e\rangle\langle g| + \frac{\hbar\Omega^{\star}(\overline{x})}{2}|g\rangle\langle e|\right), \tag{2.129}$$

where $\Omega(\overline{x})$ is the Rabi frequency given by $\hbar\Omega(\overline{x}) = \overline{\epsilon}(\overline{x}) \cdot \overline{\mu}_{eg}$. If the detuning is large compared to the Rabi frequency $|\Delta| \gg \Omega$ its effect first appears at second order perturbation theory. In this case, the energy shift $E_{g,e}^{(2)}$ is given by

$$E_{g,e}^2 = \pm\frac{\left|\langle e|\hat{H}|g\rangle\right|^2}{\hbar\delta} = \pm\hbar\frac{\Omega^2(x)}{4\Delta}. \tag{2.130}$$

This energy shift is the so-called ac-Stark shift and defines the optical potential of atoms in the state $|g\rangle$. If the atoms are illuminated with counter-propagating laser beams that interfere, the atoms will feel the standing-wave pattern resulting from the interference. This periodic landscape modulation of the energy experienced by the atoms is the so-called optical lattice potential. Finally, we can write the optical potential $\hat{V}_{latt}(x)$ as

$$\hat{V}(x) = -\hbar\frac{\Omega^2(x)}{4\Delta}. \tag{2.131}$$

The simplest possible lattice is a one-dimensional lattice. It is defined by a Rabi frequency $\Omega(x) = 2\Omega_0 \sin(kx)$ which yields a periodic trapping potential given by

$$V_{latt}(x) = V_0 \sin^2(kx) = \frac{\hbar\Omega_0^2}{\Delta}\sin^2(kx), \tag{2.132}$$

where $k = 2\pi/\lambda$ is the magnitude of the laser-light wave vector and V_0 is the lattice depth.

Periodic potentials in higher dimensions can be created by superimposing more laser beams. To create a two-dimensional lattice potential, for example, two orthogonal sets of counter-propagating laser beams can be used. In this case, the lattice potential has the form:

$$\hat{V}_{latt}(x,y) = V_0 \left(\cos^2(ky) + \cos^2(kx) + 2\epsilon_1 \cdot \epsilon_2 \cos\phi \cos(ky)\cos(kx)\right), \tag{2.133}$$

where k is the wave vector magnitude, ϵ_1 and ϵ_2 are polarization vectors of the counter-propagating set and ϕ is the phase between them. A simple square lattice can be created by choosing orthogonal polarization between the standing wave. In this case, the interference term vanishes and the resulting potential is just the sum of two superimposed $1D$ lattice potentials.

2.6.2 Fermionic Hamiltonian in optical lattice: tight binding approximation

In the previous section we have seen that in absence of gauge potential and Zeeman field, the Hamiltonian for the interacting particles is given by eq. (2.124). By using the second quantization formalism, we can rewrite the Hamiltonian for interacting fermion as follows:

$$\begin{aligned}\hat{H} = \sum_{\sigma} \int d\overline{r} \hat{\psi}^{\dagger}_{\sigma}(\overline{r}) \left[-\frac{\hbar^2}{2m}\nabla^2 + \hat{V}_{\sigma}(\overline{r}) + \hat{V}_{latt}(\overline{r})\right] \hat{\psi}_{\sigma}(\overline{r}) + \\ + \frac{1}{2}\sum_{\sigma,\sigma'} \int d\overline{r} \int d\overline{r}' \hat{\psi}^{\dagger}_{\sigma,\sigma'}(\overline{r}) \hat{\psi}^{\dagger}_{\sigma'}(\overline{r}') U^{\sigma,\sigma'}_{int}\left(\overline{r} - \overline{r}'\right) \hat{\psi}_{\sigma'}(\overline{r}) \hat{\psi}_{\sigma}(\overline{r}')\end{aligned} \tag{2.134}$$

with

$$\left\{\hat{\psi}_{\sigma}(\overline{r}), \hat{\psi}^{\dagger}_{\sigma'}(\overline{r}')\right\} = \delta(\overline{r} - \overline{r}')\delta_{\sigma,\sigma'}, \qquad \left\{\hat{\psi}_{\sigma}(\overline{r}), \hat{\psi}_{\sigma}(\overline{r})\right\} = \left\{\hat{\psi}^{\dagger}_{\sigma}(\overline{r}), \hat{\psi}^{\dagger}_{\sigma}(\overline{r})\right\} = 0 \tag{2.135}$$

For sufficiently deep lattice potentials, the atomic field operators can be expanded in terms of localized Wannier functions. Suppose that the atoms can be loaded in the lowest band, where they will reside under controlled conditions. Then one can restrict the basis to include only lowest band Wannier functions $\omega_0(x)$ i.e. $\psi_{\sigma}(x) = \sum_j \hat{a}_{j,\sigma}\omega_0(\overline{x} - \overline{x}_j)$ where $\hat{a}_j$ is the annihilation operator at site j which obeys fermionic operator. Substituting in the Hamiltonian we obtain:

$$\hat{H} = \sum_{\sigma}\sum_{ij} J^{\sigma}_{ij}\left(\hat{a}^{\dagger}_{i,\sigma}\hat{a}_{j,\sigma} + \hat{a}^{\dagger}_{j,\sigma}\hat{a}_{i,\sigma}\right) + \sum_{\sigma}\sum_{j} \epsilon_{j,\sigma}\hat{a}^{\dagger}_{j,\sigma}\hat{a}_{j,\sigma} + \sum_{\sigma,\sigma'}\sum_{j} \frac{U^{\sigma,\sigma'}}{2}\hat{n}_{j,\sigma}\left(\hat{n}_{j,\sigma} - 1\right) \tag{2.136}$$

The first sum is carried out only in the nearest-neighbour sites and represents the hopping term where the coefficient J^{σ}_{ij} is:

$$J^{\sigma}_{i,j} = \int d\overline{r}\omega_{\sigma}\left(\overline{r} - \overline{r}_i\right)\left\{\frac{-\hbar}{2m}\nabla^2 + V_{latt}(\overline{r})\right\}\omega_{\sigma}\left(\overline{r} - \overline{r}_j\right). \tag{2.137}$$

The term $\epsilon_{i,\sigma}$ represents the chemical potential that is defined as:

$$\epsilon_j = \int d\overline{r} V_{\sigma}(\overline{r})\left|\omega_{\sigma}(\overline{r} - \overline{r}_j)\right|^2. \tag{2.138}$$

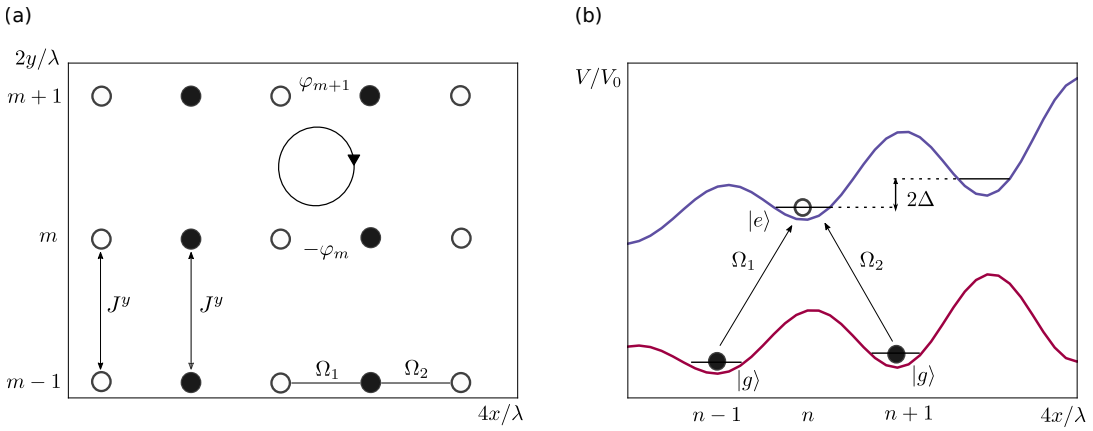

Figure 2.18: **Setup to engineer an artificial gauge field in an optical lattice.** (a) Two superimposed state-dependent optical lattices for atoms in the internal states $|g\rangle$ (white dots) and $|e\rangle$ (black dots). The optical potential is chosen such that only the hopping J^y in the y-direction is allowed. (b) The hopping in the x-direction is realized with Raman transitions between the states $|g\rangle$ and $|e\rangle$. A Peierls phase can be induced by working with spatially-dependent Rabi frequencies.

As regards the repulsion interaction $U_{int}^{\sigma,\sigma'}$ we obtain that:

$$U_{int}^{\sigma,\sigma'} = \frac{4\pi\hbar^2}{m} a_{\sigma,\sigma'} \int d\overline{r}\, |\omega_\sigma(\overline{r})|^2 \, |\omega_{\sigma'}(\overline{r})|^2 \,, \tag{2.139}$$

where $a_{\sigma,\sigma'}$ is the scattering length. Since the interactions are short range, we take into account only the interactions between two particles which take up the same site.

2.6.3 Artificial gauge field

Charged particles moving along alternative paths through a magnetic field pick up a relative phase dependent on the magnetic flux enclosed by the paths. This phenomenon is called the Aharonov-Bohm effect and it has been experimentally demonstrated [82].

In ultracold atoms, the orbital physics of the magnetic field effect cannot be simulated directly because of the charge neutrality of the atoms. Therefore new experimental methods had to be developed to avoid this limitation by designing effective systems whose dynamics are governed by a Hamiltonian analogue to the one of a charged particle in a magnetic field. In this sense, the same physics can be obtained in this set-up using artificial gauge fields.

Various ways exist to make neutral particles pick up a geometric phase using artificial gauge fields:

- rotating the atomic gas,
- lattice shaking,
- spatial dependent optical couplings,
- Laser-assisted tunnelling.

Here we sketch the laser-assisted tunnelling method introduced by Jaksch and Zoller in [25]. More details on methods to implement light-induced gauge fields can be found in review articles [33–38].

The key idea is shown in Fig. 2.18 (a). A state-dependent optical lattice is realized for atoms in the state $|g\rangle$ and $|e\rangle$: the optical potential is chosen such that only the hopping in the y-direction is allowed. The dynamics of atoms in this optical lattice can be described by the Hamiltonian:

$$\hat{H}_l = \sum_{mn} J_y \left(\hat{a}^\dagger_{m,n} \hat{a}_{m,n} + H.C. \right) + \sum_m \omega_{eg} \hat{a}^\dagger_{m,n} \hat{a}_{m,n}. \tag{2.140}$$

The energy difference between the two hyperfine states is $\omega_{eg} > 0$ and the operators $\hat{a}_{mn}$ are annihilation operators for atoms in the lowest motional band located at the site $X_{(n,m)} = (x_n, y_m)$ where $x_n = n\lambda/4$ and $y_m = m\lambda/2$. In addition there is an energy offset of Δ between two adjacent sites in the x-direction as shown in Fig. 2.18 (b).

In the x-direction, the hopping is assisted through a Raman transition from $|g\rangle$ to $|e\rangle$. The Peierls phase can be engineered by choosing a spatially dependent Rabi frequency $\Omega_{1,2}(r) = \omega e^{iqy}$.

Then one can find the following Hamiltonian describing the effect of Raman lasers:

$$\hat{H}_{AL} = \sum_{nm} \left(\gamma_{n,m} \hat{a}^\dagger_{n,m} \hat{a}_{n-1,m} + H.c. \right) - \sum_{n,m} \Delta \hat{a}^\dagger_{nm} \hat{a}_{nm}. \tag{2.141}$$

Here the matrix element $\gamma_{n,m}$ can be written as:

$$\gamma_{m,m} = \frac{1}{2} e^{i2\pi\alpha m} \Omega \Gamma_y(\alpha) \Gamma_x, \tag{2.142}$$

the matrix elements

$$\Gamma_x = \int dx \omega^\star(x) \omega(x - \lambda/4) \qquad \Gamma_y(\alpha) = \int dy \omega^\star(y) \cos(4\pi\alpha m) \omega(y), \tag{2.143}$$

where $\omega_\alpha(r)$ are the Wannier functions. Finally, we obtain the following Hamiltonian:

$$\hat{H} = J \sum_{mn} \left(e^{i2\pi\alpha m} \hat{a}^\dagger_{n,m} \hat{a}_{n+1,m} + \hat{a}^\dagger_{n,m} \hat{a}_{n,m+1} + H.c. \right). \tag{2.144}$$

Chapter 3

Creutz-Hubbard model

In chapter 2 we have seen that understanding and classifying all phases of matter is one of the most important challenges of condensed matter physics. In particular, we showed that the theory of symmetry breaking cannot explain all possible phenomena encouraging further efforts to provide a general classification. For this reason, the ten-fold way turned out to be a fundamental tool for the classification of non-interacting phases of matter. In contrast to symmetry-broken phases, phase transitions can exist inside the same symmetry class. In this case, the transitions between different phases can only occur via gap-closing continuous phase transitions, but there is neither symmetry breaking nor any underlying local order parameter. In this way, these new phases are characterized by a topological invariant.

In this chapter, we will study a particular ladder model: the so called Creutz Hubbard model [83–87] in presence of repulsive Hubbard interactions.

The Creutz ladder, a model originally proposed in the field of high-energy physics and later transported to condensed matter by the same authors, has been studied previously with bosons [88, 89]. Recently, it was shown that the Creutz ladder, when charged with spinful fermions and exposed to attractive interactions, gives rise to a BCS description [90]. For spinless fermions, we are aware of only a single study, however, with a different focus on an additional superconductor wave pairing [91].

Moreover, in this chapter, we will study the imbalanced Creutz-ladder proposed in [59]. This model belongs to the AIII symmetry class and therefore realizes a different SPT phase of the original model. It represents a particular case of AIII topological ladder discussed in sec. 2.5.3. More precisely, we investigate the influence of both energy imbalance between the two fermionic species appearing in the model, and Hubbard interactions. We show that the two adjustments to the original model evoke a competition between the topological phase and two types of quantum magnetism. At large imbalance, the system is driven through a phase transition of Ising universality towards a paramagnetic phase. For large interactions, on the contrary, long-range ferromagnetic order arises as in the symmetry-broken phase of the quantum Ising model. Away from these limiting scenarios, we introduce effective theories by mapping the original system to models of quantum magnetism.

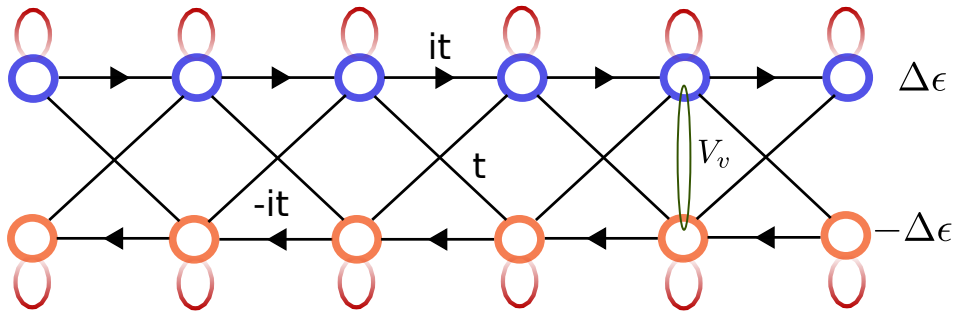

Figure 3.1: **Hopping and interaction processes in the imbalanced Creutz-Hubbard model**. The sites of the two-legged ladder are represented by blue ($l = u$) and orange ($l = d$) dots. Particles can hop from one site to another along the black lines. For the complex hopping amplitudes, we indicate the direction by arrows. The imbalance terms are expressed as on-site hoppings. Moreover, particles on the same lattice site j interact through a repulsive Hubbard interaction V_v.

3.1 The Model

The Imbalanced Creutz-Hubbard model is defined by the following Hamiltonian

$$\hat{H}_{CH} = \hat{H}_C + \hat{V}_{Hubb}, \tag{3.1}$$

where $\hat{H}_C$ represents the free fermionic model

$$\hat{H}_C = \hat{H}_{FB} + \hat{V}_{Imb}, \tag{3.2}$$

with $\hat{H}_{FB}$ is the kinetic term and $\hat{V}_{Imb}$ the imbalance term. Finally $\hat{V}_{Hubb}$ is a repulsive Hubbard one-site repulsive interaction.

To detail the Hamiltonian, we introduce a one-dimensional ladder lattice where the sites (rungs) are labelled as $j \in \{1, ..., N\}$ and the legs (labelling the internal degree of freedom) are denoted with $l \in \{u, d\}$ (see Fig 3.1). The fermionic operator $\hat{c}^{(\dagger)}_{j,l}$ creates (annihilates) a particle at given site.

The kinetic term reads

$$\hat{H}_{FB} = \sum_{j,l} \left\{ -t\hat{c}^\dagger_{j+1,l}\hat{c}_{j,\bar{l}} + te^{is_l\frac{\theta}{2}}\hat{c}^\dagger_{j+1,l}\hat{c}_{j,l} + H.C. \right\}, \tag{3.3}$$

where $s_{u/d} = \pm 1$ and $\bar{l}$ labels the opposite rung to l, namely $\bar{u} = l$ and $\bar{d} = u$. H_{FB} contains all kinetic terms of the full model. The first term describes diagonal tunnelling, the second term represents the horizontal tunnelling along the ladder, with tunneling strength t (see Fig 3.1). One particularity of the model is the imaginary hopping coefficients $te^{\pm i\frac{\theta}{2}}$. For neutral atoms, these can originate from artificial gauge fields. As a consequence, the particles acquire a phase factor $e^{i\frac{\theta}{2}}$ when moving from one site to the next. In this context, we have that $\theta = \pi$.

Instead the imbalance term is

$$\hat{V}_{Imb} = \sum_{j,l} \frac{\Delta\epsilon}{2} s_l \hat{n}_{j,l}, \tag{3.4}$$

where $\Delta\epsilon$ is the energy imbalance between the legs of the ladder. It favors the occupation of one particle species energetically.

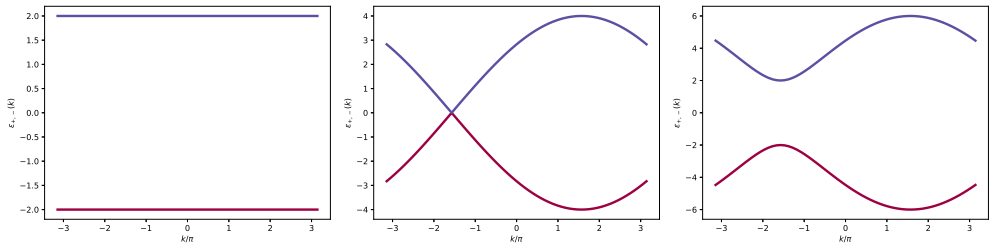

Figure 3.2: **Dispersion relation and winding of the imbalanced Creutz ladder**.Dispersion bands of the imbalanced Creutz ladder in different regimes: in the TI-phase with flat bands ($\Delta\epsilon = 0.0$, purple), at the critical point ($\Delta\epsilon = 4.0$, red) and in the oPM-phase ($\Delta\epsilon = 8.0$, orange).

Finally the interaction term is defined by

$$\hat{V}_{Hubb} = \sum_{j,l} \frac{V_v}{2} \hat{n}_{j,l} \hat{n}_{j,\bar{l}}, \tag{3.5}$$

where V_v is the density-density interaction strength between fermions residing in neighboring sites along vertical bonds of the ladder.

3.2 Non-interacting regime

In this section, we will study the model without interaction. In this limit, we can solve the model analytically. This allows us to identify two phases in this regime. In momentum space we can rewrite the Hamiltonian in the following way:

$$\hat{H} = \sum_k \Psi^\dagger(k) \mathcal{H}(k) \Psi(k) = \sum_k \Psi^\dagger(k) \left[\overline{B}(k) \cdot \overline{\sigma} \right] \Psi(k), \tag{3.6}$$

with $\overline{B}(k) = 2t\,(\Delta\epsilon - \cos(k), 0, \sin(k))$ and $\overline{\sigma} = (\sigma_x, \sigma_y, \sigma_z)$ and $q \in [-\pi, \pi]$. The dispersion relation is

$$\epsilon_\pm(k) = \pm 2t \sqrt{1 + \left(\frac{4t}{\Delta\epsilon}\right)^2 + 2\left(\frac{4t}{\Delta\epsilon}\right)\sin(k)}, \tag{3.7}$$

For $\Delta\epsilon/t = 4$, the single-particle gap closes indicating a phase transition (see Fig. 3.2).

To determine whether the two phases separated by the critical point are SPT or trivial we need to investigate the symmetry of Hamiltonian and the Bloch sphere.

As discussed in sec. 2.3, analyzing the symmetry of this Hamiltonian we can identify the topological nature of the system. In fact, the A-Z classification [71] allows the categorization of topological phases in one dimension according to their time-reversal $\mathcal{T}$, their particle-hole $\mathcal{C}$ and their sublattice/chiral symmetry $\mathcal{S}$ (see Tab. 2.1). Their action on the fermionic operators $\hat{c}^{(\dagger)}_{j,\sigma}$ reads:

$$\mathcal{T}\hat{c}_{j,\sigma}\mathcal{T}^{-1} = U_{T\sigma,\sigma'}^{\star}\hat{c}_{j,\sigma} \qquad \mathcal{T}\hat{c}^\dagger_{j,\sigma}\mathcal{T}^{-1} = \hat{c}^\dagger_{j,\sigma'}U_{T\sigma',\sigma}, \tag{3.8}$$

$$\mathcal{C}\hat{c}_{j,\sigma}\mathcal{C}^{-1} = U_{C\sigma,\sigma'}\hat{c}^\dagger_{j,\sigma} \qquad \mathcal{C}\hat{c}^\dagger_{j,\sigma}\mathcal{C}^{-1} = \hat{c}_{j,\sigma'}U_{C\sigma',\sigma}^{\star}, \tag{3.9}$$

$$\mathcal{S}\hat{c}_{j,\sigma}\mathcal{S}^{-1} = U_{S\sigma,\sigma'}\hat{c}^\dagger_{j,\sigma} \qquad \mathcal{S}\hat{c}^\dagger_{j,\sigma}\mathcal{S}^{-1} = \hat{c}_{j,\sigma'}U_{S\sigma',\sigma}^{\star}, \tag{3.10}$$

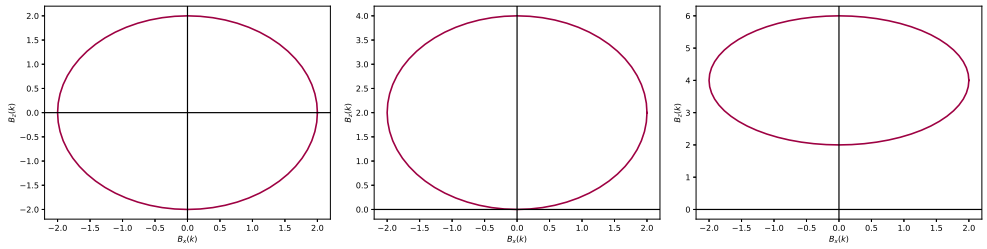

Figure 3.3: Winding of the spinor $(B_x(q), B_y(q))$ for the parameters $\Delta\epsilon = 0.0, 4.0, 8.0$: Within the topological phase the spinor encircles the origin (black cross), while in the non-topological phase it does not.

where T, C and S are 2×2 unitary matrices satisfying $T^\star T = C^\star C = \pm 1$ and $S = TC^\star$, up to an arbitrary phase factor such that $S^2 = 1$. The Hamiltonian $\mathcal{H}(k)$ in eq. 3.6 is invariant under a symmetry $\hat{\mathcal{M}} = \hat{\mathcal{T}}, \hat{\mathcal{C}}, \hat{\mathcal{S}}$, if only if

$$\hat{\mathcal{M}}\hat{H}\hat{\mathcal{M}}^{-1}. \tag{3.11}$$

In momentum space the requirements in eqs. (3.8-3.10) lead to the more familiar ones:

$$\hat{\mathcal{T}}\mathcal{H}\hat{\mathcal{T}}^{-1} = \mathcal{H} \quad \rightarrow \quad \hat{U}_T\mathcal{H}^\star(k)\hat{U}_T^\dagger = \mathcal{H}(-k), \tag{3.12}$$

$$\hat{\mathcal{C}}\mathcal{H}\hat{\mathcal{C}}^{-1} = \mathcal{H} \quad \rightarrow \quad \hat{U}_C\mathcal{H}^\star(k)\hat{U}_C^\dagger = -\mathcal{H}(-k), \tag{3.13}$$

$$\hat{\mathcal{S}}\mathcal{H}\hat{\mathcal{S}}^{-1} = \mathcal{H} \quad \rightarrow \quad \hat{U}_S\mathcal{H}(k)\hat{U}_S^\dagger = -\mathcal{H}(k). \tag{3.14}$$

Applying these rules to our Hamiltonian we can find a chiral symmetry operator fulfilling the equation 3.14 that is

$$U_S = \sigma_y. \tag{3.15}$$

As regards the other symmetries, neither a time-reversal operator nor a particle-hole operator can be found for general Hamiltonian parameters. Therefore the imbalanced Creutz ladder falls into the AIII class of the A-Z classification. Due to the symmetry properties of the system, the Bloch sphere is constrained to the B_xB_y plane. For $\Delta\epsilon/t < 4$, the Bloch vector describes a circle around the origin when running the wavevector through the Brillouin zone at $k \in [-\pi, \pi]$. This property identifies a quantized winding number $\nu = 1$ in this regime. For $\Delta\epsilon/t > 4$, on the contrary, the origin is not enclosed by the path, i.e. $\nu = 0$(see Fig. 3.3) Therefore the first phase with $\Delta\epsilon < 4$ is an AIII topological insulator and the second phase is a trivial phase. As mentioned in sec. 2.4, more formally, the topological property, can also be identified by integrating the Berry connection $\mathcal{A}_\pm(k) = i\langle\epsilon_\pm|\partial_k|\epsilon_\pm(k)\rangle$ over the Brillouin zone, where$|\epsilon_\pm(k)\rangle$ are the eigenstates of the Hamiltonian (see sec. 2.4.1). This yields the Zak phase $\phi_{Zak} = \int_{BZ} dk\mathcal{A}_\pm(k)$ is equal to π or zero. The Zak phase takes the value $\phi_{Zak} = \pi$ for the upper and lower band in the topological phase and $\phi_{Zak} = 0$ in the non-topological region.

Finally, we analyze a particular case: the perfect balance case $\Delta\epsilon = 0$. In this regime, the model displays flat bands such that $\partial_k\epsilon_\pm(k) = 0$. This means that the velocity of the particles is zero and they cannot propagate along the lattice. This flat band insulator is neither a band insulator nor a Mott insulator, but it shares aspects of both. As for a band insulator, the insulating property is not due to correlations, however, like a Mott-insulator, the particles are localized.

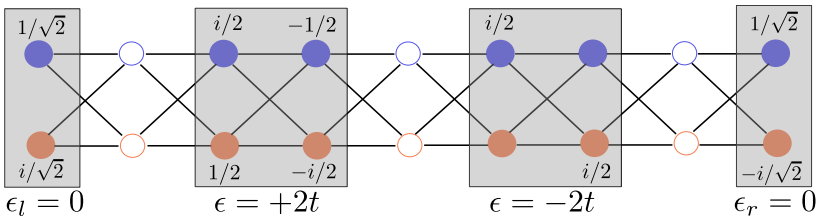

Figure 3.4: **Eigenstates of the balanced Creutz ladder.** The bulk solutions of the Creutz ladder without imbalance $\Delta\epsilon = 0$ can be expressed in terms of localized Aharonov-Bohm cages.

For this particular case we can write the Hamiltonian in terms of Aharonov-Bohm cages for which any movement is suppressed:

$$|+2t\rangle = \omega_{j,+}^\dagger|0\rangle \qquad \omega_{j,+}^\dagger = \frac{1}{2}\left(i\hat{c}_{j,u}^\dagger + \hat{c}_{j,d}^\dagger - \hat{c}_{j+1,u}^\dagger - i\hat{c}_{j+1,d}^\dagger\right), \tag{3.16}$$

$$|-2t\rangle = \omega_{j,-}^\dagger|0\rangle \qquad \omega_{j,-}^\dagger = \frac{1}{2}\left(i\hat{c}_{j,u}^\dagger + \hat{c}_{j,d}^\dagger + \hat{c}_{j+1,u}^\dagger + i\hat{c}_{j+1,d}^\dagger\right). \tag{3.17}$$

The eigenstates are superpositions of particles living on the four sites of neighboring rungs of the ladder. The flat band Hamiltonian can be equivalently described in this plaquette basis as:

$$\hat{H}_{FB} = \sum_j \sum_{\alpha=\pm} \epsilon_\alpha \omega_{j,\alpha}^\dagger \omega_{j,\alpha}, \tag{3.18}$$

where every plaquette has the same energy $\epsilon_\pm = \pm 2t$. For open boundary conditions however, we can only form $2(N-1)$ bulk states, and we require $2N - (2N-2) = 2$ more states to determine a basis. These missing states reside on the left and right sites,

$$|0\rangle_L = \hat{l}^\dagger|0\rangle \qquad \hat{l}^\dagger = \frac{1}{\sqrt{2}}\left(\hat{c}_{1,u}^\dagger + i\hat{c}_{1,d}^\dagger\right), \tag{3.19}$$

$$|0\rangle_R = \hat{r}^\dagger|0\rangle \qquad \hat{r}^\dagger = \frac{1}{\sqrt{2}}\left(\hat{c}_{N,u}^\dagger - i\hat{c}_{N,d}^\dagger\right), \tag{3.20}$$

and yield one additional contribution $\hat{H}_{boundary} = \sum_{\eta=r,l} \hat{\eta}^\dagger\hat{\eta}$ to the Hamiltonian 3.18, with $\epsilon_l = \epsilon_l = 0$ a pair of zero-energy topological edge states (see Fig. 3.4).

Turning on the imbalance $\Delta\epsilon$ then leads to an effective hopping between these plaquettes:

$$V_{imb} = \frac{\Delta\epsilon}{4}\sum_{j=2}^{N-1}\left(\hat{\omega}_{j-1,+}^\dagger - \hat{\omega}_{j-1,-}^\dagger\right)\left(\hat{\omega}_{j,+} + \hat{\omega}_{j,-}\right) + \frac{\Delta\epsilon}{4}\sum_\alpha \sqrt{2}\left(-\hat{l}^\dagger\hat{\omega}_{1,\alpha} - i\alpha\hat{r}^\dagger\hat{\omega}_{N-1,\alpha}\right) + H.C.. \tag{3.21}$$

It deforms the flat energy bands up to $\Delta\epsilon = 4t$, where the gap closes and reopens. An important observation in this context is that the edge modes maintain zero energy throughout the TI-region.

3.3 Phase Diagram

In Fig. 3.5 we show the phase diagram of the Creutz-Hubbard ladder. It was only studied for positive imbalances in Ref. [59]. Here we extended the study to negative ones, proving the mirror symmetry. In Fig. 3.5 we can distinguish three parameter regimes:

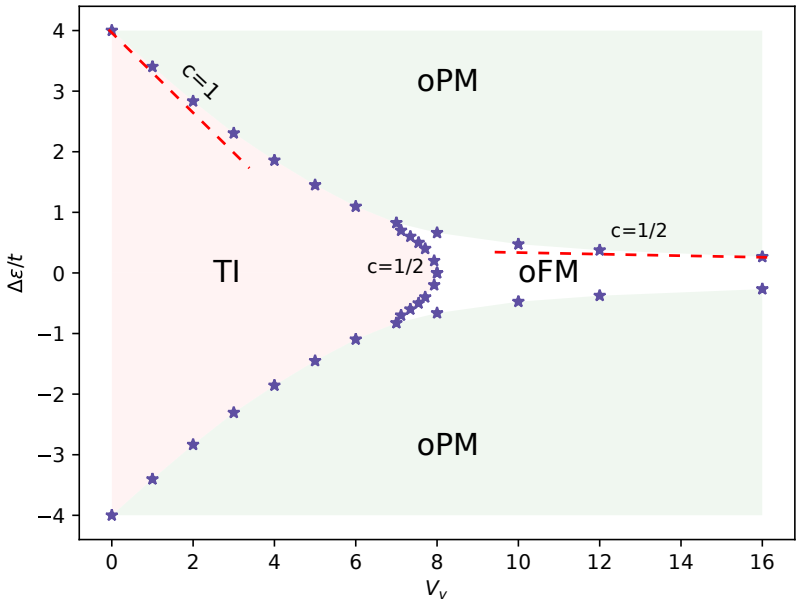

Figure 3.5: **Complete phase diagram of the imbalanced Creutz-Hubbard model.** The model has three gapped phases: a topological insulator phase (TI), an orbital paramagnet (oPM) and an orbital ferromagnet phase (oFM). Stars denote critical points as determined numerically, the dashed lines are results of a perturbative approach (red) and a self-consistent mean-field analysis (red).

- **Weak interactions**: It can be understood as a ferromagnetic coupling between the two chains in the Ising model description. We can explore the influence of this coupling on the individual chains through a self-consistent mean-field approach that allows us to analytically predict the critical line.

- **Intermediate interactions**: In this regime, neither the kinetic term nor the interaction can be treated in a perturbative manner. However, it turns out that indeed an effective model arises that correctly predicts the phase transition for the balanced model.

- **Strong interactions**: We derive an effective spin model in an analog fashion to the Heisenberg model arising in the strong-coupling limit of the Hubbard model. This effective model explains the observed orbital paramagnetic and ferromagnetic phases and yields a prediction of the critical line separating them.

In the following sections we will describe in detail the phase diagram in Fig. 3.5.

3.3.1 TI-PM phase transition

In this section, we study the phase transition between the topological insulator and the orbital paramagnetic phase. We will introduce an effective model for weak interactions and we will study the phase transitions through mean-field theory (MF). Then we combine these results of MF with numerical study with matrix product state (MPS) (for more details see Chap. 6 and 7).

Weakly-interacting regime

Consider the free part of the Creutz-Hubbard Hamiltonian $\hat{H}_C$ defined in the Eq. (3.2). Introducing the spinor notation we can rewrite the Hamiltonian in the following way

$$\hat{H}_C = t\sum_j c_j^\dagger \left(i\sigma_z - \sigma_x\right) c_{j+1} + \frac{\Delta\epsilon}{4}\sum_j c_j^\dagger \sigma_z c_j + H.c. \tag{3.22}$$

where $\hat{c}_j = (\hat{c}_{j,u}, \hat{c}_{j,d})^T$.

Via the transformation $c_j = (-i\sigma_z)^j \tilde{c}_j$, we obtain that the hopping along the two legs becomes now identical at the price of having site-dependent diagonal hopping terms that connect neighboring sites in opposite legs of the ladder:

$$\hat{H}_C = t\sum_j \tilde{c}_j^\dagger \left(-1 + (-1)^j \sigma_y\right) \tilde{c}_{j+1} + \frac{\Delta\epsilon}{4}\sum_j \tilde{c}_j^\dagger \sigma_z \tilde{c}_j + H.c.. \tag{3.23}$$

We now define two sets of Majorana fermions $\hat{u}_{j,1}$, $\hat{u}_{j,2}$ and $\hat{d}_{j,1}$, $\hat{d}_{j,2}$ with the characteristic properties

$$\hat{u}_{j,1}^\dagger = \tilde{c}_{j,u}^\dagger + \tilde{c}_{j,u} = \hat{u}_{j,1} \qquad \{\hat{u}_{j,1}, \hat{u}_{l,1}\} = \delta_{j,l}, \tag{3.24}$$

$$\hat{d}_{j,1}^\dagger = \tilde{c}_{j,d}^\dagger + \tilde{c}_{j,d} = \hat{d}_{j,1} \qquad \left\{\hat{d}_{j,1}, \hat{d}_{l,1}\right\} = \delta_{j,l}. \tag{3.25}$$

The Hamiltonian can be expressed in the new basis $m_j = \left(\hat{u}_{j,1}, \hat{d}_{j,1}, \hat{u}_{j,2}, \hat{d}_{j,2}\right)^T$ as:

$$\hat{H}_C = \frac{i}{4}\left[t\sum_j m_j^T \begin{bmatrix} 2i(-1)^{j+1}\sigma_y & -2I \\ 2I & 2i(-1)^{j+1}\sigma_y \end{bmatrix} m_{j+1} + \frac{\Delta\epsilon}{4}\sum_j m_j^T \begin{bmatrix} 0 & 2\sigma_z \\ 2\sigma_z & 0 \end{bmatrix} m_j\right]. \tag{3.26}$$

Defining a new Majorana fermion from the symmetric and anti-symmetric combinations, $\tilde{m}_j = \left(a_j, \tilde{a}_j, b_j, \tilde{b}_j\right)^T$

$$\hat{a}_j = \frac{\hat{d}_{j,1} + \hat{u}_{j,2}}{\sqrt{2}} \qquad \hat{\tilde{a}}_j = \frac{\hat{u}_{j,1} + \hat{d}_{j,2}}{\sqrt{2}} \tag{3.27}$$

$$\hat{b}_j = \frac{\hat{u}_{j,1} - \hat{d}_{j,2}}{\sqrt{2}} \qquad \hat{\tilde{b}}_j = \frac{\hat{d}_{j,1} - \hat{u}_{j,2}}{\sqrt{2}}, \tag{3.28}$$

the Hamiltonian reads:

$$\hat{H}_C = \frac{2i}{4}\left[t\sum_j \tilde{m}_j^T \begin{bmatrix} 0 & I + (-1)^j\sigma_z \\ -I - (-1)^j\sigma_z & 0 \end{bmatrix} \tilde{m}_{j+1}\right] + \frac{\Delta\epsilon}{4}\sum_j \tilde{m}_j^T \begin{bmatrix} -i\sigma_y & 0 \\ 0 & -i\sigma_y \end{bmatrix} \tilde{m}_j, \tag{3.29}$$

and corresponds to two independent Majorana systems [78]. To better understand the independent chains we can define a new fermionic operator:

$$\begin{bmatrix} a_j \\ \tilde{a}_j \\ b_j \\ \tilde{b}_j \end{bmatrix} = \begin{bmatrix} i & -i & 0 & 0 \\ 1 & 1 & 0 & 0 \\ 0 & 0 & i & -i \\ 0 & 0 & 1 & 1 \end{bmatrix} \begin{bmatrix} p_{j,1} \\ p_{j,1}^\dagger \\ p_{j,2} \\ p_{j,2}^\dagger \end{bmatrix} \qquad \text{for} \quad \text{j} \quad \text{odd} \tag{3.30}$$

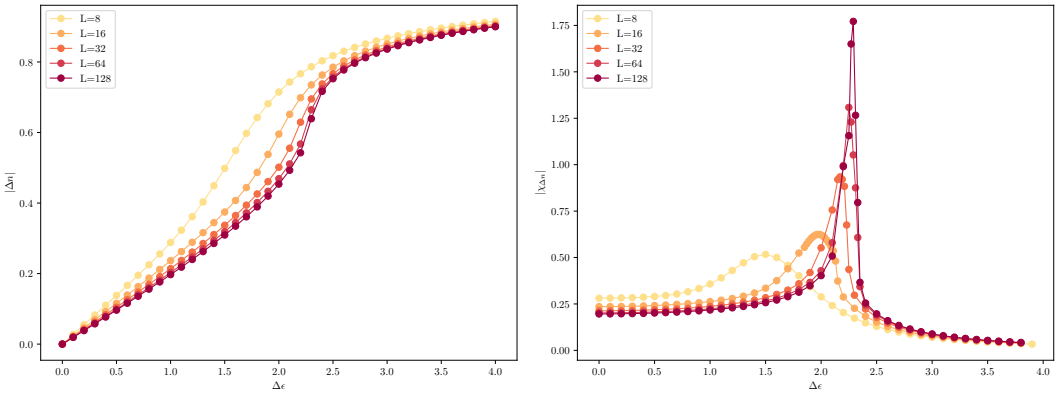

Figure 3.6: **TI-oPM transition.** The left panel shows the ground state imbalance (or equivalently, the mean-field magnetization) $\Delta n = \sum_j \sigma_j^z$ as obtained through MPS calculations on a lattice with bond dimension $\chi = 200$. The right panel represents the divergence of the paramagnetic susceptibility $\chi_{\Delta n}$ as an indicator of the phase transition.

$$\begin{bmatrix} a_j \\ \tilde{a}_j \\ b_j \\ \tilde{b}_j \end{bmatrix} = \begin{bmatrix} 0 & 0 & i & -i \\ 0 & 0 & 1 & 1 \\ i & -i & 0 & 0 \\ 1 & 1 & 0 & 0 \end{bmatrix} \begin{bmatrix} p_{j,1} \\ p_{j,1}^\dagger \\ p_{j,2} \\ p_{j,2}^\dagger \end{bmatrix} \quad \text{for} \quad \text{j} \quad \text{even.} \tag{3.31}$$

Then the Hamiltonian reads

$$\hat{H}_C = t \sum_{n=1,2} \sum_j (-1)^n \left[i(-1)^j \hat{p}_{j,n}^\dagger \hat{p}_{j+1,n} - i\hat{p}_{j,n}^\dagger \hat{p}_{j+1,n}^\dagger + H.C \right] + \frac{\Delta\epsilon}{4} \sum_{n=1,2} \sum_j \left(2\hat{p}_{j,n}^\dagger \hat{p}_{j,n} - 1 \right), \tag{3.32}$$

and after an additional transformation we obtain that:

$$\hat{H}_c = -t \sum_j \sum_n \left(\hat{r}_{j,n}^\dagger \hat{r}_{j+1,n} + \hat{r}_{j,n}^\dagger \hat{r}_{j+1,n}^\dagger + H.C. \right) + \frac{\Delta\epsilon}{4} \sum_j \sum_n \left(2\hat{r}_{j,n}^\dagger \hat{r}_{j,n} - 1 \right). \tag{3.33}$$

In the new notation, we can identify two fully independent subsystems, which do not display particle number conservation. Both terms can be identified as Ising models. Under a Jordan-Wigner transformation

$$\hat{r}_{j,n}^\dagger = \prod_{l<j} \left(-\sigma_{l,n}^z \right) \sigma_{j,n}^+ \tag{3.34}$$

the Hamiltonian takes the form

$$\hat{H}_C = \sum_{j,n} \left(-t\sigma_{j,n}^x \sigma_{j+1,n}^x + \frac{\Delta\epsilon}{4} \sigma_{j,n}^z \right). \tag{3.35}$$

We now consider the model with Hubbard-like interactions for the first time. In particular, we take a look at the regime of small interactions $V_v < t$ and study how these interactions alter the results of the non-interacting model. Applying the series of transformations presented above we obtain that the interaction term reads

$$\hat{H}_{Hub} = \frac{V_v}{2} \sum_j \left(\hat{r}_{j,1}^\dagger \hat{r}_{j,1} + \hat{r}_{j,2}^\dagger \hat{r}_{j,2} + i\hat{r}_{j,1}^\dagger \hat{r}_{j,2} - i\hat{r}_{j,2}^\dagger \hat{r}_{j,1} - 2\hat{r}_{j,1}^\dagger \hat{r}_{j,1} \hat{r}_{j,2}^\dagger \hat{r}_{j,2} \right). \tag{3.36}$$

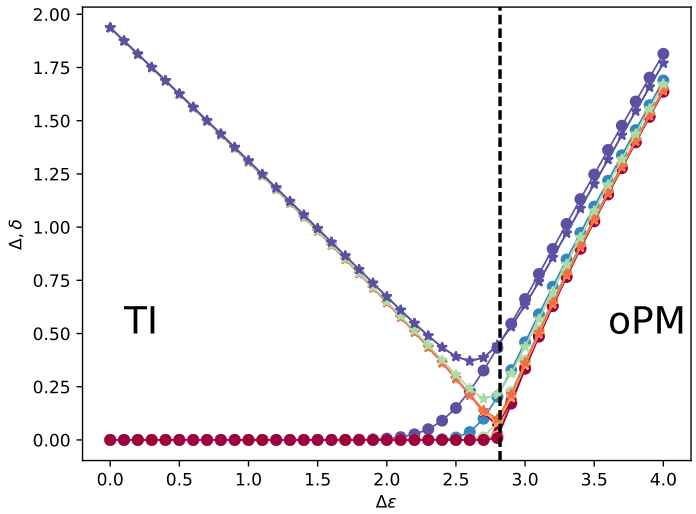

Figure 3.7: **Energy gaps along the TI-oPM transition.** We show the single-particle gap E_δ (stars) and the two-particle gap E_Δ (dots). E_Δ converges to zero in the topological phase due to the presence of a zero-energy edge mode, and to a non-zero value in the paramagnetic phase. Here different colors represent different lengths.

For half filling we have $\langle \hat{r}^\dagger_{j,1}\hat{r}_{j,2} - \hat{r}^\dagger_{j,2}\hat{r}_{j,1}\rangle = 0$, simplifying the Hamiltonian to

$$\hat{H}_{Hub} = \frac{V_v}{2}\sum_j \left(\hat{r}^\dagger_{j,1}\hat{r}_{j,1} + \hat{r}^\dagger_{j,2}\hat{r}_{j,2} - \hat{r}^\dagger_{j,1}\hat{r}_{j,1}\hat{r}^\dagger_{j,2}\hat{r}_{j,2}\right). \tag{3.37}$$

The Jordan-Wigner transformation translates this expression to a ferromagnetic coupling between the two Ising models:

$$\hat{H}_{Hubb} = \frac{V_v}{4}\sum_j \left(1 - \sigma^z_{j,1}\sigma^z_{j,2}\right). \tag{3.38}$$

In all parameter regimes, the imbalanced Creutz-Hubbard model can be understood as two coupled quantum Ising chains. For weak interactions $V_v < t$, we can treat the mutual effect of chains on each other through an MF decoupling which renormalizes the original transverse magnetization term:

$$\hat{H} = \sum_{j,n} = \left(-t\sigma^x_{j,n}\sigma^x_{j+1,n} + \frac{\Delta\epsilon - V_v m_n}{4}\sigma^z_{j,n}\right). \tag{3.39}$$

This approximation is very accurate for considerably large interactions. Going beyond the numerical approach, and knowing that the analytical result for a simple Ising chain:

$$M(\alpha) = \begin{cases} 2\frac{1-\alpha^2}{\pi\alpha}\left(\prod(\alpha^2,\alpha) - K(\alpha)\right), & \text{for} \quad \alpha < 1 \\ 2\frac{\alpha^2-1}{\pi\alpha}\prod(1/\alpha^2, 1/\alpha), & \text{for} \quad \alpha > 1 \end{cases}, \tag{3.40}$$

we can obtain the equation that predicts the critical line separating the topological and the non-topological phase in the weak coupling limit (dashed line in Fig. 3.5).

Increasing the interaction we study the model using an MPS based algorithm i.e. DMRG. In Fig. 3.6 we show the density imbalance $\Delta N = \sum_j (\hat{n}_{j,u} - \hat{n}_{j,d})$ and the susceptibility $\chi_{\Delta N} = \frac{\partial(\Delta N)}{\partial \Delta\epsilon}$. In particular, we show that fixing V_v we can determine

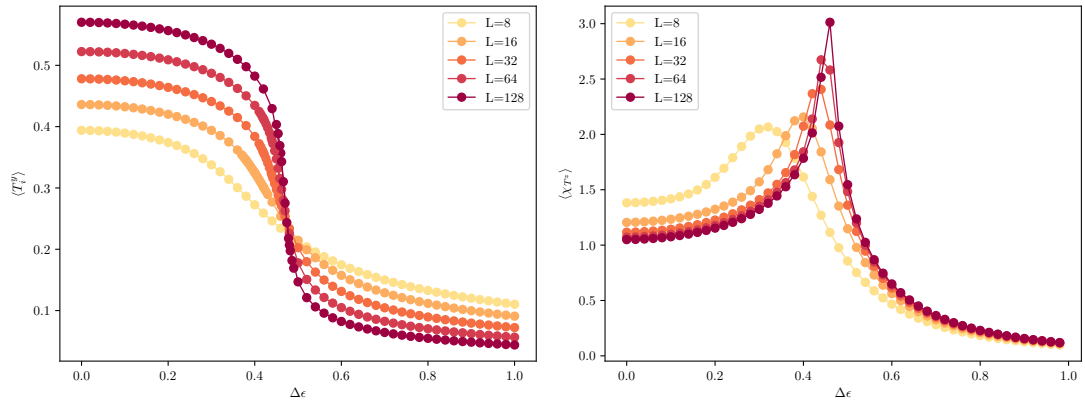

Figure 3.8: **oFM-oPM transition.** The left panel shows the ground state magnetization $\langle T^y \rangle$ as obtained through MPS calculations on a lattice for different lengths. The right panel represents the divergence of the susceptibility χ_{T^z} as an indicator of the phase transition.

the critical point through the divergence of the susceptibility. Moreover, we can study the phase transition looking at the behavior of the degeneracy of the ground state for different fillings. We define one- and two-particle energy gaps as

$$E_\Delta = \lim_{N\to\infty} \frac{1}{2} \left(E(N+2) + E(N-2) - 2E(N)\right) \tag{3.41}$$

$$E_\delta = \lim_{N\to\infty} \frac{1}{2} \left(E(N+2) + E(N-2) - 2E(N)\right) \tag{3.42}$$

We observe that a single particle that is added to the half-filled model will occupy a zero-energy edge mode in the topological phase. In the non-topological phase, a particle added to the system will occupy a mode in the higher energy band. Lifting it therefore costs a non-zero energy $E(N+1) - E(N)$. This is reflected by the behavior of E_δ. The energy gap E_Δ, on the contrary, is non-zero in any gapped phase, as in both the topological and non-topological system, at least one of the particles has to overcome the energy gap. At the critical point, the gap closes. We can use these definitions to identify a conventional insulator by $E_\Delta \neq E_\delta \neq 0$ and the topological insulator by $E_\Delta \neq E_\delta = 0$. Fig. 3.7 shows that the predicted behavior is observed.

3.3.2 Strongly-interacting regime: oFM-oPM phase transition

In this section, we will study the phase transition between the ferromagnetic and paramagnetic phase transition that occurs at strong interaction. Before discussing the DMRG results we will show that in the limit of $V_v \gg t$, it is possible to find an effective model that can be understood in analogy to the Heisenberg model. In fact, in the strong-coupling limit, the ground state of the system is described by a Mott insulator phase in which the double-occupancy of a rung is fully suppressed due to the strong on-site repulsion. We apply the second order perturbation theory, where the unperturbed Hamiltonian is $\hat{H}_{Hubb} = V_v \sum_j \hat{n}_{j,u}\hat{n}_{j,d}$,where the ground state of $\hat{H}_{Hubb}$ is degenerate. The Fock basis is:

$$\{|\uparrow\uparrow\rangle, |\downarrow\downarrow\rangle, |\uparrow\downarrow\rangle, |\downarrow\uparrow\rangle, |\downarrow\uparrow, 0\rangle|0, \downarrow\uparrow\rangle\}\,. \tag{3.43}$$

In this basis we can write the Hamiltonian as

$$P\hat{H}_{eff}P = P\hat{H}_{Hubb}P + P\hat{H}_C P + P\hat{H}_C Q \frac{1}{E_0 - Q\hat{H}Q} Q\hat{H}_C P, \tag{3.44}$$

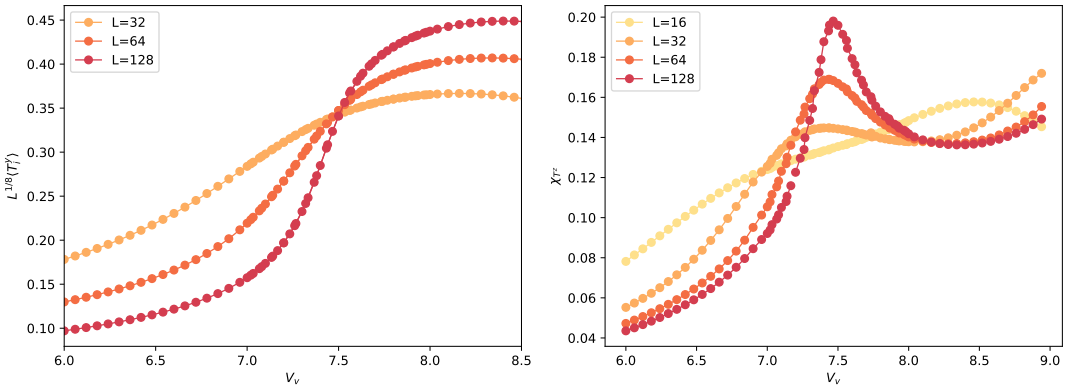

Figure 3.9: **TI-oFM transition.** The left panel shows the ground state magnetization $\langle T^y \rangle$ as obtained through MPS calculations on a lattice for different lengths. The right panel represents the divergence of the susceptibility χ_{T^z} as an indicator of the phase transition.

where P and Q are projectors defined as

$$P = \sum_m |m\rangle\langle m|, \quad \text{where} \quad |m\rangle \in \{|\uparrow\uparrow\rangle, |\downarrow\downarrow\rangle, |\uparrow\downarrow\rangle, |\downarrow\uparrow\rangle\}, \tag{3.45}$$

$$Q = \sum_m |m\rangle\langle m|, \quad \text{where} \quad |m\rangle \in \{|\downarrow\uparrow, 0\rangle|0, \downarrow\uparrow\rangle\}. \tag{3.46}$$

In this basis the Creutz-Hubbard model can be mapped in a spin model:

$$PH_{eff}P = \frac{1}{4}JN + J\sum_j T_j^y T_{j+1}^y + \Delta\epsilon \sum_j T_j^z, \tag{3.47}$$

where $J = -8t^2/V_v$, T_j^y and T_j^z are spin operators defined as:

$$T_j^y = \frac{1}{2}\left(-i\hat{c}_{j,u}^\dagger \hat{c}_{j,d} + i\hat{c}_{j,d}^\dagger \hat{c}_{j,u}\right) \qquad T_j^z = \frac{1}{2}\left(\hat{c}_{j,u}^\dagger \hat{c}_{j,u} - \hat{c}_{j,d}^\dagger \hat{c}_{j,d}\right). \tag{3.48}$$

This orbital quantum Ising model predicts the existence of two phases: a disordered paramagnetic phase for large imbalances and a long-range orbital ferromagnetic phase for small imbalances. Moreover, we expect a phase transition to occur for:

$$\frac{\Delta\epsilon}{t} = \frac{4t}{V_v}, \tag{3.49}$$

as indicated by the red dashed line in Fig. 3.5. To test this prediction, we calculate the observables of the effective Ising model, the paramagnetic magnetization $\langle T_j^z \rangle$ and the ferromagnetic magnetization $\langle T_j^y \rangle$. As the determination of the latter can suffer from incomplete symmetry-breaking, we compute the structure factor

$$S_{T_y,T_y}(k) = \frac{1}{N^2}\sum_{l,j} e^{ik(l-j)}\langle T_l^y T_j^y \rangle, \tag{3.50}$$

and extract the magnetization from

$$\langle T_j^y \rangle = \sqrt{S_{T_y,T_y}(0)} \tag{3.51}$$

In Fig. 3.8 the two magnetizations show the expected behavior of a quantum Ising transition. In Fig. 3.5 the prediction of the effective model and numerical results agree well even for moderate interaction strengths.

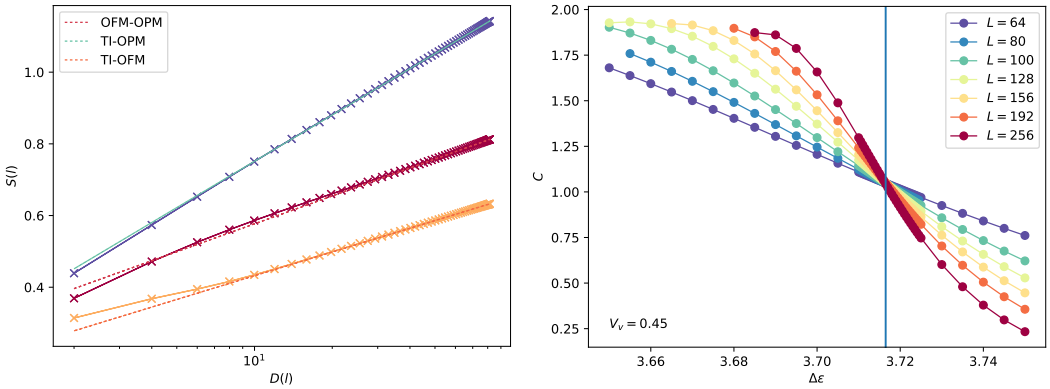

Figure 3.10: **Central Charge.** In the left panel, the scaling of the entanglement entropy with respect to the size of the bi-partitions is studied for the three transitions in the model. In the right, panel we showed the FSS of the central charge showing that it can capture the phase transition for weak interactions.

3.3.3 Intermediate regime: TI-oFM phase transition

In section 3.2, we showed that it is possible to study the model without interaction through the Ahranov-Bohm cages deriving an effective model. Now we will write the interaction Hamiltonian in terms of the cages. The interaction term is

$$\hat{V}_{Hubb} = \hat{V}_{nn} + \hat{V}_{pt} + \hat{V}_{dt}, \tag{3.52}$$

where V_{nn} is a nearest-neighbor interaction

$$\hat{V}_{nn} = \frac{V_v}{2} \sum_{\alpha=\pm} (\hat{n}_l \hat{n}_{1,\alpha} + \hat{n}_r \hat{n}_{N-1,\alpha}) + \frac{V_v}{4} \sum_{j=2}^{N-1} \sum_{\alpha\beta=\pm} \hat{n}_{j-1,\alpha} \hat{n}_{j,\beta}. \tag{3.53}$$

Here $\hat{n}_{j,\alpha} = \hat{\omega}^\dagger_{j,\alpha} \hat{\omega}_{j,\alpha}$ with $\alpha = \pm$ are the number operators in the plaquette basis, and $\hat{n}_\eta = \eta^\dagger \eta$ with $\eta \in \{l, r\}$ are the corresponding edge terms. Instead V_{pt} represents a pair-tunnelling term:

$$\hat{V}_{pt} = \tilde{J} \sum_{j=2}^{N-1} \hat{\omega}^\dagger_{j-1,+} \hat{\omega}_{j-1,-} \left(\hat{\omega}^\dagger_{j,-} \hat{\omega}_{j,+} + \hat{\omega}^\dagger_{j,+} \hat{\omega}_{j,-} \right) + H.c, \tag{3.54}$$

where $J = V_v/4$. This term corresponds to an anti-correlated pair tunneling along the rungs of neighboring sites. Finally, there is a density-assisted tunneling term

$$\hat{V}_{dt} = T_d \sum_\alpha \left(\hat{n}_{j-1,+} + \hat{n}_{j-1,-} - \hat{n}_{j+1,+} - \hat{n}_{j+1,-} \right) \hat{\omega}^\dagger_{j,+} \hat{\omega}_{j,-} + 2T_d \left(\hat{n}_l \hat{\omega}^\dagger_{1,+} \hat{\omega}_{1,-} \hat{n}_r - \hat{\omega}^\dagger_{N-1,+} \hat{\omega}_{N-1,-} \right) \tag{3.55}$$

The effective model identifies the paramagnetic susceptibility as a valid indicator of the transition (see Fig. 3.9). Indeed we observe that the divergence of this quantity continues to indicate a transition in the model with imbalance.

3.3.4 Characterization of critical lines through the entanglement entropy

An alternative approach to study the nature of critical lines is the investigation of quantum-information features. A quantity of particular interest in this context is the

so-called entanglement entropy

$$S(l) = -\mathrm{Tr}\hat{\rho}_\mathrm{l} \log\left(\rho_\mathrm{l}\right), \tag{3.56}$$

where ρ_l is the density matrix for a bi-partition of the system. For a critical system with open boundary conditions, the entanglement entropy links directly to the central charge c of the conformal field theory underlying the critical phase [92]

$$S(l) = \frac{c}{6} \ln\left(\frac{2L}{\pi} \sin\left(\frac{\pi l}{L}\right)\right) \tag{3.57}$$

As the entanglement entropy is a conceptual building block of tensor networks, it is easily accessible in the numerical simulations.

For the weak-coupling limit, we have seen that the model can be written as two Ising models coupled. Due to the fact that the critical point in a single quantum Ising model has a conformal charge $c = 1/2$, we expect that the central charge $c = 1$ in the critical line between the topological insulator and the paramagnetic phase. Moreover, in the non-interacting limit, the model at the critical point can be understood as a massless Dirac fermion with central charge $c = 1$.

In the strong-coupling limit, we found an effective description through another quantum Ising model, but this time a single copy, predicting a central charge $c = 1/2$. Finally, for the intermediate regime, we understood the relevant physics explaining the transition between topological insulator and ferromagnetic phase by yet another Ising model, hence again we expect $c = 1/2$. An analysis of the entanglement entropy scaling on the critical lines confirms all three predictions, see Fig. 3.10.

Chapter 4

Renormalization group flows for topological Hamiltonian

In this chapter we will study the connection between condensed matter and high energy physics in the field of SPT phases.

One of the major examples of the cross-fertilization of fundamental ideas between these two disciplinas is the theory of spontaneous symmetry breaking, which is both paramount to our current understanding of phase transitions in condensed matter and to the standard model describing elementary particles and their interactions. These parallelisms become clearer under the language of interacting quantum fields. In this context a multi-disciplinar approach based on concepts of scaling and critical phenomena leads to the so-called the so called renormalization group, which has turned out to be the key to understand many-body effects in condensed matter systems and the relativistic quantum field theory.

Although these topological quantum phase transitions cannot be understood from the principle of spontaneously symmetry breaking mentioned above, they can still be characterized by the closure of a many-body energy-gap, such that the scaling phenomena should be also relevant. According the connection of continuum relativistic quantum field theories, scaling and RG to these topological phases might offer a systematic route to understand correlation effects.

In this chapter we study the Wilson-Hubbard topological matter, which can be described in terms of relativistic QFT of massive Wilson fermions with four-Fermi interactions in the vicinity of a topological band inversion point. We show that a wilsonian RG offers a neat qualitative picture to understand these topological phases and a quantitative scheme to obtain the phase boundaries. In particular we will show that a wilsonian RG approach combined with the so-called topological Hamiltonian, provide a quantitative route to understand interaction induced topological phase transitions that occur in the Wilson-Hubbard model. Moreover by means of exhaustive numerical simulations based on matrix product state (MPS) we will check the goodness of our results.

4.1 Quantum field theories as representation of non-interacting topological insulators

In this section, we describe a generic lattice Hamiltonian [93–96] that can host different classes of non-interacting topological insulators [5, 6, 13], as well as a continuum quantum field theory that captures its long-wavelength properties, including the underlying topological features. This will serve us to review certain aspects of topological insulators, and to set the notation used throughout this manuscript.

4.1.1 Continuum Dirac QFTs and topological invariants

A fundamental ingredient of this work is the massive Dirac quantum field theory in a $D = (d+1)$-dimensional Minkowski space-time [97], which can serve as a building block to construct a representative QFT for various topological insulating phases [94]. In the Hamiltonian formulation, this quantum field theory (QFT) can be written as

$$H_{\mathrm{D}} = \int_{\Lambda^d} \frac{\mathrm{d}^d k}{(2\pi)^d} \Psi^\dagger_\mu(\boldsymbol{k}) [h_{\mathrm{D}}(\boldsymbol{k})]^{\mu,\nu} \Psi_\nu(\boldsymbol{k}), \;\; h_{\mathrm{D}}(\boldsymbol{k}) = \alpha_i k^i + m\beta, \tag{4.1}$$

where $\Psi(\boldsymbol{k}), \Psi^\dagger(\boldsymbol{k})$ are the spinor fermionic field operators fulfilling $\{\Psi_\mu(\boldsymbol{k}), \Psi^\dagger_\nu(\boldsymbol{k}')\} = (2\pi)^d \delta_{\mu,\nu} \delta^{(d)}(\boldsymbol{k} - \boldsymbol{k}')$, and the momentum lies below a certain ultra-violet (UV) cutoff to regulate the QFT, namely $\boldsymbol{k} \in \Lambda^d$ if $|k_i| \leq \Lambda_{\mathrm{c}}$ (i.e. $\Lambda^d \to \mathbb{R}^d$ as the cutoff is removed $\Lambda_{\mathrm{c}} \to \infty$). In the above expression, $\{\alpha_i\}_{i=1}^d$ and β are the so-called Dirac matrices, which are mutually anti-commuting Hermitian matrices that square to the identity, and we use natural units $\hbar = c = 1$ together with Einstein's summation criterion. Depending on the particular choice of the Dirac matrices [98], the single-particle Hamiltonian $h_{\mathrm{D}}(\boldsymbol{k})$ may, or may not, respect the following discrete symmetries: time-reversal symmetry T is fulfilled if $U_{\mathsf{T}} h_{\mathrm{D}}(-\boldsymbol{k})^* U_{\mathsf{T}}^\dagger = h_{\mathrm{D}}(\boldsymbol{k})$; particle-hole symmetry C takes place when $U_{\mathsf{C}} h_{\mathrm{D}}(-\boldsymbol{k})^* U_{\mathsf{C}}^\dagger = -h_{\mathrm{D}}(\boldsymbol{k})$; and the so-called sub-lattice symmetry S occurs if $U_{\mathsf{S}} h_{\mathrm{D}}(\boldsymbol{k}) U_{\mathsf{S}}^\dagger = -h_{\mathrm{D}}(\boldsymbol{k})$, where we have introduced various unitary rotations $U_{\mathsf{T}}, U_{\mathsf{C}}, U_{\mathsf{S}}$ [99, 100]. We note that these discrete symmetries can be related to the ten-fold classification of symmetric spaces [71] via the corresponding time-evolution operator $U_{\mathrm{D}}(t) = e^{-ith_{\mathrm{D}}(\boldsymbol{k})}$.

To give concrete examples that shall be used throughout this work, let us consider *(i)* the $(2+1)$-dimensional QFT (4.1) with $\alpha_1 = \sigma^x$, $\alpha_2 = \sigma^y$, and $\beta = \sigma^z$ expressed in terms of Pauli matrices. In this case, there is no unitary operator that can fulfil any of the above transformations, and the Dirac QFT thus explicitly breaks the time-reversal, particle-hole, and sub-lattice symmetries. In this case, the time-evolution operator $U_{\mathrm{D}}(t) = e^{-ith_{\mathrm{D}}(\boldsymbol{k})}$ lies in the so-called unitary symmetric space [94], labelled as A. From this parent Hamiltonian, one may use a Kaluza-Klein-type dimensional reduction by compactifying the second spatial direction into a vanishingly small circle [93, 94]. *(ii)* The resulting $d = 1$ Dirac QFT (4.1) with $\alpha_1 = \sigma^x$, and $\beta = \sigma^z$, now respects the sub-lattice symmetry with $U_{\mathsf{S}} = \sigma^y$, but breaks both time-reversal and particle-hole symmetries. In this case, the time-evolution operator belongs to the chiral unitary symmetric space, labeled as AIII. We note that this idea of dimensional reduction allows one to find representatives of all ten possible symmetric spaces starting from a higher-dimensional Dirac QFT [93, 94].

To understand the use of these QFTs as building blocks of topological insulators, let us consider the zero-temperature groundstate $|\epsilon_{\mathrm{gs}}\rangle = \prod_{\boldsymbol{k}\in\Lambda^d} |\epsilon_-(\boldsymbol{k})\rangle$, which is obtained by occupying all the single-particle modes $|\epsilon_-(\boldsymbol{k})\rangle$ with energies $\epsilon_-(\boldsymbol{k}) = -\sqrt{m^2 + \boldsymbol{k}^2}$.

As was mentioned in sec. 2.4, depending on the dimensionality and the discrete symmetries of the Hamiltonian introduced above, one can define a *topological invariant* that characterizes each ground-state. These topological invariants, which cannot be modified by perturbations that respect the corresponding symmetries unless a quantum phase transition takes place, can be defined through momentum integrals of either the so-called *Chern characters* or *Chern-Simons forms* [94]. For the examples cited above, one finds that: *(i)* the $d = 2$ Dirac QFT in the A class is characterized by the integral of the first Chern character $\mathsf{ch}_1 = \frac{i}{2\pi}\partial_{k^i}\langle\epsilon_-(\boldsymbol{k})|\partial_{k^j}|\epsilon_-(\boldsymbol{k})\rangle dk^i \times dk^j$,

$$\mathsf{Ch}_1 = \int_{\Lambda^2} \mathsf{ch}_1 = \frac{m}{2|m|}. \tag{4.2}$$

This topological invariant, which is known as the first Chern number (see sec. 2.4.2), cannot change unless $m = 0$, which signals a quantum phase transition. *(ii)* For the $d = 1$ Dirac QFT in the AIII class, the integral of the first Chern-Simons form $\mathsf{Q}_1 = \frac{\mathrm{i}}{2\pi}\langle\epsilon_-(k)|\partial_k|\epsilon_-(k)\rangle dk$ yields the Chern-Simmons invariant

$$\mathsf{CS}_1 = \int_{\Lambda^1} \mathsf{Q}_1 = \frac{m}{4|m|}. \tag{4.3}$$

In contrast to the Chern number, this quantity is not gauge invariant, and one typically defines an associated Wilson loop $\mathsf{W}_1 = e^{i2\pi\mathsf{CS}_1}$, which gives a quantized topological invariant that cannot change unless $m = 0$. We emphasize that similar topological invariants can be constructed for any particular higher-dimensional Dirac QFT [94], which allows one to find the required building blocks for all 10 possible topological insulators-superconductors [99,100], excluding the appearance of additional crystalline symmetries.

4.1.2 Discretized QFTs, fermion doubling and invariants

From a condensed-matter perspective [101], the above Dirac QFT (4.1) will arise as a low-energy approximation that tries to capture the relevant physics of a particular material at long wavelengths $\xi \gg a$ or, equivalently, at low momenta $|k_i| \leq \Lambda_{\mathrm{c}} \ll 2\pi/a$. Here, a is the lattice constant of the material, which serves as natural UV regulator of the QFT. Paradigmatic examples of massless Dirac QFTs in condensed-matter setups appear in the so-called one-dimensional Luttinger liquids [102] and two-dimensional graphene [103]. On the other hand, for a non-vanishing mass/gap, these continuum QFTs (4.1) can serve as building blocks to construct a low-energy approximation of topological insulators. Let us now introduce some peculiarities of the lattice regularization from the perspective of lattice field theory (LFT) [104].

A naive approach is to discretize the spatial derivatives of the Dirac Hamiltonian that lead to the linear dependence on momentum in Eq. (4.1). By introducing a Bravais lattice $\Lambda_\ell = a\mathbb{Z}^d = \{\boldsymbol{x} : x_i/a \in \mathbb{Z}, \forall i = 1, \cdots, d\}$, the corresponding Hamiltonian LFT can be expressed as follows

$$H_{\mathrm{D}} = \sum_{\boldsymbol{x}\in\Lambda_\ell} a^d \Big(\Psi^\dagger(\boldsymbol{x})\frac{\mathrm{i}\alpha_i}{2a}\Psi\Big(\boldsymbol{x} + a\boldsymbol{u}^i\Big) + m\,\Psi^\dagger(\boldsymbol{x})\frac{\beta}{2}\Psi(\boldsymbol{x}) + \mathrm{H.c.}\Big), \tag{4.4}$$

where $\{\boldsymbol{u}^i\}_{i=1}^d$ are the unit vectors of the Bravais lattice. Moreover, the lattice spinor fields $\Psi(\boldsymbol{x}), \Psi^\dagger(\boldsymbol{x})$ display the desired anti-commutation algebra in the continuum limit

$\{\Psi_\mu(\boldsymbol{x}), \Psi^\dagger_\nu(\boldsymbol{x}')\} = \frac{1}{a^d}\delta_{\mu,\nu}\delta_{\boldsymbol{x},\boldsymbol{x}'} \to \delta_{\mu,\nu}\delta^{(d)}(\boldsymbol{x}-\boldsymbol{x}')$. Transforming the field operators to momentum space,

$$\Psi_\mu(\boldsymbol{x}) = \int_{\mathrm{BZ}^d} \frac{\mathrm{d}^d k}{(2\pi)^d} e^{\mathrm{i}\boldsymbol{k}\cdot\boldsymbol{x}} \Psi_\mu(\boldsymbol{k}), \tag{4.5}$$

one obtains a QFT similar to Eq. (4.1), where momenta now lie within the so-called Brillouin zone $\Lambda^d \to \mathrm{BZ}^d = (-\frac{\pi}{a}, \frac{\pi}{a}]^{\times d}$, and the single-particle Hamiltonian is

$$h_{\mathrm{D}}(\boldsymbol{k}) = \frac{1}{a}\alpha_i \sin(k^i a) + m\beta. \tag{4.6}$$

The energy spectrum of this lattice Hamiltonian becomes $\epsilon_\pm(\boldsymbol{k}) \approx \pm\sqrt{m^2+\boldsymbol{k}^2}$ at long wavelengths $\xi \sim k_i^{-1} \gg a$, and thus reproduces the energy of the massive Dirac fermion. However, there are other points at the borders of the Brillouin zone that lead to a similar dispersion relation (i.e. Dirac points), and thus give rise to additional relativistic fermions, the so-called *fermion doublers*. In fact, there is an even number $N_{\mathrm{D}} = 2^d$ of Dirac points, labelled by $\boldsymbol{k}_{\boldsymbol{n}} = \frac{\pi}{a} n_i \boldsymbol{u}^i$ with $n_i \in \{0,1\}$, which lead to a dispersion relation that is approximately described by a massive relativistic particle $\epsilon_\pm(\boldsymbol{k}_{\boldsymbol{n}}+\boldsymbol{k}) \approx \pm\sqrt{m^2+\boldsymbol{k}^2}$ at long wavelengths $\xi \sim k_i^{-1} \gg a$. The effective QFT around each of these points corresponds to an instance of the massive Dirac QFT $h_{\mathrm{D}}(\boldsymbol{k}_{\boldsymbol{n}}+\boldsymbol{k}) \approx \alpha_i^{\boldsymbol{n}} k^i + m\beta$ with a different choice of the Dirac matrices $\alpha_i^{\boldsymbol{n}} = (-1)^{n_i}\alpha_i$. Let us note that this effective QFT is defined within a certain long-wavelength cutoff where the linearization is valid, such that $\Lambda^d = (-\pi/l_{\mathrm{c}}, \pi/l_{\mathrm{c}}]^{\times d}$ in Eq. (4.1). As will become clear below, using the perspective of the renormalization group (RG) [105], we shall approach this continuum limit by setting the parameters of the lattice Hamiltonian close to a quantum phase transition, where the characteristic correlation length diverges $\xi/l_{\mathrm{c}} \to \infty$, and effectively $\Lambda^d \to \mathbb{R}^d$. Accordingly, we get N_{D} copies of the desired continuum QFT (4.1).

From the perspective of LFT, the presence of fermion doublers with $\boldsymbol{n} \neq 0$ is an unfortunate nuisance, as they will inevitably couple to the target $\boldsymbol{n} = 0$ Dirac QFT as soon as additional interaction terms are included [104]. Moreover, the presence of the doublers is a generic feature for different lattice discretizations, and is related to the difficulty of incorporating chiral symmetry on the lattice [106, 107].

From the perspective of topological insulators, the presence of these doublers is already important at the non-interacting level. In the lattice, the even number of relativistic fermions can be divided into two sets $S_\pm$ with opossite chiralities, each of which contains an equal number $|S_\pm| = 2^{(d-1)}$of Dirac points: $\boldsymbol{n} \in S_\pm$ if $(-1)^{\sum_i n_i} = \pm 1$. This sign difference is translated into an opposite Chern character (4.2) or Chern-Simons form (4.3), such that the topological invariant obtained by integrating over the whole Brillouin zone vanishes (i.e. summing an equal number of positive and negative contributions over all Dirac points yields a zero topological invariant). Accordingly, due to the presence of the spurious fermion doublers, this naive lattice Hamiltonian (4.4) fails at reproducing the non-vanishing topological invariant in Eq. (4.2) or (4.3) of the single massive Dirac QFT (4.1). For the representative examples discussed above, one finds that: *(i)* there are a $N_{\mathrm{D}} = 4$ Dirac points for the $d = 2$ Dirac QFT in the A class, such that the integral of the first Chern character $\mathsf{Ch}_1 = \int_{\Lambda^2} \mathsf{ch}_1 = \frac{m}{2|m|}(1-1-1+1) = 0$. *(ii)* For the $d = 1$ Dirac QFT in the AIII class, there are $N_{\mathrm{D}} = 2$ Dirac points, such that integral of the first Chern-Simons form $\mathsf{CS}_1 = \int_{\Lambda^1} \mathsf{Q}_1 = \frac{m}{4|m|}(1-1) = 0$, leading to a trivial Wilson loop $\mathsf{W}_1 = 1$. We conclude that the groundstate of such naive lattice models corresponds to a trivial insulator, and not to the desired SPT phase.

4.1.3 Wilson and continuum QFTs of topological insulators

We now discuss a possible route to get around the effect of the spurious doublers, which is well-known in LFT [108–112], and corresponds to a generic model of non-interacting topological insulators [93–96]. The route is based on Wilson's prescription to construct lattice Hamiltonians that yield a different mass $m_{\boldsymbol{n}}$ for each of the fermion doublers [113]. This can be achieved by modifying Eq. (4.4), and introducing the so-called *Wilson-fermion Hamiltonian* LFT

$$H_{\mathrm{W}} = H_{\mathrm{D}} + \sum_{\boldsymbol{x}\in\Lambda_\ell} a^d \Big(\Psi^\dagger(\boldsymbol{x}) \frac{\delta m_i \beta}{2} \Psi\Big(\boldsymbol{x} + a\boldsymbol{u}^i\Big) + \mathrm{H.c.}\Big), \tag{4.7}$$

where the parameters δm_i quantify certain mass shifts. In this case, transforming the lattice Hamiltonian to momentum space, $H_{\mathrm{W}} = \int_{\mathrm{BZ}^d} \frac{\mathrm{d}^d k}{(2\pi)^d} \Psi^\dagger_\mu(\boldsymbol{k}) [h_{\mathrm{W}}(\boldsymbol{k})]^{\mu,\nu} \Psi_\nu(\boldsymbol{k})$, yields the following single-particle Hamiltonian

$$h_{\mathrm{W}}(\boldsymbol{k}) = \frac{1}{a}\alpha_i \sin(k^i a) + (m + \delta m_i \cos(k^i a))\beta. \tag{4.8}$$

We perform again a long-wavelength approximation around the different momenta $\boldsymbol{k}_{\boldsymbol{n}} = \frac{\pi}{a} n_i \boldsymbol{u}^i$, namely setting $\boldsymbol{k} \to \boldsymbol{k} + \boldsymbol{k}_{\boldsymbol{n}}$ such that $|\boldsymbol{k}| \ll \pi/l_{\mathrm{c}}$. The Wilson-fermion LFT (5.4) yields a *continuum Wilson-fermion QFT* described by N_{D} instances of the massive Dirac QFT (4.1), each describing a relativistic fermion with a different Wilson mass

$$H_{\mathrm{W}} \approx \int_{\Lambda^d} \frac{\mathrm{d}^d k}{(2\pi)^d} \sum_{\boldsymbol{n}} \Psi^\dagger_{\boldsymbol{n},\mu}(\boldsymbol{k}) [h^{\boldsymbol{n}}_{\mathrm{D}}(\boldsymbol{k})]^{\mu,\nu} \Psi_{\boldsymbol{n},\nu}(\boldsymbol{k}). \tag{4.9}$$

Here, we have introduced the spinorial fermionic operators $\Psi^\dagger_{\boldsymbol{n}}(\boldsymbol{k}), \Psi_{\boldsymbol{n}}(\boldsymbol{k})$ that create-annihilate Dirac fermions with a Wilson mass $m_{\boldsymbol{n}}$, and the single-particle Hamiltonians

$$h^{\boldsymbol{n}}_{\mathrm{D}}(\boldsymbol{k}) = \alpha^{\boldsymbol{n}}_i k^i + m_{\boldsymbol{n}}\beta, \quad m_{\boldsymbol{n}} = m + \sum_i (-1)^{n_i} \delta m_i. \tag{4.10}$$

We note once more that this effective QFT is defined within a certain cutoff, such that $\Lambda^d = (-\pi/l_{\mathrm{c}}, \pi/l_{\mathrm{c}}]^{\times^d} \to \mathbb{R}^d$ in the vicinity of a critical point (i.e. continuum limit $\xi/l_{\mathrm{c}} \to \infty$). This limit, as well as the meaning of the approximation symbol in Eq. (4.9), will be discussed below in light of the RG.

From a QFT perspective, setting the lattice parameters m and δm_i in such a way that $m_{\boldsymbol{n}} \sim a^{-1} \gg m_{\boldsymbol{0}} \geq 0 \ \forall\, \boldsymbol{n} \neq \boldsymbol{0}$, effectively sends all fermion doublers to very high energies (on the order of the UV cutoff). Accordingly, it could be expected that they will not contribute to the low-energy phenomena described by the single Dirac fermion at $\boldsymbol{k}_{\boldsymbol{0}} = \boldsymbol{0}$. For $\delta m_i = -m/d$, it is only the Dirac point at $\boldsymbol{k}_{\boldsymbol{0}}$ that is massless, and can serve as the starting point to study quarks coupled to gauge fields in lattice quantum chromodynamics [104, 113].

From the perspective of topological insulators, the situation is complicated by the fact that the topological invariants are non-local quantities obtained by integrating over all momenta (4.2)-(4.3), and are thus also sensitive to the doublers even if they lie at very large energies. In fact, the presence of the doublers is crucial to turn the above invariants in Eq. (4.2) or (4.3) into *integer topological numbers*, making the Wilson-fermion QFT (4.9) a generic quantum-field-theory representative of topological insulators [94].

This can be easily observed for the examples introduced above: *(i)* the $d = 2$ Wilson-fermion QFT representative of the A class of topological insulators can be related to the

integer quantum Hall effect [8], where integer Chern numbers underlie the quantization of the transverse conductance [11]. For the corresponding groundstate of the Wilson QFT (4.9), the integral of the first Chern character yields

$$\mathsf{Ch}_1 = \int_{\Lambda^2} \mathsf{ch}_1 = \sum_{\boldsymbol{n}} p_{\boldsymbol{n}} \frac{m_{\boldsymbol{n}}}{2|m_{\boldsymbol{n}}|} = \sum_{\boldsymbol{n}} \tfrac{1}{2} p_{\boldsymbol{n}} \mathrm{sgn}(m_{\boldsymbol{n}}), \tag{4.11}$$

where we have introduced $p_{\boldsymbol{n}} = \exp\{\mathrm{i}\pi \sum_i n_i\}$. Accordingly, if the lattice parameters δm_i are such that a *mass inversion* occurs for some of the Wilson fermions, it becomes possible to obtain a non-vanishing integer-valued topological invariant $\mathsf{Ch}_1 \in \mathbb{Z}$, which can be related to the plateaus of the quantum Hall effect observed at integer fillings [11]. In addition, the edge states responsible for the transverse conductance in the integer quantum Hall effect [12] have a counterpart in the Wilson LFT: they correspond to the so-called domain-wall fermions [108–112], which are masless Dirac fermions localized at the boundaries of the lattice. Something similar occurs for the *(ii)* $d = 1$ Wilson LFT of the AIII class of topological insulators, where

$$\mathsf{CS}_1 = \int_{\Lambda^1} \mathsf{Q}_1 = \sum_{\boldsymbol{n}} p_{\boldsymbol{n}} \frac{m_{\boldsymbol{n}}}{4|m_{\boldsymbol{n}}|} = \sum_{\boldsymbol{n}} \tfrac{1}{4} p_{\boldsymbol{n}} \mathrm{sgn}(m_{\boldsymbol{n}}). \tag{4.12}$$

One thus obtains a non-trivial Wilson loop $\mathsf{W}_1 = e^{\mathrm{i}2\pi \mathsf{CS}_1} = -1$ whenever an odd number of mass inversions take place. Once again, if one introduces an interface between the topological phase and a non-topological one (e.g. considering a finite system with boundaries), gapless edge excitations localized to the interface appear, which are related to the zero-energy Jackiw-Rebbi modes localised at a mass-inversion point [114].

Let us note that alternative discretizations that also lead to Dirac fermions with different Wilson masses, thus displaying topological features and edge states, have also appeared in condensed-matter contexts [49, 81, 115, 116]. From the perspective of LFTs, these edge modes correspond to lower-dimensional versions of the aforementioned domain-wall fermions. From the perspective of topological insulators, the properties of these phases can be shown to be robust against any perturbation, e.g. disorder, that respects the symmetry of the given symmetry class. A problem of current interest in the community is to understand the interplay of these topological properties and correlation effects brought by interactions [117–119].

4.2 Euclidean action

In this section, we present a functional-integral description of the previous generic lattice Hamiltonian (5.4) when Hubbard-type interactions [29] between the fermions are included. This functional integral will be the starting point to develop RG techniques that allow us to understand the fate of the topological phases as the interactions are switched on.

Let us consider the Wilson lattice Hamiltonian (5.4) in the so-called lattice units $a = 1$, and introduce Hubbard-type contact interactions describing the repulsion of fermions. This leads to the following *Wilson-Hubbard lattice* Hamiltonian

$$H_{\mathrm{WH}} = H_{\mathrm{W}} + \sum_{\nu,\mu} \sum_{\boldsymbol{x} \in \Lambda_\ell} \Psi^\dagger_\mu(\boldsymbol{x}) \Psi^\dagger_\nu(\boldsymbol{x}) \frac{u_{\mu\nu}}{2} \Psi_\nu(\boldsymbol{x}) \Psi_\mu(\boldsymbol{x}), \tag{4.13}$$

where we have introduced interaction strengths $u_{\mu\nu} > 0$. In general, the relation of these parameters to the spinorial indexes will depend on the nature of the orbitals

that determine the fermionic spinors $\Psi(\boldsymbol{x}), \Psi^\dagger(\boldsymbol{x})$. For the previous examples of A and AIII topological insulators, due to Pauli exclusion principle, one simply finds $u_{\mu\nu} = (1-\delta_{\mu,\nu})u$ for $u > 0$.

We are interested in computing the partition function of the Wilson-Hubbard Hamiltonian $\mathsf{Z} = \mathrm{Tr}\{\exp(-\beta H_{\mathrm{WH}})\}$, where β is the inverse temperature, as it contains all the relevant information about the possible quantum phase transitions in the zero-temperature limit $\beta \to \infty$. This partition function can be expressed as a functional integral by means of fermionic coherent states [101]. We thus introduce Grassmann spinors $\psi(\boldsymbol{x},\tau), \overline{\psi}(\boldsymbol{x},\tau)$ at each lattice point $\boldsymbol{x} \in \Lambda_\ell$ and imaginary time $\tau \in (0,\beta)$, which are composed of mutually anti-commuting Grassman fields $\{\psi_\mu(\boldsymbol{x},\tau), \overline{\psi}_\nu(\boldsymbol{x}',\tau')\} = \{\psi_\mu(\boldsymbol{x},\tau), \psi_\nu(\boldsymbol{x}',\tau')\} = \{\overline{\psi}_\mu(\boldsymbol{x},\tau), \overline{\psi}_\nu(\boldsymbol{x}',\tau')\} = 0$. Since the Wilson-Hubbard Hamiltonian is already normal-ordered, one can readily express the zero-temperature partition function as a functional integral $\mathsf{Z} = \int [\mathrm{d}\overline{\psi}\mathrm{d}\psi] e^{-S_{\mathrm{WH}}[\overline{\psi},\psi]}$, where the Euclidean action is a functional of the Grassmann fields

$$S_{\mathrm{WH}}[\overline{\psi},\psi] = \int_0^\infty \mathrm{d}\tau \sum_{\boldsymbol{x}\in\Lambda_\ell} (\overline{\psi}(\boldsymbol{x},\tau)\partial_\tau \psi(\boldsymbol{x},\tau) + H_{\mathrm{WH}}(\overline{\psi},\psi)), \tag{4.14}$$

and $H_{\mathrm{WH}}(\overline{\psi},\psi)$ results from substituting the fermion field operators by Grassmann variables in the normal-ordered Hamiltonian (4.13). By Fourier transforming to frequency and momentum space $\psi_\mu(\boldsymbol{x},\tau) = \int_{\mathbb{R}} \frac{\mathrm{d}\omega}{2\pi} \int_{\mathrm{BZ}^d} \frac{\mathrm{d}^d k}{(2\pi)^d} e^{\mathrm{i}(\boldsymbol{k}\cdot\boldsymbol{x}-\omega\tau)} \psi_\mu(\boldsymbol{k},\omega)$, the action becomes

$$S_{\mathrm{WH}}[\overline{\psi},\psi] = S_{\mathrm{W}}[\overline{\psi},\psi] + \delta S_{\mathrm{W}}[\overline{\psi},\psi] + \delta S_{\mathrm{H}}[\overline{\psi},\psi]. \tag{4.15}$$

Here, we have introduced the free action S_{W} for the Wilson QFT (4.9) with single-particle Hamiltonian (4.10), namely

$$S_{\mathrm{W}} = \int_{\boldsymbol{k},\omega} \sum_{\boldsymbol{n}} \overline{\psi}_{\boldsymbol{n},\mu}(\boldsymbol{k},\omega)[-\mathrm{i}\omega\mathbb{I} + h^{\boldsymbol{n}}_{\mathrm{D}}(\boldsymbol{k})]^{\mu,\nu} \psi_{\boldsymbol{n},\nu}(\boldsymbol{k},\omega), \tag{4.16}$$

where the integration symbol is $\int_{\boldsymbol{k},\omega} = \int_{\mathbb{R}} \frac{\mathrm{d}\omega}{2\pi} \int_{\Lambda^d} \frac{\mathrm{d}^d k}{(2\pi)^d}$. Since this QFT arises at long wavelengths, we must also include corrections to this approximation in δS_{W}, namely

$$\delta S_{\mathrm{W}} = \int_{\boldsymbol{k},\omega} \sum_{\boldsymbol{n}} \overline{\psi}_{\boldsymbol{n},\mu}(\boldsymbol{k},\omega)[\delta h^{\boldsymbol{n}}_{\mathrm{D}}(\boldsymbol{k})]^{\mu,\nu} \psi_{\boldsymbol{n},\nu}(\boldsymbol{k},\omega), \tag{4.17}$$

where we have introduced

$$\delta h^{\boldsymbol{n}}_{\mathrm{D}}(\boldsymbol{k}) = (-1)^{n_i} \left[\Big(\sin(k^i) - k^i\Big) \alpha_i + \delta m_i \Big(\cos(k^i) - 1\Big) \beta \right]. \tag{4.18}$$

Finally, the Hubbard interactions lead to the quartic term

$$\delta S_{\mathrm{H}} = \int_{\{\boldsymbol{k},\omega\}} \sum_{\{\boldsymbol{n}\}} \frac{u_{\mu\nu}}{2} \overline{\psi}_{\boldsymbol{n}_4,\mu}(4) \overline{\psi}_{\boldsymbol{n}_3,\nu}(3) \psi_{\boldsymbol{n}_2,\nu}(2) \psi_{\boldsymbol{n}_1,\mu}(1), \tag{4.19}$$

where we have introduced the short-hand notations $\psi_{\boldsymbol{n}_j,\mu}(j) = \psi_{\boldsymbol{n}_j,\mu}(\boldsymbol{k}_j,\omega_j)$ for $j \in \{1,2,3,4\}$ [120], $\sum_{\{\boldsymbol{n}\}} = \sum_{\boldsymbol{n}_1,\boldsymbol{n}_2,\boldsymbol{n}_3,\boldsymbol{n}_4}$, and $\int_{\{\boldsymbol{k},\omega\}} = \prod_j \int_{\boldsymbol{k}_j,\omega_j} (2\pi)^2 \delta(\omega_4 + \omega_3 - \omega_2 - \omega_1)\delta(\boldsymbol{q}_4 + \boldsymbol{q}_3 - \boldsymbol{q}_2 - \boldsymbol{q}_1)$, where $\boldsymbol{q}_j = \boldsymbol{k}_{\boldsymbol{n}_j} + \boldsymbol{k}_j$ is the momentum about the different Dirac points. The goal of this work is to study the interplay of the quadratic and quartic terms in the Wilson-Hubbard action (4.15) from the point of view of the RG [120].

4.3 Renormalization group of Wilson fermions and the topological Hamiltonian

In this section, we discuss generic properties of interacting topological insulators in light of the RG. Since we are interested in the continuum QFT description of interacting topological insulators, we must focus on phenomena at long length scales ξ, where it makes sense to partition the action (4.15) into a long-wavelength term $S_{\rm W}$ (4.16), and the perturbations caused by shorter-wavelength corrections $\delta S_{\rm W}$ (4.17) and by the interactions $\delta S_{\rm H}$ (4.19). Since $\xi \gg l_{\rm c}$, the physical properties of interest should not depend on our choice of the cutoff in the action (4.15). Therefore, we should be able to change the cutoff $l_{\rm c} \to l'_{\rm c} = s l_{\rm c} > l_{\rm c}$ for $s > 1$ (i.e. $\Lambda_{\rm c} \to \Lambda'_{\rm c} = \Lambda_{\rm c}/s < \Lambda_{\rm c}$) without modifying the physics. This can only be achieved if one allows for the microscopic coupling parameters of the Wilson-Hubbard action (4.15) to run with the cutoff $\{g_i(\Lambda_{\rm c})\}$ (i.e. $\{m_{\boldsymbol{n}}(\Lambda_{\rm c}), u_{\mu\nu}(\Lambda_{\rm c})\}$), which is the essence of the renormalization group [120,121]. The Wilsonian RG prescription allows us to calculate such an *RG flow* in a systematic fashion, and associates the change of the bare couplings to the dressing of the long-wavelength fields by the short-wavelength modes that must be integrated out as the cutoff is lowered [105].

4.3.1 Wilsonian RG by coarse graining and rescaling

By writing the Grassmann fields in terms of the short-wavelength (fast) and long-wavelength (slow) modes, $\psi^{\rm f}_{\boldsymbol{n},\mu}(\boldsymbol{k},\omega) = \psi_{\boldsymbol{n},\mu}(\boldsymbol{k},\omega)$ for $\Lambda_{\rm c} \geq |\boldsymbol{k}| \geq \Lambda_{\rm c}/s$, and $\psi^{\rm s}_{\boldsymbol{n},\mu}(\boldsymbol{k},\omega) = \psi_{\boldsymbol{n},\mu}(\boldsymbol{k},\omega)$ for $\Lambda_{\rm c}/s \geq |\boldsymbol{k}| \geq 0$, respectively, the Wilsonian RG can be divided into two steps:

(i) In the first one, one *coarse grains* the action by integrating out the fast modes, such that the new coarse-grained action can be expressed, up to an irrelevant constant, as follows

$$S'_{\rm WH}[\overline{\psi}^{\rm s}, \psi^{\rm s}] = S_{\rm W}[\overline{\psi}^{\rm s}, \psi^{\rm s}] - \log \left\langle e^{-\delta S_{\rm WH}\left[\overline{\psi}^{\rm s}, \overline{\psi}^{\rm f}, \psi^{\rm s}, \psi^{\rm f}\right]} \right\rangle_{\rm f}, \tag{4.20}$$

In this expression, we have grouped all the perturbations in $\delta S_{\rm WH}[\overline{\psi}^{\rm s}, \overline{\psi}^{\rm f}, \psi^{\rm s}, \psi^{\rm f}] = \delta S_{\rm W}[\overline{\psi}^{\rm f}, \psi^{\rm f}] + \delta S_{\rm H}[\overline{\psi}^{\rm s}, \overline{\psi}^{\rm f}, \psi^{\rm s}, \psi^{\rm f}]$, and defined their expectation value with respect to the non-interacting partition function

$$\langle e^{-\delta S_{\rm WH}[\overline{\psi}^{\rm s}, \overline{\psi}^{\rm f}, \psi^{\rm s}, \psi^{\rm f}]} \rangle_{\rm f} = \int_{d\Lambda} e^{-S_{\rm W}[\overline{\psi}^{\rm f}, \psi^{\rm f}]} e^{-\delta S_{\rm WH}[\overline{\psi}^{\rm s}, \overline{\psi}^{\rm f}, \psi^{\rm s}, \psi^{\rm f}]} / \int_{d\Lambda} e^{-S_{\rm W}[\overline{\psi}^{\rm f}, \psi^{\rm f}]}, \tag{4.21}$$

where we have introduced a short-hand notation for the integral over the fast modes $\int_{d\Lambda} = \int_{\Lambda_{\rm c}/s \leq |\boldsymbol{k}| \leq \Lambda_{\rm c}} \prod_k {\rm d}\overline{\psi}^{\rm f}(\boldsymbol{k},\omega) {\rm d}\psi^{\rm f}(\boldsymbol{k},\omega)$. Note that we are neglecting $\delta S_H[f,f,f,f]$ since it is of even higher order in ψ^f and moreover, it would make the integrals not Gaussian. To evaluate this expectation value, we will make use of the free-fermion propagator (i.e. the single-particle Green's function).

$$G^0_{\mu\nu}({\rm i}\omega, \boldsymbol{k}) = \langle \overline{\psi}_\mu(\boldsymbol{k},\omega) \psi_\nu(\boldsymbol{k},\omega) \rangle_{\rm f} = \left[\left({\rm i}\omega - h^{\boldsymbol{n}}_{\rm D}(\boldsymbol{k}) \right)^{-1} \right]_{\mu\nu}. \tag{4.22}$$

(ii) In the second step of the RG transformation, one *rescales* the momentum and frequency

$$\boldsymbol{k} \to \boldsymbol{k}' = s\boldsymbol{k}, \;\; \omega \to \omega' = s\omega, \tag{4.23}$$

such that the original cutoff is restored $\Lambda'_{\rm c} \to s\Lambda'_{\rm c} = \Lambda_{\rm c}$ [1]. In this situation, one can compare the original (4.15) and coarse-grained (4.20) actions, trying to extract

[1] The rescaling of k and Ω is the same thanks to the Lorentz invariance.

the dressing of the couplings $\{m_{\boldsymbol{n}}(\Lambda_{\rm c}), u_{\mu\nu}(\Lambda_{\rm c})\}$ by the fast modes that have been integrated out during the coarse-graining step. This rescaling must be accompanied by a *scale transformation* for the slow modes

$$\psi^{\rm s}_{\boldsymbol{n},\mu}(\boldsymbol{k},\omega) \to \psi'_{\boldsymbol{n},\mu}(\boldsymbol{k}',\omega') = s^{-\Delta_\psi}\psi^{\rm s}_{\boldsymbol{n},\mu}(\boldsymbol{k}'/s,\omega'/s), \tag{4.24}$$

where Δ_ψ is the so-called scaling dimension of the fermion fields, which are homogeneous under the rescaling of momenta and frequencies.

The scaling dimension is chosen in such a way that the massless part of the free action (4.16) becomes invariant under rescaling, i.e. the terms of the QFT (4.9)-(4.10) for vanishing couplings $m = \delta m_i = u_{\mu\nu} = 0$, generally denoted as $\boldsymbol{g} = \boldsymbol{0}$, do not get modified. Let us note that it is customary in RG treatments of QFT to define dimensionless couplings $\boldsymbol{g}$ [121].

Accordingly, the action for the naive Dirac fermions corresponds to a *fixed point* under the RG subsequent coarse-graining and rescaling transformations, as it remains unaltered

$$\begin{aligned} S_{\rm WH}[\overline{\psi},\psi;\boldsymbol{g}=\boldsymbol{0},\Lambda_{\rm c}] \xrightarrow{(i)} S'_{\rm WH}[\overline{\psi}^{\rm s},\psi^{\rm s};\boldsymbol{g}=\boldsymbol{0},\Lambda'_{\rm c}] \xrightarrow{(ii)} \\ \xrightarrow{(ii)} S'_{\rm WH}[\overline{\psi}',\psi';\boldsymbol{g}=\boldsymbol{0},\Lambda_{\rm c}] = S_{\rm WH}[\overline{\psi},\psi;\boldsymbol{g}=\boldsymbol{0},\Lambda_{\rm c}]. \end{aligned} \tag{4.25}$$

This is achieved by choosing the fermion scaling dimension of $\Delta_\psi = (d+2)/2$ as a function of the spatial dimensionality d [120]. In the present case, considering that $\Delta_\psi = (d+2)/2$, and that the action (4.15) is dimensionless, one finds that the interactions $u_{\mu\nu}$ must be dimensionless, whereas the mass can be adimensionalized by $m_{\boldsymbol{n}} \to m_{\boldsymbol{n}}\Lambda_{\rm c}$ after substituting $m \to m\Lambda_{\rm c}$ and $\delta m_i \to \delta m_i \Lambda_{\rm c}$.

To proceed with the RG program in practice, and extract the flow of the couplings, we must be able to calculate the coarse-grained action (4.20). In perturbative RG, this is performed by applying a perturbative expansion in some small parameter. The cumulant expansion offers a systematic procedure to reach the desired order of the perturbation

$$\log\left\langle e^{-\delta S_{\rm WH}\left[\overline{\psi}^{\rm s},\overline{\psi}^{\rm f},\psi^{\rm s},\psi^{\rm f}\right]}\right\rangle_{\rm f} = \sum_{n=1}^{\infty}\frac{(-1)^n}{n!}\left\langle \delta S_{\rm WH}\left[\overline{\psi}^{\rm s},\overline{\psi}^{\rm f},\psi^{\rm s},\psi^{\rm f}\right]^n\right\rangle_{\rm c,f} \tag{4.26}$$

where $\langle \delta S_{\rm WH}[\overline{\psi}^{\rm s},\overline{\psi}^{\rm f},\psi^{\rm s},\psi^{\rm f}]^n\rangle_{\rm c,f}$ is the n-th cumulant of the perturbation obtained by integrating over the fast modes, e.g. the mean $\langle \delta S^1_{\rm WH}\rangle_{\rm c,f} = \langle \delta S_{\rm WH}\rangle_{\rm f}$, the variance $\langle \delta S^2_{\rm WH}\rangle_{\rm c,f} = \langle \delta S^2_{\rm WH}\rangle_{\rm f} - \langle \delta S_{\rm WH}\rangle^2_{\rm f}$, and so on.

4.3.2 Tree-level RG flow and adiabatic band flattening

With this machinery, we can now discuss some generic features of the RG for the Wilson-Hubbard matter (4.15), making connections to the underlying topological insulators, and to the possible quantum phase transitions that connect them to other non-topological states of matter. At zero order of the cumulant expansion, it is straightforward to calculate the RG flow of the dimensionless Wilson masses $m_{\boldsymbol{n}}$ (4.10) appearing in the long-wavelength action (4.16). According to Eq. (4.20), after the two RG steps, the masses only get a contribution from rescaling

$$m_{\boldsymbol{n}}\Lambda_{\rm c} \to m_{\boldsymbol{n}}\Lambda_{\rm c}\, s, \quad \beta_{m_{\boldsymbol{n}}} = \frac{{\rm d}m_{\boldsymbol{n}}}{{\rm d}\log s} = m_{\boldsymbol{n}}, \tag{4.27}$$

where $\beta_{m_{\boldsymbol{n}}}$ are the beta functions generally defined as $\beta(\boldsymbol{g}) = \partial \boldsymbol{g}/\partial \log s$ where s represent the energy scale.

Accordingly, the effect of the Wilson masses gets amplified ($s > 1$) as one integrates more and more short-wavelength modes. Therefore, one says that the mass terms are *relevant perturbations* that take us away from the infrared (IR) RG fixed point of the $N_{\rm D}$ massless non-interacting Dirac fermions. Note also that the above RG flow respects the sign of the Wilson masses at the initial cutoff $\Lambda_{\rm c}$. Hence, if $\mathrm{sgn}(m_{\boldsymbol{n}}) = \pm 1$ at $\Lambda_{\rm c}$, then $m_{\boldsymbol{n}} \to \pm\infty$ in the IR limit (i.e. positive masses become more positive, whereas negative masses become more negative, as one focuses on longer and longer length scales). This will be of crucial importance for our study of the topological features of the Wilson-Hubbard model.

It is also straightforward to calculate the flow of the shorter-wavelength perturbations (4.17) at first-order of the cumulant expansion. The RG transformation affects the terms in Eq. (4.18) as follows

$$\delta h^{\boldsymbol{n}}_{\rm D}(\boldsymbol{k}) \xrightarrow{(i)+(ii)} s\delta h^{\boldsymbol{n}}_{\rm D}(\boldsymbol{k}/s) = \sum_{\ell=1}^{\infty} \frac{(-1)^{\ell+n_i}}{(2\ell+1)!}\alpha_i (k^i)^{2\ell+1} s^{-2\ell} + \frac{(-1)^{\ell+n_i}}{(2\ell)!}\delta m_i \Lambda_{\rm c} (k^i)^{2\ell} \beta s^{1-2\ell}, \tag{4.28}$$

all of which decrease under the RG since $s > 1$, and $\ell \geq 1$.

These results allow us to understand the approximation symbol in Eqs. (4.9) formally as the result of the RG flow towards the long-wavelength IR limit (i.e. the shorter-wavelength corrections are *irrelevant perturbations* in the RG sense, and can be thus safely discarded). Moreover, in the non-interacting regime, the RG offers an interesting picture of the topological insulating phases based solely on the action (4.16). The IR limit corresponds to sending the Wilson masses to $m_{\boldsymbol{n}} \to \pm\infty$ such that, in comparison, the dispersion of the bands becomes vanishingly small and we can approximate $\epsilon^{\boldsymbol{n}}_{\pm}(k) \approx \pm m_{\boldsymbol{n}}$. Therefore, the RG transformation amounts to a continuous deformation into an equivalent flat-band model $h^{\boldsymbol{n}}_{\rm D}(k) \xrightarrow{(i)+(ii)} |m_{\boldsymbol{n}}| \sum_{\boldsymbol{k}\in\Lambda^d} (P_+(\boldsymbol{k}) - P_-(\boldsymbol{k}))$, where $P_\pm(\boldsymbol{k})$ are orthogonal projectors onto the flat bands [13]. Since the signs of the Wilson masses $\mathrm{sgn}(m_{\boldsymbol{n}})$ are preserved under the RG flow, the running of the Wilson masses can be considered as an adiabatic transformation that preserves the above topological invariants (4.11)-(4.12). Accordingly, if there is a mass inversion at the original cutoff responsible for a non-vanishing integer topological invariant, the groundstate of the model at the IR limit will indeed correspond to a topological insulating state of the equivalent flat-band model.

Despite the fact that the RG flow of the Wilson masses seems to imply that the excitations become infinitely heavy in the IR, and that the effective low-energy QFT should be trivial [121], non-zero integer topological invariants (4.11)-(4.12) indicate that the system can indeed display a non-trivial quantized response at low energies. In fact, even if the bulk excitations become infinitely heavy, the Wilson-fermion LFT with mass inversion would display massless edge excitations in a finite lattice with boundaries, such that the IR behavior is not trivial. The conservation of the topological invariant under the RG is a different manifestation of the non-triviality of the IR QFT with boundaries (i.e. bulk-edge correspondence). The quantum phase transition between a topological insulator and a trivial band insulator will thus be marked by the mass inversion for one of the $N_{\rm D}$ Wilson fermions, which we label as $\boldsymbol{n}_\star$. Hence, the critical point of the non-interacting model is marked by $m_{\boldsymbol{n}_\star} = 0$, and thus corresponds to the RG fixed point of a massless Dirac fermion, which controls the scaling properties of the quantum phase transition.

4.3.3 Interacting RG and the topological Hamiltonian

The question now is to study how this neat RG picture is modified as the quartic Hubbard interactions are switched on. Considering again the first-order cumulant $\langle \delta S_{\rm H}[\overline{\psi}^{\rm s}, \overline{\psi}^{\rm f}, \psi^{\rm s}, \psi^{\rm f}]\rangle_{\rm f}$ at the so-called *tree level* (i.e. processes that only involve the slow Grassmann fields), the Hubbard interaction strengths flow with

$$u_{\mu\nu} \to s^{1-d} u_{\mu\nu}, \quad \beta_{u_{\mu\nu}} = \frac{{\rm d}u_{\mu\nu}}{{\rm d}\log s} = (1-d)u_{\mu\nu}. \tag{4.29}$$

which implies that the interactions are a *marginal perturbation* for the $d = 1$ case, and irrelevant in higher dimensions.

Let us note that, even when the interactions are irrelevant, they can modify how the Wilson masses run, and affect considerably the shape of the phase diagram. Our goal then is to go beyond tree level, and explore how the interactions change the above RG flow and the topological insulating phases. On general grounds, we expect that the interactions will modify the $\beta_{m_{\boldsymbol{n}}}$ function of the masses (4.27), such that the bare Wilson masses get renormalized by the Hubbard couplings

$$m_{\boldsymbol{n}} \to \tilde{m}_{\boldsymbol{n}} = m_{\boldsymbol{n}} + \delta m_{\boldsymbol{n}}(u_{\mu\nu}). \tag{4.30}$$

More generally, as a consequence of the interaction, the free-fermion propagator (4.22) of the long-wavelength action (4.16) will be transformed into $G^0({\rm i}\omega, \boldsymbol{k}) \to G({\rm i}\omega, \boldsymbol{k})$, where

$$G^{-1}({\rm i}\omega, \boldsymbol{k}) = {\rm i}\omega - h^{\boldsymbol{n}}_{\rm D}(\boldsymbol{k}) - \Sigma^{\boldsymbol{n}}_{\rm D}({\rm i}\omega, \boldsymbol{k}), \tag{4.31}$$

and $\Sigma^{\boldsymbol{n}}_{\rm D}({\rm i}\omega, \boldsymbol{k})$ is the so-called self-energy, which includes various many-body scattering events that modify the propagation of fermions. This quantity includes, among other non-static effects, the aforementioned renormalization of the fermion masses. Regarding its connection to topological insulators, it has recently been demonstrated that only the static part of the self-energy $\Sigma^{\boldsymbol{n}}_{\rm D}(0, \boldsymbol{k})$ carries the relevant information for the topological properties [122]. Accordingly, one can define a *topological Hamiltonian* [123, 124] that incorporates the effects of interactions on the topological properties as follows

$$h^{\boldsymbol{n}}_{\rm top}(\boldsymbol{k}) = h^{\boldsymbol{n}}_{\rm D}(\boldsymbol{k}) + \Sigma^{\boldsymbol{n}}_{\rm D}(0, \boldsymbol{k}). \tag{4.32}$$

The calculation of topological invariants for interacting systems then parallels the discussion of the previous sections, as the topological Hamiltonian can be interpreted as a dressed single-particle Hamiltonian. This notion has become very useful in the literature, as numerical tools such as dynamical mean-field theory [125–128] or quantum Monte Carlo [129–131] are ideally suited to calculate the zero-frequency self energy.

In our work, we shall be interested in understanding how the analytical techniques based on perturbative RG can be combined with the topological Hamiltonian to understand the fate of topological insulators as interactions are increased. From the preceding discussion, it is clear that the aforementioned renormalization of the Wilson masses will enter the zero-frequency self-energy as $\Sigma^{\boldsymbol{n}}_{\rm D}(0, \boldsymbol{k}) = \delta m_{\boldsymbol{n}}(u_{\mu\nu})\beta$, where β corresponds here to the Dirac matrix. Using the topological Hamiltonian (4.32) provides us with a direct way to extend the topological invariants (4.11)-(4.12) to the correlated regime, as we can calculate exactly the previous topological invariants. In our case, we simply need to consider the renormalized masses

$$\mathsf{Ch}_1 = \sum_{\boldsymbol{n}} \tfrac{1}{2} p_{\boldsymbol{n}} {\rm sgn}(\tilde{m}_{\boldsymbol{n}}) \tag{4.33}$$

for the two-dimensional A Chern insulators in (4.11), and

$$\mathsf{CS}_1 = \sum_{\boldsymbol{n}} \tfrac{1}{4} p_{\boldsymbol{n}} \mathrm{sgn}(\tilde{m}_{\boldsymbol{n}}) \tag{4.34}$$

for the one-dimensional AIII topological insulators in (4.12).

A quantitative calculation of the renormalization of the Wilson masses will depend on the particular model under study. In the following, we shall develop this RG program in detail for a one-dimensional case, which serves as a neat playground where our analytical predictions can be confronted to precise numerical simulations [50, 59, 132–134]. We will use this example to test qualitatively the above RG picture of interacting topological insulators.

4.4 Renormalization group flows for the imbalanced Creutz-Hubbard ladder

In this section, we consider a simple modification [59] of a lattice model leading to a $d = 1$ Wilson-fermion Hamiltonian [83]. This model will be used as a testbed for the RG of interaction effects in AIII topological insulators.

4.4.1 Wilson-Hubbard matter on a π-flux two-leg ladder

The imbalanced Creutz model, studied in detail in Chap. 3, consists of spinless fermions on a two-leg ladder [59]. These fermions are created and annihilated by $c^\dagger_{j,\ell}, c_{j,\ell}$, where $j \in \{1, \ldots, N\}$ labels the lattice sites within the upper or lower legs $\ell \in \{\mathrm{u}, \mathrm{d}\}$ of the ladder, and evolve according to the tight-binding Hamiltonian

$$H_{\mathrm{C}} = \sum_{j,\ell} \left(-t_\ell c^\dagger_{j+1,\ell} c_{j,\ell} - t_{\mathrm{x}} c^\dagger_{j+1,\ell} c_{j,\bar{\ell}} + \frac{\Delta\epsilon_\ell}{4} c^\dagger_{j,\ell} c_{j,\ell} + \mathrm{H.c.} \right). \tag{4.35}$$

Here, $t_\ell = te^{-\mathrm{i}\pi s_\ell/2}$ represents the horizontal hopping strength dressed by a magnetic π-flux, t_{x} stands for the diagonal hopping, $\Delta\epsilon_\ell = s_\ell \Delta\epsilon$ with $\Delta\epsilon > 0$ is an energy imbalance between the legs of the ladder, and we use the notation $s_{\mathrm{u}} = 1$ ($s_{\mathrm{d}} = -1$), and $\bar{\ell} = \mathrm{d}(\bar{\ell} = \mathrm{u})$ for $\ell = \mathrm{u}$ ($\ell = \mathrm{d}$). In this section, we start by setting $\hbar = 1$, and derive an effective microscopic effective speed of light c with which one can normalise all parameters, achieving the desired natural units.

In the thermodynamic limit, the rungs of the ladder play the role of the 1D Bravais lattice $ja \to \boldsymbol{x} \in \Lambda_\ell$ introduced above Eq. (4.4), while the ladder index $\ell \in \{\mathrm{u}, \mathrm{d}\}$ plays the role of the spinor degrees of freedom of the Fermi field $\Psi(\boldsymbol{x}) = (c_{j,\mathrm{u}}, c_{j,\mathrm{d}})^{\mathrm{t}}$. Making a gauge transformation $c_{j,\ell} \to e^{\mathrm{i}\pi j/2} c_{j,\ell}$ [2], one finds that the above imbalanced Creutz model can be rewritten as a 1D Wilson Hamiltonian (5.4) in lattice units $a = 1$, provided that one makes the following identification of Dirac matrices $\alpha_1 = \sigma^x$, $\beta = \sigma^z$, and bare dimensionless parameters $m = \Delta\epsilon/4t_{\mathrm{x}}$ $\delta m = t/t_{\mathrm{x}}$. According to the general discussion above, we should find $N_{\mathrm{D}} = 2$ Wilson fermions with masses $m_n \propto (\Delta\epsilon \pm 4t)$, such that the critical point separating topological and normal insulators corresponds to $\Delta\epsilon = 4t$ [59].

Since these effects should be independent of the gauge choice, we will stick to the original lattice formulation (4.35), which essentially implies that the Dirac points will be shifted from $k_n = \pi n \to k_n = \frac{\pi}{2}(1 - 2n)$, where we recall that $n \in \{0, 1\}$ (i.e.

[2] This transformation is the analogous Kawamoto-Smit rotation in [61].

$k_0 = \pi/2$ and $k_1 = -\pi/2$). This can be readily seen in momentum-space, where $H_{\rm C} = \int_{-\pi}^{+\pi} \frac{dk}{2\pi} \Psi^\dagger(k) h_{\rm C}(k) \Psi(k)$ with the single-particle Hamiltonian

$$h_{\rm C}(k) = -2t_{\rm x}\sigma^x \cos k + \left(\tfrac{1}{2}\Delta\epsilon + 2t \sin k\right)\sigma^z. \tag{4.36}$$

The energy dispersion around the above Dirac points $k \to k_n + k$, becomes $\epsilon_\pm(k_n+k) \approx \pm\sqrt{\tilde{m}_n^2 c^4 + c^2 k^2}$, where the effective speed of light is $c = 2t_{\rm x}$ and the Wilson masses are $\tilde{m}_n = \frac{1}{4t_{\rm x}^2}\left(\frac{\Delta\epsilon}{2} + (-1)^n 2t\right)$. To make contact with the previous convention $c = 1$, we normalize the Hamiltonian by the effective speed of light, and thus obtain the dimensionless masses

$$m_n = \left(\frac{\Delta\epsilon}{4t_{\rm x}} + (-1)^n \frac{t}{t_{\rm x}}\right), \tag{4.37}$$

which confirm the above expectation $m_n \propto (\Delta\epsilon \pm 4t)$.

In this non-interacting regime, one finds that the integral of the Chern-Simon form $\mathsf{Q}_1 = \frac{\rm i}{2\pi}\langle\epsilon_-(k)|\partial_k|\epsilon_-(k)\rangle dk$ in the chiral basis over the whole Brillouin zone, which is proportional to the so-called Zak's phase [135], yields $\mathsf{CS}_1 = \int_{-\pi}^{\pi} \mathsf{Q}_1 = \frac{1}{2}\theta(1 - \Delta\epsilon/4t)$, where $\theta(x)$ is the Heaviside step function. This expression is fully equivalent to Eq. (4.12), which was obtained in the long-wavelength limit by adding the contributions of the pair of Wilson fermions

$$\mathsf{CS}_1 = \tfrac{1}{4}(\mathrm{sgn}(m_0) - \mathrm{sgn}(m_1)). \tag{4.38}$$

Let us note that $\Delta\epsilon < 4t$ corresponds to the inverted mass regime, since $m_1 \propto (\Delta\epsilon - 4t) < 0$, and $m_0 \propto (\Delta\epsilon + 4t) > 0$ lead to a non-trivial Wilson loop $\mathsf{W}_1 = e^{{\rm i}2\pi\mathsf{CS}_1} = -1$, signaling a topological insulating ground-state. Note also that considering negative values of the imbalance would lead to a similar topological phase for $-4t < \Delta\epsilon < 0$ with the role of the positive and negative Wilson masses interchanged $m_1 > 0, m_0 < 0$.

The presence of the energy imbalance breaks both time-reversal $U_{\mathsf{T}} h_{\rm C}(-k)^* U_{\mathsf{T}}^\dagger = +h_{\rm C}(q)$ and particle-hole $U_{\mathsf{C}} h_{\rm C}(-k)^* U_{\mathsf{C}}^\dagger = -h_{\rm C}(k)$ symmetries, since the term $(\frac{1}{2}\Delta\varepsilon + 2t_{\rm x}\sin k)$ in Eq. (4.36) is neither even, nor odd, under $k \leftrightarrow -k$. Hence, the above symmetries cannot be fulfilled for any unitary U_{T} or U_{C}. On the other hand, there is a discrete sublattice symmetry $U_{\mathsf{S}} h_{\rm C}(k) U_{\mathsf{S}}^\dagger = -h_{\rm C}(k)$ with the operator $U_{\mathsf{S}} = \sigma_y$. Accordingly, the regime $\Delta\epsilon < 4t$ with $\mathsf{W}_1 = -1$ can be interpreted as a 1D AIII *topological insulator* [59, 61] (for more details see the sec. 3.2) .

The goal of this section is to study the fate of this topological phase in the presence of 4-Fermi terms

$$H_{\rm CH} = H_{\rm C} + \frac{V_{\rm v}}{2}\sum_j \sum_\ell c^\dagger_{j,\ell}\, c^\dagger_{j,\bar{\ell}}\, c_{j,\bar{\ell}}\, c_{j,\ell}, \tag{4.39}$$

which can be understood as Hubbard density-density interactions (4.13) along the rungs of the ladder. In Ref. [59], we obtained a numerical estimate of the phase diagram for this Creutz-Hubbard model using Matrix-Product-State methods [50] (see Fig. 4.1). In the present work, we will use these tools to benchmark the RG calculations, and test the validity of their connection to the topological Hamiltonian.

4.4.2 Euclidean action and continuum QFT description

In this subsection, we present the Euclidean action for the continuum description of the Creutz-Hubbard ladder, which will be valid in the vicinity of the second-order quantum phase transition. We thus focus on the vicinity of $\Delta\epsilon = 4t$, where the Wilson

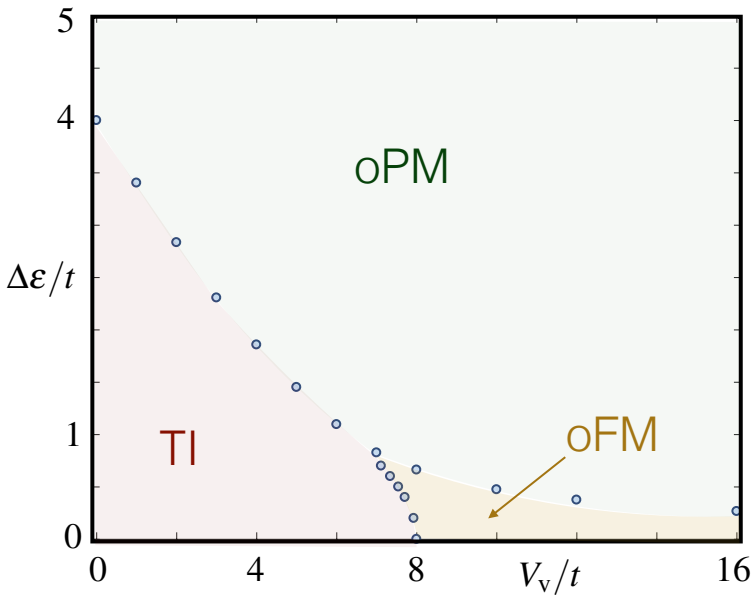

Figure 4.1: **Phase diagram of the imbalanced Creutz-Hubbard ladder:** Phase diagram displaying a topological insulator (TI) phase, and two other non-topological phases, namely an orbital phase with long-range ferromagnetic Ising order (oFM), and an orbital paramagnetic phase (oPM). The blue circles label numerical results, and the colored phase boundaries are a guide to the eye.

fermion at $k_1 = -\pi/2$ becomes massless, while the one at $k_0 = +\pi/2$ has a large positive mass. We note that setting $t = t_{\rm x}$ makes this mass very heavy $m_0 = 2$, such that the corresponding Wilson fermion lies already at the cutoff of the theory (i.e. maximum energy of the band). In any case, regardless of the particular value of $t/t_{\rm x}$, the fate of this fermion is to end in such a large mass limit as one approaches the IR limit of the RG transformations (i.e. the mass term is a relevant perturbation (4.27)). We thus believe that, without loss of generality, one can set $t = t_{\rm x}$ from the outset. Considering that this heavy fermion has a big positive mass, the topological invariant (4.38) is fully controlled by the mass of the lighter fermion around k_1, such that a non-trivial integer-valued Wilson loop is obtained provided that

$$\mathsf{W}_1 = e^{\mathrm{i}2\pi\mathsf{CS}_1} = -1, \quad \text{if } \operatorname{sgn}(m_1) = -1. \tag{4.40}$$

We start by reorganizing the action (4.15) for the Creutz-Hubbard Hamiltonian (4.39) in the regime $V_{\rm v} < \Delta\epsilon \approx 4t = 4t_{\rm x}$ in a form that simplifies the RG calculations beyond tree level (4.27)-(4.29), namely $S_{\rm CH} = S_0 + \delta S$ with

$$S_0 = \int_{\{k,\omega\}} \sum_{\eta=\mathrm{R,L,u,d}} \overline{\psi}_\eta(k,\omega)(-\mathrm{i}\omega + \epsilon_\eta(k))\psi_\eta(k,\omega), \tag{4.41}$$

where we have introduced the flavor index η to label the different Wilson fermions: *(i)* $\eta \in \{\mathrm{R},\mathrm{L}\}$ refers to the right- ($s_{\rm R} = 1$) as and left-moving ($s_{\rm L} = -1$) modes around the Dirac point k_1, $\psi_\eta(k,\omega) = (\psi_{1,\mathrm{u}}(k,\omega) - s_\eta\psi_{1,\mathrm{d}}(k,\omega)/\sqrt{2}$, which have energies $\epsilon_\eta(k) = s_\eta k$. The Wilson-mass term of the fermions around this point m_1, which is small for $\Delta\epsilon \approx 4t$, will be included in δS. In addition, *(ii)* we define the flavours $\eta \in \{\mathrm{u},\mathrm{d}\}$ for the positive- and negative-frequency modes around the point k_0, $\psi_\eta(k,\omega) = \psi_{0,\eta}(k,\omega)$, which have energies $\epsilon_\eta(k) = \pm m_0$. We note that the corrections to this heavy-mass

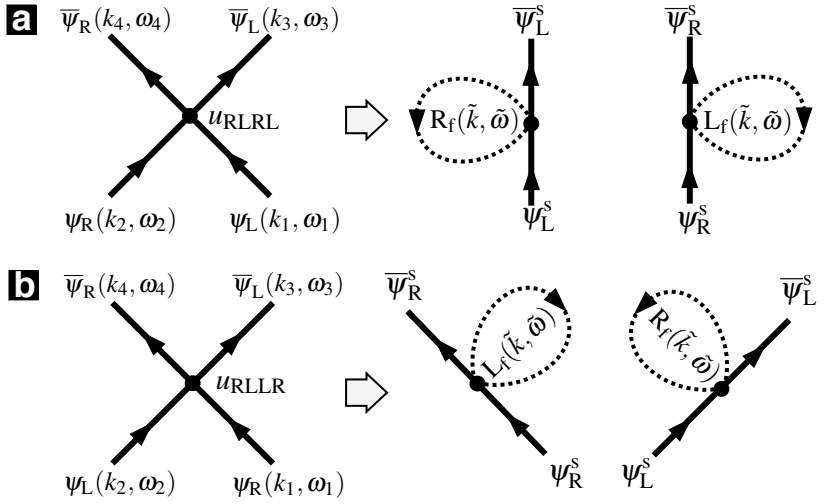

Figure 4.2: **One-loop tadpole diagrams around k_1:** **(a)** (left) Forward scattering of $(\eta_1,\eta_2)=(\mathrm{L},\mathrm{R})$ fermions onto $(\eta_3,\eta_4)=(\mathrm{L},\mathrm{R})$. (right) Tadpole diagrams by joining an incoming and outgoing line of the same $\eta\in\{\mathrm{L},\mathrm{R}\}$ flavor into a loop. The momentum inside the loop is constrained to a small region around the cutoff $\Lambda_\mathrm{c}/s\leq\tilde{k}\leq\Lambda_\mathrm{c}$. The loop integrals over the fast modes are labelled by $\eta_\mathrm{f}(\tilde{k},\tilde{\omega})$ and depicted by dashed closed lines. **(b)** (left) Backward scattering of $(\eta_1,\eta_2)=(\mathrm{R},\mathrm{L})$ fermions onto $(\eta_3,\eta_4)=(\mathrm{L},\mathrm{R})$. (right) Corresponding tadpole diagrams.

limit (i.e. $\delta\epsilon_\eta(k)\approx\mp k^2$) can be included in δS. However, as occurred for the shorter-wavelength corrections (4.17), these perturbations are IR irrelevant already at tree level.

The perturbations that are relevant and marginal at tree level are contained in $\delta S=\delta S_\mathrm{m}+\delta S_\mathrm{int}$, where

$$\delta S_\mathrm{m}=\int_{\{k,\omega\}}\sum_{\eta=\mathrm{L,R}} m_1\Lambda_\mathrm{c}\overline{\psi}_\eta(k,\omega)\psi_{\bar{\eta}}(k,\omega), \tag{4.42}$$

and we have introduced $\bar{\eta}=\mathrm{L}$ ($\bar{\eta}=\mathrm{R}$) for $\eta=\mathrm{R}$ ($\eta=\mathrm{L}$). Clearly, the mass term mixes the right- and left-moving fermions around k_1, breaking explicitly the chiral symmetry of the free masless Dirac fermion (4.41) [101]. The correction due to the Hubbard interaction (4.39), which must be normalized by the effective speed of light $c=2t_\mathrm{x}=2t$, can be expressed in a form similar to Eq. (4.19), namely

$$\delta S_\mathrm{int}=-\frac{1}{4}\int_{\{k,\omega\}}\sum_{\{\boldsymbol{\eta}\}} u_{\boldsymbol{\eta}}\overline{\psi}_{\eta_4}(4)\overline{\psi}_{\eta_3}(3)\psi_{\eta_2}(2)\psi_{\eta_1}(1), \tag{4.43}$$

where we use similar conventions as below Eq. (4.19), and define $\sum_{\{\boldsymbol{\eta}\}}=\sum_{\eta_1,\eta_2,\eta_3,\eta_4}$. These interaction terms describe the scattering between an incoming pair of fermions (η_1,η_2) onto an outgoing pair (η_3,η_4). Note that the dimensionless couplings $u_{\boldsymbol{\eta}}=u_{\eta_4,\eta_3,\eta_2,\eta_1}$ should be antisymmetric with respect to $\eta_4\leftrightarrow\eta_3$, or $\eta_2\leftrightarrow\eta_1$, as a consequence of the anti-commuting nature of the Grassmann variables [120]. Additionally, the particular form of the Hubbard interaction in Eq. (4.39) leads to couplings $u_{\boldsymbol{\eta}}$ without any momentum dependence.

In combination, these two features limit the possible scattering events underlying the action (4.43). For instance, for scattering processes that take place in the vicinity of a single point k_n, the only allowed couplings are $u_\mathrm{RLLR}:=V_\mathrm{v}/2t$, and $u_\mathrm{uddu}:=2V_\mathrm{v}/t$,

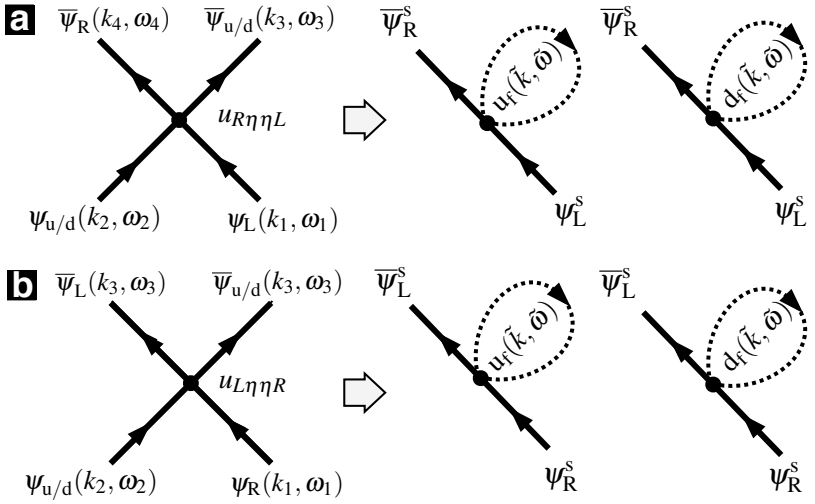

Figure 4.3: **One-loop tadpole diagrams involving k_1 and k_0: (a)** (left) Scattering of $(\eta_1,\eta_2)=(\mathrm{L},\mathrm{u/d})$ fermions onto $(\eta_3,\eta_4)=(\mathrm{u/d},\mathrm{R})$. (right) Tadpole corrections to the mass of the light fermions by joining an incoming and outgoing line of the heavy fermions (we use the same conventions as in Fig. 4.2) . **(b)** Same as for **(a)** but for the scattering of $(\eta_1,\eta_2)=(\mathrm{R},\mathrm{u/d})$ fermions onto $(\eta_3,\eta_4)=(\mathrm{u/d},\mathrm{L})$.

together with all the possible permutations

$$\begin{aligned} u_{\rm RLLR} &= -u_{\rm LRLR} = -u_{\rm RLRL} = u_{\rm LRRL} := V_{\rm v}/2t, \\ u_{\rm uddu} &= -u_{\rm udud} \;=\; -u_{\rm dudu} \;=\; u_{\rm duud} := 2V_{\rm v}/t, \end{aligned} \tag{4.44}$$

All these scattering processes preserve the number of fermions with a given flavor η (see the left panels of Figs. 4.2 **(a)** and **(b)** for the two possible scattering channels with an outgoing $(\eta_3,\eta_4)=(\mathrm{L},\mathrm{R})$ pair).

In addition, there will be scattering processes that involve fermions from both Dirac points k_0 and k_1, which can be organized in two sets. The first set consists of scattering processes that conserve the number of fermions around each point, but may change their flavour e.g. a $L\leftrightarrow R$ and $u\leftrightarrow d$, namely

$$\begin{aligned} u_{\rm RuuR} &= -u_{\rm RuuL} = -u_{\rm LuuR} = u_{\rm LuuL} := V_{\rm v}/4t, \\ u_{\rm RddR} &= \;\; u_{\rm RddL} = \;\; u_{\rm LddR} = u_{\rm LddL} := V_{\rm v}/4t, \\ u_{\rm LudL} &= -u_{\rm RudR} = -u_{\rm RudL} = u_{\rm LudR} := V_{\rm v}/4t, \\ u_{\rm LduL} &= -u_{\rm RduR} = -u_{\rm LduR} = u_{\rm RduL} := V_{\rm v}/4t, \end{aligned} \tag{4.45}$$

plus all permutations $\eta_1\eta_2$, $\eta_3\eta_4$ with their relative signs. The second set corresponds to the so-called Umklapp scattering, i.e. processes where the number of fermions around each point changes in pairs

$$\begin{aligned} u_{\rm udRL} &= -u_{\rm udLR} = -u_{\rm duRL} = u_{\rm duLR} := V_{\rm v}/t, \\ u_{\rm LRdu} &= -u_{\rm LRud} = -u_{\rm RLud} = u_{\rm RLud} := V_{\rm v}/t. \end{aligned} \tag{4.46}$$

We note that momentum conservation can still be achieved up to a reciprocal lattice vector $\pm 2(k_1-k_0)=\pm 2\pi$.

Equations (4.41)-(4.43) set the stage for the RG study of correlation effects in the one-dimensional AIII topological insulator beyond tree level. As discussed in detail below, in the vicinity of $\Delta\epsilon = 4t = 4t_{\rm x}$, we shall use these corrections to predict the critical line separating topological and normal insulating phases at finite repulsive interactions $V_{\rm v}>0$.

4.5 Loop-expansion: running of the Wilson masses and topological invariants in presence of interactions

In this subsection, we consider the first- and second-order terms of the cumulant expansion (4.26) of the quartic interactions (4.43), focussing on its effects on the renormalization of the Wilson masses and the topological invariant. This will allow us to determine the critical line that connects to the non-interacting RG fixed point separating the topological and trivial insulators, and to show that such a critical line delimits the region of the phase diagram where the ground-state corresponds to a correlated topological insulator.

4.5.1 Vanishing tadpoles considering light Wilson fermions

In the regime $\Delta\epsilon \approx 4t = 4t_{\rm x}$, the Wilson masses fulfil $|m_1| \ll |m_0|$, and one may expect that the heavy fermions around k_0 shall not have any influence on the lighter fermions around k_1, which in turn determine the onset of a topological phase (i.e. the mass-inversion point $m_1 < 0$). Following this line of reasoning, to see how this Wilson mass runs with the cutoff $m_1(\Lambda_{\rm c})$, and determine how the RG fixed point $m_1 = 0$ changes with interactions, it would suffice to consider scattering events (4.43) in the vicinity of k_1, i.e. scattering between left- and right-moving modes described by the first line of Eq. (4.44). The first-cumulant correction to the coarse-grained action would then arise from the following terms

$$\begin{aligned}\langle \delta S_{\rm int}^{k_1}\rangle_{\rm f} =& \frac{1}{4}\int_{\{k,\omega\}} \sum_{\eta={\rm L,R}} u_{\eta\bar\eta\bar\eta\eta}\left(\left\langle \overline{\psi}^{\rm f}_{\bar\eta}(3)\psi^{\rm f}_{\bar\eta}(2)\right\rangle_{\rm f} \overline{\psi}^{\rm s}_{\eta}(4)\psi^{\rm s}_{\eta}(1) + \left\langle \overline{\psi}^{\rm f}_{\eta}(4)\psi^{\rm f}_{\eta}(1)\right\rangle_{\rm f} \overline{\psi}^{\rm s}_{\bar\eta}(3)\psi^{\rm s}_{\bar\eta}(2)\right)\\ &+\frac{1}{4}\int_{\{k,\omega\}} \sum_{\eta={\rm L,R}} u_{\eta\bar\eta\eta\bar\eta}\left(\left\langle \overline{\psi}^{\rm f}_{\bar\eta}(3)\psi^{\rm f}_{\eta}(1)\right\rangle_{\rm f} \overline{\psi}^{\rm s}_{\eta}(4)\psi^{\rm s}_{\bar\eta}(2) + \left\langle \overline{\psi}^{\rm f}_{\eta}(4)\psi^{\rm f}_{\bar\eta}(2)\right\rangle_{\rm f} \overline{\psi}^{\rm s}_{\bar\eta}(3)\psi^{\rm s}_{\eta}(1)\right),\end{aligned} \tag{4.47}$$

where $\langle \overline{\psi}^{\rm f}_{\eta}(j)\psi^{\rm f}_{\eta}(j')\rangle_{\rm f} = \delta(\omega_j-\omega_{j'})\delta(k-k')/({\rm i}\omega_j - \epsilon_\eta(k))$ is obtained from the free-fermion propagator (4.22) by working on the corresponding eigenbasis of the non-interacting single-particle Hamiltonian.

These contributions can be depicted in terms of the so-called *tadpole diagrams* (see the right panels of Figs. 4.2 **(a)** and **(b)** for $\eta = {\rm L}$), which include a single closed loop over the fast modes. It is already apparent from the fast-mode loops of these figures, without any further calculation, that these terms can only contribute with $\langle \delta S_{\rm int}^{k_1}\rangle_{\rm f} \propto (\overline{\psi}^{\rm s}_{\rm R}(k,\omega)\psi^{\rm s}_{\rm R}(k,\omega) + \overline{\psi}^{\rm s}_{\rm L}(k,\omega)\psi^{\rm s}_{\rm L}(k,\omega))$, which is an irrelevant common shift of the on-sites energies for the slow modes. However, there is no one-loop term that yields a correction to the mass term mixing the different fermion chiralities $\langle \delta S_{\rm int}^{k_1}\rangle_{\rm f} \propto (\overline{\psi}^{\rm s}_{\rm R}(k,\omega)\psi^{\rm s}_{\rm L}(k,\omega) + \overline{\psi}^{\rm s}_{\rm L}(k,\omega)\psi^{\rm s}_{\rm R}(k,\omega))$, inducing thus a non-vanishing mass (4.42) around k_1. This result is in contradiction to the numerical data displayed in Fig. 4.1, where the non-interacting critical point at $\Delta\epsilon = 4t$ flows towards smaller values of the imbalance linearly $(\Delta\epsilon - 4t) \propto -V_{\rm v}$, for $V_{\rm v} \ll \Delta\epsilon$. Accordingly, the Wilson mass corresponding to this fixed point m_1 should get a renormalization $\tilde{m}_1 = m_1 + \delta m_1(V_{\rm v})$ (4.30) linear in the interaction strength $\delta m_1(V_{\rm v}) \propto V_{\rm v}$. We can thus conclude that, when restricting to the slow modes of the continuum description, it is not possible to obtain non-zero tadpole corrections that can account for the numerical phase diagram.

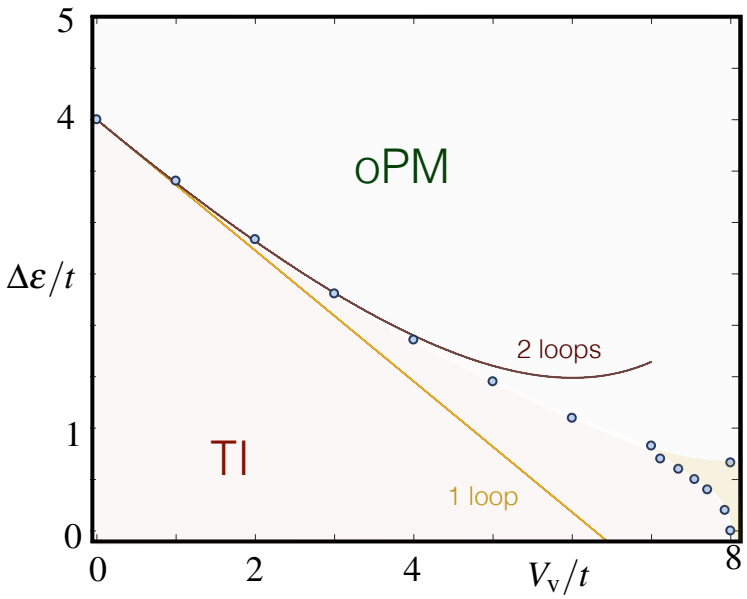

Figure 4.4: **Benchmark of the RG prediction for the critical line:** Comparison of the one-loop (4.52) (yellow line) and two-loop (4.55) (red line) predictions of the critical line. The blue circles label numerical results of Fig. 4.1 in the region of weak to moderate interactions.

We note, at this point, that 4-Fermi continuum QFTs can display the phenomenon of dynamical mass generation, where an interacting massless Dirac fermion acquires a mass that spontaneously breaks chiral symmetry [136]. The scaling of the dynamically-generated mass with the interaction strength is, however, non-perturbative [61, 136], and cannot account for the aforementioned linear dependence. We will extend on the interplay of lattice effects and a dynamically-generated mass in the last section with our conclusions and outlook.

4.5.2 Tadpoles considering also heavy Wilson fermions

Let us now explore how a linear running of the Wilson mass can be obtained by considering the effect that the heavy fermion around k_0 may have on the lighter mass m_1 of the fermion around k_1. The heavy fermion around k_0, lying at the cutoff of the theory, may indeed renormalize the parameters of the QFT when integrated out during the RG coarse-graining. Inspecting Eqs. (4.45)-(4.46), one realizes that the couplings $u_{\rm LuuR}, u_{\rm RuuL}, u_{\rm LddR}, u_{\rm RddL}$, together with their corresponding permutations, can lead to tadpole diagrams that indeed induce a correction to the mass (see Fig. 4.3). The first-cumulant contribution to the coarse-grained action yields

$$\langle \delta S_{\rm int}^{k_1 k_0} \rangle_{\rm f} = \frac{1}{4} \int_{\{k,\omega\}} \sum_{\eta={\rm u,d}} 4 \left(u_{{\rm R}\eta\eta{\rm L}} \left\langle \overline{\psi}_\eta^{\rm f}(4) \psi_\eta^{\rm f}(1) \right\rangle_{\rm f} \overline{\psi}_{\rm R}^{\rm s}(3) \psi_{\rm L}^{\rm s}(2) + u_{{\rm L}\eta\eta{\rm R}} \left\langle \overline{\psi}_\eta^{\rm f}(4) \psi_\eta^{\rm f}(1) \right\rangle_{\rm f} \overline{\psi}_{\rm L}^{\rm s}(3) \psi_{\rm R}^{\rm s}(2) \right), \tag{4.48}$$

where the additional factor of 4 comes from considering the contribution of all possible permutations, e.g. $u_{\rm LuuR} = -u_{\rm uLuR} = -u_{\rm LuRu} = u_{\rm uLRu}$, all of which contribute equally.

If we now perform the loop integrals, we obtain $\int_{\mathbb{R}} \frac{{\rm d}\omega_4}{2\pi} \int_{\frac{\Lambda_{\rm c}}{s}}^{\Lambda_{\rm c}} \frac{{\rm d}k_4}{(2\pi)} \int_{\mathbb{R}} \frac{{\rm d}\omega_1}{2\pi} \int_{\frac{\Lambda_{\rm c}}{s}}^{\Lambda_{\rm c}} \frac{{\rm d}k_1}{(2\pi)} \left\langle \overline{\psi}_\eta^{\rm f}(4) \psi_\eta^{\rm f}(1) \right\rangle_{\rm f} = \mp \frac{\Lambda_{\rm c}}{\pi}(1 - \frac{1}{s})$ for $\eta = {\rm u, d}$, respectively. To compare with the original action, we must now rescale the momentum and frequency (5.43) to reset the original cutoff. Accordingly,

the slow modes should also be transformed

$$\psi^{\mathrm{s}}_{\mathrm{R/L}}(k,\omega) \to \psi'_{\mathrm{R/L}}(k',\omega') = s^{-(d+2)/2}\psi^{\mathrm{s}}_{\mathrm{R/L}}(k'/s,\omega'/s), \tag{4.49}$$

such that the first-order cumulant (4.48) contributes with a correction to the Wilson mass (4.42), namely

$$\langle \delta S^{k_1 k_0}_{\mathrm{int}} \rangle_{\mathrm{f}} = \int_{k,\omega} \sum_{\eta=\mathrm{L,R}} \delta m_1^{(1)} \Lambda_{\mathrm{c}} \overline{\psi}_\eta(k,\omega)\psi_{\bar{\eta}}(k,\omega). \tag{4.50}$$

Here, we have introduced the Wilson mass shift to one loop $\delta m_1^{(1)}$, which modifies the β_{m_1} function in the following way

$$\delta m_1^{(1)} = \frac{V_{\mathrm{v}}}{2\pi t}(s-1), \quad \beta_{m_1} = \frac{\mathrm{d}m_1}{\mathrm{d}\log s} = m_1 + \delta\beta^{(1)}_{m_1}. \tag{4.51}$$

The RG fixed point is then determined by the bare lattice parameters that lead to a vanishing β_{m_1} function, namely

$$\frac{\Delta\epsilon}{4t} - 1 = -\frac{V_{\mathrm{v}}}{2\pi t} \implies \left.\frac{\Delta\epsilon}{t}\right|_{\mathrm{c}} = 4 - \frac{2}{\pi}\frac{V_{\mathrm{v}}}{t}. \tag{4.52}$$

The comparison of this prediction with the numerical results shows a good agreement in the regime of weak interactions (see the yellow line in Fig. 4.4). We note that this one-loop correction to the mass agrees exactly with a self-consistent mean-field treatment that relies on the mapping of the Creutz-Hubbard model to a pair of coupled quantum Ising models [59]. The advantage of the present RG approach is that, on the hand, it can be improved systematically by considering higher orders in the cumulant expansion. On the other hand, as discussed below, we can not only predict the position of the critical line, but also show that the region it delimits corresponds to a correlated AIII topological insulator.

4.5.3 Two-loop corrections to the light Wilson mass

Let us now move on to the second-order cumulant contributions (4.26) to the coarse-grained action, which will yield two-loop corrections to the Wilson mass that can be accounted for by considering the so-called one-particle irreducible Feynman diagrams with two interaction vertices and two external lines with right- and left-moving fermions.

In analogy to the discussion below Eq. (4.47), we note that it is not possible to obtain two-loop corrections to the mass by simply focusing on the light fermion around k_1 (i.e. scattering events in first line of Eq. (4.44)). By incorporating the interactions with the heavy fermion around k_0, we can have the contributions to the Wilson mass depicted in Fig. 4.5, where we recall that the closed loops are formed by heavy-fermion propagators. In contrast to the standard situation in other interacting QFTs [137], where the double tadpole of Fig. 4.5 **(a)** would contribute to the mass, here we find that only the "saturn diagram" of Fig. 4.5 **(b)** does contribute with a second-order shift of the mass

$$\left\langle \left(\delta S^{K_1 K_0}_{\mathrm{int}}\right)^2 \right\rangle_{\mathrm{c,f}} = \int_{k,\omega} \sum_{\eta=\mathrm{L,R}} \delta m_1^{(2)} \Lambda_{\mathrm{c}} \overline{\psi}_\eta(k,\omega)\psi_{\bar{\eta}}(k,\omega). \tag{4.53}$$

Here, we have introduced the two-loop mass shift

$$\delta m_1^{(2)} = -\frac{3}{8\pi^2}\frac{V_{\mathrm{v}}^2}{m_0 t^2}(s-1), \quad \beta_{m_1} = m_1 + \delta\beta^{(1)}_{m_1} + \delta\beta^{(2)}_{m_1}. \tag{4.54}$$

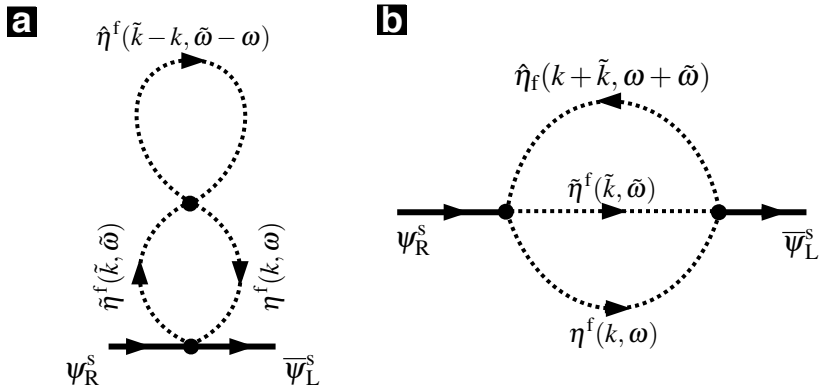

Figure 4.5: **Two-loop diagrams for the Wilson mass term: (a)-(b)** Possible two-loop diagrams for the correction to the mass of the light fermions $\eta_j \in \{\mathrm{L},\mathrm{R}\}$ by virtual creation-annihilation of light/heavy fermions in fast modes $\eta,\tilde{\eta},\hat{\eta} \in \{\mathrm{R},\mathrm{L},\mathrm{u},\mathrm{d}\}$.

which should be evaluated for the mass of the heavy fermions $m_0 = \Delta\epsilon/4t+1$ at the bare lattice parameters that yield the RG fixed point with first-order corrections (4.52), such that $m_0 = 2 - V_{\mathrm{v}}/2\pi t$. Hence, the critical line of the model with two-loop corrections follows from the condition of a vanishing β_{m_1} function, and yields

$$\left.\frac{\Delta\epsilon}{t}\right|_{\mathrm{c}} = 4 - 2\left(\frac{V_{\mathrm{v}}}{\pi t}\right) + \frac{3}{4}\left(\frac{V_{\mathrm{v}}}{\pi t}\right)^2 \frac{1}{4-\left(\frac{V_{\mathrm{v}}}{\pi t}\right)}. \tag{4.55}$$

The comparison of this prediction with the numerical results shows a much better agreement in the regime of weak to intermediate interactions (see the red line of Fig. 4.4).

4.5.4 RG flows and the effective topological Hamiltonian

Let us now consider the nature of the two phases separated by this critical line from the perspective of the topological Hamiltonian (4.32). As discussed below Eq. (4.32), the renormalization of the Wilson masses (4.30) contributes to the zero-frequency self-energy in a very simple manner, which allows to diagonalize the topological Hamiltonian (4.32) in complete analogy to the single-particle one. In the present case, the topological Hamiltonian can be expressed as

$$h_{\mathrm{top}}(k) = -2t\sigma^x \cos k + \left(\tfrac{1}{2}\Delta\tilde{\epsilon} + 2t\sin k\right)\sigma^z, \tag{4.56}$$

where the previous two-loop corrections contribute to

$$\Delta\tilde{\epsilon} = \Delta\epsilon + \frac{2}{\pi}V_{\mathrm{v}} - \frac{3V_{\mathrm{v}}}{4\pi^2 t}\left(4 - \frac{V_{\mathrm{v}}}{\pi t}\right). \tag{4.57}$$

The calculation of the topological invariants now directly yields Eq. (4.34), and we obtain a non-zero topological invariant for the correlated topological insulator when

$$\mathsf{W}_1 = e^{\mathrm{i}2\pi\mathsf{CS}_1} = -1, \quad \text{if } \mathrm{sgn}(\tilde{m}_1) = -1. \tag{4.58}$$

Since we know the two-loop corrections to the mass, we can characterize the nature of the insulating phases separated by the critical line: *(i)* for $\frac{\Delta\epsilon}{t} > \left.\frac{\Delta\epsilon}{t}\right|_{\mathrm{c}}$ (i.e. above the critical line), the mass $\tilde{m}_1 > 0$, such that $\mathsf{CS}_1 = 0$, and the Wilson loop is trivial

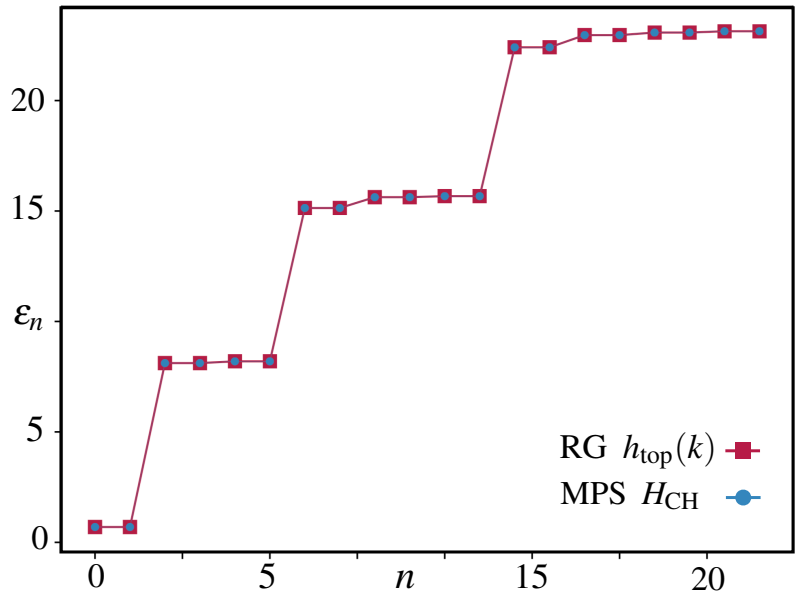

Figure 4.6: **Entanglement spectrum of the Creutz-Hubbard ladder:** Lowest $N_{\rm ES} = 22$ eigenvalues of the entanglement spectrum $\epsilon_n \in {\rm ES}(\rho_\ell)$ for the Creutz-Hubbard ladder (4.39) for $\Delta\epsilon = 2.2t$, $V_{\rm v} = 0.2t$, which lies inside the TI region of Fig. 4.4. We compare the results obtained via the MPS numerical simulations (squares), and via the RG-corrected topological Hamiltonian (circles) (4.56).

$\mathsf{W}_1 = 1$. Accordingly, the ground-state corresponds to a normal band insulator. *(ii)* for $\frac{\Delta\epsilon}{t} < \frac{\Delta\epsilon}{t}\Big|_{\rm c}$ (i.e. below the critical line), the mass $\tilde{m}_1 < 0$, such that $\mathsf{CS}_1 = \frac{1}{2}$, and the Wilson loop is $\mathsf{W}_1 = -1$. Accordingly, the ground-state corresponds to a topological AIII insulator. This behaviour is in complete agreement with Fig. 4.1, and thus can serve as a quantitative test of the validity of the RG picture of correlated topological insulators presented in this work.

4.6 Entanglement spectroscopy: symmetry-protected topological phases and critical Luttinger liquids

In this subsection, we shall explore additional features of the zero-temperature Creutz-Hubbard ladder to benchmark the RG-corrected topological Hamiltonian (4.36). These features will become manifest in the bipartite correlations of a ground-state partitioned into two blocks of length ℓ and $L-\ell$, where $L = Na$ is the length of the whole ladder. In particular, we shall be interested in two types of correlations: entanglement entropies, and bi-partite fluctuations. The former are related to the so-called entanglement spectrum, which serves to characterize the topological properties of an interacting topological insulator as a symmetry-protected topological (SPT) phase. The latter will be used to characterize the critical line delimiting the topological-insulating region in more detail.

4.6.1 SPT entanglement and the topological Hamiltonian

Let us start by focusing on the entanglement of the ground-state, which can defined via the block reduced density matrices $\rho_\ell = {\rm Tr}_{L-\ell}\{|\epsilon_{\rm gs}\rangle\langle\epsilon_{\rm gs}|\}$. Among the various

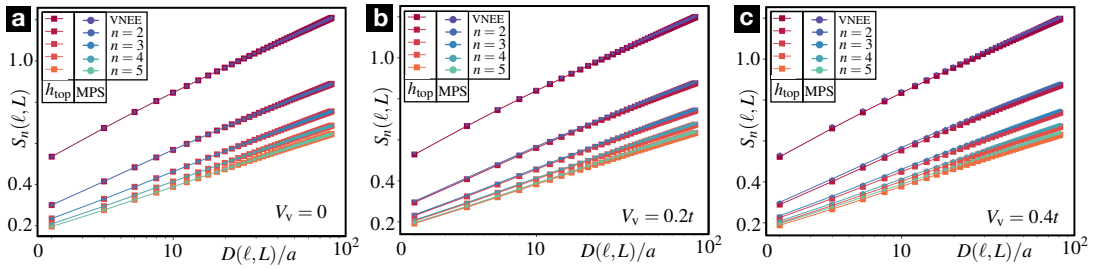

Figure 4.7: **Entanglement entropies of the critical Creutz-Hubbard ladder:** Von Neumann and Rényi block entanglement entropies are represented as a function of the block chord length. The Hubbard interaction strengths are set to **(a)** $V_{\rm v} = 0$, **(b)** $V_{\rm v} = 0.2t$, and **(c)** $V_{\rm v} = 0.4t$, while the corresponding energy imbalance $\Delta\epsilon$ is set to the critical value of Eq. (4.55) predicted by the RG calculations.

existing measures of entanglement on a bi-partite scenario [138], the *entanglement entropies* (EEs) enjoy a privileged status within the realm of quantum many-body systems [139,140]. In particular, the so-called Rényi EEs are defined for all $n > 0$

$$S_n(\ell, L) = \frac{1}{1-n} \log\left(\mathrm{Tr}\left\{(\rho_\ell)^n\right\}\right), \tag{4.59}$$

and include the Von Neuman entanglement entropy (VNEE) $S(\ell, L) = -\mathrm{Tr}\{\rho_\ell \log(\rho_\ell)\} = \lim_{n\to 1} S_n(\ell, L)$ as a limiting case. Moreover, the Rényi EEs are related to the moments of the reduced density matrix [141], and can be used to construct the full *entanglement spectrum* [142], which is defined by the set of all eigenvalues $\mathrm{ES}(\rho_\ell) = \sigma(H_{\rm E})$ of the entanglement Hamiltonian $H_{\rm E}$, obtained by expressing the reduced density matrix as an equilibrium Gibbs state $\rho_\ell \propto e^{-H_{\rm E}}$.

For non-interacting systems, $H_{\rm E}$ has a closed-form expression as a quadratic operator that can be derived exactly from the exact diagonalization of the original Hamiltonian [143]. For interacting systems, the entanglement spectrum $\epsilon_n \in \mathrm{ES}(\rho_\ell)$ can be obtained approximately by the MPS simulations [50], which give direct access to the Schmidt values λ_n of the bipartition, such that $\epsilon_n = -2\log\lambda_n$ (see the Appendix A for more details). As shown in [144–146], the entanglement spectrum can be used to characterize SPT phases such as correlated topological insulators, as it displays an exact degeneracy related to the existence of many-body edge modes [144–146]. In Fig. 4.6, we show how this feature is fulfilled clearly for the correlated AIII topological insulator (4.39). As a comparison, we display the entanglement spectrum of the full Creutz-Hubbard ladder (4.39), and that of the RG-corrected topological Hamiltonian (4.36), which can be calculated exactly via the two-point correlation functions [147,148]. Both methods display the aforementioned degeneracies for the correlated topological insulator (4.58), and show a clear quantitative agreement providing an additional test of the validity of the RG-corrected topological Hamiltonian approach.

It is also worth mentioning that our predictions can be provided experimentally. In [149–151] the authors proposed an immediate, scalable recipe for implementation of the entanglement Hamiltonian, and measurement of the corresponding entanglement spectrum as spectroscopy of the Bisognano-Wichmann Hamiltonian [152] with synthetic quantum systems.

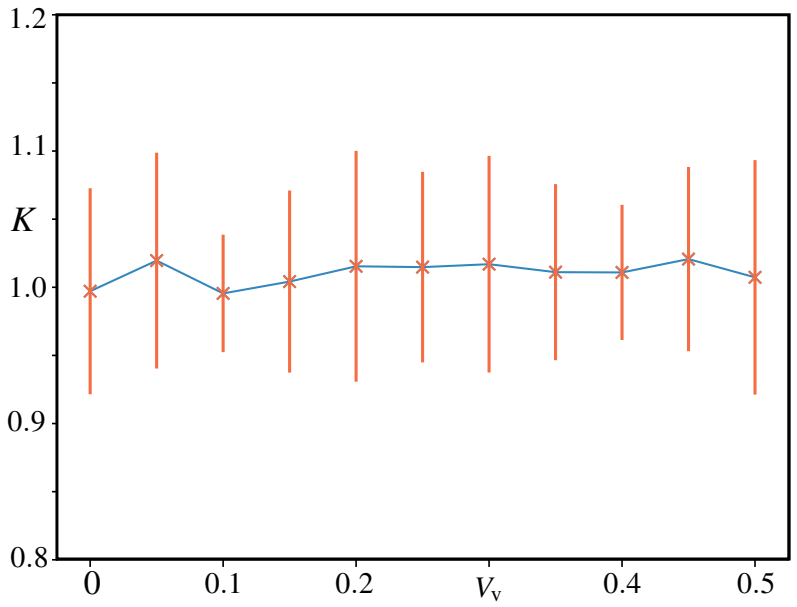

Figure 4.8: **Luttinger parameter at criticality:** The Luttinger parameter K is extracted by fitting the bi-partite fluctuations $\mathcal{F}(\ell, L)$ obtained by the MPS numerical simulations to the linear logarithmic scaling with the chord length of Eq. (4.65). For each critical point $(\Delta\epsilon, V_v)$, we extract the thermodynamic value of the Luttinger parameter by extracting the corresponding K_L values for various lengths $L/a \in [64, 192]$, and fitting them to $K_L = K + c_1/L + c_2/L^2$.

4.6.2 Bi-partite fluctuations and the Luttinger parameter

We now explore the scaling region of the quantum phase transition between the topological and trivial band insulators (see Fig. 4.4) from the perspective of bi-partite correlations (for more details see the Appendix B). In Fig. 4.7, we represent the critical Rényi EEs (4.59) obtained by the two approaches as a function of the so-called chord length $D(\ell, L) = (2L/\pi)\sin(\pi\ell/L)$. As can be observed in this figure, the agreement between effective RG model and full one, is very good for weak interactions, but small deviations become apparent in the higher-order Rényi EEs as the Hubbard interactions increase and we move along the critical line of Fig. 4.4.

We would like to understand the origin of these small differences. On the one hand, they might simply be caused by inaccuracies in the RG-corrected imbalance (4.57). However, for the range of Hubbard interactions hereby explored, we have found that the differences in the critical points are vanishingly small. On the other hand, they might be caused by the approximations inherent to the topological Hamiltonian (4.32), namely considering only the static part of the self-energy to define an effective single-particle Hamiltonian. In the present context, the critical properties of the topological Hamiltonian (4.36) are always governed by a single massless Dirac fermion, which might not be an accurate description of the scaling region of the full Creutz-Hubbard ladder as one moves along the critical line by increasing the interactions.

In order to explore this question further, we will explore the particular scaling of the critical bi-partite correlations with the chord distance. Due to non-extensive nature of the EEs $S_n(\ell, L) = S_n(L-\ell, L)$, the bipartite correlations might be expected to be contained within the boundary of the bipartition, which leads to the so-called entropic logarithmic area laws [56]. As occurs for the VNEE [153], the Rényi EEs also display area-law violations for one-dimensional critical systems [92, 154], which

contain information about the underlying conformal field theory (CFT) that describes the long-wavelength properties of the system [155]. For open boundary conditions, one finds that the Rényi EEs can be expressed as

$$S_n(\ell, L) = S_n^{\mathrm{CFT}}(\ell, L) + \delta S_n(\ell, L), \tag{4.60}$$

which contains a logarithmic violation of the area law that depends on the central charge c of the CFT

$$S_n^{\mathrm{CFT}}(\ell, L) = \frac{c}{12}\left(1 + \frac{1}{n}\right) \log D(\ell, L), \tag{4.61}$$

together with a non-universal correction $\delta S_n(\ell, L)$. We note that the logarithmic scaling of these EEs for various interactions displayed in Fig. 4.7 is consistent with a central charge $c \approx 1$, which corresponds to the CFT of a free compactified boson [155]. This agrees with the leading-order scaling of the Rényi EEs for the topological Hamiltonian (4.36), such that the aforementioned deviations must be contained in the non-universal terms $\delta S_n(\ell, L)$. In particular, one possibility is that the Luttinger parameter, which is always fixed to $K = 1$ for the RG-corrected topological Hamiltonian (4.36), becomes $K \neq 1$ for the full Creutz-Hubbard ladder (4.39).

As first realized for the Von Neumann EE with open boundary conditions [156], the non-universal corrections to the Rényi EEs [157] for systems whose critical behavior is described by the free-boson CFT (i.e. Luttinger liquids [158]) find the following closed-form expression

$$\delta S_n(\ell, L) = F_n\left(\frac{\ell}{L}\right) \frac{\cos(2k_{\mathrm{F}}\ell + \omega)}{\left(2\sin(k_{\mathrm{F}}) D(\ell, L)\right)^{K/n}}, \tag{4.62}$$

where k_{F} is Fermi's momentum, K is the so-called Luttinger parameter, $F_n(\ell/L)$ is a scaling function, and ω is a constant phase-shift that controls the oscillating nature of the corrections. For instance, for spin-$\frac{1}{2}$ Heisenberg-type Luttinger liquids (i.e. XXZ model), where $k_{\mathrm{F}} = \pi/2$, one finds $\omega = 0$ such that the correlations display a characteristic alternating behavior [156, 157]. On the other hand, for hard-core bosons with dipolar interactions at quarter filling, where $k_{\mathrm{F}} = \pi/4$, one needs to set $\omega \approx \pi/2$ to capture the oscillations [159].

We note that this characteristic oscillatory behavior is in principle useful to extract numerically the corresponding Luttinger parameter [160] (see the Appendix B). Unfortunately, for the Creutz-Hubbard ladder, we have found that these oscillations are absent, such that the fitting procedure to extract the Luttinger parameter is not sufficiently accurate. We now provide an alternative route to extract the Luttinger parameter by exploring the quantum noise in models with a conserved quantity, such as the total fermion number $N = \sum_j \left(c^\dagger_{j,\mathrm{u}} c_{j,\mathrm{u}} + c^\dagger_{j,\mathrm{d}} c_{j,\mathrm{d}}\right)$ in the Creutz-Hubbard ladder (4.39). As first realized in [161], noise in certain quantum-transport scenarios can be directly related to entropic entanglement measures. In fact, for free-fermion systems [162], it can be shown rigorously that any Rényi EE (4.59) can be reconstructed from the knowledge of the noise cumulants for a certain bi-partition of the system. In free-fermion systems where the noise is purely Gaussian, it suffices to consider the second cumulant (i.e. variance) of the conserved quantity restricted to the bi-partition N_ℓ, which is sometimes referred to as the bi-partite fluctuations

$$S_n^{\mathrm{free}}(\ell, L) = \frac{\pi^2}{12}\left(1 + \frac{1}{n}\right)\mathcal{F}(\ell, L), \quad \mathcal{F}(\ell, L) = \langle (N_\ell - \langle N_\ell \rangle)^2 \rangle. \tag{4.63}$$

In the case of models that can be mapped onto the free-boson $c = 1$ CFT (i.e. Luttinger liquids), a similar expression holds as fluctuations are Gaussian [163]. The difference is that the Luttinger parameter also appears in the proportionality

$$S_n^{\mathrm{CFT}}(\ell, L) = \frac{\pi^2}{12K}\left(1 + \frac{1}{n}\right)\mathcal{F}(\ell, L). \tag{4.64}$$

Using the expression of the CFT prediction for the Renyi-entropy (4.61), one finds that the bi-partite fluctuations of a Luttinger liquid with conserved particle number should scale with the chord distance as follows

$$\mathcal{F}(\ell, L) = \frac{K}{\pi^2}\log(D(\ell, L)). \tag{4.65}$$

Accordingly, the bi-partite fluctuations of a critical Luttinger liquid also show an area-law violation, and one can use them to extract the underlying Luttinger parameter K [72].

It is worth mentioning that has been another method to extract K developed in [164].

In Fig. 4.8, we represent the Luttinger parameter K for the critical Creutz-Hubbard ladder in the thermodynamic limit. We modify the Hubbard interaction strengths V_{v}, and fix the energy imbalance $\Delta\epsilon$ to the RG-predicted value $\Delta\epsilon_{\mathrm{c}}$ of Eq. (4.55), such that the system lies at the critical line. The bi-partite fluctuations $\mathcal{F}(\ell, L)$ are numerically calculated using our MPS algorithm, and the value of K is extracted following the procedure detailed in the corresponding caption. As this figure shows, the Luttinger parameter remains very close to the value $K \approx 1$, which would correspond to a free massless Dirac fermion as the CFT controlling the critical scaling. Let us note, however, that this numerical procedure has turned out to be very sensitive to small variations of the parameters. The error bars displayed in Fig. 4.8 correspond to the Luttinger parameter obtained by modifying the energy imbalance within $(\Delta\epsilon_{\mathrm{c}} - 0.01t, \Delta\epsilon_{\mathrm{c}} + 0.01t)$ for 10 different values of $\Delta\epsilon$, and obtaining the standard deviation of all the corresponding Luttinger parameters K. Accordingly, although it seems that the Luttinger parameter remains at $K \approx 1$ as the interactions are increased, our numerical results are not conclusive, as minor modifications in $\Delta\epsilon$ can lead to large variations in K. In case $K = 1$ all along the critical line, the aforementioned differences might be caused by further non-universal and finite-size corrections. However, we note again that due to the sensitivity found in this problem, further numerical analysis shall be required in the future to clarify this point.

[72] After completion of the results presented in this manuscript, we learned of the recent paper [164], which also proposed a new method to extract the Luttinger Parameter with very good results.

Chapter 5

Gross-Neveu model

In the previous chapter we have seen that the topological phases are not only relevant in condensed matter systems but also arise in the context of high-energy physics for certain lattice formulation of quantum field theories (QFTs).

In this chapter, we focus on strongly-correlated SPT phases of a paradigmatic model of high energy physics: the Gross-Neveu model. This QFT describes Dirac fermions with N flavors interacting via quartic interaction in 1 spatial and 1 time dimension. It was originally introduced as a toy model that shares several fundamental features with quantum chromodynamics. We consider a Wilson type discretization of the QFT and term the lattice version as the Gross-Wilson model. In particular we will study the strongly-correlated SPT phases in the Gross-Neveu model using methods of contemporary theoretical physics and numerical simulations. Moreover we present a scheme for the experimental realization of this discretized QFT using cold-atom quantum simulators. In this way we hope that the Gross-Neveu model will get upgrade from a toy model used to understand same essential features of more realistic high-energy QFTs, into a corner stone in the classification of correlated topological phases of interest in condensed matter and quantum information, which can also be explored in a realistic experiment of atomic optical lattice.

5.1 High-energy physics, condensed matter and cold atoms

5.1.1 The Gross-Neveu quantum filed theory

The Gross-Neveu model is a relativistic QFT describing N species (flavors) of a massless Dirac field, which live in a (1+1)-dimensional spacetime and interact via four-fermion terms [136]. This model originates from its higher-dimensional counterparts, the so-called Nambu-Jona-Lasinio models [165, 166], which were introduced as alternatives to non-Abelian gauge theories [167]. Pre-dating quantum chromodynamics (QCD) [168, 169], these models offer a simplified framework to study essential features of the strong interaction, such as dynamical mass generation by chiral symmetry breaking. In addition to these features, the lower-dimensional Gross-Neveu model was introduced post-QCD as a tractable QFT displaying asymptotic freedom in a renormalizable framework. In contrast to some of its higher-dimensional cousins, this feature permits to derive rigorous results concerning the renormalization group and the convergence of perturbation theory [170–172].

In the continuum, this model is described by the following normal-ordered Hamil-

tonian $H = \int \mathrm{d}x : \mathcal{H}$: with

$$\mathcal{H} = -\sum_{n=1}^{N} \overline{\psi}_n(x) \mathrm{i}\gamma^1 \partial_x \psi_n(x) - \frac{g^2}{2N} \left(\sum_{n=1}^{N} \overline{\psi}_n(x) \psi_n(x) \right)^2 . \tag{5.1}$$

Here, $\psi_n(x), \overline{\psi}_n(x) = \psi_n^\dagger(x)\gamma^0$ are two-component spinor field operators for the n-th fermionic species, and $\gamma^0 = \sigma^z$, $\gamma^1 = \mathrm{i}\sigma^y$ are the gamma matrices, which can be expressed in terms of Pauli matrices for a (1+1)-dimensional Minkowski spacetime, leading to the chiral matrix $\gamma^5 = \gamma^0\gamma^1 = \sigma^x$ [1]. Therefore, the Gross-Neveu model describes a collection of N copies of massless Dirac fields coupled via the quartic interactions.

The first term in Eq. (5.1) corresponds to the kinetic energy of the massless Dirac fermions, where we use natural units $\hbar = c = 1$, whereas the second term describes two-body interactions between pairs of fermions that scatter off each other with a strength g^2/N. This model has a global, discrete chiral symmetry $\psi_n(x) \to \gamma^5 \psi_n(x)$, $\forall x$, as follows directly from the anti-commutation relations of the Dirac matrices. Additionally, a global $U(N)$ internal symmetry becomes apparent by introducing $\Psi(x) = (\psi_1(x), \cdots, \psi_N(x))^{\mathrm{t}}$, after rewriting the Gross-Neveu Hamiltonian density as

$$\mathcal{H} = -\overline{\Psi}(x) \mathrm{i}\gamma^1 \partial_x \Psi(x) - \frac{g^2}{2N} \left(\overline{\Psi}(x) \Psi(x) \right)^2 , \tag{5.2}$$

which is invariant under the transformation $\Psi(x) \to u \otimes \mathbb{I}_2 \Psi(x)$, $\forall x$, with the unitary matrix $u \in U(N)$. We note that the fields have classical mass dimension $d_\psi = 1/2$, while the interaction couplings are dimensionless $d_g = 0$.

In the limit where the number of flavors N is very large, D. J. Gross and A. Neveu showed that this model yields a renormalizable QFT displaying asymptotic freedom, i.e. the interaction strength g^2 is a relevant perturbation in the infra-red (IR), but becomes weaker at high energies in the ultra-violet (UV) limit [136]. Moreover, even if the discrete chiral symmetry prevents the fermions from acquiring a mass to all orders in perturbation theory, they showed that a mass can be dynamically generated through the spontaneous breaking of this chiral symmetry, which can be captured by large-N methods. In contrast to the Higgs mechanism, where masses can be generated by introducing additional scalar fields that undergo spontaneous symmetry breaking themselves, here a physical mass (i.e. gap) is generated dynamically as a non-perturbative consequence of the four-fermion interactions. These results are exact in the $N \to \infty$ limit, and it is possible to calculate the leading corrections for a finite, but still large, N.

A different strategy to explore such non-perturbative effects is the so-called lattice field theory (LFT), which discretizes the fermion fields on a uniform lattice $\Lambda_{\mathrm{s}} = a\mathbb{Z}_{N_{\mathrm{s}}} = \{x : x/a = n \in \mathbb{Z}_{N_{\mathrm{s}}}\}$, where N_{s} is the number of lattice sites, and a is the lattice spacing [104]. A naive discretization of the derivative of the Dirac operator

[1] In the Hamiltonian formulation, one also uses the Dirac matrices $\boldsymbol{\alpha}, \beta$, such that $\mathcal{H}_{\mathrm{D}}(x) = \sum_n \psi_n^\dagger(x)(\mathrm{i}\boldsymbol{\alpha} \cdot \boldsymbol{\nabla} + \beta m)\psi_n(x)$ [98]. In the one-dimensional case, one can chose $\alpha_x = \sigma^x$ and $\beta = \sigma^z$, such that the gamma matrices are defined as $\gamma^0 = \beta$ and $\gamma^1 = \beta\alpha_x = \mathrm{i}\sigma^y$. Accordingly, the chiral gamma matrix $\gamma^5 = \gamma^0\gamma^1 = \sigma^x$ coincides with the α_x Dirac matrix. The time-reversal T and charge-conjugation C matrices must fulfill $T\boldsymbol{\alpha}^* T^\dagger = -\boldsymbol{\alpha}$, $T\beta^* T^\dagger = \beta$, and $C\boldsymbol{\alpha}^* C^\dagger = \boldsymbol{\alpha}$, $C\beta^* C^\dagger = -\beta$ [98]. In $(3+1)$-dimensions, these equations are fulfilled by choosing $T = -\mathrm{i}\alpha_x\alpha_z$, and $C = \mathrm{i}\beta\alpha_y$. In the one-dimensional case, there is only one remaining Pauli matrix $\alpha_y = \sigma^y$, such that $C = \mathrm{i}\sigma^z\sigma^y = \gamma^5$. The time-reversal condition can be fulfilled by taking $\alpha_z = \sigma^y$, such that $T = -\mathrm{i}\sigma^x\sigma^y = \gamma^0$. The complete time-reversal, and charge-conjugation, anti-unitary operators lead to $\psi_n(x^0, \boldsymbol{x}) \to T\psi_n(-x^0, \boldsymbol{x})$, and $\psi_n(x^0, \boldsymbol{x}) \to C\psi_n^*(x^0, \boldsymbol{x})$, such that $\overline{\psi}_n\psi_n \to \overline{\psi}_n\psi_n$, and $\overline{\psi}_n\gamma^5\psi_n \to \mp\overline{\psi}_n\gamma^5\psi_n$ [97].

yields the Hamiltonian $H_{\rm N} = a\sum_{x\in\Lambda_{\rm s}} :\mathcal{H}_{\rm N}:$, which describes a system of interacting fermions hopping between neighboring sites of a one-dimensional lattice

$$\mathcal{H}_{\rm N} = \left(\overline{\Psi}(x)\frac{-i\gamma^1}{2a}\Psi(x+a) + \text{H.c.}\right) - \frac{g^2}{2N}\Big(\overline{\Psi}(x)\Psi(x)\Big)^2. \tag{5.3}$$

Here, the lattice fields fulfill the desired anti-commutation algebra in the continuum limit $\{\Psi_\mu(x), \Psi^\dagger_\nu(x')\} = \frac{1}{a}\delta_{\mu,\nu}\delta_{x,x'} \to \delta_{\mu,\nu}\delta(x-x')$ as $a\to 0$, where $\mu,\nu\in\{1,\cdots,2N\}$.

Unfortunately, this naive discretization also leads to spurious fermion doublers which, for $g^2 = 0$, correspond to massless Dirac fields appearing as long-wavelength excitations around the corners of the Brillouin zone [106]. In the present case, the Brillouin zone is $\text{BZ}_{\rm s} = \{k = 2\pi n/N_{\rm s}\} = (-\pi/a, \pi/a]$ such that, in addition to the target massless Dirac field around $k = 0$, a single doubler arises around the corner $k = \pi/a$ [173]. Note that, as soon as the interactions are switched on $g^2 > 0$, there will be scattering processes where the doubler affects the properties of the massless Dirac field, such that the continuum limit may differ from the desired QFT (5.1). Among several possible strategies to cope with the presence of such fermion doublers [104], K. Wilson considered introducing a momentum-dependent mass term, the so-called Wilson mass, that sends all the doublers to the cutoff of the lattice field theory [113]. In this way, one expects that these heavy fermions will not influence the universal long-wavelength properties of the continuum limit.

For the Hamiltonian QFT of interest (5.1), this can be accomplished by introducing an additional Wilson term in the naive discretization (5.3) leading to $H_{\rm W} = a\sum_{x\in\Lambda_{\rm s}} :\mathcal{H}_{\rm W}:$, where

$$\mathcal{H}_{\rm W} = \mathcal{H}_{\rm N} + \left(\overline{\Psi}(x)\frac{r}{2a}\big(\Psi(x) - \Psi(x+a)\big) + \text{H.c.}\right), \tag{5.4}$$

which will be referred to as the Gross-Neveu-Wilson (GNW) model in this work. Here, $r\in[0,1]$ is the so-called Wilson parameter. In the continuum limit, and for $g^2 = 0$, the mass of the doubler around $k = \pi/a$ becomes $m_\pi = 2r/a$, while the Dirac fermion around $k = 0$ remains massless $m_0 = 0$. We will set $r = 1$ henceforth, such that the doubler mass coincides with the UV energy cutoff of the QFT. On the other hand, the Dirac field around $k = 0$ remains massless, and one expects that the IR limit will be governed by the desired chiral-invariant QFT.

This situation gets more involved when the interactions are switched on $g^2 > 0$, as the additional Wilson terms (5.4) break explicitly the discrete chiral symmetry (i.e. $r\overline{\Psi}(x)\Psi(x) \to -r\overline{\Psi}(x)\Psi(x)$ under the discrete chiral transformation since $\gamma^5\gamma^0\gamma^5 = -\gamma^0$). Accordingly, the vanishing mass $m_0 = 0$ of the Dirac fermion around $k = 0$ is no longer protected by the discrete chiral symmetry, and it can become finite even for perturbative interactions in contrast to the continuum model. Since one is interested in recovering the QFT (5.1) for massless Dirac fermions, it is thus necessary to approach the continuum limit using a different strategy. The idea is to introduce an additional mass term in the lattice Hamiltonian (5.4) leading to $\tilde{H}_{\rm W} = a\sum_{x\in\Lambda_{\rm s}} :\tilde{\mathcal{H}}_{\rm W}:$, where we have introduced

$$\tilde{\mathcal{H}}_{\rm W} = \mathcal{H}_{\rm W} + m\overline{\Psi}(x)\Psi(x), \tag{5.5}$$

and m is a bare mass parameter. By tuning this mass as a function of the interaction strength $m(g^2)$, one must search for a critical line $m = m_{\rm c}(g^2)$ where the renormalized mass of the Dirac fermion around $k = 0$ vanishes $\tilde{m}_0 = 0$, such that the correlation length fulfills $\xi \gg a$ (i.e. a second-order quantum phase transition). In this case, the physical quantities of interest become independent of the underlying lattice, and

one expects to recover the desired continuum QFT. The key question is to analyze if such continuum scale-invariant limit corresponds to the chiral-invariant Gross-Neveu model (5.1), or if a QFT of a different nature emerges in the IR limit. The answer to this question may depend on the possible phases of the lattice field theory (5.4) and the different critical lines in between them. Therefore, addressing this question requires a detailed non-perturbative approach using for instance large-N methods on the lattice, or Monte-Carlo methods from lattice field theory. In this work, we will present a detailed large-N analysis of the lattice GNW model, applying it to the prediction of its phase diagram, and benchmarking it with numerical simulations for the $N = 1$ single-flavour case.

5.1.2 Symmetry-protected topological phases for interacting fermions

A wide variety of phases transitions can be understood according to Landau's theory of spontaneous symmetry breaking [1], which exploits the notion of symmetry and local order parameters to classify various phases of matter. Nowadays, we understand that Landau's theory does not exhaust all possibilities, as one can find different phases of matter within the same symmetry class that can only be connected via phase transitions where the symmetry is not broken. These so-called symmetry-protected topological (SPT) phases cannot be described by local order parameters, but require instead the use of certain topological invariants to characterize their groundstate (e.g. topological insulators and superconductors [5, 13] described in sec. 2.5.1 and 2.5.2). These topological invariants are in turn related to observables displaying quantized values that are robust with respect to perturbations that respect these symmetries (i.e. the topological numbers can only change via a gap-closing phase transition). Accordingly, these new phases of matter can be organized within different symmetry classes, as occurs for the fermionic topological insulators [94,99]. Despite having a gapped bulk, these insulators display a quantized conductance (e.g. integer quantum Hall effect [8] presented in sec. 2.1) related to a topological invariant (e.g. first Chern number [11] mentioned in sec. 2.4.2). A bulk-edge correspondence allows to understand this topological robustness by the appearance of current-carrying edge excitations through a band-inversion process, corresponding to mid-gap states that are exponentially localized within the boundaries of the material (e.g. one-dimensional edge modes where fermions cannot back-scatter due to disorder [174]).

The connection between SPT phases and LFTs is very natural for three-dimensional time-reversal-invariant topological insulators [5]. Here, the band-inversion process yielding the topological phase leads to an odd number of massless Dirac fermions localized within the boundaries of the material. As emphasized in [95, 175], this band inversion can be understood in terms of lower-dimensional versions of domain-wall fermions [108], whereby an odd number of Wilson doubler masses change their sign, contributing each with a two-dimensional massless Dirac fermion localized at the boundary. In fact, we note that the Wilson-like terms in Eq. (5.4) arise very naturally in the low-energy description of topological insulating materials in various dimensionalities [13].

Let us now discuss how these topological effects also appear in the non-interacting limits of the GNW model (5.3)-(5.5). Here, the band inversion would occur when tuning the bare mass to lie within $m \in (m_\pi, m_0)$, where we recall that $m_0 = 0$ and $m_\pi = 2/a$ correspond to the masses of the Wilson fermions. To understand the SPT phase in this LFT, we consider periodic boundary conditions, such that the Hamiltonian in momentum space is $\tilde{H}_{\rm W} = \sum_{n=1}^{N} \sum_{k \in {\rm BZ_s}} \psi_n^\dagger(k) \mathsf{h}_k(m) \psi_n(k)$, where we have introduced

the flavor-independent single-particle Hamiltonian

$$\mathsf{h}_k(m) = \left(m + \frac{1-\cos ka}{a}\right)\gamma^0 - \frac{\sin ka}{a}\gamma^5. \tag{5.6}$$

By a straightforward diagonalization, one finds

$$\tilde{H}_{\mathrm{W}} = \sum_{n=1}^{N}\sum_{k\in \mathrm{BZ_s}}\sum_{\eta=\pm}\epsilon_\eta(k)\psi^\dagger_{n,\eta}(k)\psi_{n,\eta}(k), \tag{5.7}$$

where $\psi^\dagger_{n,\eta}(k), \psi_{n,\eta}(k)$ are the creation-annihilation operators of a fermionic excitation with flavor n in the energy band

$$\epsilon_\pm(k) = \pm\frac{1}{a}\sqrt{(ma+1-\cos ka)^2 + \sin^2 ka}. \tag{5.8}$$

This band structure has a non-zero gap for $m > 0$, yielding an insulating phase. In order to show that this insulator is topological, and an instance of a SPT phase, we note that this band structure has an associated topological invariant that can be defined through the Berry connection $\mathcal{A}_n(k) = \mathrm{i}\langle\epsilon_{n,-}(k)|\partial_k|\epsilon_{n,-}(k)\rangle$, where we have introduced the single-particle negative-energy states $|\epsilon_{n,-}(k)\rangle = \psi^\dagger_{n,-}(k)|0\rangle$. In our case (5.6), the Berry connection can be expressed as

$$\mathcal{A}_n(k) = \frac{1}{2}\frac{(1+ma)\cos ka - 1}{1+(1+ma)^2 - 2(1+ma)\cos ka}, \tag{5.9}$$

which allows to construct a topological invariant, the so-called Zak's phase [135], as the integral of the Berry connection over the Brillouin zone. From Eq. (5.9), the total Zak's phase $\varphi_{\mathrm{Zak}} = \sum_n \int_{\mathrm{BZ_s}} \mathrm{d}k\mathcal{A}_n(k)$ can be expressed as

$$\varphi_{\mathrm{Zak}} = N\pi\big(\theta(2+ma) - \theta(ma)\big), \tag{5.10}$$

where $\theta(x)$ is Heaviside's step function. We note that, as occurs with the Chern number and the transverse conductivity in the quantum Hall effect [11], the topological Zak's phase can be related to an observable: the electric polarization [176–178].

Since the groundstate is constructed by filling all negative-energy states $|\mathrm{gs}\rangle = \prod_{k\in\ \mathrm{BZ_s}}|\epsilon_-(k)\rangle$, the above integral over the whole Brillouin zone (5.10) characterizes the topological features of the LFT groundstate. Accordingly, this LFT hosts a SPT phase in the parameter regime $m_\pi < m < m_0$ for N odd, which coincides with the band-inversion regime introduced above. This regime can be interpreted as the result of a mass-inversion process, whereby the mass of some of the Wilson fermions gets inverted. This becomes apparent after rewriting the Zak's phase in terms of the N Wilson masses

$$\tilde{m}_0 = m, \quad \tilde{m}_\pi = m + 2/a. \tag{5.11}$$

Indeed, a non-trivial topological invariant (i.e. $\varphi_{\mathrm{Zak}}/2\pi \notin \mathbb{Z}$) can only be achieved when an odd number of fermion doubler pairs display a different mass sign

$$\varphi_{\mathrm{Zak}} = \tfrac{1}{2}N\pi\big(\mathrm{sgn}(\tilde{m}_\pi) - \mathrm{sgn}(\tilde{m}_0)\big). \tag{5.12}$$

We note that this SPT phase can be identified with a one-dimensional topological insulator in the so-called chiral-orthogonal BDI class [13, 94, 99] (see sec. 2.3), which would display zero-energy modes localized at the edges of the chain for open boundary

conditions. Note that this chiral symmetry class is not related to the standard notion of chirality in QCD, which is indeed broken by the GNW model. Instead, it is related to the ten-fold Cartan's classification of symmetric spaces, and its connection to single-particle Hamiltonian via the time-evolution operator [99]. For the non-interacting GNW single-particle Hamiltonian (5.6), we find that time-reversal T yields $T^\dagger h_{-k}(m)^* T = h_k(m)$ where $T = -\mathrm{i}\sigma^x\sigma^y = \gamma^0$, and charge-conjugation C leads to $C^\dagger h_{-k}(m)^* C = -h_k(m)$ where $C = \mathrm{i}\sigma^z\sigma^y = \gamma^5$. The combination of these two anti-unitary symmetries is called chiral, or sub-lattice, symmetry $\mathsf{S} = \mathsf{TC}$, and yields $S^\dagger h_k(m) S = -h_k(m)$ with $S = \gamma^0\gamma^5 = \gamma^1$. To avoid confusion with the chiral symmetry of high-energy physics, which is a fundamental ingredient in low-energy effective descriptions of QCD, and pivotal in our previous discussion of the GNW model, we will refer to the S as the sublattice symmetry. Since $T^2 = C^2 = S^2 = +1$, the corresponding GNW topological insulator with an odd number N of fermion flavors (5.12) is in the BDI class.

We note that the ten symmetric spaces that classify the topological insulators/superconductors also correspond to the target spaces of effective non-linear-sigma model describing the long-wavelength properties of the edge/boundary. When such a non-linear-sigma model includes a topological term, the edge modes are robust and evade Anderson localization in the presence of symmetry-preserving disorder [99]. This perspective allows us to understand the difference of N even/odd in the GNW model. For N even, there can be a symmetry-preserving disorder that couples the different flavors of the edge states, leading to scattering/localization and destroying the BDI topological protection. On the other hand, for N odd, at least one of the edge modes will remain robust against inter-flavor scattering, and thus evade Anderson localization. We note that similar parity effects can occur also in models with more than one fermion doubler in the regime where an even number of Wilson masses gets inverted, as occurs for higher-dimensional time-reversal topological insulators [95].

In contrast to the LFT perspective described in Sec. 5.1.1, where one is mainly interested in searching for the second-order quantum phase transitions to recover a continuum limit described by the QFT of interest (5.1); the study of symmetry-protected topological phases focuses on the topological gapped phases away from criticality. Interestingly, even in the non-interacting regime, the emerging QFTs governing their response to external fields turns out to be very different from the original discretized QFT, and can be described in terms of topological quantum field theories (e.g. Chern-Simons or axion QFTs) [93]. A generic question of current interest in the study of SPT phases is to explore the interplay of topological features and strong-correlation effects as interactions between the fermions are switched on [117].

For the GNW lattice model (5.3)-(5.5), the interactions do not modify the symmetry class as $\overline{\Psi}\Psi \to \overline{\Psi}\Psi$, and $\overline{\Psi}\gamma^5\Psi \to \mp\overline{\Psi}\gamma^5\Psi$ under time-reversal and charge-conjugation transformations, respectively. Accordingly, the quartic terms in Eq. (5.2), or its chiral extension introduced in Eq. (5.16) below, do not modify the aforementioned BDI symmetry class. A question of potential interest for both the SPT and LFT communities is the precise determination of the critical lines of the lattice model $m_c(g^2)$ for non-perturbative interactions. From this knowledge, the LFT community can explore the nature of the continuum QFT in the vicinity of the critical line, while the SPT community may study how the topological phase is modified in presence of interactions. As argued above, a possible tool to study non-perturbative effects could be large-N methods, or Monte-Carlo methods in Euclidean lattice field theory. We remark, however, that the standard Euclidean approach where time is also discretized [104] can lead to qualitative differences of the phase diagram in the (m, g^2) plane. Discretizing time

introduces additional fermion doublers, which may lead to additional critical lines that are not present in the Hamiltonian approach (5.3)-(5.5) with continuous time [179]. Although this is not relevant when one is only interested in the nature of the continuum QFT, it will be of relevance for topological insulators where one is interested in the finite region of phase space with the topological gapped phase. In this work, we will show that special care in the Euclidean lattice formulation is required in order to recover the relevant phase diagram.

For one-dimensional models, the study of lattice field theories in the Hamiltonian approach can be efficiently accomplished using variational methods based on Matrix Product States (MPS) [180–184]. In this work, we shall confront predictions of the large-N approximation with results from MPS numerical methods for the study of topological insulating phases in the GNW model with Wilson fermions.

5.1.3 Cold atoms quantum simulators of high-energy physics

As an alternative to Monte-Carlo numerical methods in lattice field theory, one may follow R. P. Feynman's insight [16], and develop schemes to control a quantum-mechanical device such that its dynamics reproduces faithfully that of the model of interest (i.e. quantum simulation). From this perspective, a very appealing application of the future fault-tolerant quantum computers will be their ability to function as universal quantum simulators [17] that can address complicated quantum many-body problems relevant for different disciplines of physics and chemistry. Prior to the development of quantum error correction and large-scale fault-tolerant quantum computers, one may consider building special-purpose quantum simulators that are designed to tackle a particular family of models. This is the case of cold-atom quantum simulators of lattice models [18, 19] discussed in sec. 2.6, where neutral atoms are laser-cooled to very low temperatures in deep optical lattices [20].

In the continuum, neutral-atom systems are typically described by a Hamiltonian QFT, albeit a non-relativistic one [20], with $H = \int d^3x : (\mathcal{H}_0 + \mathcal{V}_{\rm I}) :$ containing

$$\mathcal{H}_0 = \sum_{n,\sigma} \Psi^\dagger_{n,\sigma}(\boldsymbol{x}) \left(\left(\frac{-\nabla^2}{2m_n} + \epsilon^n_\sigma \right) \delta_{\sigma,\sigma'} + V^n_{\sigma,\sigma'}(\boldsymbol{x}) \right) \Psi_{n,\sigma'}(\boldsymbol{x}), \tag{5.13}$$

where $\Psi^\dagger_{m,\sigma}(\boldsymbol{x}), \Psi_{m,\sigma}(\boldsymbol{x})$ are field operators that create-annihilate an atom of the n-th species in the internal state σ. This Hamiltonian contains *(i)* the kinetic energy for a multi-species gas of Alkali atoms of mass m_n, where $n \in \{1, \cdots N_{\rm sp}\}$ labels the atomic species/isotope; *(ii)* the internal energy ϵ^n_σ of the atomic groundstate manifold, which typically consists of various hyperfine levels characterized by the quantum numbers associated to the total angular momentum $\sigma \in \{F, M_F\}$; and *(iii)* the single-particle terms $V^{\sigma,\sigma'}_n(\boldsymbol{x})$, which contain the trapping potential that confines the n-th atomic species and, possibly, additional radiation-induced terms that drive transitions between the different atomic levels $\sigma \to \sigma'$. In particular, we shall be interested in periodic trapping potentials due to the ac-Stark-shift of pairs of retro-reflected laser beams, which will depend on the atomic species, but not on the particular hyperfine level (i.e. state-independent optical lattices). We also consider laser-induced Raman transitions via highly off-resonant excited states. Altogether, this leads to

$$\begin{aligned} V^n_{\sigma,\sigma'}(\boldsymbol{x}) = & \sum_{\nu=x,y,z} \left(V^n_{0,\nu} \sin^2(k_{{\rm L},\nu} x_\nu) + \tfrac{1}{2} m_n \omega^2_{n,\nu} x^2_\nu \right) \delta_{\sigma,\sigma'} \\ & + \sum_l \Omega^{n,l}_{\sigma,\sigma'} \cos(\boldsymbol{\Delta k}_l \cdot \boldsymbol{x} - \Delta\omega_l t + \varphi_l), \end{aligned} \tag{5.14}$$

where $V^n_{0,\nu}$ is the ac-Stark shift for the n-th atomic species stemming from the retro-reflected beams with wave-vector $k_{\mathrm{L},\nu}$ along the ν-axis. Additionally, $\omega_{n,\nu}$ is the frequency of a residual harmonic trapping due to the intensity profile of the lasers. Finally, $\Omega^{n,l}_{\sigma,\sigma'}$ is the two-photon Rabi frequency for the Raman transition induced by the l-th pair of laser beams with wave-vector (frequency) difference $\boldsymbol{\Delta k}_l$ ($\Delta\omega_l$), and phase φ_l.

In addition, at sufficiently low temperatures, the neutral atoms also interact by contact scattering processes leading to

$$\mathcal{V}_{\mathrm{I}} = \frac{1}{2}\sum_{\sigma,\sigma'}\sum_{n,n'} U^{n,n'}_{\sigma,\sigma'}\Psi^{\dagger}_{n,\sigma}(\boldsymbol{x})\Psi^{\dagger}_{n,'\sigma'}(\boldsymbol{x})\Psi_{n',\sigma'}(\boldsymbol{x})\Psi_{n,\sigma}(\boldsymbol{x}), \tag{5.15}$$

where the interaction strengths $U^{n,n'}_{\sigma,\sigma'}$ depends on the s-wave scattering lengths $a_{\sigma\sigma'}$ of the corresponding channels, some of which can be controlled by Feshbach resonances [20]. We also note that fully-symmetric interactions between all species can be achieved by using alkali-earth atoms [185], which could be an interesting property for the experimental realization of higher number of flavors N in the Gross-Neveu-Wilson model.

As announced above, in the regime of deep optical lattices $V^n_{0,\nu} \gg E^n_{\mathrm{R}} = \boldsymbol{k}^2_{\mathrm{L}}/2m_n$, one can introduce the basis of so-called Wannier functions, which are localized to the minima of the potential, and show that this non-relativistic QFT yields a family of Hubbard-type models with tunable parameters [30, 186–190]. Therefore, by doing controlled table-top experiments with cold atoms, it becomes possible to explore the physics of strongly-correlated electrons in solids, which has opened a fruitful avenue of research in quantum simulations of condensed-matter models [18, 19]. More recently, several works have explored the possibility of extending this cold-atom Hubbard toolbox [31] to the quantum simulation of high-energy physics, including relativistic QFTs [95, 191–198], gauge field theories [199–204], theories for coupled Higgs and gauge fields [205–209], and also theories of relativistic fermions interacting with Abelian/non-Abelian gauge fields [210–217].

In this work, we shall be concerned with a cold-atom realization of the Gross-Neveu model using a Wilson-fermion discretization (5.3)-(5.5). We note that there are cold-atom proposals to implement this QFT (5.1) with optical superlattices lattices by a different discretization [194], via the so-called staggered fermions [173, 179]. Since we are interested in the connection of this model with correlated SPT phases, we will instead focus on the Wilson-fermion approach of Eqs. (5.3)-(5.5). Building on previous proposals for the quantum simulation of Wilson fermions [59, 95, 218, 219], we present in this work a simplified scheme to realize the GNW model using a two-component single-species Fermi gas confined in a one-dimensional optical lattice with laser-assisted tunneling.

5.2 Large-N expansion phase diagram

As advanced in the previous sections, our goal is to determine the critical lines of the GNW model (5.3)-(5.5) as a function of the coupling strength $m(g^2)$ for non-perturbative interactions. We start by developing a large-N expansion for the partition function $Z = \mathrm{Tr}\left\{\exp\left(-\beta\tilde{H}_{\mathrm{W}}\right)\right\}$, where $\beta = 1/T$ is the inverse temperature for $k_{\mathrm{B}} = 1$. In the continuum, large-N methods were first employed by Gross and Neveu to prove that the groundstate of their eponymous model (5.1) displays a non-zero vacuum expectation value $\sigma_0 = \langle\overline{\Psi}(x)\Psi(x)\rangle \neq 0\ \forall x$, as soon as a non-vanishing interaction $g^2 >$

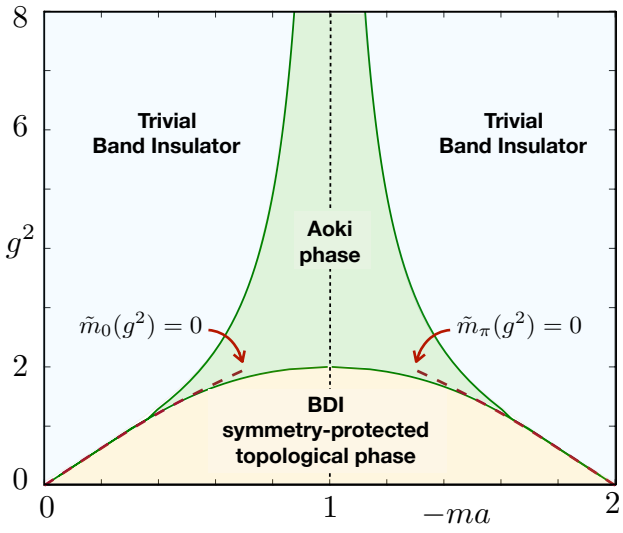

Figure 5.1: **Symmetry-protected topological phases in the lattice Gross-Neveu model from large-N methods:** The two green solid lines correspond to the critical lines $m_c(g^2)$ obtained from the numerical solution of the gap equations (5.24), while the red dashed lines corresponds to the analytical solution obtained from the vanishing of the dynamically-generated (5.29) Wilson masses (5.32). The identification of the different regions as a trivial and topological insulators, or as the Aoki phase, follows our discussion below Eq. (5.32).

0 is switched on [136]. In this way, the discrete chiral symmetry $\Psi(x) \to \mathbb{I}_N \otimes \gamma^5 \Psi(x)$ gets spontaneously broken, since $\sigma_0 = \langle \Psi^\dagger(x)\gamma^0\Psi(x)\rangle \to -\langle \Psi^\dagger(x)\gamma^0\Psi(x)\rangle = -\sigma_0$ is no longer fulfilled when the vacuum expectation value is developed.

This non-perturbative result can be obtained using functional techniques to calculate an effective action for an auxiliary bosonic $\sigma(x)$ field, which condenses due to the formation of particle–anti-particle pairs, and acquires a non-zero expectation value $\langle\sigma(x)\rangle = \sigma_0 \neq 0$ in the chirally-broken phase. On the lattice (5.3)-(5.4), similar results are recovered in the continuum limit [220, 221], provided that the additional bare mass (5.5) is adjusted to recover the discrete chiral symmetry.

Let us now comment on a generalization of the GNW model, where the above discrete chiral symmetry is upgraded to a continuous one $\Psi(x) \to \mathbb{I}_N \otimes e^{i\theta\gamma^5}\Psi(x)$, $\forall\theta \in [0, 2\pi)$ [136]. This requires a modified four-fermion term

$$\mathcal{H} = -\overline{\Psi}(x)\mathrm{i}\gamma^1\partial_x\Psi(x) - \frac{g^2}{2N}\Big((\overline{\Psi}\Psi)^2 - (\overline{\Psi}\gamma^5\Psi)^2\Big). \tag{5.16}$$

In this case, in addition to the $\sigma(x)$ field, it is natural to introduce an additional bosonic field $\Pi(x)$, obtaining an effective action for both fields in the large-N limit. In Ref. [222, 223], S. Aoki showed that the large-N results with lattice Wilson fermions lead to a richer phase diagram displaying new regions where a discrete parity symmetry $\Psi(x) \to \eta\mathbb{I}_N \otimes \gamma^0\Psi(-x)$, where $|\eta|^2 = 1$, can also be spontaneously broken $\Pi_0 = \langle\overline{\Psi}(x)\mathrm{i}\gamma^5\Psi(x)\rangle \neq 0\ \forall x$. In this case, the particle–anti-particle pairs lead to the so-called pseudoscalar condensate $\langle\Pi(x)\rangle = \Pi_0 \neq 0$, which necessarily breaks the parity transformation of the corresponding fermion bilinear due to the vacuum expectation value $\Pi_0 = \langle\overline{\Psi}(x)i\gamma^5\Psi(x)\rangle \to -\langle\overline{\Psi}(-x)\mathrm{i}\gamma^5\Psi(-x)\rangle = -\Pi_0$. Interestingly, these results on the chiral GNW model were used to conjecture that these so-called Aoki phases

would also appear in the phase diagram of lattice quantum chromodynamics [222,223]. However, in this context, these Aoki phases are considered as unphysical lattice artifacts not present in the continuum QFT.

In this section, we discuss the role of such Aoki phases in the GN model (5.16) with a Wilson-type discretization (5.3)-(5.5), and their interplay with the topological insulating phases discussed in the previous sections. In the context of symmetry-protected topological phases, such Aoki phases are not artifacts, but become instead physical phases of matter that shall delimit the region of the phase diagram that hosts a correlated SPT phase. Moreover, from the perspective of a cold-atom implementation, these phases might also be observed in future table-top experiments. We also note that the appearance of Aoki phases is not restricted to the GNW model, but also occurs in strong-coupling calculations of $U(1)$ Wilson-type lattice gauge theories [175,224], which can be used to model the strongly-interacting limit of higher-dimensional topological insulators with long-range Coulomb interactions.

We remark that, in the limit of a single fermion flavor $N = 1$, which is the relevant case for the cold-atom implementation, the four-fermion interactions of Eq. (5.3) can be rewritten as

$$V_g = -\sum_{x\in\Lambda_\mathrm{s}} a\frac{g^2}{4N} :\!\left(\left(\overline{\Psi}(x)\Psi(x)\right)^2 - \left(\overline{\Psi}(x)\gamma^5\Psi(x)\right)^2\right)\!:, \tag{5.17}$$

which follows from a so-called Fierz identity in the language of relativistic QFTs. Accordingly, besides a change in the coupling constant $g^2 \to g^2/2$, there is no further distinction between the $N = 1$ GNW model with discrete or continuous symmetry, such that the previous Aoki phases could in principle also occur in this limiting case. However, since their prediction is based on the $N \to \infty$ results, we will have to benchmark large-N methods with other non-perturbative approaches valid for $N = 1$ (e.g. MPS numerical simulations or a potential cold-atom quantum simulation). Regarding the first approach, and give a detailed comparison of the large-N predictions with the MPS results of the phase diagram.

5.2.1 Continuous time: Hamiltonian field theory on the lattice

Let us first discuss the large-N phase diagram of the GNW model using a functional-integral representation of the partition function with a continuum Euclidean (i.e. imaginary) time τ. Introducing fermionic coherent states by means of mutually anti-commuting Grassmann variables $\Psi_k(\tau), \Psi_k^\star(\tau)$, which are defined at each point of the Brilllouin zone $k \in \mathrm{BZ_s}$ and for each imaginary time $\tau \in (0, \beta)$ [2], one can readily express the finite-temperature partition function as $\mathsf{Z} = \int [\mathrm{d}\Psi^\star \mathrm{d}\Psi] e^{-S_\mathrm{W}[\Psi^\star,\Psi]}$, where the Euclidean action is

$$S_\mathrm{W} = \int_0^\beta \mathrm{d}\tau \left(\sum_{k\in\mathrm{BZ_s}} \Psi_k^\star(\tau) \left(\partial_\tau + \mathsf{H}_k(m)\right) \Psi_k(\tau) + V_g(\Psi^\star, \Psi) \right). \tag{5.18}$$

Here, $\mathsf{H}_k(m) = \mathbb{I}_N \otimes \mathsf{h}_k(m)$ is defined in terms of the single-particle Hamiltonian in Eq. (5.6). Moreover, $V_g(\Psi^\star, \Psi)$ results from substituting the fermion field operators

[2] We use the notation $\Psi_k^\star(\tau)$ for the Grassmann variable associated to $\Psi_k^\dagger$, and refrain from using $\overline{\Psi}_k(\tau)$ to avoid possible confusions when comparing the functional approaches based on Hamiltonian and Euclidean lattice field theories.

by the Grassmann variables in the normal-ordered interaction (5.17), which leads to quartic interactions

$$V_g = -\sum_{x\in\Lambda_\mathrm{s}} a\frac{g^2}{4N}\left(\left(\Psi_x^\star(\tau)\gamma^0\Psi_x(\tau)\right)^2 - \left(\Psi_x^\star(\tau)\gamma^1\Psi_x(\tau)\right)^2\right), \tag{5.19}$$

Let us note that the propagator associated to the free part of the action displays two poles at $k \in \{0, \pi/a\}$ when $-ma \in \{0, 2\}$, which correspond to the aforementioned Dirac fermions around the corners of the Brillouin zone.

The first step in the large-N approximation is to introduce two auxiliary real scalar fields $\sigma(x), \Pi(x)$ with classical mass dimension $d_\sigma = d_\Pi = 1$, such that the partition function can be expressed as a new functional integral over both Grassmann and real auxiliary fields $\mathsf{Z} = \int[\mathrm{d}\Psi^\star\mathrm{d}\Psi\mathrm{d}\sigma\mathrm{d}\Pi]e^{-\tilde{S}_\mathrm{W}[\Psi^\star,\Psi,\sigma,\Pi]}$. Therefore, the new Euclidean action must fulfill $\int[\mathrm{d}\sigma\mathrm{d}\Pi]e^{-\tilde{S}_\mathrm{W}[\Psi^\star,\Psi,\sigma,\Pi]} = e^{-S_\mathrm{W}[\Psi^\star,\Psi]}$ up to an irrelevant constant, such that the thermodynamic properties of the system are not modified by the introduction of the auxiliary fields. The idea is to chose a particular action where the four-fermion terms can be understood as effective interactions carried by the auxiliary bosonic fields. Moreover, assuming that these fields are homogeneous, the new action becomes

$$\tilde{S}_\mathrm{W} = \int_0^\beta \mathrm{d}\tau\left(\sum_{k\in\mathrm{BZ}_\mathrm{s}} \Psi_k^\star(\tau)\left(\partial_\tau + \tilde{\mathsf{H}}_k\right)\Psi_k(\tau) + N\frac{N_\mathrm{s}a}{g^2}(\sigma^2+\Pi^2)\right), \tag{5.20}$$

where $\tilde{\mathsf{H}}_k = \mathbb{I}_N \otimes \tilde{\mathsf{h}}_k$, and the fermionic single-particle Hamiltonian now depends on the auxiliary bosonic fields

$$\tilde{\mathsf{h}}_k = \left(m + \sigma + \frac{1-\cos ka}{a}\right)\gamma^0 - \frac{\sin ka}{a}\gamma^5 + \mathrm{i}\Pi\gamma^1. \tag{5.21}$$

Essentially, the σ field modifies the mass term of the Dirac fermion, and a vacuum expectation value of the former would thus renormalize the fermion mass, resembling the dynamical mass generation of the continuum model.

The second step in the large-N approximation is to integrate over the fermionic Grassmann fields, obtaining an effective action for the auxiliary bosons $\mathsf{Z} = \int[\mathrm{d}\sigma\mathrm{d}\Pi]e^{-NS_\mathrm{eff}[\sigma,\Pi]}$. This step can be readily performed since the Grassmann integral is Gaussian, which leads to

$$S_\mathrm{eff} = \beta L\left(\frac{1}{g^2}\left(\sigma^2+\Pi^2\right) - \int_{k,\omega}\log\left(\omega^2 + \epsilon_k^2(m+\sigma,\Pi)\right)\right), \tag{5.22}$$

where $L = N_\mathrm{s}a$ is the length of the chain, and we have introduced an abbreviation for the integral over momentum and Matsubara frequencies $\int_{k,\omega} = \int_{\mathrm{BZ}_\mathrm{s}}\frac{\mathrm{d}k}{2\pi}\int_{-\infty}^{\infty}\frac{\mathrm{d}\omega}{2\pi}$, assuming already the zero-temperature limit which is the regime of interest of this work. Here, the energies of the new fermionic single-particle Hamiltonian $\epsilon_k(m+\sigma,\Pi)$ have been expressed in terms of the function

$$\epsilon_k(x,y) = \frac{1}{a}\sqrt{(xa+1-\cos ka)^2 + \sin^2 ka + (ya)^2}. \tag{5.23}$$

When the number of fermion flavors is very large $N \to \infty$, the partition function $\mathsf{Z} = \int[\mathrm{d}\sigma\mathrm{d}\Pi]e^{-NS_\mathrm{eff}[\sigma,\Pi]}$ with the effective action (5.22) yields a groundstate obtained from the saddle point equations $\partial_\sigma S_\mathrm{eff}|_{(\sigma_0,\Pi_0)} = \partial_\Pi S_\mathrm{eff}|_{(\sigma_0,\Pi_0)} = 0$. Non-vanishing values of σ_0, Π_0 are related to the breaking of the discrete chiral or parity symmetries discussed above. For instance, the boundary of the aforementioned Aoki phases can

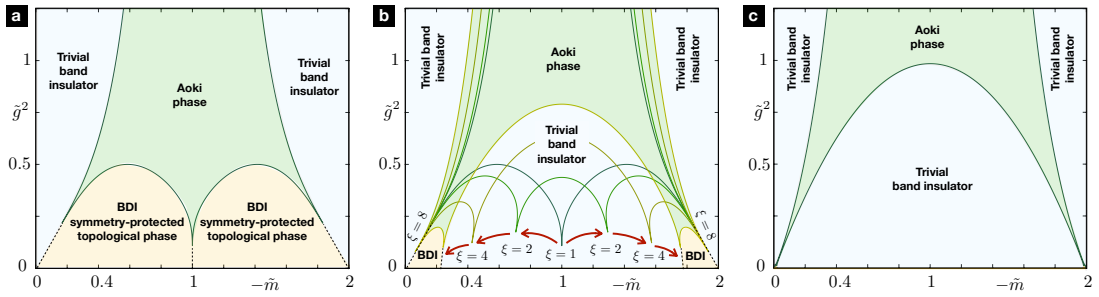

Figure 5.2: **Symmetry-protected topological phases in the Gross-Neveu model on anisotropic Euclidean lattices:** Large-N phase diagram obtained from the self-consistent solution of Eqs. (5.40)-(5.41) on: **(a)** Isotropic Euclidean lattice $\xi = 1$ with $N_\tau = N_\mathrm{s} = 512$ sites (i.e. square lattice). In comparison to the continuum-time phase diagram of Fig. 5.1, one observes that the region of the symmetry-protected topological phase (shaded yellow area) is deformed into a pair of lobes, each of which contains an BDI topological insulator in the space-like dimension. The Aoki phase (green area) adopts a trident-like shape. **(b)** Sequence of anisotropic Euclidean lattices with $N_\mathrm{s} = N_\tau/\xi = 512$ sites, and $\xi = 1, 2, 4, 8$ (i.e. rectangular lattices). The solid lines represent how the boundary of the Aoki phase gets distorted as the anisotropy increases. The two BDI topological-insulating lobes shrink and move in opposite directions, leaving an intermediate lobe hosting a trivial band insulator. **(c)** Anisotropic Euclidean lattice with $\xi = 128$, showing the fate of the topological phases in the continuum limit.

be obtained from the self-consistent solution of these saddle-point equations imposing $\Pi_0 = 0$. Using contour techniques for the frequency integrals, and substituting $ka \to k$ in the momentum integrals, we can express the pair of saddle-point equations as follows

$$\frac{1}{g^2} = \frac{\mathsf{K}(\theta_0)}{\pi(1+\eta_0)}, \qquad ma = \frac{(1-\eta_0)^2}{2\eta_0} - \frac{g^2}{2\pi}\frac{(1+\eta_0)}{\eta_0}\mathsf{E}(\theta_0). \tag{5.24}$$

Here, we have used the complete elliptic integrals of the first and second kind

$$\mathsf{K}(x) = \int_0^{\frac{\pi}{2}} \frac{\mathrm{d}k}{\sqrt{1 - x\sin^2 k}}, \quad \mathsf{E}(x) = \int_0^{\frac{\pi}{2}} \mathrm{d}k \sqrt{1 - x\sin^2 k}, \tag{5.25}$$

as well as the following parameters

$$\eta_0 = 1 + ma + \sigma_0 a, \quad \theta_0 = \frac{4\eta_0}{(1+\eta_0)^2}. \tag{5.26}$$

In general, the solution of the pair of gap equations (5.24) must be performed numerically, and leads to the critical lines that delimit the Aoki phase (i.e. solid green lines in Fig. 5.1). These lines can be interpreted as different flows of the bare mass $m_\mathrm{c}(g^2)$ that determine the second-order phase transitions where a scale-invariant QFT should emerge. Note that this figure displays a clear reflection symmetry with respect to the axis $-ma = 1$. In fact, using the expression of the elliptic integrals in terms of hypergeometric functions [225], it follows that $\mathsf{K}(x) = (1-x)^{-1/2}\mathsf{K}(x/(x-1))$, and $\mathsf{E}(x) = (1-x)^{1/2}\mathsf{E}(x/(x-1))$, which can be exploited to show that the gap equations (5.24) can be rewritten as

$$\frac{1}{g^2} = \frac{\mathsf{K}\left(\frac{\theta_0}{\theta_0 - 1}\right)}{\pi(1-\eta_0)}, \quad ma = \frac{(1-\eta_0)^2}{2\eta_0} - \frac{g^2}{2\pi}\frac{(1-\eta_0)}{\eta_0}\mathsf{E}\left(\frac{\theta_0}{\theta_0 - 1}\right). \tag{5.27}$$

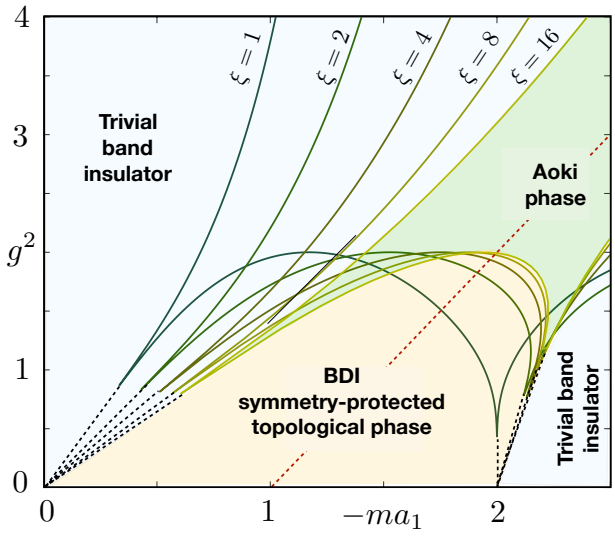

Figure 5.3: **Phase diagram in the Euclidean lattice Gross-Neveu model with rescaled couplings:** The solid lines delimiting the Aoki phase with rescaled couplings (5.43) get distorted as the anisotropy parameter increases $\xi \in \{1, 2, 4, 8, 16\}$, and display a finite lobe hosting the symmetry-protected topological phase even in the continuum limit. As ξ is increased, the BDI topological insulator and the Aoki phase display a mirror symmetry with respect to the red dashed line.

These gap equations can now be related to the original ones in Eq. (5.24) under the following transformation

$$ma \to -2 - ma, \quad \sigma_0 \to -\sigma_0, \tag{5.28}$$

which corresponds to the aforementioned reflection symmetry about $-ma = 1$, and leads to $\eta_0 \to -\eta_0$ and $\theta_0 \to \theta_0/(\theta_0 - 1)$. Accordingly, there should only be three distinct phases in the regime $-ma \in [0, 2]$, with the Aoki phase being completely absent for $ma > 0$ and $ma < -2$.

To make a connection to the continuum results [136], and interpret this phase diagram in light of the symmetry-protected topological phases of Sec. 5.1.2, we note that a solution to the gap equations (5.24) can be found analytically in the regime of small interactions and masses $g^2, |ma| \ll 1$. In this case, one can assume that $\eta_0 = 1 + \delta\eta_0$ with $|\delta\eta_0| \ll 1$, and perform a Taylor expansion of Eq. (5.24) to find that the σ-field acquires the following non-zero vacuum expectation value

$$\tilde{\sigma}_0 = \frac{g^2}{\pi a} + \frac{8}{a} e^{-2\pi/g^2}. \tag{5.29}$$

The first contribution stems for the perturbative renormalization of the bare mass $ma \approx -g^2/2\pi$, while the $1/g^2$ behavior of the second contribution highlights that the large-N expansion captures non-perturbative effects, recalling the chiral symmetry breaking by dynamical mass generation of the continuum case [136]. We also note that, as the UV cutoff is removed $a \to 0$, the interaction strength must decrease $g^2 \to 0$ to maintain a finite scalar condensate (5.29), which shows that the continuum GNW model is an asymptotically free QFT.

As announced above, such a vacuum expectation value (5.29) then leads to a small renormalization of the Wilson masses (5.11), $\tilde{m}_k \to \tilde{m}_k(g^2)$, valid in the regime $g^2, |m| \ll 1$. We can thus ascertain that the large mass of the fermion doubler will only be perturbed slightly, remaining thus at the cutoff, and maintaining $\mathrm{sgn}(\tilde{m}_\pi(g^2)) = +1$. Conversely, the sign of the light-fermion mass $\mathrm{sgn}(\tilde{m}_0(g^2))$ may indeed change as the interactions g^2 are increased. According to Eq. (5.12), we can write the topological invariant in this regime as $\varphi_{\mathrm{Zak}} = \frac{1}{2}N\pi\{1-\mathrm{sgn}(\tilde{m}_0(g^2))\}$, such that the region hosting a correlated BDI topological-insulating groundstate corresponds to the parameter region with $\tilde{m}_0(g^2) < 0$.

In order to locate this region, we substitute the saddle-point solution (5.29) into Eq. (5.20), and perform a long-wavelength approximation $|k| < \Lambda \ll 1/a$, yielding the effective free-fermion action

$$\tilde{S}_{\mathrm{W}} = \int_0^\beta \mathrm{d}\tau \sum_{|k|<\Lambda} \Psi_k^\star(\tau) \left(\partial_\tau + \tilde{\mathsf{H}}_k(\tilde{\sigma}_0)\right) \Psi_k(\tau), \tag{5.30}$$

up to an irrelevant constant. Here, we have introduced $\tilde{\mathsf{H}}_k(\tilde{\sigma}_0) = \mathbb{I}_N \otimes \tilde{\mathsf{h}}_k(\tilde{\sigma}_0)$, where the single-particle Hamiltonian for a massive Dirac fermion is

$$\tilde{\mathsf{h}}_k(\tilde{\sigma}_0) \approx \gamma^0 \left(\tilde{m}_0 + \tilde{\sigma}_0\right) - \gamma^5 k, \tag{5.31}$$

which allows us to identify the renormalized Wilson mass

$$\tilde{m}_0 = m \to \tilde{m}_0(g^2) = m + \tilde{\sigma}_0. \tag{5.32}$$

The leftmost red dashed line of Fig. 5.1 corresponds to the points where this renormalized mass vanishes $\tilde{m}_0(g^2) = 0$. We note that this analytical solution matches the lower critical line obtained by the numerical solution of the gap equations (5.24) remarkably well, even considerably beyond the perturbative regime $g^2, |ma| \ll 1$. Following Eq. (5.32), the area below this line fulfills $-m > \tilde{\sigma}_0$, such that the interacting Dirac fermion has a negative renormalized mass $\tilde{m}_0(g^2) < 0$, leading to $\varphi_{\mathrm{Zak}} = N\pi$ and to an SPT phase for N odd.

An analogous behavior can be found in the regime $g^2, |ma+2| \ll 1$, where the light fermion is around $k = \pi/a$, while the heavy one corresponds to $k = 0$ (i.e. the Wilson fermions interchange their roles). Using the previous symmetry (5.28) to locate the critical line $\tilde{m}_\pi(g^2) = 0$ in this parameter regime, we can readily predict the value of this renormalized mass $\tilde{m}_\pi = m + 2/a \to \tilde{m}_\pi(g^2) = m + 2/a - \tilde{\sigma}_0$. The vanishing of this mass leads to the rightmost red dashed line of Fig. 5.1, which again agrees very well with the numerical solution of the gap equations. Since the heavy fermion around $k = 0$ has a large negative mass, the topological invariant becomes $\varphi_{\mathrm{Zak}} = \frac{1}{2}N\pi\{\mathrm{sgn}(\tilde{m}_\pi(g^2)) + 1\}$, and one can identify the symmetry-protected phase displaying $\varphi_{\mathrm{Zak}} = N\pi$ for N odd, with the parameter region fulfilling $\tilde{m}_\pi(g^2) > 0$, and thus $-m < 2 - \tilde{\sigma}_0$ (i.e. shaded yellow area below the dashed line).

At larger couplings and intermediate masses, we must resort to the numerical solution of the gap equations, and search for a region of phase diagram that can be adiabatically connected to these two areas hosting a topological phase. This is precisely the shaded yellow lobe of Fig. 5.1, which is separated from other phases by a gap-closing line. The area above these lines, given by $\tilde{m}_0(g^2) > 0$, and $\tilde{m}_\pi(g^2) < 0$, determines a regime where both renormalized Wilson masses have the same sign, such that the gapped phase has no topological features, corresponding either to a trivial band insulator (grey area in Fig. 5.1), or to the aforementioned Aoki phase where the $\mathbb{Z}_2$ parity symmetry $\Psi(x) \to \mathbb{I}_N \otimes \gamma^0 \Psi(x)$ is spontaneously broken (green area in Fig. 5.1).

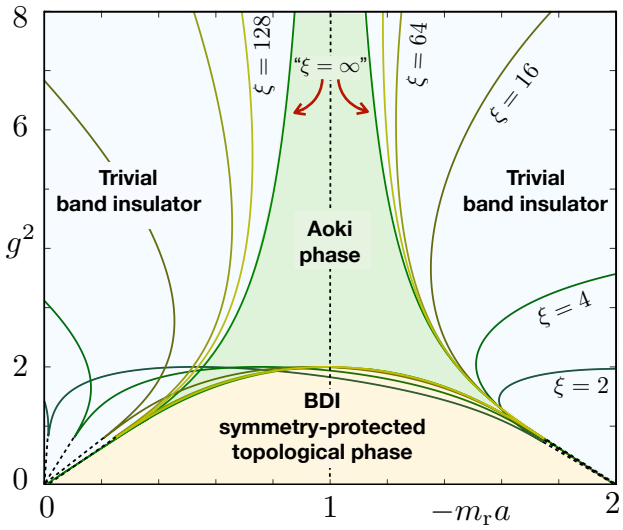

Figure 5.4: **Phase diagram in the Euclidean lattice Gross-Neveu model with renormalized mass:** The solid lines delimiting the Aoki phase as a function of the renormalized mass for $\xi \in \{2, 4, 16, 64, 128\}$ show the tendency towards the mirror-symmetric behavior about $-m_{\rm r}a = 1$. The Hamiltonian prediction is also displayed, where $m_{\rm r}a = ma$, which is labelled by $\xi = \infty$.

5.2.2 Discretized time: Euclidean field theory on the lattice

We now move on to the discussion of the large-N phase diagram of the GNW lattice model using a discretized Euclidean time $x_0 = \tau$. This is the most common formalism in lattice field theory computations [104], and can become the starting point to apply other methods such as Monte-Carlo numerical techniques. As emphasized below, it will be important to understand the connection between the lattice and Hamiltonian approaches, requiring a careful treatment of the continuum-time limit to understand lattice artifacts that can change qualitatively the shape of the phase diagram.

In Euclidean LFT, both space- and time-like coordinates $\{x_\nu\}_{\nu=0,1}$ are discretized into an Euclidean lattice $\Lambda_E = \{\boldsymbol{x} : x_0/a_0 = n_\tau \in \mathbb{Z}_{N_\tau},\ x_1/a_1 = n_{\rm s} \in \mathbb{Z}_{N_{\rm s}}\}$, where $N_\tau(N_{\rm s})$ is the number of lattice sites in the time (space) -like direction, and a_0 (a_1) is the corresponding lattice spacing. Therefore, a similar discussion to the one around Eqs. (5.3)-(5.5) must also be applied to the Euclidean time derivative appearing in the action (5.18), such that nearest-neighbor hoppings along the time-like direction also appear. Introducing fermionic coherent states on the Euclidean lattice, and their corresponding Grassmann variables $\Psi_{\boldsymbol{x}}, \overline{\Psi}_{\boldsymbol{x}}$, the finite-temperature partition function can be expressed as $\mathsf{Z} = \int [\mathrm{d}\overline{\Psi}\mathrm{d}\Psi] e^{-S^E_{\rm W}[\overline{\Psi},\Psi]}$, where the Euclidean action is

$$S^E_{\rm W} = a_0 a_1 \sum_{\boldsymbol{x}\in\Lambda_E} \left(\mathcal{S}^E_0[\overline{\Psi},\Psi] + \mathcal{V}^E_g[\overline{\Psi},\Psi] \right). \tag{5.33}$$

Here, the action is divided into: *(i)* the free quadratic term

$$\mathcal{S}^E_0 = \overline{\Psi}_{\boldsymbol{x}} \left(m + \sum_\nu \frac{1}{a_\nu} \right) \Psi_{\boldsymbol{x}} - \sum_\nu \sum_{s=\pm} \overline{\Psi}_{\boldsymbol{x}} \left(1 - \frac{s\hat{\gamma}_\nu}{2a_\nu} \right) \Psi_{\boldsymbol{x}+sa_\nu \mathbf{e}_\nu}, \tag{5.34}$$

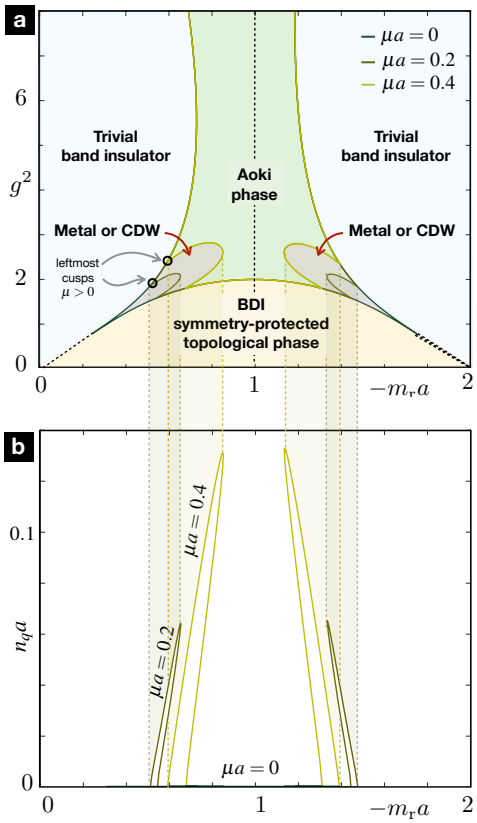

Figure 5.5: **Large-N phase diagram for a non-zero chemical potential: (a)** Solid lines delimit the Aoki phase as determined on a $512 \times 512\xi$ lattice with $\xi = 128$, for chemical potential $\mu a = 0, 0.2, 0.4$. As the chemical potential increases, the region hosting a parity-breaking groundstate diminishes, leaving behind a droplet-shaped region between the trivial and topological phases of the half-filled case, which we conjecture corresponds to a new metallic phase. **(b)** The solid lines lines show the charge density $n_q(m_\mathrm{r})$ at the phase boundary of each chemical potential, obtained by fixing the interaction strength $g^2 = g_\mathrm{c}^2(m_\mathrm{r})$ to the corresponding critical line. We observe that the charge density becomes non-zero only in the new line connecting the two cusps for a finite chemical potential.

which is expressed in terms of the Euclidean gamma matrices $\hat{\gamma}_0 = \gamma^0$, $\hat{\gamma}_1 = \mathrm{i}\gamma^1$, and the unit vectors $\{\mathbf{e}_\nu\}$ of a rectangular lattice; and *(ii)* the interacting quartic term

$$\mathcal{V}_g^E[\overline{\Psi}, \Psi] = -\frac{g^2}{4N}\left(\left(\overline{\Psi}_{\boldsymbol{x}}\Psi_{\boldsymbol{x}}\right)^2 - \left(\overline{\Psi}_{\boldsymbol{x}}\hat{\gamma}_5\Psi_{\boldsymbol{x}}\right)^2\right), \tag{5.35}$$

which is expressed in terms of the chiral matrix $\hat{\gamma}_5 = \gamma^5$.

Lattice approach with dimensionless fields

Let us note that, in the lattice Wilson approach [226], it is customary to work with dimensionless fields $\boldsymbol{\psi}_{\boldsymbol{x}} = \sqrt{a_0 + a_1}\Psi_{\boldsymbol{x}}$, and rewrite the action as follows $S_\mathrm{W}^E = S_{\mathrm{W},0}^E + \mathcal{V}_{\tilde{g}}^E[\overline{\boldsymbol{\psi}}, \boldsymbol{\psi}]$. The free part

$$S_{\mathrm{W},0}^E = \sum_{\boldsymbol{x}\in\Lambda_E}\left(\overline{\boldsymbol{\psi}}_{\boldsymbol{x}}\left(\tilde{m}+1\right)\boldsymbol{\psi}_{\boldsymbol{x}} - \sum_{\nu,s}\kappa_\nu\overline{\boldsymbol{\psi}}_{\boldsymbol{x}}\left(1 - s\hat{\gamma}_\nu\right)\boldsymbol{\psi}_{\boldsymbol{x}+s\mathbf{e}_\nu}\right), \tag{5.36}$$

is expressed in term of dimensionless tunnelings κ_ν, and the dimensionless mass $\tilde{m}$. Similarly, the interacting term is obtained from Eq. (5.35) by substituting the fields $\Psi \to \boldsymbol{\psi}$ and the coupling constant $g \to \tilde{g}$ by the dimensionless ones.

Since the Grassmann variables must fulfill periodic (anti-periodic) boundary conditions along the space (time) -like directions, one can move into momentum space $\boldsymbol{\psi}_{\boldsymbol{k}}, \overline{\boldsymbol{\psi}}_{\boldsymbol{k}}$, where the dimensionless quasi-momenta belong to the Euclidean Brillouin zone $\mathrm{BZ}_E = \{\boldsymbol{k} : k_0 = 2\pi(n_\tau + 1/2)/N_\tau,\ k_1 = 2\pi n_{\mathrm{s}}/N_{\mathrm{s}}\} = (0, 2\pi]^2$. Then, one can rewrite the action as

$$S^E_{\mathrm{W}} = \sum_{\boldsymbol{k}\in \mathrm{BZ}_E} \overline{\boldsymbol{\psi}}_{\boldsymbol{k}} \mathsf{S}_{\boldsymbol{k}}(\tilde{m}) \boldsymbol{\psi}_{\boldsymbol{k}} + \sum_{\boldsymbol{x}\in\Lambda_E} \mathcal{V}^E_{\tilde{g}}(\overline{\boldsymbol{\psi}}, \boldsymbol{\psi}). \tag{5.37}$$

where we have introduced $\mathsf{S}_{\boldsymbol{k}}(\tilde{m}) = \mathbb{I}_N \otimes \mathsf{s}_{\boldsymbol{k}}(\tilde{m})$, together with the single-flavor action

$$\mathsf{s}_{\boldsymbol{k}}(\tilde{m}) = \left(\tilde{m} + 1 - 2\sum_\nu \kappa_\nu \cos k_\nu\right) \mathbb{I}_2 + 2\mathrm{i} \sum_\nu \kappa_\nu \sin k_\nu \hat{\gamma}_\nu. \tag{5.38}$$

Let us note that, in contrast to the continuum-time free action (5.18), this Euclidean action leads to a propagator with four poles at $\boldsymbol{k} \in \{(0,0), (0,\pi), (\pi,0), (\pi,\pi)\}$ when the bare mass equals $-\tilde{m} \in \{0, 4\kappa_0, 4\kappa_1, 4(\kappa_0+\kappa_1)\}$, each of which corresponds to a long-wavelength Dirac fermion. Accordingly, there is an additional doubling due to the discretization of the the Euclidean time direction (i.e. the extra fermions with $k_0 = \pi$ shall be referred to as time doublers).

At this point, the discussion parallels that of the Hamiltonian formalism of Sec. 5.2.1 via the corresponding steps for the large-N approximation. First, the auxiliary dimensionless lattice fields $\tilde{\sigma}_{\boldsymbol{x}}, \tilde{\Pi}_{\boldsymbol{x}}$ are introduced, such that the action can be rewritten as $\mathsf{Z} = \int [\mathrm{d}\overline{\boldsymbol{\psi}} \mathrm{d}\boldsymbol{\psi} \mathrm{d}\tilde{\sigma} \mathrm{d}\tilde{\Pi}] e^{-\tilde{S}^E_{\mathrm{W}}[\overline{\boldsymbol{\psi}}, \boldsymbol{\psi}, \tilde{\sigma}, \tilde{\Pi}]}$, where

$$\tilde{S}^E_{\mathrm{W}} = \sum_{\boldsymbol{k}\in\mathrm{BZ}_E} \overline{\boldsymbol{\psi}}_{\boldsymbol{k}} \tilde{\mathsf{S}}_{\boldsymbol{k}}(\tilde{m}+\tilde{\sigma}, \Pi) \boldsymbol{\psi}_{\boldsymbol{k}} + N \frac{N_{\mathrm{s}} N_\tau}{\tilde{g}^2} (\tilde{\sigma}^2 + \tilde{\Pi}^2). \tag{5.39}$$

Here, we have assumed again that the auxiliary fields are homogeneous, introducing $\tilde{\mathsf{S}}_{\boldsymbol{k}}(\tilde{\sigma}, \tilde{\Pi}) = \mathbb{I}_N \otimes \tilde{\mathsf{s}}_{\boldsymbol{k}}(\tilde{\sigma}, \tilde{\Pi})$, such that the new single-flavor action can be obtained from Eq. (5.38) using $\tilde{\mathsf{s}}_{\boldsymbol{k}}(\tilde{m}+\tilde{\sigma}, \Pi) = \mathsf{s}_{\boldsymbol{k}}(\tilde{m}+\tilde{\sigma}) + \mathrm{i}\hat{\gamma}_5 \tilde{\Pi}$. The second and third steps are the same, since the action is quadratic in Grassmann fields, and the saddle-point solutions control the large-N limit. In this case, the gap equations can be expressed as

$$\frac{N_{\mathrm{s}} N_\tau}{\tilde{g}^2} = \sum_{\boldsymbol{k}\in\mathrm{BZ}_E} \frac{1}{\left(1 - 2\sum_\nu \kappa_\nu \cos k_\nu + \tilde{m} + \tilde{\sigma}\right)^2 + \sum_\nu 4\kappa_\nu^2 \sin^2 k_\nu + \tilde{\Pi}^2}, \tag{5.40}$$

$$-\frac{\tilde{m} N_{\mathrm{s}} N_\tau}{\tilde{g}^2} = \sum_{\boldsymbol{k}\in\mathrm{BZ}_E} \frac{1 - 2\sum_\nu \kappa_\nu \cos k_\nu}{\left(1 - 2\sum_\nu \kappa_\nu \cos k_\nu + \tilde{m} + \tilde{\sigma}\right)^2 + \sum_\nu 4\kappa_\nu^2 \sin^2 k_\nu + \tilde{\Pi}^2}, \tag{5.41}$$

which are equivalent to those derived in [220] upon a different definition of the microscopic couplings.

We have solved this system of non-linear equations for different Euclidean lattices with $N_\tau = \xi N_{\mathrm{s}}$, setting $N_{\mathrm{s}} = 512$ sites in the space-like direction, and using $\xi = \frac{a_1}{a_0} \in \{1, 2, 4, \cdots, 128\}$ to approach the time-continuum limit $\xi \to \infty$ (see Fig. 5.2). Let us note that the dimensionless tunnelings can be expressed in terms of the anisotropy parameter as $\kappa_0 = \xi/2(1+\xi)$, and $\kappa_1 = 1/2(1+\xi)$. At this point, it is worth mentioning that the number of lattice sites in the time-like direction N_τ is also modified in the LFT community to explore non-zero temperatures. In that case, however, the κ_ν parameters

remain constant as N_τ is varied (i.e. the Euclidean lattice is rectangular, but the unit vectors remain the same).

In Fig. 5.2**(a)**, we represent the solution of the gap equations for the isotropic lattice $\xi = 1$, such that $\kappa_0 = \kappa_1 = \frac{1}{4}$. We note that the characteristic trident-shaped phase diagram is in qualitative agreement with the results of S. Aoki [222, 223]. In order to interpret this phase diagram in terms of the symmetry-protected topological phases, let us recall the distribution of the poles described below Eq. (5.38). At $\tilde{g}^2 = 0$, we observe that the critical points separating the different phases correspond to $-\tilde{m} \in \{0, 1, 2\}$, which lie exactly at the aforementioned poles signaling the massless Dirac fermions. For $-\tilde{m} \in (0, 1)$, the only Dirac fermion with a negative mass is that around $\boldsymbol{k} = (0, 0)$, while the other 3 doublers have a positive mass. According to the Euclidean generalization of Eq. (5.12), namely

$$\begin{aligned}\varphi_{\text{Zak}} = \tfrac{1}{2} N\pi \Big(&\operatorname{sgn}\left(\tilde{m}_{(0,\pi)}\right) - \operatorname{sgn}\left(\tilde{m}_{(0,0)}\right) \\ &+ \operatorname{sgn}\left(\tilde{m}_{(\pi,0)}\right) - \operatorname{sgn}\left(\tilde{m}_{(\pi,\pi)}\right) \Big),\end{aligned} \tag{5.42}$$

we see that $\varphi_{\text{Zak}} = N\pi$ for $-\tilde{m} \in (0, 1)$, corresponding to the BDI topological insulator for N odd. For $-\tilde{m} \in (1, 2)$, the Wilson fermions around $\boldsymbol{k} = (0, \pi)$ and $\boldsymbol{k} = (\pi, 0)$ also invert their masses, leading to $\varphi_{\text{Zak}} = -N\pi$, and yielding again an BDI topological insulator for N odd. These two areas, extend on to the neighboring lobes of Fig. 5.2**(a)** using a similar reasoning as the one presented around Eq. (5.30). Therefore, the whole region below the trident that delimits the parity-broken Aoki phase corresponds to the BDI topological insulator. We note, however, that the black dashed lines in this figure, and subsequent ones, do not follow from the solution of the large-N gap equations, but are included as a useful guide to the eye to delimit the SPT phases. In Sec. 5.3 below, we will show that they indeed correspond to a critical line delimiting the SPT phase of a carefully-defined time-continuum limit.

Let us start exploring how this phase diagram changes as the time-continuum limit is approached, and compare the results to those of Fig. 5.1. In Fig. 5.2**(b)**, we represent the phase boundaries for an increasing number of lattice sites $N_\tau = \xi N_{\text{s}}$ with anisotropies $\xi \in \{1, 2, 4, 8\}$. Here, one can observe how the central prong of the Aoki phase separating the topological-insulating lobes is split into two peaks, each of which goes in a different direction as ξ is increased. We note that this behavior differs markedly from the finite-temperature studies, which show that the lobe structure disappears completely as N_τ is varied [222,223]. Therefore, the anisotropy in the lattice constants gives rise to a different playground, which must be understood in terms of the symmetry-protected topological phases.

Since $\kappa_0 \to 1/2$, while $\kappa_1 \to 0$, as the anisotropy $\xi \to \infty$, one can identify the left-moving prong with the pole at $\boldsymbol{k} = (0, \pi)$ with mass $-ma \to 4\kappa_1 \to 0$, and thus approaching the lower left corner. Similarly, the right-moving one can be identified with the pole at $\boldsymbol{k} = (\pi, 0)$ with mass $-ma = 4\kappa_0 \to 2$ approaching the lower right corner. As a result of this movement, and considering the signs of the corresponding Wilson masses, one finds that the region between these two poles correspond to a situation where both space- (time-) like doublers have a negative (positive) mass, such that the topological invariant vanishes $\varphi_{\text{Zak}} = 0$, and one gets a trivial band insulator. Unfortunately, as the anisotropy increases, the two BDI topological lobes get smaller and smaller, such that the symmetry-protected topological phases vanish as we approach the time-continuum limit, and the central lobe corresponds to a trivial band insulator

(see Fig. 5.2**(c)**).

This result seems to be in contradiction with our findings for the Hamiltonian formalism in Fig. 5.1, which predict that the central lobe should correspond to the correlated SPT phase with $\varphi_{\text{Zak}} = N\pi$. Moreover, since each of the two prongs now contain a pair of massless Dirac fermions, the continuum QFT that should emerge in the long-wavelength limit is no-longer that of the Gross-Neveu model for N flavors, but rather that of the Gross-Neveu model for $2N$ flavors, which would indeed modify the universal features of the phase transition, and not only the non-universal shape of the critical line. As mentioned at the beginning of this section, the Euclidean approach can lead to lattice artifacts that can modify qualitatively the phase diagram, and a detailed and careful account of the time-continuum limit is required to understand them. We address precisely this issue in the two following subsections.

Large-N phase diagrams with rescaled couplings

We have found that one of the problems leading to the apparent contradiction between the phase diagrams is the standard use of dimensionless quantities in the Euclidean lattice approach (5.36). A detailed derivation of this action, which starts from the original action (5.33) rescaling the fields, shows that the dimensionless parameters are related to the original ones by the following expression

$$\tilde{m} = \frac{1}{1+\xi} m a_1, \;\; \tilde{g}^2 = \frac{\xi}{(1+\xi)^2} g^2. \tag{5.43}$$

Although apparently innocuous, this rescaling changes qualitatively the shape of the phase diagram (see Fig. 5.3). In order to understand the main features of this phase diagram, the location of the non-interacting poles will be very useful again. For instance, at $g^2 = 0$, we note that the pole at $-\tilde{m} = 4\kappa_0$ gets mapped into $-ma_1 = 4(1+\xi)\kappa_1$. Therefore, as the time-continuum limit is approached, this pole tends to $-ma_1 \to 2$ as $\xi \to \infty$, and no longer to the origin. Likewise, both time-like doublers at $-\tilde{m} \in \{4\kappa_0, 4(\kappa_0+\kappa_1)\}$ are mapped into $-ma_1 \to \infty$ in the time-continuum limit. Accordingly, in the region of interest displayed in Fig. 5.3, these time doublers have a very large positive mass. Inspecting the sign of the corresponding Wilson masses, we can conclude that the region $-ma_1 \in (0,2)$ will host an BDI topological insulator, while a trivial insulator will set in for $-ma_1 > 2$.

Following a similar reasoning as in previous subsections, we know that these critical points surrounding the topological phase will flow as the interactions are switched on and the σ field acquires an non-zero vacuum expectation value. Accordingly, we identify the lobe of Fig. 5.3 as the BDI topological insulator that also appeared in the continuum-time Hamiltonian formalism of Fig. 5.1. Moreover, the universal features are now in agreement as the critical lines are controlled by a single pole, and the long-wavelength limit should now be controlled by the Gross-Neveu model for N flavors.

Let us remark that, although the rescaled solution looks somewhat closer to the Hamiltonian results, there are still qualitative differences in the lattice approach that deserve a deeper understanding. For instance, the phase diagram does no longer display the mirror symmetry about $-ma_1 = 1$ (5.28).

Continuum limit and connection to the Hamiltonian approach

In order to understand these differences, and the connection to the gap equations continuum limit (5.24), let us consider the original action with dimensional

fields (5.33). Following the same steps as before, one can integrate the fermion fields, $\mathsf{Z} = \int [\mathrm{d}\sigma \mathrm{d}\Pi] e^{-N S_{\rm eff}[\sigma,\Pi]}$, finding the following effective action

$$S_{\rm eff} = \frac{L_{\rm s} L_\tau}{g^2}\Big(\sigma^2 + \Pi^2\Big) - \sum_{\boldsymbol{k}\in \mathrm{BZ}_E} \log\left(\frac{\sin^2 k_0 a_0}{a_0^2} + s^2_{\boldsymbol{k}}(m+\sigma,\Pi)\right), \tag{5.44}$$

which is the Euclidean lattice version of Eq. (5.22). Here, we have introduced the corresponding lengths $L_\tau = N_\tau a_0$, $L_{\rm s} = N_{\rm s} a_1$, together with the following function

$$s^2_{\boldsymbol{k}}(x,y) = \left(x + \sum_\nu \frac{1-\cos k_\nu a_\nu}{a_\nu}\right)^2 + \frac{\sin^2 k_1 a_1}{a_1^2} + y^2. \tag{5.45}$$

If we now take the limit of $N \to \infty$, the saddle point conditions $\partial_\sigma S_{\rm eff}|_{(\sigma_0,\Pi_0)} = \partial_\Pi S_{\rm eff}|_{(\sigma_0,\Pi_0)} = 0$ lead to the following pair of gap equations, which are equivalent to Eqs. (5.40)-(5.41) but using dimensional couplings and dimensional fields,

$$\begin{aligned} \frac{L_{\rm s} L_\tau}{g^2} &= \sum_{\boldsymbol{k}\in \mathrm{BZ}_E} \frac{1}{\sin^2(k_0 a_0)/a_0^2 + s^2_{\boldsymbol{k}}(m+\sigma,\Pi)}, \\ -\frac{m L_{\rm s} L_\tau}{g^2} &= \sum_{\boldsymbol{k}\in \mathrm{BZ}_E} \frac{\sum_\nu (1-\cos k_\nu a_\nu)/a_\nu}{\sin^2(k_0 a_0)/a_0^2 + s^2_{\boldsymbol{k}}(m+\sigma,\Pi)}. \end{aligned} \tag{5.46}$$

In order to make a connection to the gap equations obtained with the Hamiltonian formalism (5.24), we should take the continuum limit in the imaginary time direction $N_\tau \to \infty$, and $a_0 \to 0$, such that $L_\tau = L_{\rm s}$ remains constant imposing $\xi = a_1/a_0 \to \infty$. To deal with the additional time doublers mentioned above, let us introduce a UV cutoff $\Lambda_\tau \ll 1/a_0$, and make a long-wavelength approximation around $k_0 \in \{0, \pi/a_0\}$. We find that the gap equation (5.40) becomes

$$\begin{aligned} \frac{L_{\rm s} L_\tau}{g^2} \approx & \sum_{|k_0|<\Lambda_\tau} \sum_{k_1 \in \mathrm{BZ}_{\rm s}} \frac{1}{(k_0)^2 + \epsilon^2_{k_1}(m+\sigma,\Pi)} + \\ & + \sum_{|k_0|<\Lambda_\tau} \sum_{k_1 \in \mathrm{BZ}_{\rm s}} \frac{1}{(k_0)^2 + \epsilon^2_{k_1}(m+2/a_0+\sigma,\Pi)}, \end{aligned} \tag{5.47}$$

where we have used the single-particle energies of Eq. (5.23) and the spatial Brillouin zone, after identifying $a = a_1$. We note that the first line of this expression comes from the contribution around $k_0 = 0$, while the second line stems from the time doublers around $k_0 = \pi/a_0$.

We observe that the effective Wilson mass of these doublers becomes very large in the continuum limit $m + 2/a_0 \to \infty$ if one keeps the bare mass m non-zero. Hence, these doublers become very massive, and their contribution to above gap equation should become vanishingly small as described below Eq. (5.43). To prove that, let us get rid of the cutoff $\Lambda_\tau \to \infty$, and use $\sum_{|k_0|<\Lambda_\tau} \to L_\tau \int_{-\infty}^{\infty} \mathrm{d}k_0/2\pi$. After performing the integral using contour techniques, we directly obtain

$$\begin{aligned} \frac{1}{g^2} = & \int_{-\pi}^{\pi} \frac{\mathrm{d}k_1}{4\pi} \frac{1}{\sqrt{(ma+\sigma a + (1-\cos k_1 a))^2 + \sin^2 k_1 a}} \\ & + \int_{-\pi}^{\pi} \frac{\mathrm{d}k_1}{4\pi} \frac{1}{\sqrt{(ma+\sigma a + (1+2\xi-\cos k_1 a))^2 + \sin^2 k_1 a}}, \end{aligned} \tag{5.48}$$

where we have also taken the continuum limit in the space-like direction. Using the definition of the complete elliptic integrals (5.25), this equation can be expressed

$$\frac{1}{g^2} = \frac{\mathsf{K}(\theta_0)}{\pi(1+\eta_0)} + \frac{\mathsf{K}(\tilde{\theta}_0)}{\pi(1+\tilde{\eta}_0)}. \tag{5.49}$$

Here, we have used the parameters of Eq. (5.26), together with

$$\tilde{\eta}_0 = 1 + ma + 2\xi + \sigma_0 a, \quad \tilde{\theta}_0 = \frac{4\tilde{\xi}_0}{(1+\tilde{\xi}_0)^2}, \tag{5.50}$$

which determine the contribution of the time doublers to the gap equation (i.e. second term of Eq. (5.48)). In the continuum limit, we take $\xi \to \infty$, such that $\tilde{\eta}_0 \to \infty$, and $\tilde{\theta}_0 \to 0$. This makes $\mathsf{K}(\tilde{\theta}_0) \to \pi/2$, such that the time-doubler contribution vanishes, and we recover exactly the gap equation of the Hamiltonian approach (5.24).

The continuum limit of the remaining gap equation (5.41) follows the same lines: we perform a long-wavelength approximation around the time doublers, let the cutoff $\Lambda_\tau \to \infty$, and use contour integration to find

$$\begin{aligned} -\frac{ma}{g^2} = &\int_{-\pi}^{\pi} \frac{\mathrm{d}k_1}{4\pi} \frac{1-\cos k_1 a}{\sqrt{(ma+\sigma a+(1-\cos k_1 a))^2+\sin^2 k_1 a}} \\ &+ \int_{-\pi}^{\pi} \frac{\mathrm{d}k_1}{4\pi} \frac{1+2\xi-\cos k_1 a}{\sqrt{(ma+\sigma a+(1+2\xi-\cos k_1 a))^2+\sin^2 k_1 a}}. \end{aligned} \tag{5.51}$$

Using the definition of the complete elliptic integrals (5.25), this equation becomes

$$\begin{aligned} \frac{-ma}{g^2} = &\frac{(1-\eta_0)^2\mathsf{K}(\theta_0)}{2\pi(1+\eta_0)} + \frac{(1+\eta_0)^2\mathsf{E}(\theta_0)}{2\pi\eta_0(1+\eta_0)} \\ &+ \frac{2\xi\mathsf{K}(\tilde{\theta}_0)}{\pi(1+\tilde{\eta}_0)} + \frac{(1+\tilde{\eta}_0)^2\mathsf{E}(\tilde{\theta}_0)-(1-\tilde{\eta}_0)^2\mathsf{K}(\tilde{\theta}_0)}{2\pi\tilde{\eta}_0(1+\tilde{\eta}_0)}, \end{aligned} \tag{5.52}$$

where the contribution of the time doublers is expressed in the second line. In this case, taking the time-continuum limit $\xi \to \infty$, such that $\mathsf{E}(\tilde{\theta}_0) \to \pi/2$, leads to

$$ma = \frac{(1-\eta_0)^2}{2\eta_0} - \frac{g^2}{2\pi}\frac{(1+\eta_0)}{\eta_0}\mathsf{E}(\theta_0) - \frac{g^2}{2}, \tag{5.53}$$

which contains an additional $-g^2/2$ term with respect to the gap equation of the Hamiltonian formalism (5.24).

We thus find that, in contrast to the first gap equation (5.49), the contribution of the time doublers is no longer vanishing in this case, but can instead be understood as a finite renormalization of the bare mass

$$ma \to m_{\mathrm{r}} a = ma + g^2/2. \tag{5.54}$$

It is precisely this renormalization which is responsible for the lack of the mirror symmetry (5.28) in Fig. 5.3, and its qualitative difference with respect to the Hamiltonian prediction of Fig. 5.1. These results can thus help us to identify the corresponding mirror symmetry, which is no longer about the vertical line $-ma = 1$, but instead about $-m_{\mathrm{r}}a = 1$, which corresponds to the red dashed line $-ma = 1 + g^2/2$ of Fig. 5.3.

To study in more detail the onset of this symmetry in the continuum limit, and the quantitative agreement with the Hamiltonian prediction, we plot the phase diagram with the corresponding renormalized mass in Fig. 5.4, and superimpose the

continuum-time prediction of Fig. 5.1. This figure shows the clear agreement between both approaches, and highlights the importance of performing a careful analysis of the continuum limit in order to avoid Euclidean lattice artifacts that can lead to qualitatively different predictions, even questioning the universal aspects of the emerging QFTs (see Fig. 5.2). It also highlights the fact that the time doublers, despite becoming infinitely heavy in the continuum limit, can leave an imprint in the non-universal properties of the low-energy phase diagram, such as the particular value of the critical points (see the tilted phase diagram of Fig. 5.4). From the perspective of the renormalization group, this effect does not come as a surprise, since the time doublers lie at the cutoff of the continuum-time limit of the lattice field theory, and their integration can thus renormalize the parameters of the long-wavelength light-fermion modes. In this case, a careful analysis of the gap equations has allowed us to extract an additive renormalization $\delta m = g^2/2a$ which, as usual in discretized QFTs, depends on the remaining UV cutoff and shows that the bare mass must be fine tuned to a cutoff-dependent value to yield the physical mass of the low-energy excitations.

Extent of the Aoki phase and tri-critical points

Let us now focus on a question of interest that has not been discussed in detail in the previous sections, namely the extent of the Aoki phase. As already noted above, the solution of the gap equations, either in the Hamiltonian theory (5.24) or in the time-continuum limit of the Euclidean approach (5.40)-(5.41), can only determine the critical lines that delimit the Aoki phase with $\Pi \neq 0$. The question we consider in this section is whether the Aoki phase extends all the way down to $(ma, g^2) = (0, 0)$, and $(ma, g^2) = (-2, 0)$ or, instead, it terminates at a non-zero value of the coupling strength. In this later case, there would be a direct transition between the BDI symmetry-protected phase and the trivial band insulator, not separated by an intermediate parity-broken Aoki phase.

In order to address this point, we apply large-N techniques away from half filling via the introduction of a chemical potential $\tilde{\mu}$ in the GNW model. Following the orthodox prescription for Euclidean LFTs [227], the hopping term $\kappa_\nu\,(1 - s\hat{\gamma}_\nu)$ of the Euclidean action $S^E_{\rm W}$ (5.36) is modified to $e^{s\tilde{\mu}\delta_{\nu 0}}\kappa_\nu\,(1 - s\hat{\gamma}_\nu)$, such that time-like hopping is promoted in the forwards direction by a factor $e^{\tilde{\mu}}$, and suppressed by $e^{-\tilde{\mu}}$ when hopping backwards. As a consequence, one can study the phase diagram of the GNW model at finite densities by solving the gap equations (5.40)-(5.41) with the sum over over the time-like momenta now given by $k_0 = 2\pi(n_\tau + 1/2)/N_\tau - \mathrm{i}\tilde{\mu}$.

Moreover, using the Euclidean partition function, one finds that the conserved fermion charge density $n_q = -\frac{\partial \ln \mathsf{Z}}{\partial \tilde{\mu}}$ is

$$n_q = \frac{\kappa_0}{\mathsf{Z}} \sum_{\boldsymbol{x},s} \int [\mathrm{d}\overline{\Psi}\mathrm{d}\Psi]\overline{\Psi}_{\boldsymbol{x}}(\hat{\gamma}_0 - s)e^{s\tilde{\mu}}\Psi_{\boldsymbol{x}+s\mathbf{e}_0}e^{-S^E_{\rm W}[\overline{\Psi},\Psi]}. \tag{5.55}$$

Setting $\tilde{\mu} \to 0$, this quantity becomes proportional to the expectation value of the time-like component of the vector current $J^E_\mu(\boldsymbol{x}) = \overline{\Psi}_{\boldsymbol{x}}(1+\hat{\gamma}_\mu)\Psi_{\boldsymbol{x}-\mathbf{e}_\mu} - \overline{\Psi}_{\boldsymbol{x}}(1-\hat{\gamma}_\mu)\Psi_{\boldsymbol{x}+\mathbf{e}_\mu}$ [226], which is the discretized version of the continuum vector current $J^E_\mu(\boldsymbol{x}) =: \overline{\Psi}(\boldsymbol{x})\hat{\gamma}_\mu\Psi(\boldsymbol{x})$: for Wilson fermions. Therefore, the time-like component is simply related to the fermion density in the continuum limit, and we can readily explore situations away from half-filling $n_q \neq 0$. Interestingly, while the gap equations (5.40)-(5.41) remain symmetrical under the transformation (5.28) using the renormalized mass (5.54), the charge density $n_q(\tilde{m}, \tilde{g}^2, \tilde{\mu})$ has only an approximate symmetry.

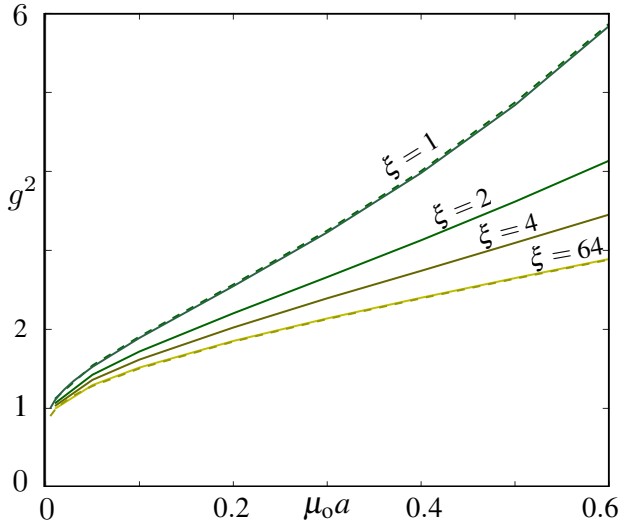

Figure 5.6: **Location of the onset and tri-critical point of the phase diagram:** the leftmost cusp of the phase boundary yields an estimate for the onset chemical potential $\mu_o(g^2)$. Results are obtained from solution of the gap equations (5.40)-(5.41) on $512 \times 512\xi$, except for 'the dashed lines corresponding to $512 \times 1024\xi$ lattices. The limiting vale of g^2 as $\mu_o a \to 0$ marks the tri-critical point separating the half-filled Aoki phase, from the trivial and topological insulators.

We now solve the gap equations (5.40)-(5.41) with a dimensional chemical potential $\mu \equiv \xi\tilde{\mu} \neq 0$, which yield the phase diagram of Fig. 5.5**(a)**, where the axes have been rescaled to match those of Fig. 5.4. We see that, as a consequence of the non-zero-chemical potential, the leftmost and rightmost cusps of the half-filled phase diagram of Fig. 5.4 split into a couple of cusps each, such that the region hosting the Aoki phase becomes smaller. The decrease of the Aoki phase can be qualitatively understood as follows. For $\mu > 0$, one expects that the charge density n_q will eventually rise from the value $n_q = 0$ characterizing the half-filled regime. As a consequence, a Fermi surface will be formed in a certain parameter regime, which consists of two disconnected Fermi points in 1+1d. This has the effect of disfavoring the particle–anti-particle pairing required for the pseudoscalar condensate $\langle \Pi(x) \rangle \neq 0$, since the excitation energy for such a zero-momentum pair would be on the order of $\Delta\epsilon \sim 2\mu$. Accordingly, the Aoki phase should shrink as the chemical potential is increased. This is corroborated by the curves for $n_q(m_{\rm r})$ in Fig. 5.5**(b)**, which rise above zero only around the borders of the droplet-shaped region between the two newly-formed cusps for $\mu > 0$ (see the grey regions in Fig. 5.5**(a)**). These are precisely the regions where the half-filled Aoki phase has been expelled from. We also note that Fig. 5.5**(b)** shows an approximate symmetry about $-m_{\rm r}a = 1$ which we expect to become exact for $\xi \to \infty$. Let us now describe how these results can be used to determine, in a controlled way, the extent of the Aoki phase at half-filling. The empty circles of Fig. 5.5**(a)** mark the so-called onset, beyond which the ground state has a non-zero charge density (i.e. $n_q > 0$ for $\mu > \mu_o(g^2)$). By numerically obtaining such onsets for a variety of parameters and time discretizations, we obtain Fig. 5.6. We note that the variation for finite ξ is probably due to non-universal effects since in the sums over the Brillouin zone of Eqs. (5.40)-(5.40), as the chemical potential enters as e.g. $\sinh(\xi\mu a)$. One observes from this figure

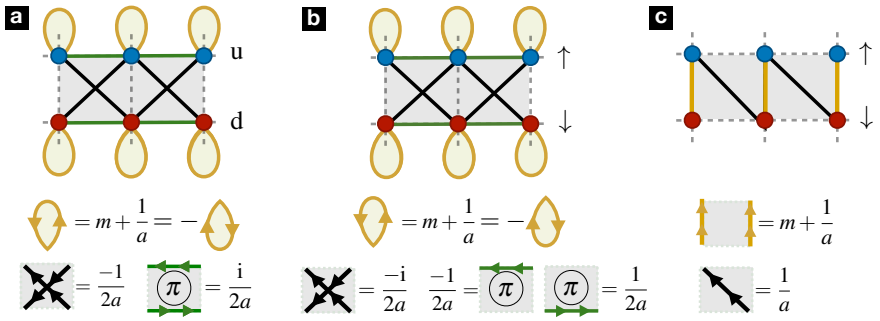

Figure 5.7: **Scheme for the Wilson-fermion kinetic energy: (a)** The spinor index of the fermionic field can be pictured as the legs of a virtual ladder $\ell \in \{\mathrm{u}, \mathrm{d}\}$, which connects the GNW model to the imbalanced Creutz-Hubbard ladder (5.57) after a gauge transformation. Fermions can hop diagonally between the legs of the ladder with a tunneling strength $-t_\times = -1/2a$ (black crossed lines), and horizontally along the legs of the ladder with a tunneling strength $-t_\mathrm{h} = \pm i/2a$ that is complex due to an external magnetic π-flux $-t_\mathrm{h} = -e^{\mathrm{i}\int \mathrm{d}l A_{\mathrm{ext}}(x)}/2a$ (green horizontal lines). The yellow circles stand for an energy imbalance $\pm\Delta\epsilon/2 = \pm(m+1/a)$ between the upper and lower legs. **(b)** In the cold-atom implementation, the legs of the synthetic ladder correspond to a couple of hyperfine states $\sigma \in \{\uparrow, \downarrow\}$, such that the original GNW model (5.3)-(5.5) is similar to the Creutz-Hubbard ladder **(a)** but with different tunneling strengths $-t_\times = i/2a$ (black crossed lines), and $-t_\mathrm{h} = \pm 1/2a$ (green lines), which preserves the overall π-flux around square plaquettes. **(c)** Using a different choice for the gamma matrices $\gamma^0 = \sigma^x$, $\gamma^5 = \sigma^y$, the discretization yields a much simpler tunneling for $r = 1$. The kinetic energy consists only of diagonal $t_\mathrm{d} = 1/a$ (black lines) and vertical $t_\mathrm{v} = (m+1/a)$(yellow lines) hoppings.

that all curves come closer in the limit $\mu \to 0$, and seem to approach a limit as $\xi \to \infty$. This limiting value corresponds to the point where half-filled Aoki phase terminates, proving that these phase does not extend all the way down to the weak coupling limit, but only survives down to $g^2(\mu_o = 0) \approx 0.8$ according to the results of Fig. 5.6.

Let us note that extracting this limiting value is numerically hard; for instance, the curvature appears slightly sensitive to temperature, as revealed by calculations on $512 \times 1024\xi$ lattices. However, our approximate prediction $g^2(\mu_o = 0) \approx 0.8$ is consistent with the cusps of Fig. 5.4, where the Aoki phase terminates. Fig. 5.6 therefore strengthens our belief in the existence of a tricritical point at non-zero $g^2(\mu_o = 0)$; for couplings below this value there is a direct transition between trivial and topological insulating phases as m is varied, and no parity breaking Aoki phase is encountered in the middle.

So far, we have used the large-N results for a non-zero chemical potential to extract features of the half-filled phase diagram by taking the limit $\mu \to 0$ in a controlled manner. However, we note that another interesting question would be to study the fate of the symmetry-protected topological phases, and the appearance of other new phases of matter, in the GNW model away from half filling. In that respect, we note that our large-N results point towards the appearance of a new phase (i.e. droplet-shape region of Fig. 5.5). Since we have argued that the finite charge densities appear due to the formation of a Fermi surface, it is reasonable to expect that such densities will not drop abruptly to zero as we move away from the critical line. In that sense, the droplet-shaped region may either correspond to a metallic phase where the Fermi points occur at different momenta as the microscopic parameters are modified, or maybe to a kind of charge-density-wave where the fermionic density forms a regular periodic pattern.

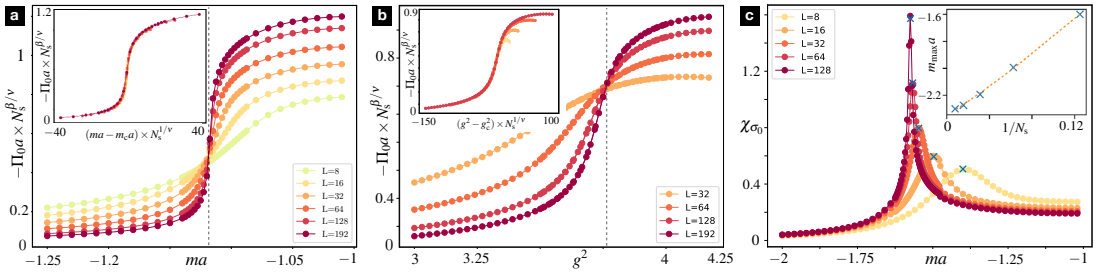

Figure 5.8: **Finite-size scaling for the quantum phase transitions of the Gross-Neveu-Wilson model: (a)** (Main panel) Rescaling of the pseudoscalar condensate $\Pi_0 a = \langle \bar{\Psi} \mathrm{i}\gamma^5 \Psi \rangle a$ with a power of the number of lattice sites $N_\mathrm{s}^{\beta/\nu}$ as a function of the bare mass ma. Assuming Ising critical exponents $\beta = 1/8$ and $\nu = 1$, we find a crossing for different lengths, signaling the critical point $m_\mathrm{c}a$ between the trivial band insulator and the Aoki phase. (Inset) Collapse of the data around the critical point, showing that the choice of Ising critical exponents leads to the correct universality. **(b)** Same as **(a)**, but studying the finite-size scaling of the pseudoscalar condensate as a function of the interactions g^2. The corresponding critical point g_c^2 describes the transition between the SPT phase and the Aoki phase with Ising exponents $\beta = 1/8$ and $\nu = 1$. **(c)** The transition between the trivial band insulator and the SPT phase is captured by the divergence of the

Understanding the nature of this phase lies outside of the scope of the present work, and will be the subject of a future work. We advance at this point that the density-matrix renormalization group methods discussed in the following section could be adapted to study situations away from half filling, and are a potential tool to address the nature of this new phase. Moreover, we also note that the sign problem for $\mu \neq 0$ can be safely avoided for any discretized Gross-Neveu or Nambu-Jonal-Lasinio models, such that Monte Carlo techniques [228, 229] could also be applied to the present problem, and extensions thereof.

5.3 Large-N benchmark via MPS

In this section, we test the above large-N prediction for the single-favor GNW lattice model using numerical routines based on matrix product states (MPS) [50] (i.e. a variational version of real-space density-matrix renormalization group method [50, 133, 134]). On the one hand, this can be considered as the most stringent test of the validity of the large-N approach, as we are indeed very far from the large-N limit. On the other hand, the choice of $N = 1$ is also motivated by the fact that the single-flavor GNW model can be realized in cold-atom experiments following the scheme of Sec. 5.1.3 described below. Note that the $N = 1$ flavor of the continuum Gross-Neveu QFT (5.2) with an additional mass term corresponds to the so-called massive Thirring model [230, 231]. The discretization of this QFT using the Wilson approach allows us to discuss the occurrence of symmetry-protected topological phases in this LFT, and use it to benchmark the large-N predictions for the phase diagram of the GNW model with a finite number of flavors.

5.3.1 High-energy physics to condensed matter mapping

We consider the GNW lattice Hamiltonian (5.3)-(5.5) for a single fermion flavor $N = 1$. By performing a $U(1)$ gauge transformation to the spinors $\Psi(x) \rightarrow$

$e^{-i\frac{\pi}{2a}x}\Psi(x)$, which can be understood as an instance of a Kawamoto-Smit phase rotation in LFTs [232], and using the algebraic properties of the gamma matrices, we can rewrite $\tilde{H}_{\rm W} \to \tilde{H}_{\rm W} = a\sum_{x\in\Lambda_\ell} :\tilde{\mathcal{H}}_{\rm W}:$, where

$$\begin{aligned}\tilde{\mathcal{H}}_{\rm W} =&\Psi^\dagger(x)\left(-\frac{\gamma^5}{2a}+\mathrm{i}\frac{r\gamma^0}{2a}\right)\Psi(x+a)+\text{H.c.}\\ &+\Psi^\dagger(x)\left(m+\frac{r}{a}\right)\gamma^0\Psi(x)-\frac{g^2}{2N}\Big(\Psi^\dagger(x)\gamma^0\Psi(x)\Big)^2.\end{aligned} \tag{5.56}$$

In this notation, the Hamiltonian looks similar to the Hubbard model [29], a paradigm of strongly-correlated electrons in condensed matter [233], with an additional spin-orbit coupling. Note that this formulation only differs from Eqs. (5.3)-(5.5) on the particular distribution of the complex tunnellings, which can be understood as a gauge transformation on a background magnetic field maintaining an overall π-flux. Indeed, the defining property of the above Kawamoto-Smit phases is that they yield a π-flux through an elementary plaquette.

In order to understand the origin of this magnetic flux, let us introduce the following notation for the Dirac spinor $\Psi(x) = (c_{\rm u}(x), c_{\rm d}(x))^{\rm t} \to (c_{i,{\rm u}}, c_{i,{\rm d}})^{\rm t}/\sqrt{a}$ for $N = 1$. Here, the dimensionless fermion operators $c_{i,\ell}$ depend on a spinor index $\ell \in \{{\rm u},{\rm d}\}$ that can be interpreted in terms of the upper ($\ell = {\rm u}$) and lower ($\ell \in {\rm d}$) legs of a synthetic ladder, and $i \in \{1,\cdots,N_{\rm s}\}$ labels the positions of the rungs of the ladder (see Fig. 5.7**(a)**). Considering our particular choice of gamma matrices $\gamma^5 = \sigma^x$, $\gamma^0 = \sigma^z$, the corresponding Hamiltonian $\tilde{H}_{\rm W}$ for the chosen Wilson parameter $r = 1$ can be rewritten as

$$\begin{aligned}H_{\rm W} =&\frac{-1}{2a}\sum_{i,\ell}\left(c^\dagger_{i,\ell}c_{i+1,\bar{\ell}}-\mathrm{i}s_\ell c^\dagger_{i,\ell}c_{i+1,\ell}+\text{H.c.}\right)\\ &+\sum_{i,\ell}\left(\left(m+\frac{1}{a}\right)s_\ell c^\dagger_{i,\ell}c_{i,\ell}+\frac{g^2}{2a}c^\dagger_{i,\ell}c^\dagger_{i,\bar{\ell}}c_{i,\bar{\ell}}c_{i,\ell}\right),\end{aligned} \tag{5.57}$$

where we have introduced $s_\ell = +1$ ($s_\ell = -1$) for the upper $\ell = {\rm u}$ (lower $\ell = {\rm d}$) leg of the ladder, and $\bar{\ell} = {\rm d},{\rm u}$ for $\ell = {\rm u},{\rm d}$. As can be seen in Fig. 5.7**(a)**, there is a net π-flux due to an Aharonov-Bohm phase that the fermion would pick when tunneling around an elementary plaquette.

In particular, Eq. (5.57) can be understood as a generalized Hubbard model on a ladder corresponding to the imbalanced Creutz-Hubbard model [59], which is an interacting version of the so-called Creutz ladder [83,84,86,87]. The first line in Eq. (5.57) describes the horizontal and diagonal tunneling of fermions with strength $\tilde{t} = 1/2a$, which are subjected to an external magnetic π-flux threading the ladder (see Fig. 5.7**(a)**). One thus finds that the UV cutoff of the GNW model $\Lambda = 1/a$ is provided by the maximum energy within the band structure $\Lambda = 2\tilde{t}$ of the Creutz-Hubbard model. Likewise, one understands that the first term in the second line of Eq. (5.57) corresponds to an energy imbalance between both legs of the ladder $\Delta\epsilon/2 = (m + 1/a)$, and yields a single-particle Hamiltonian in momentum space that is similar to Eq. (5.6), namely

$$\mathsf{h}_k^{\rm CH} = \left(\frac{\Delta\epsilon}{2}+2\tilde{t}\sin k\right)\gamma^0 - 2\tilde{t}\cos k\gamma^5. \tag{5.58}$$

Finally, the last term of Eq. (5.57) amounts to a Hubbard-type density-density interaction $V_{\rm v} n_{n,{\rm u}} n_{n,{\rm d}}$ between fermions residing on the same rung of the ladder, which repel themselves with a strength $V_{\rm v} = g^2/a$.

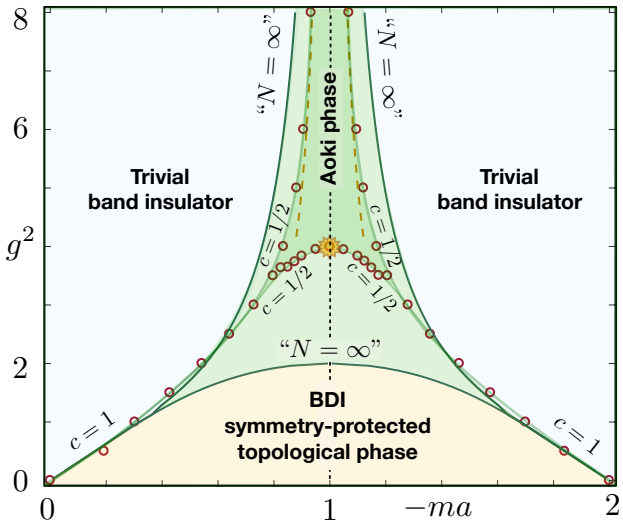

Figure 5.9: **Phase diagram from matrix-product-state methods:** The red circles represent the critical points of the $N = 1$ Gross Neveu lattice model obtained by with matrix product states. The semi-transparent green lines joining these points delimit the trivial band insulator, Aoki phase, and the BDI symmetry-protected topological phase. Note again that this SPT phase corresponds to the AIII topological insulator of the Creutz-Hubbard model .These lines are labelled by $N = 1$, and by the central charge $c \in \{1/2, 1\}$ of the conformal field theory that controls the continuum QFT at criticality. These results serve to benchmark the large-N predictions for the critical lines, which are represented by dark solid lines, and labelled with "$N = \infty$". We also include the exact critical point at $(-ma, g^2) = (1, 4)$, which is depicted by an orange star, and the strong-coupling critical lines that become exact in the limit of $g^2 \to \infty$, which are depicted by dashed orange lines. The matrix-product-states predictions match remarkably well these exact results.

According to this discussion, the high-energy-physics GNW lattice model is gauge equivalent to the condensed-matter imbalanced Creutz-Hubbard model. Similarly to the high-energy physics convention of working with dimensionless parameters $m/\Lambda = ma$ and g^2, the condensed-matter community normalizes the couplings to the tunneling strength $\tilde{t}$, such that the exact relation between the microscopic parameters of these two models is

$$ma = \frac{\Delta\epsilon}{4\tilde{t}} - 1, \;\; g^2 = \frac{V_{\mathrm{v}}}{2\tilde{t}}. \tag{5.59}$$

Let us also note that, in the condensed-matter context, the lattice constant d of the model (5.57) is fixed by the underlying Bravais lattice of the solid, which is typically set to $d = 1$ in the calculations (5.58) (i.e. lattice units). Note, however, that this does not preclude us from taking the continuum limit. In this case, the continuum limit corresponds to the low-energy limit, where $\tilde{t} = 1/2a$ (i.e. UV cutoff) is much larger than the energy scales of interest. By setting the model parameters in the vicinity of a second-order quantum phase transition, the relevant length scales fulfill $\xi_{\mathrm{l}} \gg d$, and one recovers universal features that are independent of the microscopic lattice details, and can be described by a continuum QFT.

5.3.2 Phase diagram of the $N = 1$ Gross-Neveu-Wilson model

In this section, we exploit the above mapping (5.59) to explore the phase diagram of the $N = 1$ lattice GNW model by importing some of the condensed-matter and quantum-information techniques described in [59]. In particular, we will use the numerical matrix-product-state results to benchmark the large-N predictions. We remark that this mapping also becomes very useful in the reverse direction, as certain aspects of the Creutz-Hubbard model become clarified from the high-energy perspective of the GNW model.

In the parameter regime $\Delta\epsilon/4\tilde{t} < 1$, which corresponds to a bare mass $-ma \in [0, 1]$, we found that the imbalanced Creutz-Hubbard model displays three distinct phases: an orbital paramagnet, an orbital ferromagnet, and an SPT phase [59]. The orbital paramagnet corresponds to a gapped phase of matter that is characterized by the absence of long-range order and any topological feature. Therefore, this phase should correspond to the trivial band insulator of the GNW model in Fig. 5.1.

The orbital ferromagnet, on the other hand, is a phase displaying an Ising-type long-range order due to the spontaneous breaking of a discrete orbital symmetry. Accordingly, it should correspond to the parity-broken Aoki phase of the Gross Neveu model in Fig. 5.1. To show this correspondence in more detail, let us comment on the orbital magnetization introduced for the Creutz-Hubbard ladder $T_0 = \langle T_i^y \rangle = \frac{1}{2}\langle \mathrm{i} c_{i,\mathrm{u}}^\dagger c_{i,\mathrm{d}} \rangle + \text{c.c.} \neq 0 \ \forall i$, and show that it is related to an order parameter of the GNW model. The parity symmetry of the GNW model that is broken in the Aoki phase, namely $\Psi(x) \to \eta \mathbb{I}_N \otimes \gamma^0 \Psi(-x)$ with $|\eta|^2 = 1$, corresponds to $c_{i,\mathrm{u}} \to \eta c_{N_\mathrm{s}-i,\mathrm{u}}$, and $c_{i,\mathrm{d}} \to -\eta c_{N_\mathrm{s}-i,\mathrm{d}}$ in the Creutz-Hubbard ladder. Hence, one finds that $T_0 = \langle T_i^y \rangle \to -\langle T_{N_\mathrm{s}-i}^y \rangle = -T_0$ is spontaneously broken by the orbital ferromagnet. We thus see that, in the language of the synthetic Creutz-Hubbard ladder, the pseudoscalar condensate corresponds to an Ising-type ferromagnet with a non-zero orbital magnetization $T_0 = -\Pi_0 a/2 = -\langle \overline{\Psi} \mathrm{i} \gamma^5 \Psi \rangle a/2$. This connection also teaches us that one can perform a rigorous finite-size scaling of the pseudoscalar condensate to obtain accurate predictions of the critical lines enclosing the whole Aoki phase, instead of using the various mappings discussed in [59].

Finally, as shown explicitly in [59], the Creutz-Hubbard ladder also hosts a correlated SPT phase, which displays a double-degenerate entanglement spectrum [234, 235] due to a couple of zero-energy edge modes. This phase should thus corresponds to the BDI symmetry-protected topological phase of the GNW model discussed throughout this work (see Fig. 5.1). Let us remark, however, that the topological insulator of the Creutz-Hubbard model lies in the symmetry class AIII, breaking explicitly the time-reversal T and charge-conjugation C symmetries, yet maintaining the sublattice symmetry. According to our discussion below Eq. (5.12), we see that the Creutz-Hubbard single-particle Hamiltonian breaks T: $\gamma^0 (h_{-k}^{\mathrm{CH}})^* \gamma^0 \neq h_k^{\mathrm{CH}}$, and C: $\gamma^5 (h_{-k}^{\mathrm{CH}})^* \gamma^5 \neq -h_k^{\mathrm{CH}}$, explicitly. On the other hand, the combination S = TC yields $(\gamma^1)^\dagger h_k^{\mathrm{CH}} \gamma^1 = -h_k^{\mathrm{CH}}$, such that the topological insulator of the Creutz-Hubbard ladder is in the AIII symmetry class. Therefore, the last element of our high-energy physics to condensed-matter dictionary is the mapping between the symmetry classes BDI $\leftrightarrow$ AIII, which is a direct consequence of the above local gauge transformation/Kawamoto-Smit phase rotation. Although differences will arise regarding perturbations that explicitly break/preserve the corresponding symmetries (e.g. disorder), the phase diagram of the translationally-invariant GNW model should coincide exactly with that of the Creutz-Hubbard ladder provided that one uses the relation between microscopic parameters in Eq. (5.59).

With this interesting dictionary for the correspondence of phases, and the mi-

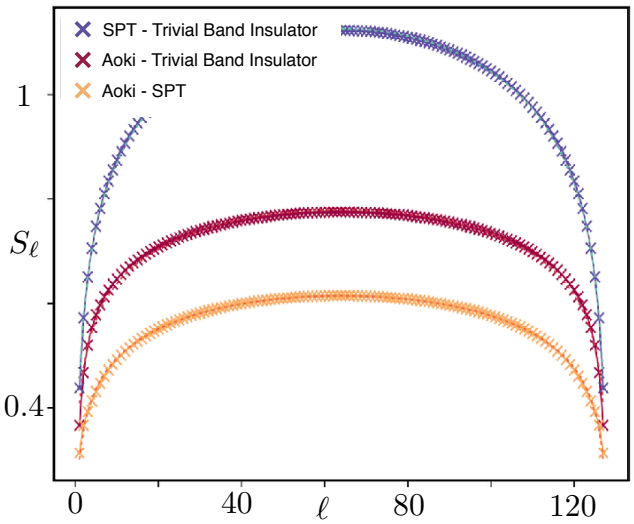

Figure 5.10: **Scaling of the block entanglement entropy :** Entanglement entropy $S_\ell = -\mathrm{Tr}\{\rho_\ell \log \rho_\ell\}$ for a ℓ-sites block reduced density matrix $\rho_\ell = \mathrm{Tr}_{N_s-\ell}\{|\mathrm{gs}\rangle\langle\mathrm{gs}|\}$ obtained from a chain of $N_s = 128$ sites. The blue, red, and yellow crosses correspond to the data for the critical points $(-ma, g^2) = (1.5787, 1.5)$, $(-ma, g^2) = (1.1182, 5)$, and $(-ma, g^2) = (1.125, 3.775)$, respectively. The solid lines correspond to the fittings with the conformal field theory predictions $S_\ell = \frac{c}{6}\log(D_\ell) + a$, where c is the central chrage, a a non-universal constant, and $D_\ell = 2N_s \sin(\pi\ell/N_s)/\pi$ is the chord distance. The fitted central charges are $c = 1.02$, $c = 0.503$, and $c = 0.49$.

croscopic parameter mapping in Eq. (5.59), we can use numerical matrix-product-state simulations, extending the parameter regime studied in [59] from $\Delta\epsilon/4\tilde{t} < 1$ to $-1 < \Delta\epsilon/4\tilde{t} < 1$. In this way, we can explore the full phase diagram diagram of the $N = 1$ GNW model, and compare it to our previous large-N predictions for $-ma \in [0, 2]$. Let us recall that the large-N approach fulfills (5.28), such that the obtained phase diagrams have a mirror symmetry about $-ma = 1$. However, it is not clear a priori if this symmetry is a property of the model, or if it is instead rooted in the approximations of the large-N prediction. We will be able to address this question with our new matrix-product-state simulations.

In Figs. 5.8 **(a)-(b)**, we discuss a representative example of the finite-size scaling of the pseudoscalar condensate $\Pi_0 = \langle\overline{\Psi}\mathrm{i}\gamma^5\Psi\rangle$ for the transition between the trivial, or topological, band insulators and the Aoki phase. One clearly sees that the matrix-product-state numerical simulations for different lengths display a crossing that gives access to the critical point (main panel of Figs. 5.8 **(a)-(b)**), and that the data collapse of (inset of Figs. 5.8 **(a)-(b)**) corroborates that this critical point lies in the Ising universality class. Note that the pseudoscalar condensate gives no information about the phase transition between the trivial and topological insulators. In order to access this information, the mapping to the Creutz-Hubbard ladder becomes very useful, as it points to the possibility of using a generalized susceptibility associated to the variation of the scalar condensate $\sigma_0 = \langle\overline{\Psi}\Psi\rangle$ with the bare mass $\chi_{\sigma_0} = \partial\sigma_0/\partial m$. As shown in the main panel of Fig. 5.8 **(c)**, this susceptibility diverges at the critical point of the thermodynamic limit, and can be used to perform a finite-size scaling.

Repeating this procedure for various critical points, we obtain the red empty circles

displayed in Fig. 5.9, which are compared with the large-N results of Fig. 5.1 represented as solid lines. We can thus conclude that the large-N predictions are qualitatively correct, as they predict the same three possible phases, and the shape of the critical lines is qualitatively similar to the matrix-product-state prediction. Moreover, the agreement between the critical lines becomes quantitatively correct in the weak-coupling limit $g^2, |ma| \ll 1$, which is the regime where the asymptotically-free Gross-Neveu QFT (5.1) is expected to emerge from the lattice model. Since both the mass and the interaction strengths are relevant perturbations growing with the renormalization-group transformations, one expects that a continuum limit with physical parameters well below the UV cutoff can be recovered provided that $g^2, |ma| \ll 1$. Let us also remark that the matrix-product-state simulations are consistent with the mirror symmetry about $-ma = 1$ of the large-N gap equations. Therefore, it seems that this symmetry is an intrinsic property of the GNW model, which is easy to understand in the non-interacting limit, but not so obvious in the interacting case. On general grounds, Fig. 5.9 shows that the large-N prediction tends to overestimate the extent of the Aoki phase, predicting that the spontaneous breaking of the parity symmetry occurs for weaker interactions and smaller masses. This trend could be improved by considering next-to-leading-order (NLO) corrections to the saddle-point solution, and will be the subject of a future study. In this sense, our results suggest that large-N methods from a high-energy context can be a useful and systematic tool to study problems of correlated symmetry-protected topological phases in condensed matter.

We now comment on further interesting features that can be learned from this dictionary, and imported from condensed matter into the high-energy physics context. In Fig. 5.9, we have highlighted with a semi-transparent orange star the critical point separating the topological and Aoki phases at $(-ma, g^2) = (1, 4)$. This point corresponds to a Creutz-Hubbard model with vanishing imbalance $\Delta\epsilon = 0$, and strong repulsion $V_{\rm v} = 8\tilde{t}$. Interestingly, it is precisely at this point that an exact quantum phase transition is found by mapping the Creutz-Hubbard ladder onto an exactly-solvable quantum impurity Ising-type model via the so-called maximally-localized Wannier functions [59]. In this way, one learns that the lattice GNW model can be solved exactly for a particular limit with relatively strong couplings, and that the corresponding quantum phase transition must lie in the Ising class. From a high-energy perspective, the whole critical line separating the topological and Aoki phases should be controlled by the continuum QFT of a Majorana fermion, and not by the standard Dirac-fermion QFT expected at weak couplings (i.e. along the critical line separating the topological and trivial insulators). We have proved this rigorously using the numerical scaling of the entanglement entropy [92,153], which shows that this critical line is characterized by a central charge $c \approx 1/2$ in agreement with the conformal field theory of a massless Majorana fermion. Conversely, at weak couplings, the scaling of the entanglement entropy yields a central charge $c \approx 1$ in agreement with the massless Dirac fermion (see Fig. 5.10).

Let us now discuss the orange dashed line of Fig. 5.9, which describes an exact solution that becomes valid in the strong-coupling limit $g^2 \gg 1$. From the parameter correspondence (5.59), this regime corresponds to the strongly-interacting Hubbard model, where one expects to find super-exchange interactions between the fermions [236, 237]. In this case, these super-exchange can be described in terms of an orbital Ising model with ferromagnetic coupling $J = -2/g^2 a$, and subjected to a transverse magnetic field $B = 2(m+1/a)$. According to the exact solution of the transverse Ising model [238], the strong-coupling critical line $J = 2B$ corresponds to $g^2 = 1/2(ma + 1)$. This line, and its mirror image, have been depicted by the orange dashed lines of Fig. 5.9, and

shows a very good agreement with the numerical critical points of the GNW model at strong-couplings $g^2 \gg 1$. Since the strong-coupling mapping yields a transverse Ising model, we learn again that the corresponding continuum QFT at criticality is that of a Majorana fermion, which is corroborated again by the matrix-product-state scaling of the entanglement entropy yielding a central charge of central charge $c \approx 1/2$ (see Fig. 5.10). Therefore, the condensed-matter mapping teaches us that the GNW lattice model has an exact solution in the strong-coupling limit, and both critical lines delimiting the Aoki phase lead to a continuum limit controlled by a Majorana-fermion QFT. These results show that condensed-matter methods can offer a useful and systematic tool to benchmark large-N methods applied to problems of asymptotically-free LFTs in a high-energy context. In future works, we will study leading order $1/N$ corrections to the present large-N approach, and see how fast they approach the exact and quasi-exact results for the phase diagram discussed in this section.

5.4 Cold atoms implementation

In this section, we describe possible routes for the cold-atom realization of the lattice GNW model starting from Eqs. (5.13)-(5.15). At this stage, we could simply build on the mapping to the Creutz-Hubbard ladder (5.57) to adopt the quantum simulation scheme recently proposed in [59]. However, this would lead to an SPT phase in a different symmetry class, so we will now focus on the cold-atom quantum simulation of the original GNW Hamiltonian (5.3)-(5.5). Moreover, as discussed below, the original arrangement of tunnellings can simplify the experimental requirements.

Therefore, in this section, we describe in detail the scheme based on a two-component $\sigma = \{\uparrow, \downarrow\}$ single-species $N_{\rm sp} = 1$ Fermi gas in a state-independent optical lattice (5.13)-(5.15). The internal states can be interpreted as a synthetic dimension [239, 240], such that the target GNW Hamiltonian density

$$\begin{aligned}\tilde{\mathcal{H}}_{\rm W} = \Psi^\dagger(x)\left(-{\rm i}\frac{\gamma^5}{2a} - \frac{r\gamma^0}{2a}\right)\Psi(x+a) + {\rm H.c.} \\ + \Psi^\dagger(x)\left(m + \frac{r}{a}\right)\gamma^0\Psi(x) - \frac{g^2}{2N}\Big(\Psi^\dagger(x)\gamma^0\Psi(x)\Big)^2.\end{aligned} \tag{5.60}$$

can be depicted using the scheme of Fig. 5.7**(b)**.

As usual [20], one makes use of the Wannier functions localized around $\boldsymbol{x}^0_{\mathbf{i}} = \sum_\nu (\pi/k_{{\rm L},\nu}) i_\nu \mathbf{e}_\nu$, where $\mathbf{i}$ is a vector of integers labelling the optical lattice minima, to transform the Fermi fields as $\Psi_\sigma(\boldsymbol{x}) = \sum_{\mathbf{i}} w(\boldsymbol{x} - \boldsymbol{x}^0_{\mathbf{i}}) f_{\mathbf{i},\sigma}$, where we have eliminated the species index from the lattice annihilation operators $f_{\mathbf{i},\sigma}$. Assuming that the optical lattice is much deeper along two axes $V_{0,y}, V_{0,z} \gg V_{0,x} \gg E_{\rm R}$, the dynamics for the time-scale of interest occurs along the x-axis, and can be described by a Hubbard-type model

$$\begin{aligned}H = -t\sum_{i,\sigma}\Big(f^\dagger_{i,\sigma}f_{i+1,\sigma} + {\rm H.c.}\Big) + \frac{U}{2}\sum_i\sum_{\sigma,\sigma'} f^\dagger_{i,\sigma}f^\dagger_{i,\sigma'}f_{i,\sigma'}f_{i,\sigma} \\ + \sum_{i,\sigma}(\epsilon_\sigma + \Delta i) f^\dagger_{i,\sigma}f_{i,\sigma} + \sum_{i,j}\sum_{\sigma,\sigma'} v^{i,j}_{\sigma,\sigma'}(t) f^\dagger_{j,\sigma'}f_{i,\sigma}.\end{aligned} \tag{5.61}$$

Here, the terms of the first line corresponds to the standard tunneling with $t = 4E_{\rm R}(V_{0,x}/E_{\rm R})^{3/4}e^{-2(V_{0,x}/E_{\rm R})^{1/2}}$, and on-site interactions $U = \sqrt{8/\pi}k_{{\rm L},x}a_{\uparrow\downarrow}E_{\rm R}(V_{0,x}V_{0,y}V_{0,z}/E_{\rm R}^3)^{1/4}$

of the cold-atom Hubbard model [20]. In addition to these terms, the second line contains the internal energies ϵ_σ, and a static gradient Δ that comes from the so-called lattice acceleration [241], i.e. the detuning of the optical-lattice beams is modified linearly in time, yielding a linear gradient (i.e. constant force) in the lattice reference frame. The remaining terms $v^{i,j}_{\sigma,\sigma'}(t)$ in Eq. (5.61) stem from the pairs of laser beams in a Raman configuration (5.14), which need to be exploited such that the tunneling dynamics of the atoms corresponds to Fig. 5.7**(b)**.

First of all, the bare tunneling must be inhibited by the gradient $t \ll \Delta$. Then, the inter-leg tunnellings of Fig. 5.7**(b)** (crossed black lines) can be laser-assisted by a Raman pair [25], which also leads to the energy imbalance terms (yellow loops). We set *(i)* the Raman frequencies to $\Delta\omega_1 = (\epsilon_\uparrow - \epsilon_\downarrow) + \Delta + \Delta\epsilon/2$, and $\Delta\omega_2 = (\epsilon_\downarrow - \epsilon_\uparrow) + \Delta - \Delta\epsilon/2$, where $\Delta\epsilon$ is small detuning, *(ii)* the two-photon Rabi frequencies (phases) to $\Omega_1 = \Omega_2 =: \Omega$ ($\varphi_1 = \varphi_2 =: \varphi$), and *(iii)* the corresponding Raman wave-vectors to $\Delta\boldsymbol{k}_1 \cdot \mathbf{e}_x = \Delta\boldsymbol{k}_2 \cdot \mathbf{e}_x = 0$. In a rotating frame, the Raman-assisted tunneling arising from the corresponding $v^{i,j}_{\sigma,\sigma'}(t)$ term contributes with

$$\begin{aligned} H_{\mathrm{R},1} = &\frac{\Delta\epsilon}{2}\sum_i \left(f^\dagger_{i,\uparrow}f_{i,\uparrow} - f^\dagger_{i,\downarrow}f_{i,\downarrow}\right) \\ &+ \sum_i \Omega e^{-\sqrt{\frac{V_{0,x}}{E_\mathrm{R}}}} \left(e^{\mathrm{i}\varphi} f^\dagger_{i,\uparrow}f_{i+1,\downarrow} + e^{\mathrm{i}\varphi} f^\dagger_{i,\downarrow}f_{i+1,\uparrow} + \mathrm{H.c.}\right), \end{aligned} \tag{5.62}$$

which contains precisely the desired crossed tunnellings for $\varphi = \pi/2$, and the energy imbalance of Fig. 5.7**(b)**.

In order to engineer the horizontal tunneling of Fig. 5.7**(b)** (green lines), we shall make use of a third Raman pair, but this time far detuned from the atomic transition $\Delta\omega_3 \ll (\epsilon_\uparrow - \epsilon_\downarrow)$. In this situation, when the corresponding laser intensities are weak, the Raman term leads to a crossed-beam ac-Stark shift that can be interpreted as slowly-moving shallow optical lattice that acts as a periodic modulation of the on-site energies

$$H_\mathrm{m}(t) = \sum_i \Omega_\sigma \cos(\Delta\mathbf{k}_3 \cdot \boldsymbol{x}^0_i - \Delta\omega_3 t + \varphi_3) f^\dagger_{i,\sigma}f_{i,\sigma}, \tag{5.63}$$

where Ω_σ is the two-photon ac-Stark shift for each of the hyperfine levels, which can be controlled by tuning the intensity and polarization of the lasers. We set *(i)* the Raman frequency in resonance with the gradient $\Delta\omega_3 = \Delta \ll (\epsilon_\uparrow - \epsilon_\downarrow)$; *(ii)* the Raman wave-vector to $\Delta\boldsymbol{k}_3 \cdot \mathbf{e}_x = k_{\mathrm{L},x}$ with respect to the static optical lattice; and *(iii)* the Raman phase $\varphi_3 = 0$. In a rotating frame, the atoms can absorb energy from this shallow moving lattice, such that the horizontal tunneling gets reactivated [39, 40, 242, 243], according to

$$H_{\mathrm{R},2} = H = -t\sum_{i,\sigma} J_1\left(\frac{\Omega_\sigma}{\Delta}\right)\left(f^\dagger_{i,\sigma}f_{i+1,\sigma} + \mathrm{H.c.}\right), \tag{5.64}$$

where we have introduced the n-th order Bessel function of the first class $J_n(x)$. According to this expression, we can laser-assist the horizontal hopping with the desired signs of Fig. 5.7**(b)** by exploiting the state-dependence of the dressed tunneling rates, and setting

$$J_1\left(\frac{\Omega_\uparrow}{\Delta}\right) = -J_1\left(\frac{\Omega_\downarrow}{\Delta}\right). \tag{5.65}$$

This can be achieved, while simultaneously maximizing the dressed tunneling, by setting $\Omega_\uparrow = 3\Delta \approx 0.6\Omega_\downarrow$.

Let us note that the cross-tunneling (5.62) will also get a multiplicative renormalization due to this periodic modulation (5.63), which will be proportional to $J_0((\Omega_\uparrow + \Omega_\downarrow)/\Delta)$. This dressing is similar to the effect exploited for the so-called coherent destruction of tunneling [244–246]. To achieve the relation of the tunnellings of Fig. 5.7**(b)**, one should modify the Rabi frequency of the Raman beams Ω, such that

$$\Omega e^{-\sqrt{\frac{V_{0,x}}{E_{\rm R}}}} J_0\left(\frac{\Omega_\uparrow + \Omega_\downarrow}{\Delta}\right) = t J_1(\Omega_\uparrow), \tag{5.66}$$

although we note that there might be other strategies to fulfill both constraints (5.65)-(5.66) simultaneously. Altogether, considering also Hubbard interactions, the correspondence between the cold-atom and the Gross-Neveu parameters is

$$\frac{1}{a} = 2tJ_1\left(\frac{\Omega_\uparrow}{\Delta}\right), \quad m = \Delta\epsilon - 2tJ_1\left(\frac{\Omega_\uparrow}{\Delta}\right), \quad \frac{g^2}{a} = U_{\uparrow\downarrow}. \tag{5.67}$$

As announced at the beginning of this section, this scheme provides a slight simplification over the proposal for the Creutz-Hubbard model [59], which required the use of an intensity-modulated superlattice, instead of the shallow moving lattice (5.63) already implemented in experiments [39, 40]. At this point, we comment on an interesting alternative that would simplify considerably the cold-atom scheme. As realized recently [219], a different choice of the gamma matrices $\gamma^0 = \sigma^x$, $\gamma^5 = \sigma^y$, simplifies considerably the tunneling of Eq. (5.60), since $\mathrm{i}\gamma^5 + r\gamma^0 = 2\sigma^+$ for a Wilson parameter $r = 1$, where we have introduced the raising operator $\sigma^+ = |\uparrow\rangle\langle\downarrow|$. Accordingly, the kinetic energy of the Wilson fermions can be depicted by the scheme of Fig. 5.7**(c)**. Let us note that the BDI symmetry class can be readily understood by realizing that the synthetic ladder of this figure can be deformed into a single chain with dimerized tunnellings, and thus corresponds to the Su-Schrieffer-Hegger BDI topological insulator [72].

This representation was exploited in [219] to propose a cold-atom realization of quantum electrodynamics with Wilson fermions in $(1+1)$ dimensions (i.e. Schwinger model). In that case, one should introduce a bosonic species to simulate the gauge field, and exploit the spin-changing boson-fermion atomic scattering to obtain the gauge-invariant tunneling of the lattice gauge theory. In our case, the required experimental tools are already contained in our previous description and, more importantly, can be considerably simplified with respect to the above discussion. The vertical tunnellings of Fig. 5.7**(c)** can be obtained from a Raman pair with $\Delta\omega_1 = (\epsilon_\uparrow - \epsilon_\downarrow)$, whereas the diagonal tunnellings require another pair of Raman beams with $\Delta\omega_2 = (\epsilon_\downarrow - \epsilon_\uparrow) + \Delta$, but no additional periodic modulations would be required. Therefore, if no additional disorder is to be considered, which could depend on the particular symmetry class and choice of gamma matrices, this later approach should be followed for the cold-atom experiment, as it simplifies the experimental requirements for the quantum simulation of the GNW model.

Let us finally comment on another interesting alternative. The non-interacting Creutz ladder has been recently realized in multi-orbital optical-lattice experiments [247] that exploit two orbital states of the optical lattice to encode the legs of the ladder, and orbital-changing Raman transitions to implement the inter-leg tunnelings. It would be interesting to study the type of multi-orbital interactions [248] that can be generated in this setup, and the possibility of simulating directly the GNW model studied in this chapter.

Part II

Tensor Network States

Chapter 6

Tensor Networks: Basic Definitions and Properties

6.1 Historical overview

Tensor network (TN) methods in the context of many-body quantum systems have been developed recently. One could however identify some precursors of them in the seminal works of Krammers and Wannier [249, 250], Baxter [251, 252], Kelland [253], Tsang [254], Nighingale and Blote [252], Derrida [255, 256], as found by T. Nishino [257–263]. Here we start their history from the Wilson numerical renormalization group (NRG) [264] . The NRG aims at finding the ground state of a spin system. The idea of the NRG is to start from a small system whose Hamiltonian can be easily diagonalized. The system is then projected on few low-energy states of the Hamiltonian. A new system is then constructed by adding several spins and a new low-energy effective Hamiltonian is obtained working only in the subspace spanned by the low-energy states of the previous step and the full Hilbert space of the new spins. In this way the low-energy effective Hamiltonian can be diagonalized again and its low energy states can be used to construct a new restricted Hilbert space. The procedure is then iterated. The original NRG has been improved, for example, by combining it with the expansion theory [265–267]. As already shown in [264] the NRG successfully tackles the Kondo problem in one dimension [268], however, its accuracy is limited when applied to generic strongly-correlated systems such as Heisenberg chains.

In the nineties, White and Noack were able to relate the poor NRG accuracy with the fact that it fails to consider properly the boundary conditions [132]. In 1992, White proposed the famous density matrix renormalization group (DMRG) that is as of today the most efficient and accurate algorithm for one-dimensional (1D) models [133, 134]. White used the largest eigenvectors of the reduced density matrix of a block as the states describing the relevant part of the low energy physics of Hilbert space. The reduced density matrix is obtained by explicitly constructing the ground state of the system on a larger region. In other words, the space of one block is renormalized by taking the rest of the system as an *environment*.

The simple idea of environment had revolutionary consequences in the RG-based algorithms. Important generalizations of DMRG were then developed, including the finite-temperature variants of matrix renormalization group [269–272], dynamic DMRG algorithms [273–276], and corner transfer matrix renormalization group by Nishino and Okunishi [257]

About ten years later, TN were re-introduced in the simplest form of matrix-product states (MPS) [255,256,277–279] in the context of the theory of entanglement in quantum many-body systems; see, e.g., [51, 280–282] [1]. In this context, the MPS encodes the coefficients of the wave functions in a product of matrices, and are thus defined as the contraction of a one dimensional TN. Each elementary tensor has three indexes: one physical index acting on the physical Hilbert space of the constituent, and two auxiliary indexes that will be contracted. The MPS structure is chosen since it represents the states whose entanglement only scales with the boundary of a region rather than its volume, something called the "area law" of entanglement. Furthermore, an MPS gives only finite correlations, thus is well suited to represent the ground states of the gapped short-range Hamiltonians. The relation between these two facts was evinced in seminal contributions [57, 92, 287–294] and led Verstraete and Cirac to prove that MPS can provide faithful representations of the ground states of 1D gapped local Hamiltoinan [295].

These results, together with the previous works that identified the outcome of converged DMRG simulations with an MPS description of the ground states [296], allowed to better understand the impressive performances of DMRG in terms of the correct scaling of entanglement of its underlying TN ansatz. The connection between DMRG and MPS stands in the fact that the projector onto the effective Hilbert space built along the DMRG iterations can be seen as an MPS. Thus, the MPS in DMRG can be understood not only as a 1D state ansatz, but also as a TN representation of the RG flows ([50, 278, 296–299], as recently reviewed in [52]).

These results from the quantum information community fueled the search for better algorithms allowing to optimize variationally the MPS tensors in order to target specific states [53]. In this broader scenario, DMRG can be seen as an alternating-least-square optimization method. Alternative methods include the imaginary-time evolution from an initial state encoded as in an MPS base of the time-evolving block decimation (TEBD) [305–308], and time-dependent variational principle of MPS [309]. Note that these two schemes can be generalized to simulate also the short out-of-equilibrium evolution of a slightly entangled state. MPS have been used beyond ground states, for example in the context of finite-temperature and low-energy excitations based on MPS or its transfer matrix [296, 310–314].

MPS have further been used to characterize states violating the area law of entanglement, such as ground states of critical systems, and ground states of Hamiltonian with long-range interactions [292, 315, 316, 316–323].

The relevance of MPS goes far beyond their use as a numerical ansatz. There have been numerous analytical studies that have led to MPS exact solutions such as the Affleck-Kennedy-Lieb-Tasaki (AKLT) state [324, 325], as well as its higher-spin / higher-dimensional generalizations [51, 277, 326–329]. MPS has also been crucial in understanding the classification of topological phases in 1D [330]. Here we will not talk about these important results, but we will focus on numerical applications even though the theory of MPS is still in full development and constantly new fields emerge such as the application of MPS to 1D quantum field theories [331].

A natural way is to extend the MPS representation, leading to the tensor product state [332], or projected entangled pair state (PEPS) [333,334]. While an MPS is made up of tensors aligned in a 1D chain, a PEPS is formed by tensors located in a 2D lattice, forming a 2D TN. Thus, PEPS can be regarded as one type of 2D tensor network states

[1] For the general theory of entanglement and its role in the physics of quantum-many body systems, see for instance [283–286].

(TNS). Note that the work of Affleck *et al* [335] can be considered as a prototype of PEPS.

The network structure of the PEPS allows us to construct 2D states that strictly fulfill the area law of entanglement entropy [58]. It indicates that PEPS can efficiently represent 2D gapped states, and even the critical and topological states, with only finite bond dimensions. Examples include resonating valence bond states [58, 336–339] originally proposed by Anderson *et al* for super-conductivity [340–344], string-net states [345–347] proposed by Wen *et al* for gapped topological orders [69, 70, 348–352], and so on.

The network structure makes PEPS so powerful that it can encode difficult computational problems including non-deterministic polynomial (NP) hard ones [58, 353, 354]. What is even more important for physics is that PEPS provides an efficient representation as a variational ansatz for calculating ground states of 2D models. However, obeying the area law costs something else: the computational complexity rises [58, 353, 355]. For instance, after having determined the ground state (either by construction or variation), one usually wants to extract the physical information by computing, e.g., energies, order parameters, or entanglement. For an MPS, most of the tasks are matrix manipulations and products which can be easily done by classical computers. For PEPS, one needs to contract a TN stretching in a 2D plain, unfortunately, most of which cannot be neither done exactly or nor even efficiently. The reason for this complexity is what brings the physical advantage to PEPS: the network structure. Thus, algorithms to compute the TN contractions need to be developed.

The PEPS are not the only TN representations in higher dimensions. Except for a chain or 2D lattice, TN can be defined with some other geometries, such as trees or fractals. Tree TNS is one example with non-trivial properties and applications [277, 326, 356–369]. Another example is multi-scale entanglement renormalization ansatz (MERA) proposed by Vidal [370–378], which is a powerful tool especially for studying critical systems [379–384] and AdS/CFT theories ([385–391], see [392] for a general introduction of CFT).

The TN can also represent operators, usually dubbed as TN operators. Generally speaking, a TN state can be considered as a linear mapping from the physical Hilbert space to a scalar given by the contraction of tensors. A TN operator is regarded as a mapping from the *bra* to the *ket* Hilbert space. Many algorithms explicitly employ the TN operator form, including the matrix product operator (MPO) for representing 1D many-body operators and mixed states, and for simulating 1D systems in and out of equilibrium [393–403], tensor product operator (also called projected entangled pair operators) for higher dimensional systems [404–416], and multiscale entangled renormalization ansatz [417–419].

This chapter is to introduce some basic definitions and concepts of TN. We will show that the TN can be used to represent quantum many-body states, where we explain MPS in 1D and PEPS in 2D systems, as well as the generalizations to thermal states and operators. The quantum entanglement properties of the TN states including the area law of entanglement entropy will also be discussed. Finally, we will present several special TN's that can be exactly contracted, and demonstrate the difficulty of contracting TN's in general cases.

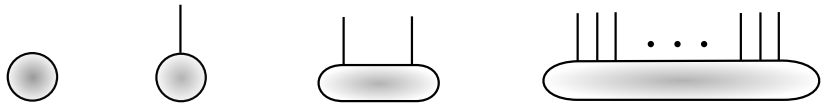

Figure 6.1: From left to right, the graphic representations of a scalar, vector, matrix and tensor.

6.2 Scalar, vector, matrix and tensor

Generally speaking, a tensor is defined as a series of numbers labelled by N indexes, with N called the *order* of the tensor [2]. In this context, a scalar, which is one number and labelled by zero index, is a 0th-order tensor. Many physical quantities are scalars, including energy, free energy, magnetization and so on. Graphically, we use a dot to represent a scalar (Fig. 6.1).

A D-component vector consists of D numbers labelled by one index, and thus is a 1st-order tensor. For example, one can write the state vector of a spin-1/2 in a chosen basis (say the eigenstates of the spin operator $\hat{S}^{[z]}$) as

$$|\psi\rangle = C_1|0\rangle + C_2|1\rangle = \sum_{s=0,1} C_s|s\rangle, \tag{6.1}$$

with the coefficients C a two-component vector. Here, we use $|0\rangle$ and $|1\rangle$ to represent spin up and down states. Graphically, we use a dot with one open bond to represent a vector (Fig.6.1).

A matrix is in fact a 2nd-order tensor. Considering two spins as an example, the state vector can be written under an irreducible representation as a four-dimension vector. Instead, under the local basis of each spin, we write it as

$$|\psi\rangle = C_{00}|0\rangle|0\rangle + C_{01}|0\rangle|1\rangle + C_{10}|1\rangle|0\rangle + C_{11}|1\rangle|1\rangle = \sum_{ss'=0}^{1} C_{ss'}|s\rangle|s'\rangle, \tag{6.2}$$

with $C_{ss'}$ a matrix with two indexes. Here, one can see that the difference between a $(D \times D)$ matrix and a D^2-component vector in our context is just the way of labelling the tensor elements. Transferring among vector, matrix and tensor like this will be frequently used later. Graphically, we use a dot with two bonds to represent a matrix and its two indexes (Fig.6.1).

It is then natural to define an N-th order tensor. Considering, e.g., N spins, the 2^N coefficients can be written as a N-th order tensor C [3], satisfying

$$|\psi\rangle = \sum_{s_1\cdots s_N=0}^{1} C_{s_1\ldots s_N}|s_1\rangle\ldots|s_N\rangle. \tag{6.3}$$

Similarly, such a tensor can be *reshaped* into a 2^N-component vector. Graphically, an N-th order tensor is represented by a dot connected with N open bonds (Fig.6.1).

In above, we use states of spin-1/2 as examples, where each index can take two values. For a spin-S state, each index can take $d = 2S + 1$ values, with d called the *bond dimension*. Besides quantum states, operators can also be written as tensors. A spin-1/2 operator $\hat{S}^\alpha$ $(\alpha = x, y, z)$ is a (2×2) matrix by fixing the basis, where we have

[2]Note that in some references, N is called the tensor *rank*. Here, the word *rank* is used in another meaning, which will be explained later.

[3]If there is no confuse, we use the symbol without all its indexes to refer to a tensor for conciseness, e.g., use C to represent $C_{s_1\ldots s_N}$.

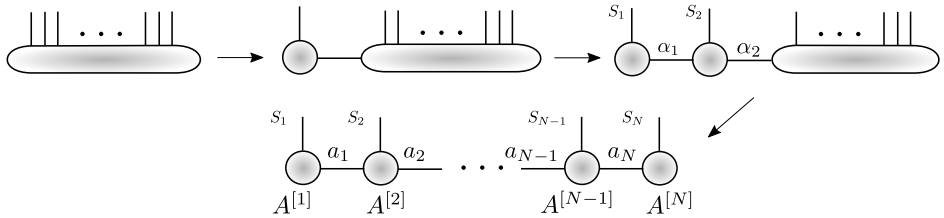

Figure 6.2: An impractical way to obtain an MPS from a many-body wave-function is to repetitively use the SVD.

$S^{\alpha}_{s_1' s_2' s_1 s_2} = \langle s_1' s_2' | \hat{S}^{\alpha} | s_1 s_2 \rangle$. In the same way, an N-spin operator can be written as a $2N$-th order tensor, with N *bra* and N *ket* indexes [4].

We would like to stress some conventions about the "indexes" of a tensor (including matrix) and those of an operator. A tensor is just a group of numbers, where their indexes are defined as the labels labelling the elements. Here, we always put all indexes as the lower symbols, and the upper "indexes" of a tensor (if exist) are just a part of the symbol to distinguish different tensors. For an operator which is defined in a Hilbert space, it is represented by a hatted letter, and there will be no "true" indexes, meaning that both upper and lower "indexes" are just parts of the symbol to distinguish different operators.

6.3 Tensor network states

Now that we have established the notation, the following sections will examine some key tensor networks for strongly interacting quantum many body systems. We begin with one dimensional models introducing the MPS. Then we will show the generalization of MPS introducing tree TN and PEPS.

6.3.1 Matrix product states

Now we take a N-spin state as an example to explain the MPS, a simple but powerful 1D TN state. In an MPS, the coefficients are written as a TN given by the contraction of N tensors. Schollwöck in his review [50] provides a straightforward way to obtain such a TN is by repetitively using SVD or QR decomposition (Fig. 6.2). First, we group the first $N-1$ indexes together as one large index, and write the coefficients as a $2^{N-1} \times 2$ matrix. Then implement SVD or any other decomposition (for example QR decomposition) as the contraction of $C^{[N-1]}$ and $A[N]$

$$C_{s_1 \cdots s_{N-1} s_N} = \sum_{a_{N-1}} C^{[N-1]}_{s_1 \cdots s_{N-1}, a_{N-1}} A^{[N]}_{s_N, a_{N-1}}. \tag{6.4}$$

Note that as a convention in this chapter, we always put the physical indexes in front of geometrical indexes and use a comma to separate them. For the tensor $C^{[N-1]}$, one can do the similar thing by grouping the first $N-2$ indexes and decompose again as

$$C_{s_1 \cdots s_{N-1} a_{N-1}} = \sum_{a_{N-2}} C^{[N-2]}_{s_1 \cdots s_{N-2}, a_{N-2}} A^{[N-1]}_{s_{N-1}, a_{N-2} a_{N-1}}. \tag{6.5}$$

[4] Note that here, we do not distinguish *bra* and *ket* indexes deliberately in a tensor, if not necessary

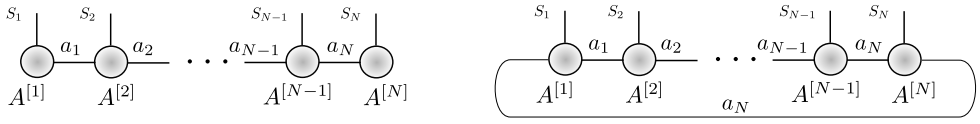

Figure 6.3: The graphic representations of the matrix product states with open (left) and periodic (right) boundary conditions.

Then the total coefficients becomes the contraction of three tensors as

$$C_{s_1\cdots s_{N-1}s_N} = \sum_{a_{N-2}a_{N-1}} C^{[N-2]}_{s_1\cdots s_{N-2},a_{N-2}} A^{[N-1]}_{s_{N-1},a_{N-2}a_{N-1}} A^{[N]}_{s_N,a_{N-1}}. \tag{6.6}$$

Repeat decomposing in the above way until each tensor only contains one physical index, we have the MPS representation of the state as

$$C_{s_1\cdots s_{N-1}s_N} = \sum_{a_1\cdots a_{N-1}} A^{[1]}_{s_1,a_1} A^{[2]}_{s_2,a_1a_2} \cdots A^{[N-1]}_{s_{N-1},a_{N-2}a_{N-1}} A^{[N]}_{s_N,a_{N-1}}. \tag{6.7}$$

One can see that an MPS is a TN formed by the contraction of N tensors. Graphically, MPS is represented by a 1D graph with N open bonds. In fact, an MPS given by Eq. (6.7) has open boundary condition, and can be generalized to periodic boundary condition (Fig. 6.3) as

$$C_{s_1\cdots s_{N-1}s_N} = \sum_{a_1\cdots a_N} A^{[1]}_{s_1,a_Na_1} A^{[2]}_{s_2,a_1a_2} \cdots A^{[N-1]}_{s_{N-1},a_{N-2}a_{N-1}} A^{[N]}_{s_N,a_{N-1}a_N}, \tag{6.8}$$

where all tensors are 3rd-order. Moreover, one can introduce translational invariance to the MPS, i.e. $A^{[n]} = A$ for $n = 1, 2, \cdots, N$. We use χ, dubbed as *bond dimension* of the MPS, to represent the dimension of each geometrical index.

MPS is an efficient representation of a many-body quantum state. For a N-spin state, the number of the coefficients is 2^N which increases exponentially with N. For an MPS given by Eq. (6.8), it is easy to count that the total number of the elements of all tensors is $Nd\chi^2$ which increases only linearly with N. The above way of obtaining MPS with decompositions is also known as tensor train decomposition (TTD) in MLA, and MPS is also called tensor-train form [420]. The main aim of TTD is investigating the algorithms to obtain the optimal tensor train form of a given tensor, so that the number of parameter can be reduced with well-controlled errors.

In physics, the above procedure shows that any states can be written in an MPS, as long as we do not limit the dimensions of the geometrical indexes. However, it is extremely impractical and inefficient, since in principle, the dimensions of the geometrical indexes $\{a\}$ increase exponentially with N. In the following sections, we will directly applying the mathematic form of the MPS without considering the above procedure.

Now we introduce a simplified notation of MPS that has been widely used in the community of physics. In fact with fixed physical indexes, the contractions of geometrical indexes are just the inner products of matrices (this is how its name comes from). In this sense, we write a quantum state given by Eq. (6.7) as

$$|\psi\rangle = tTrA^{[1]}A^{[2]}\cdots A^{[N]}|s_1s_2\cdots s_N\rangle = tTr\prod_{n=1}^{N} A^{[n]}|s_n\rangle. \tag{6.9}$$

tTr stands for summing over all shared indexes. The advantage of Eq. (6.9) is to give a general formula for an MPS of either finite or infinite size, with either periodic or open boundary condition.

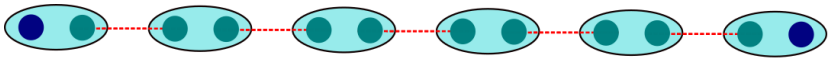

Figure 6.4: An intuitive graphic representation of the AKLT state. The big circles representing $S = 1$ spins, and the small ones are effective $S = \frac{1}{2}$ spins. Each pair of spin-1/2 connecting by a red bond forms a singlet state. The two "free" spin-1/2 on the boundary give the edge state.

6.3.2 Afflect-Kennedy-Lieb-Tasaki state

MPS is not just a mathematic form. It can represent non trivial physical states. One important example can be found with AKLT model proposed in 1987, a generalization of spin-1 Heisenberg model [324]. For 1D systems, Mermin-Wagner theorem forbids any spontaneously breaking of continuous symmetries at finite temperature with sufficiently short-range interactions. For the ground state of AKLT model called AKLT state, it possesses the *sparse anti-ferromagnetic order* [5], which provides a non-zero excitation gap under the framework of Mermin-Wagner theorem. Moreover, AKTL state provides us a precious exactly-solvable example to understand edge states and (symmetry-protected) topological orders.

AKLT state can be exactly written in an MPS with $\chi = 2$ (see [52] for example). Without losing generality, we assume periodic boundary condition. Let us begin with the AKLT Hamiltonian that can be given by spin-1 operators as

$$\hat{H} = \sum_n \left[\frac{1}{2} \hat{S}_n \cdot \hat{S}_{n+1} + \frac{1}{6} (\hat{S}_n \cdot \hat{S}_{n+1})^2 + \frac{1}{3} \right]. \tag{6.10}$$

By introducing the non-negative-defined projector $\hat{P}_2(\hat{S}_n + \hat{S}_{n+1})$ that projects the neighbouring spins to the subspace of $S = 2$, Eq. (6.10) can be rewritten in the summation of projectors as

$$\hat{H} = \sum_n \hat{P}_2(\hat{S}_n + \hat{S}_{n+1}). \tag{6.11}$$

Thus, the AKLT Hamiltonian is non-negative-defined, and its ground state lies in its kernel space, satisfying $\hat{H}|\psi_{AKLT}\rangle = 0$ with a zero energy.

Now we construct a wave-function which has a zero energy. As shown in Fig. 6.4, we put on each site a projector that maps two (effective) spins-1/2 to a *triplet*, i.e. the physical spin-1, where the transformation of the basis obeys

$$|+\rangle = |00\rangle \tag{6.12}$$

$$|\tilde{0}\rangle = \frac{1}{\sqrt{2}}(|01\rangle + |10\rangle), \tag{6.13}$$

$$|-\rangle = |11\rangle. \tag{6.14}$$

The corresponding projector is determined by the Clebsch-Gordan coefficients [421], and is a (3×4) matrix. Here, we rewrite it as a $(3\times2\times2)$ tensor, whose three components (regarding to the first index) are the ascending, z-component and descending Pauli matrices of spin-1/2 [6],

$$\sigma^+ = \begin{bmatrix} 0 & 1 \\ 0 & 0 \end{bmatrix}, \quad \sigma^z = \begin{bmatrix} 1 & 0 \\ 0 & -1 \end{bmatrix}, \quad \sigma^- = \begin{bmatrix} 0 & 0 \\ 1 & 0 \end{bmatrix}. \tag{6.15}$$

[5] One possible configuration of the sparse anti-ferromagnetic ordered state is .. ↑↓ .. ↑ . ↓↑ ... ↓. A dot represents the $S = 0$ state. Without looking at all the $S = 0$ states, the spins are arranged in the anti-ferromagnetic way.

[6] Here, one has some degrees of freedom to choose different projectors, which is only up to a gauge transformation. But once one projector is fixed, the other is also fixed.

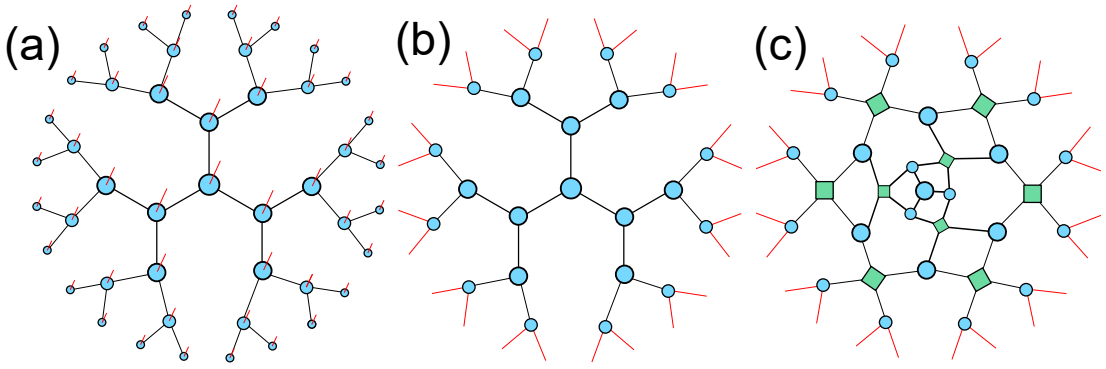

Figure 6.5: The illustration of (a) and (b) two different TTNS's and (c) MERA.

In the language of MPS, we have the tensor A satisfying

$$A_{0,aa'} = \sigma^+_{aa'}, \quad A_{1,aa'} = \sigma^z_{aa'}, \quad A_{2,aa'} = \sigma^-_{aa'}. \tag{6.16}$$

Then we put another projector to map two spin-1/2 to a singlet, i.e. a spin-0 with

$$|\bar{0}\rangle = \frac{1}{\sqrt{2}}(|01\rangle - |10\rangle) \tag{6.17}$$

The projector is in fact a (2×2) identity with the choice of Eq. (6.15),

$$I = \begin{bmatrix} 1 & 0 \\ 0 & 1 \end{bmatrix}. \tag{6.18}$$

Now, the MPS of the AKLT state with periodic boundary condition (up to a normalization factor) is obtained by Eq. (6.8), with every tensor A given by Eq. (6.16). For such an MPS, every projector operator $\hat{P}_2(\hat{S}_n + \hat{S}_{n+1})$ in the AKLT Hamiltonian is always acted on a singlet, then we have $\hat{H}|\psi_{AKLT}\rangle = 0$.

6.3.3 Tree tensor network state (TTNS) and projected entangled pair state (PEPS)

TTNS is a generalization of the MPS that can code more general entanglement states. Unlike an MPS where the tensors are aligned in a 1D array, a TTNS is given by a tree graph. Figs. 6.5 (a) and (b) show two examples of TTNS with the coordination number $z = 3$. The red bonds are the physical indexes and the black bonds are the geometrical indexes connecting two adjacent tensors. The physical ones may locate on each tensor or put on the boundary of the tree. A tree is a graph that has no loops, which leads to many simple mathematical properties that parallel to those of an MPS. For example, the partition function of a TTNS can be efficiently exactly computed. A similar but more power TN state called MERA also has such a property [Figs. 6.5 (c)]. Note an MPS can be treated as a tree with $z = 2$.

An important generalization to the TN's of loopy structures is known as projected entangled pair state (PEPS), proposed by Verstraete and Cirac [333, 334]. The tensors of a PEPS are located in, instead of a 1D chain or a tree graph, a d-dimensional lattice, thus graphically forming a d-dimensional TN. An intuitive picture of PEPS is given in Fig. 6.6, i.e., the tensors can be understood as projectors that map the physical spins into virtual ones. The virtual spins form the maximally entangled state in a way

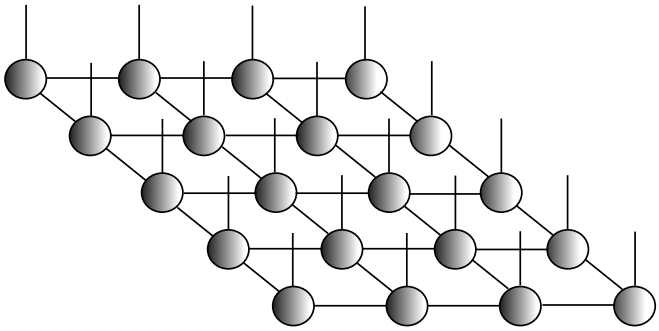

Figure 6.6: An intuitive picture of the projected entangled pair state.

determined by the geometry of the TN. Note that such an intuitive picture was firstly proposed with PEPS [333], but it also applies to TTNS.

Similar to MPS, a TTNS or PEPS can be formally written as

$$|\Psi\rangle = tTr \prod_n P^{[n]} |s_n\rangle, \tag{6.19}$$

where tTr means to sum over all geometrical indexes. Usually, we do not write the formula of a TTNS or PEPS, but give the graph instead to clearly show the contraction relations. Such a generalization makes a lot of senses in physics. One key factor regards the *area law of entanglement entropy* [92, 290–294] which we will talk about later in this chapter. In the following as two straightforward examples, we show that PEPS can indeed represents non-trivial physical states including nearest-neighbour *resonating valence bond* (RVB) and Z_2 *spin liquid* states. Note these two types of states on trees can be similarly defined by the corresponding TTNS.

6.3.4 PEPS can represent non-trivial many-body states: examples

RVB state was firstly proposed by Anderson to explain the possible disordered ground state of the Heisenberg model on triangular lattice [340, 341]. RVB state is defined as the superposition of macroscopic configurations where all spins are paired to form the singlet states (dimers). The strong fluctuations are expected to restore all symmetries and lead to a spin liquid state without any local orders. The distance between two spins in a dimer can be short range or long range. For nearest-neighbor RVB, the dimers are only be nearest neighbors (Fig. 6.7, also see [422]). RVB state is supposed to relate to high-T_c copper-oxide-based superconductor. By doping the singlet pairs, the insulating RVB state can translate to a charged superconductive state [342–344].

For the nearest-neighbour situation, an RVB state (defined on an infinite square lattice, for example) can be exactly written in a PEPS of $\chi = 3$. Without losing generality, we take the translational invariance, i.e., the TN is formed by infinite copies of several inequivalent tensors. Two different ways have been proposed to construct the nearest-neighbor RVB PEPS [58, 337]. In addition, Wang *et al* proposed a way to construct the PEPS with long-range dimers [338]. In the following, we explain the way proposed by Verstraete *et al* to construct the nearest-neighbor one [58]. There are two inequivalent tensors: the tensor defined on each site whose dimensions are $(2 \times 3 \times 3 \times 3 \times 3)$ only has five non zero elements,

$$P_{0,0000} = 1, \quad P_{1,2111} = 1, \quad P_{1,1211} = 1, \quad P_{1,1121} = 1, \quad P_{1,1112} = 1. \tag{6.20}$$

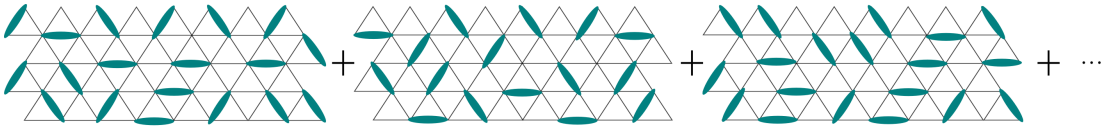

Figure 6.7: The nearest-neighbor RVB state is the superposition of all possible configurations of nearest-neighbor singlets.

We use the language of strings to understand physical meaning of the projector: the spin-up state (with the physical index $s = 0$) stands for the vacuum state and the spin-down ($s = 1$) for the occupied state of a string. In this sense, the first element $P_{0,0000}$ means it is vacuum in the physical space, thus all the geometrical spaces are vacuum. For the rest four elements, the physical space is occupied by a string that is mapped to one of the geometrical space with the same amplitude, leaving the rest three to be vacuum. For example, $P_{1,1211} = 1$ means one possibility, where the physical string is mapped to the second geometrical space while the rest three remain vacuum [7]. The rest elements are all zero, which means the corresponding configurations are forbidden. The tensor P only maps physical strings to geometrical spaces. Then a projector B is put on each geometrical bond to form the singlets in the RVB picture. B is a (3×3) matrix with only three non zero elements

$$B_{00} = 1, \quad B_{12} = 1, \quad B_{21} = -1. \tag{6.21}$$

Similarly, the first one means a vacuum state on this geometrical bond, and the rest two simply give a singlet state ($|12\rangle - |21\rangle$).

Then the infinite PEPS (iPEPS) of the nearest-neighbor RVB is given by the contraction of infinite copies of P's on the sites and B's (Fig.6.6) on the bonds as

$$|\Psi\rangle = \sum_{\{s,a\}} \prod_{n \in sites} P_{s_n, a_n^1 a_n^2 a_n^3 a_n^4} \prod_{m \in bonds} B_{a_m^1 a_m^2} \prod_{j \in sites} |s_j\rangle. \tag{6.22}$$

After the contraction of all geometrical indexes, the state is the super-position of all possible configurations consisting of nearest-neighbour dimers. This iPEPS looks different from the one given in Eq. (6.19) but they are essentially the same, because one can contract the B's into P's so that the PEPS is only formed by tensors defined on the sites.

Another example is the Z_2 spin liquid state, which is one of simplest string-net states [345–347], firstly proposed by Levin and Wen to characterize gapped topological orders [352]. Similarly with the picture of strings, the Z_2 state is the super-position of all configurations of string loops. Writing such a state with TN, the tensor on each vertex is $(2 \times 2 \times 2 \times 2)$ satisfying

$$P_{a_1 \cdots a_N} = \begin{cases} 1, & a_1 + \cdots + a_N = even, \\ 0, & otherwise. \end{cases} \tag{6.23}$$

The tensor P forces the *fusion rules* of the strings: the number of the strings connecting to a vertex must be even, so that there are no loose ends and all strings have to form loops. It is also called in some literatures the *ice rule* [423, 424] or *Gauss' law* [425]. In addition, the square TN formed solely by the tensor P gives the famous *eight-vertex model*, where the number "eight" corresponds to the eight non-zero elements (i.e. allowed sting configurations) on a vertex [426].

[7] Note that for a geometrical space, 0 and 1 are to distinguish the vacuum states with vacuum and occupied physical states, respectively.

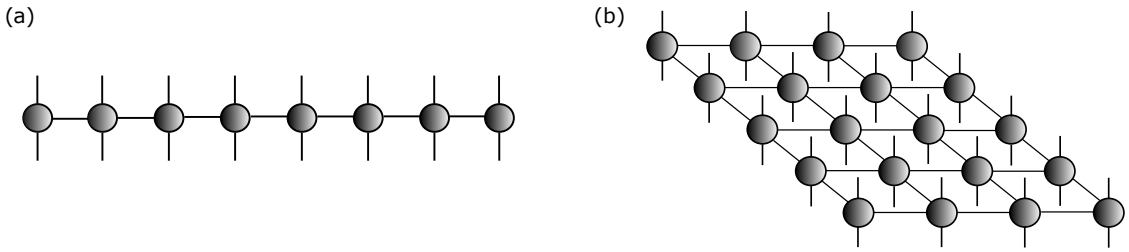

Figure 6.8: (a) The graphic representation of a matrix product operator, where the upward and downward indexes represent the *bra* and *ket* space, respectively. (b)The graphic representation of a projected entangled pair operator, where the upward and downward indexes represent the *bra* and *ket* space, respectively.

The tensors B are defined on each bond to project the strings to spins, whose non-zero elements are

$$B_{0,00} = 1, \quad B_{1,11} = 1. \tag{6.24}$$

The tensor B is a projector that maps the spin-up (spin-down) state to the occupied (vacuum) state of a string.

6.4 Tensor network operators

The MPS or PEPS can be readily generalized from representations of states to those of operators called MPO [393–396, 400–403] or projected entangled pair operator (PEPO) [8] [404–409, 411–414]. Let us begin with MPO, which is also formed by the contraction of local tensors as

$$\hat{O} = \sum_{\{s,a\}} \prod_n W^{[n]}_{s_n s'_n, a_n a_{n+1}} |s_n\rangle\langle s'_n|. \tag{6.25}$$

Different from MPS, each tensor has two physical indexes, of which one is a *bra* and the other is a *ket* index (Fig. 6.8 (a)). An MPO may represent several non-trivial physical models, for example the Hamiltonian. Crosswhite and Bacon [427] proposed a general way of constructing an MPO from called *automata*. Now we show how to construct the MPO of an Hamiltonian using the properties of a *triangular MPO*. Let us start from a general lower-triangular MPO satisfying $W^{[n]}_{::,00} = C^{[n]}$, $W^{[n]}_{::,01} = B^{[n]}$, and $W^{[n]}_{::,11} = A^{[n]}$ with $A^{[n]}$, $B^{[n]}$, and $C^{[n]}$ some $d \times d$ square matrices. We can write $W^{[n]}$ in a more explicit 2×2 block-wise form as

$$W^{[n]} = \begin{pmatrix} C^{[n]} & 0 \\ B^{[n]} & A^{[n]} \end{pmatrix} \tag{6.26}$$

If one puts such a $W^{[n]}$ in Eq. (6.25), it will give the summation of all terms in the

[8] Generally, a representation of an operator with a TN can be called tensor product operator (TPO). MPO and PEPO are two examples.

form of

$$\begin{aligned} O &= \sum_{n=1}^{N} A^{[1]} \otimes \cdots \otimes A^{[n-1]} \otimes B^{[n]} \otimes C^{[n+1]} \otimes \cdots \otimes C^{[N]} \\ &= \sum_{n=1}^{N} \prod_{\otimes i=1}^{n-1} A^{[i]} \otimes B^{[n]} \otimes \prod_{\otimes j=n+1}^{N} C^{[j]}, \end{aligned} \tag{6.27}$$

with N the total number of tensors and $\prod_{\otimes}$ the tensor product [9]. Such a property can be easily generalized to a W formed by $D \times D$ blocks.

Imposing Eq. (6.27), we can construct as an example the summation of one-site local terms, i.e., $\sum_n X^{[n]}$ [10], with

$$W^{[n]} = \begin{pmatrix} I & 0 \\ X^{[n]} & I \end{pmatrix}, \tag{6.28}$$

with $X^{[n]}$ a $d \times d$ matrix and I the $d \times d$ identity.

If two-body terms are included, such as $\sum_m X^{[m]} + \sum_n Y^{[n]} Z^{[n+1]}$, we have

$$W^{[n]} = \begin{pmatrix} I & 0 & 0 \\ Z^{[n]} & 0 & 0 \\ X^{[n]} & Y^{[n]} & I \end{pmatrix}. \tag{6.29}$$

This can be obviously generalized to L-body terms. With open boundary conditions, the left and right tensors are

$$W^{[1]} = \begin{pmatrix} I & 0 & 0 \end{pmatrix}, \tag{6.30}$$

$$W^{[N]} = \begin{pmatrix} 0 \\ 0 \\ I \end{pmatrix}. \tag{6.31}$$

Now we apply the above technique on a Hamiltonian of, e.g., the Ising model in a transverse field

$$\hat{H} = \sum_n \hat{S}_n^z \hat{S}_{n+1}^z + h \sum_m \hat{S}_m^x. \tag{6.32}$$

Its MPO is given by

$$W^{[n]} = \begin{pmatrix} I & 0 & 0 \\ \hat{S}^z & 0 & 0 \\ h\hat{S}^x & \hat{S}^z & I \end{pmatrix}. \tag{6.33}$$

Such a way of constructing an MPO is very useful. Another example is the Fourier transformation to the number operator of Hubbard model in momentum space $\hat{n}_k = \hat{b}_k^\dagger \hat{b}_k$. The Fourier transformation is written as

$$\hat{n}_k = \sum_{m,n=1}^{N} e^{i(m-n)k} \hat{b}_m^\dagger \hat{b}_n, \tag{6.34}$$

[9] For $n = 0$, $A^{[0]}$ (or $B^{[0]}$, $C^{[0]}$) does not exist but can be defined as a scalar 1, for simplicity of the formula.

[10] Note that $X^{[n_1]}$ and $X^{[n_2]}$ are not defined in a same space with $n_1 \neq n_2$, Thus, precisely speaking, $\sum$ here is the direct sum. We will not specify this when it causes no confuse

with $\hat{b}_n$ ($\hat{b}_n^\dagger$) the annihilation (creation) operator on the n-th site. The MPO representation of such a Fourier transformation is given by

$$\hat{W}_n = \begin{pmatrix} \hat{I} & 0 & 0 & 0 \\ \hat{b}^\dagger & e^{ik}\hat{I} & 0 & 0 \\ \hat{b} & 0 & e^{-ik}\hat{I} & 0 \\ \hat{b}^\dagger\hat{b} & e^{+ik}\hat{b}^\dagger & e^{-ik}\hat{b} & \hat{I} \end{pmatrix} \tag{6.35}$$

with $\hat{I}$ the identical operator in the corresponding Hilbert space.

The MPO formulation also allows for a convenient and efficient representation of the Hamiltonians with longer range interactions [428]. The geometrical bond dimensions will in principle increase with the interaction length. Surprisingly, a small dimension is needed to approximate the Hamiltonian with long-range interactions that decay polynomially [404].

Besides, MPO can be used to represent the time evolution operator $\hat{U}(\tau) = e^{-\tau\hat{H}}$ with *Trotter-Suzuki decomposition*, where τ is a small positive number called *Trotter-Suzuki step* [306, 307]. Such an MPO is very useful in calculating real, imaginary, or even complex time evolutions, which we will present later in detail. An MPO can also give a mixed state.

Similarly, PEPS can also be generalized to projected entangled pair operator (PEPO, Fig. 6.8 (b)), which on a square lattice for instance can be written as

$$\hat{O} = \sum_{\{s,a\}} \prod_n W^{[n]}_{s_n s'_n, a_n^1 a_n^2 a_n^3 a_n^4} |s_n\rangle\langle s'_n|. \tag{6.36}$$

Each tensor has two physical indexes (*bra* and *ket*) and four geometrical indexes. Each geometrical bond is shared by two adjacent tensors and will be contracted.

6.5 Tensor networks and quantum entanglement

The numerical methods based on TN face great challenges, primarily that the dimension of the Hilbert space increases exponentially with the size. Such an "*exponential wall*" has been treated in different ways by many numeric algorithms, including the DFT methods [429] and QMC approaches [430].

The power of TN has been understood in the sense of quantum entanglement: the entanglement structure of low-lying energy states can be efficiently encoded in TNS's. It takes advantage of the fact that not all quantum states in the total Hilbert space of a many-body system are equally relevant to the low-energy or low-temperature physics. It has been found that the low-lying eigenstates of a gapped Hamiltonian with local interactions obey the area law of the entanglement entropy [431].

More precisely speaking, for a certain subregion $\mathcal{R}$ of the system, its reduced density matrix is defined as $\hat{\rho}_\mathcal{R} = \mathrm{Tr}_\mathcal{E}(\hat{\rho})$, with $\mathcal{E}$ denotes the spatial complement of $\mathcal{R}$. The entanglement entropy is defined as

$$S(\rho_\mathcal{R}) = -\mathrm{Tr}\{\rho_\mathcal{R}\log(\rho_\mathcal{R})\}. \tag{6.37}$$

Then the area law of the entanglement entropy [289, 294] reads

$$S(\rho_\mathcal{R}) = O(|\partial\mathcal{R}|), \tag{6.38}$$

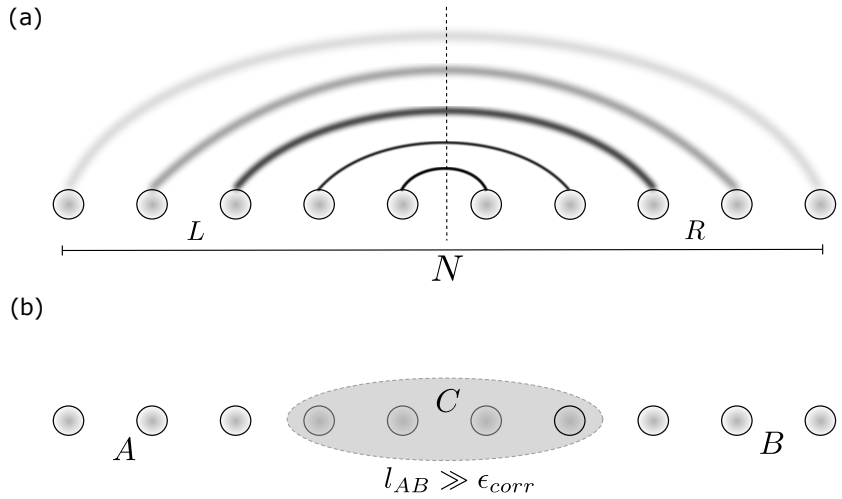

Figure 6.9: (a) Bipartition of a 1D system into two half chains. Significant quantum correlations in gapped ground states occur only on short length scales. (b) The argue the 1D area law, the chain is separated into three sub-systems denoted by A, B and C. If the correlation length ξ_{corr} is much larger than the size of B (denoted by l_{AC}), the reduced density matrix by tracing B approximately satisfies $\hat{\rho}_{AC} \simeq \hat{\rho}_A \otimes \hat{\rho}_C$.

with $|\partial\mathcal{R}|$ the size of the boundary. In particular, for a D-dimensional system, one has

$$S = O(l^{D-1}), \tag{6.39}$$

with l the length scale. This means that for 1D systems, $S = const.$ The area law suggests that the low-lying eigenstates stay in a "small corner" of the full Hilbert space of the many-body system, and that they can be described by a much smaller number of parameters. We shall stress that the locality of the interactions is not sufficient to the area law. Vitagliano, *el al* show that simple 1D spin models can exhibit volume law, where the entanglement entropy scales with the bulk [432, 433].

The area law of entanglement entropy is intimately connected to another fact that a non-critical quantum system exhibits a finite correlation length. The correlation functions between two blocks in a gapped system decay exponentially as a function of the distance of the blocks [287], which is argued to lead to the area law. An intuitive picture can be seen in Fig. 6.9 (a). Let us consider a 1D gapped quantum system whose ground state $|\psi_{ABC}\rangle$ possesses a correlation length ξ_{corr}. By dividing into three subregions A, B and C, the reduced density operator $\hat{\rho}_{AC}$ is obtained when tracing out the block B, i.e. $\hat{\rho}_{AC} = \mathrm{Tr_B}|\psi_{\mathrm{ABC}}\rangle\langle\psi_{\mathrm{ABC}}|$ (see Fig. 6.9 (b)). In the limit of large distance between A and C blocks with $l_{AC} \gg \xi_{corr}$, one has the reduced density matrix satisfying

$$\hat{\rho}_{AC} \simeq \hat{\rho}_A \otimes \hat{\rho}_C, \tag{6.40}$$

up to some exponentially small corrections. Then $|\psi_{ABC}\rangle$ is a purification [11] of a mixed state with the form $|\psi_{AB_l}\rangle \otimes |\psi_{B_rC}\rangle$ that has no correlations between A and C; here B_l and B_r sit at the two ends of the block B, which together span the original block.

[11] Purification: Let ρ be a density matrix acting an a Hilbert space $\mathcal{H}_A$ of finite dimension n. Then there exist a Hilbert space $\mathcal{H}_B$ and a pure state $|\psi\rangle \in \mathcal{H}_A \otimes \mathcal{H}_B$ such that the partial trace of $|\psi\rangle\langle\psi|$ with respect to $\mathcal{H}_B$: $\rho = Tr_B|\psi\rangle\langle\psi|$. We say that $|\psi\rangle$ is the purification of $\hat{\rho}$.

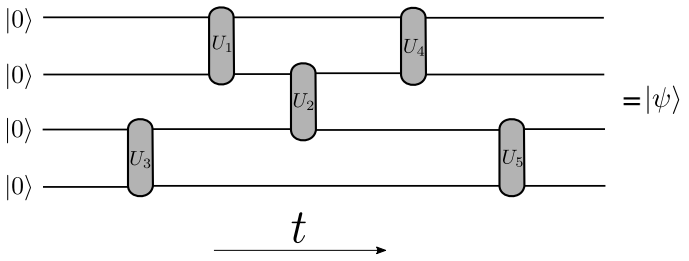

Figure 6.10: The TN representation of a quantum circuit. Two-body unitaries act on a product state of a given number of constituents $|0\rangle \otimes \cdots \otimes |0\rangle$ and transform it into a target entangled state $|\psi\rangle$.

It is well known that all possible purifications of a mixed state are equivalent to each other up to a local unitary transformation on the virtual Hilbert space. This naturally implies that there exists a unitary operation $\hat{U}_B$ on the block B that completely disentangles the left from the right part as

$$\hat{I}_A \otimes \hat{U}_B \otimes \hat{I}_C |\psi_{ABC}\rangle \to |\psi_{AB_l}\rangle \otimes |\psi_{B_r C}\rangle. \tag{6.41}$$

$\hat{U}_B$ implies that there exists a tensor $B_{s,aa'}$ with $0 \leq a, a', s \leq \chi - 1$ and basis $\{|\psi^A\rangle\}$, $\{|\psi^B\rangle\}$, $\{|\psi^C\rangle\}$ defined on the Hilbert spaces belonging to A, B, C such that

$$|\psi_{ABC}\rangle \simeq \sum_{saa'} B_{s,aa'} |\psi_a^A\rangle |\psi_s^B\rangle |\psi_{a'}^C\rangle. \tag{6.42}$$

This argument directly leads to the MPS description and gives a strong hint that the ground states of a gapped Hamiltonian is well represented by an MPS of finite bond dimensions, where B in Eq. (6.42) is analog to the tensor in an MPS. Let us remark that every state of N spins has an exact MPS representation if we allow χ grow exponentially with the number of spins [51]. The whole point of MPS is that a ground state can typically be represented by an MPS where the dimension χ is small and scales at most polynomially with the number of spins: this is the reason why MPS-based methods are more efficient than exact diagonalization.

For the 2D PEPS, it is more difficult to strictly justify the area law of entanglement entropy. However, we can make some sense of it from the following aspects. One is the fact that PEPS can exactly represent some non-trivial 2D states that satisfies the area law, such as the nearest-neighbour RVB and Z_2 spin liquid mentioned above. Another is to count the dimension of the geometrical bonds $\mathcal{D}$ between two subsystems, from which the entanglement entropy satisfies an upper bound as $S \leq \log \mathcal{D}$ [12].

After dividing a PEPS into two subregions, one can see that the number of geometrical bonds N_b increase linearly with the length scale, i.e. $N_b \sim l$. It means the dimension $\mathcal{D}$ satisfies $\mathcal{D} \sim \chi^l$, and the upper bound of the entanglement entropy fulfils the area law given by Eq. (6.39), which is

$$S \leq O(l). \tag{6.43}$$

However, as we will see later, such a property of PEPS is exactly the reason that makes it computationally difficult.

[12] One can see this with simply a flat entanglement spectrum, $\lambda_n = 1/\mathcal{D}$ for any n.

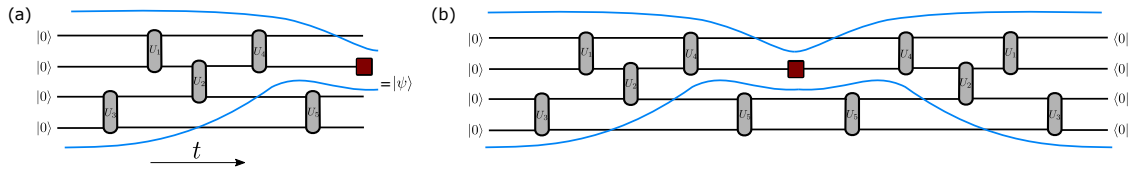

Figure 6.11: The past casual cone of the red site (A). The unitary gate U_5 does not affect the reduced density matrix of the red site. This is verified by computing explicitly ρ_A by tracing over all the others constituents. In the TN of ρ_A, U_5 is contracted with $U_5^\dagger$, which gives an identity.

6.6 Tensor networks for quantum circuits

A special case of TN are quantum circuits [434]. Quantum circuits encode computations made on qubits (or qudits in general). Fig. 6.10 demonstrates the TN representation of a quantum circuit made by unitary gates that act on a product state of many constituents initialized as $\prod_\otimes |0\rangle$.

An example of quantum circuits. In order to make contact with TN, we will consider the specific case of quantum circuits where all the gates act on at most two neighbors. An example of such circuit is the Trotterized evolution of a system described by a nearest-neighbour Hamiltonian $\hat{H} = \sum_{i,i+1} \hat{h}_{i,i+1}$, where $i, i+1$ label the neighbouring constituents of a one- dimensional system. The evolution operator for a time t is $\hat{U}(t) = exp(-i\hat{H}t)$, and can be decomposed into a sequence of infinitesimal time evolution steps [305] (more details will be given in Sec. 7.3.3)

$$\hat{U}(t) = lim_{N\to\infty} \exp(-i\frac{t}{N}\hat{H})^N. \tag{6.44}$$

In the limit, we can decompose the evolution into a product of two-body evolution

$$\hat{U}(t) = lim_{\tau\to 0} \prod_{i,i+1} \hat{U}(\tau)_{i,i+1}. \tag{6.45}$$

where $\hat{U}_{i,i+1}(\tau) = \exp(-i\tau\hat{h}_{i,i+1})$ and $\tau = t/N$. This is obviously a quantum circuit made by two-qubit gates with depth N. Conversely, any quantum circuit naturally possesses an arrow of time; it transforms a product state into an entangled state after a sequence of two-body gates.

Casual cone. One interesting concept in a quantum circuit is that of the causal cone illustrated in Fig. 6.11, which becomes explicit with the TN representations. Given a quantum circuit that prepares (i.e., evolves the initial state to) the state $|\psi\rangle$, we can ask a question: which subset of the gates affect the reduced density matrix of a certain sub-region A of $|\psi\rangle$? This can be seen by constructing the reduced density matrix of the sub-region A $\rho_A = tr_{\bar{A}}|\psi\rangle\langle\psi|$ with $\bar{A}$ the rest part of the system besides A.

The TN of the reduced density matrix is formed by a set of unitaries that define the past causal cone of the region A (see the area between the green lines in Fig. 6.11). The rest unitaries (for instance the $\hat{U}_5$ and its conjugate in the right sub-figure of Fig. 6.11) will be eliminated in the TN of the reduced density matrix. The contraction of the causal cone can thus be rephrased in terms of the multiplication of a set of transfer matrices, each performing the computation from t to $t-1$. The maximal width of these transfer matrices defines the width of the causal cone, which can be used as a good

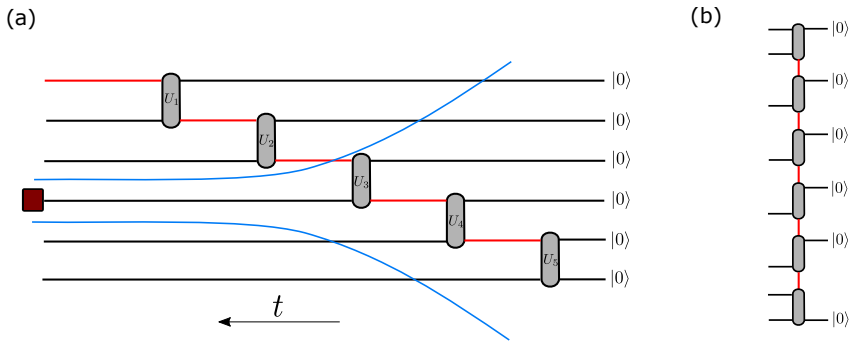

Figure 6.12: The MPS as a quantum circuit. Time flows from right to left so that the lowest constituent is the first to interact with the auxiliary D-level system. Here we show the past causal cone of a single constituent. Similarly, the past causal cone of A made by adjacent constituent has the same form starting from the upper boundary of A.

measure of the complexity of computing ρ_A [435]. The best computational strategy one can find to compute exactly ρ_A will indeed always scale exponentially with the width of the cone [434].

Unitary tensor networks and quantum circuits. The simplest TN, the MP can be interpreted as a sequential quantum circuit [436]. The idea is that one can think of the MPS as a sequential interaction between each constituent (a d- level system) an ancillary D-level system (the auxiliary qDit, red bonds). The first constituent interacts (say the bottom one shown in Fig. 6.12) and then sequentially all the constituents interact with the same $D-$level system. With this choice, the past causal cone of a constituent is made by all the MPS matrices below it. Interestingly in the MPS case, the causal cone can be changed using the gauge transformations, something very different to what happens in two dimensional TN's. This amounts to finding appropriate unitary transformations acting on the auxiliary degrees of freedom that allow to re-order the interactions between the $D-$level system and the constituents. In such a way, a desired constituent can be made to interact first, then followed by the others. An example of the causal cone in the center gauge used in iDMRG calculation [437] is presented in Fig. 6.13. This idea allows to minimize the number of tensors in the causal cone of a given region. However, the scaling of the computational cost of the contraction is not affected by such a temporal reordering of the TN, since in this case the width of the cone is bounded by one unitary in any gauge. The gauge choice just changes the number of computational steps required to construct the desired ρ_A. In the case that A includes non-consecutive constituents, the width of the cone increases linearly with the number of constituents, and the complexity of computing ρ_A increases exponentially with the number of constituents.

Again, the gauge degrees of freedom can be used to modify the structure of the past causal cone of a certain spin. As an example, the iDMRG center gauge is represented in Fig. 6.13 (a).

An example of a TN with a larger past causal cone can be obtained by using more than one layers of interactions. Now the support of the causal cone becomes larger since it includes transfer matrices acting on two D-level systems (red bonds shown in Fig. 6.13). Notice that this TN has loops but it still exactly contractible since the width of the causal cone is still finite.

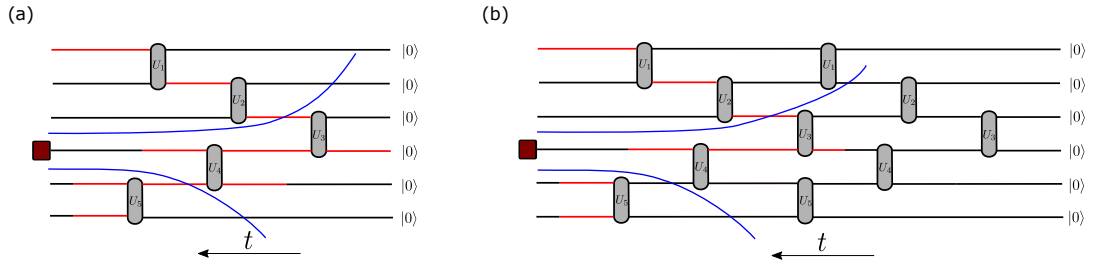

Figure 6.13: (a) Using the gauge degrees of freedom of an MPS, we can modify its past causal cone structure to make its region as small as possible, in such a way decreasing the computational complexity of the actual computation of specific ρ_A. A convenient choice is the center gauge used in iDMRG. (b) The width of the causal cone increases as we increase the depth of the quantum circuit generating the MPS state.

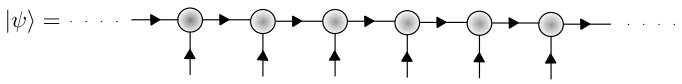

Figure 6.14: The MPS wave-function representation in left canonical form.

6.7 Definition of exactly contractible tensor network states

The notion of the past causal cone can be used to classify TNS's based on the complexity of computing their contractions. It is important to remember that the complexity strongly depends on the object that we want to compute, not just the TN. For example, the complexity of an MPS for a N-qubit state scales only linearly with N. However, to compute the n-site reduced density matrix, the cost scales exponentially with n since the matrix itself is an exponentially large object. Here we consider to compute scalar quantities, such as the observables of one- and two-site operators.

We define the a TNS to be *exactly contractible* when it is allowed to compute their contractions with a cost that is a polynomial to the elementary tensor dimensions D. A more rigorous definition can be given in terms of their tree width see e.g. [434]. From the discussion of the previous section, it is clear that such a TNS corresponds to a bounded causal cone for the reduced density matrix of a local sub-region. In order to show this, we now focus on the cost of computing the expectation value of local operators and their correlation functions on a few examples of TNS's.

The relevant objects are thus the reduced density matrix of a region A made of a few consecutive spins, and the reduced density matrix of two disjoint blocks A_1 and A_2 of which each made of a few consecutive spins. Once we have the reduced density matrices of such regions, we can compute arbitrary expectation values of local operators by $\langle \mathcal{O} \rangle = tr(\rho_A \mathcal{O})$ and $\langle \mathcal{O}_{A_1} \mathcal{O}'_{A_2} \rangle = tr(\rho_{A_1 \cup A_2} \mathcal{O}_{A_1} \mathcal{O}'_{A_2})$ with $\mathcal{O}_A$, $\mathcal{O}_{A_1}$, $\mathcal{O}'_{A_2}$ arbitrary operators defined on the regions A, A_1, A_2.

6.7.1 MPS wave functions

The simplest example of the computation of the expectation value of a local operator is obtained by considering MPS wave-functions [52,278]. Fig. 6.14 shows an MPS in the left-canonical form. Rather than putting the arrows of time, here we put the direction in which the tensors in the TN are isometric. In other words, an identity is obtained by

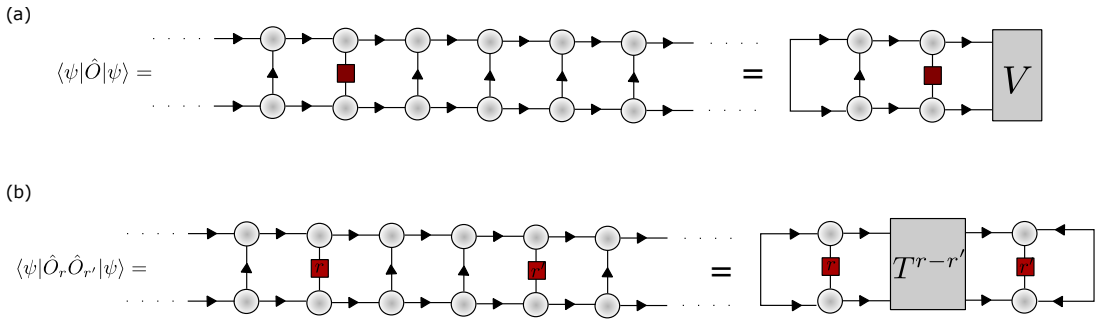

Figure 6.15: (a) The expectation value of a single-site operator with an MPS wave-function. (b) Two-point correlation function of an MPS wave-function.

contracting the inward bonds of a tensor in $|\psi\rangle$ with the outward bonds of its conjugate in $\langle\psi|$ (Fig. 6.15). Note that $|\psi\rangle$ and $\langle\psi|$ have opposite arrows, by definition. These arrows are directly on the legs of the tensors. The arrows in $|\psi\rangle$ are in the opposite direction than the time, by comparing Fig. 6.12 with Fig. 6.15. The two figures indeed represent the MPS in the same gauge. This means that the causal cone of an observable is on the right of that observable, as shown on the second line of Fig. 6.15, where all the tensors on the left side are annihilated as a consequence of the isometric constraints. We immediately have that the causal cone has at most the width of two. The contraction becomes a power of the transfer operator of the MPS $E = \sum_i A^i \otimes A^{i\dagger}$, where A_i and $A^{i\dagger}$ represent the MPS tensors and its complex conjugate. The MPS transfer matrix E only acts on two auxiliary degrees of freedom. Using the property that E is a completely positive map and thus has a fixed point [52], we can substitute the transfer operator by its largest eigenvector v, leading to the final TN diagram that encodes the expectation value of a local operator.

In Fig. 6.15 (b), we show the TN representation of the expectation value of the two-point correlation functions. Obviously, the past-causal cone width is bounded by two auxiliary sites. Note that in the second line, the directions of the arrows on the right side are changed. This in general does not happen in more complicated TN's as we will see in the next subsection. Before going there, we would like to comment the properties of the two-point correlation functions of MPS. From the calculation we have just performed, we see that they are encoded in powers of the transfer matrix that evolve the system in the real space. If that matrix can be diagonalized, we can immediately see that the correlation functions naturally decay exponentially with the ratio of the first to the second eigenvalue.

6.7.2 Tree tensor network wave functions

An alternative kind of wave-functions are the TTNS's [300–304, 361, 363]. In a TTNS, one can add the physical bond on each of the tensor, and use it as a many-body state defined on a Caley-tree lattice [361]. Here, we we will focus on the TTNS with physical bonds only on the outer leafs of the tree.

The calculations with a TTNS normally correspond to the contraction of tree TN's. A specific case of a two-to-one TTNS is illustrated in Fig. 6.16, named binary Caley tree. This TN can be interpreted as a quantum state of multiple spins with different boundary conditions. It can also be considered as a hierarchical TN, in which each layer corresponds to a different level of coarse-graining renormalization group (RG)

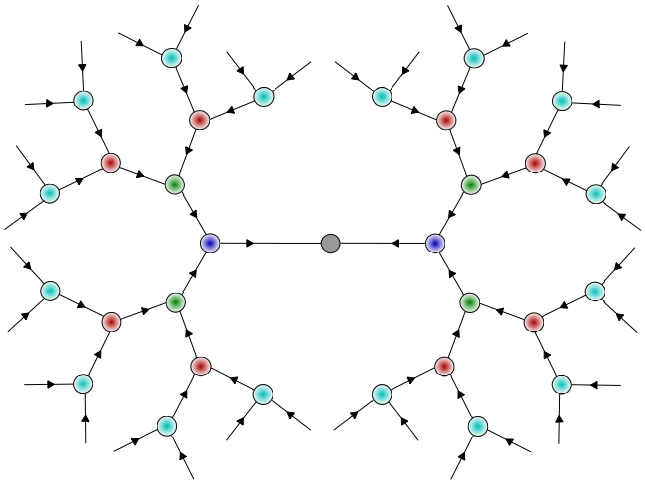

Figure 6.16: A binary TTNS made of several layers of third-order tensors. Different layers are identified with different colors. The arrows flow in the opposite direction of the time while being interpreted as a quantum circuit.

transformation [363]. In the figure, different layers are colored differently. In the first layer, each tensor groups two spins into one and so on. The tree TN can thus be interpreted a specific RG transformation. Once more, the arrows on the tensors indicate the isometric property of each individual tensor that; the directions are opposite as the time, if we interpret the tree TN as a quantum circuit. Note again that $|\psi\rangle$ and $\langle\psi|$ have opposite arrows, by definition.

The expectation value of a one-site operator is in fact a tree TN shown in Fig. 6.17. We see that many of the tensors are completely contracted with their Hermitian conjugates, which simply give identities. What are left is again a bounded causal cone. If we now build an infinite TTNS made by infinitely many layers, and assume the scale invariance, the multiplication of infinitely many power of the scale transfer matrix can be substituted with the corresponding fixed point, leading to a very simple expression for the TN that encodes the expectation value of a single site operator.

Similarly, if we compute the correlation function of local operators at a given distance, as shown in Fig. 6.18, we can once more get rid of the tensors outside the casual cone. Rigorously we see that the causal cone width now increases to four sites, since it consists of two different two-site branches. However, if we order the contraction as shown in the middle, we see that the contractions boil down again to a two-site causal cone. Interestingly, since the computation of two-point correlations at very large distance involve the power of transfer matrices that translate in scale rather than in space, one would expect that these matrices are all the same (as a consequence of scale-invariance for example). Thus, we would get polynomially decaying correlations [438].

6.7.3 MERA wave-function

Until now, we have discussed with the TN's that, even if they can be embedded in a 2D space, they contain no loops. In the context of network complexity theory, they are called mean-field networks [439]. However, there are also TN's with loops that are exactly contractible [434]. A particular case is that of a 1D MERA (and its generalizations) [370, 371, 373, 375, 441]. The MERA is again a TN that can be embedded in a 2D plane, and that is full of loops as seen in Fig. 6.19. This TN has a

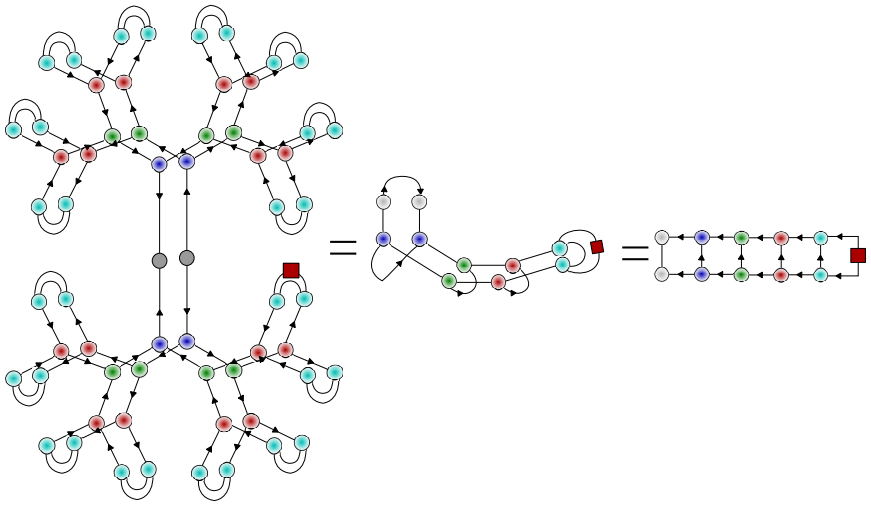

Figure 6.17: The expectation value of a local operator of a TTNS. We see that after applying the isometric properties of the tensors, the past causal cone of a single site has a bounded width. The calculation again boils down to a calculation of transfer matrices. This time the transfer matrices evolve between different layers of the tree.

very peculiar structure, again, inspired from RG transformation [440]. MERA can also be interpreted as a quantum circuit where the time evolves radially along the network, once more opposite to the arrows that indicate the direction along which the tensors are unitary. The MERA is a layered TN, with where layer (in different colors in the figure) is composed by the appropriate contraction of some third-order tensors (isometries) and some forth-order tensors (disentangler). The concrete form of the network is not really important [441]. In this specific case we are plotting a two-to-one MERA that was discussed in the original version of Ref. [375]. Interestingly, an operator defined on at most two sites gives a bounded past-causal cone as shown in Fig. 6.20 (a).

As in the case of the TTNS, we can indeed perform the explicit calculation of the past causal cone of a single site operators (Fig.6.20 (a)). There we show that the TN contraction of the required expectation value, and then simplify it by taking into account the contractions of the unitary and isometric tensors outside the casual cone with a bounded width involving at most four auxiliary constituents.

The calculation of a two-point correlation function of local operators follows a similar idea and leads to the contraction shown in Fig.6.20 (b). Once more, we see that the computation of the two-point correlation function can be done exactly due to the bounded width of the corresponding casual cone.

6.7.4 Sequentially generated PEPS wave functions

The MERA and TTNS can be generalized to two dimensional lattices [363, 373]. The generalization of MPS to 2D, on the other hand, gives rise to PEPS. In general, it belongs to the 2D TN's that cannot be exactly contracted [58, 443].

However for a subclass of PEPS, one can implement the contract exactly, which is called sequentially generated PEPS [442]. Differently from the MERA where the computation of the expectation value of any sufficiently local operator leads to a bounded causal cone, sequentially generated PEPS have a central site, and the local observables around the central site can be computed easily. However, the local observables in other

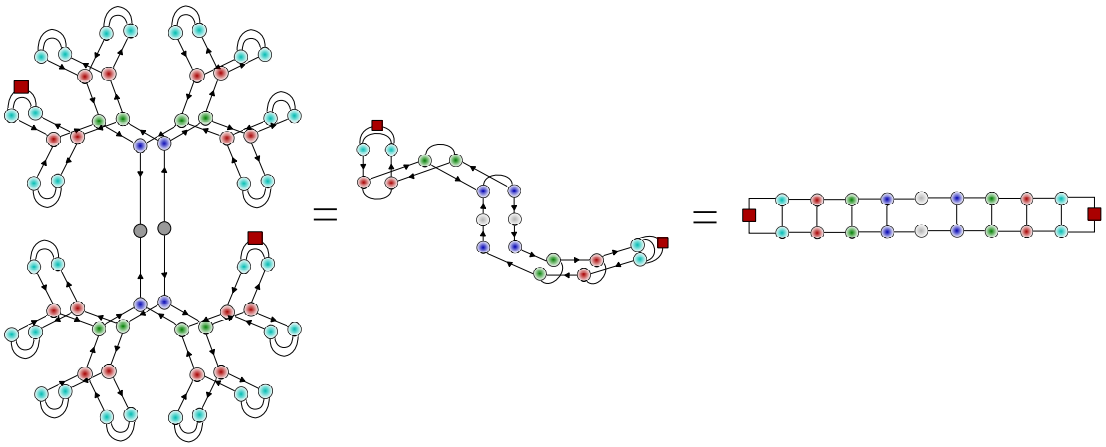

Figure 6.18: The computation of the correlation function of two operators separated by a given distance boils down to the computation of a certain power of a transfer matrices. The computation of the casual cone can be simplified in a sequential way, as depicted in the last two sub-figures.

regions of the TN give larger causal cones. For example, we represent in Fig.6.21 a sequentially generated PEPS for a 3×3 lattice. The norm of the state is computed in (b), where the TN boils down to the norm of the central tensor. Some of the reduced density matrices of the system are also easy to compute, in particular those of the central site and its neighbors [Fig. 6.21 (c)]. Other reduced density matrices, such as those of spins close to the corners, are much harder to compute. As illustrated in Fig. 6.21 (d), the causal cone of a corner site in a 3×3 PEPS has a width 2. In general for an $L \times L$ PEPS, the casual cone would have a width $L/2$.

Differently from MPS, the causal cone of a PEPS cannot be transformed by performing a gauge transformation. However, as firstly observed by F. Cucchietti (private communication), one can try to approximate a PEPS of a given causal cone with another one of a different causal cone, by for example moving the center site. This is not an exact operation, and the approximations involved in such a transformation need to be addressed numerically. The systematic study of the effect of these approximations have been studied recently in [444, 445]. In general, we have to say that the contraction of a PEPS wave-function can only be performed exactly with exponential resources. Therefore, efficient approximate contraction schemes are necessary to deal with PEPS.

For the reduced density matrix of any of the corners with a $L \times L$ PEPS, which is the most consuming case, it leads to a causal cone with a width up to $L/2$. That means the computation is exponentially expensive with the size of the system.

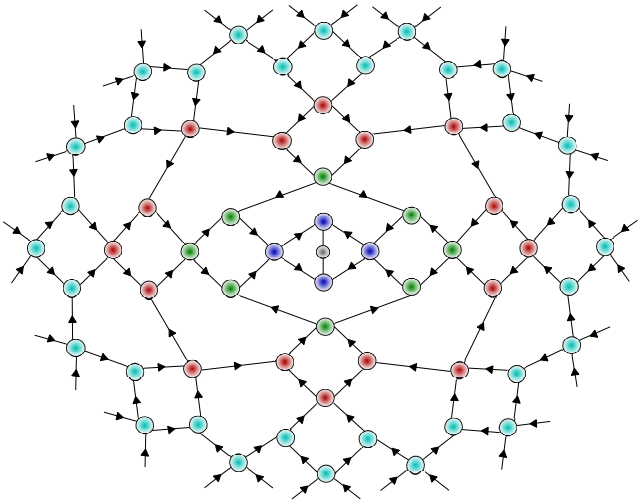

Figure 6.19: The TN of MERA. The MERA has a hierarchical structure consisting of several layers of disentanglers and isometries. The computational time flows from the center towards the edge radially, when considering MERA as a quantum circuit. The unitary and isometric tensors and the network geometry are chosen in order to guarantee that the width of the causal cone is bounded.

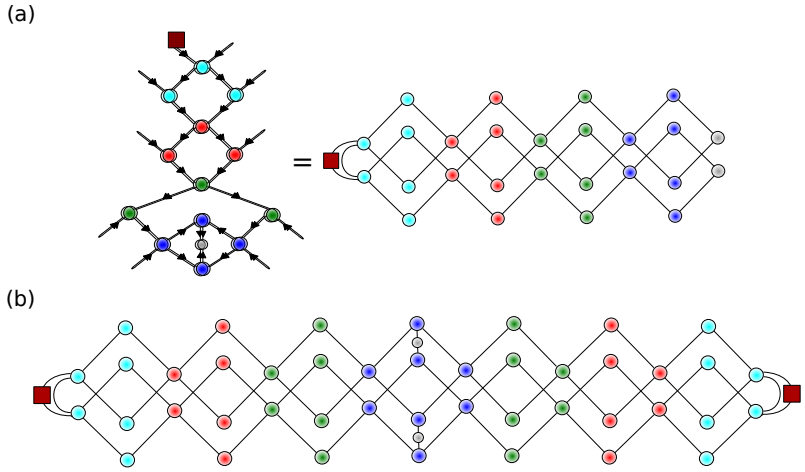

Figure 6.20: (a) Past causal cone of a single-site operator for a MERA. (b) Two-point correlation function in the MERA.

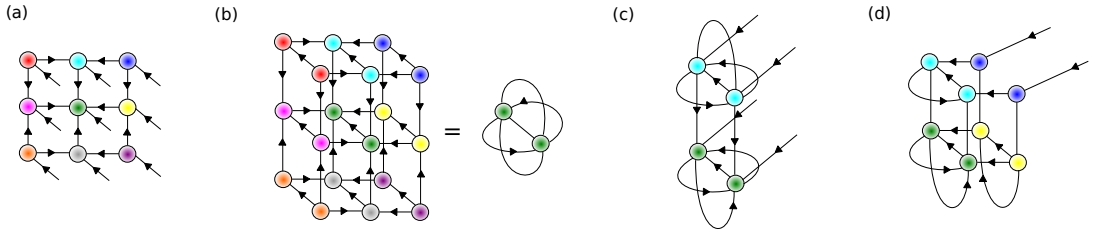

Figure 6.21: (a) A sequentially generated PEPS. All tensors but the central one (green in the figure) are isometries, from the in-going bonds (marked with ingoing arrows) to the outgoing ones. The central tensor represents a normalized vector on the Hilbert space constructed by the physical Hilbert space and the four copies of auxiliary spaces, one for each of its legs. (b) The norm of such PEPS, after implementing the isometric constraints, boils down to the norm of its central tensor. (c) The reduced density matrices of a PEPS that is sequentially generated containing two consecutive spins (one of them is the centralspin. (d) The reduced density matrix of a local region far from the central site is generally hard to compute, since it can give rise to an arbitrarily large causal cone. For the reduced density matrix of any of the corners with a $L \times L$ PEPS, which is the most consuming case, it leads to a causal cone with a width up to $L/2$. That means the computation is exponentially expensive with the size of the system.

Chapter 7

Tensor network algorithms

In chapter 6 we introduced the TN states in 1D and higher dimensions and we showed that only in some special cases these can be solved exactly.

In fact, TN's cannot be contracted exactly (with #P-complete computational complexity [354]), efficient algorithms are strongly desired. In 2007, Levin and Nave generalized the NRG idea to TN and proposed the tensor renormalization group (TRG) approach [446]. TRG consists of two main steps in each RG iteration: contraction and truncation. In the contraction step, the TN is deformed by singular value decomposition (SVD) of matrix in such a way that certain adjacent tensors can be contracted without changing the geometry of the TN graph. This procedure reduces the number of tensors N to N/ν, with ν an integer that depends on the way of contracting. After reaching the fixed point, one tensor represents in fact the contraction of infinite number of original tensors, which can be seen as the approximation of the whole TN.

After each contraction, the dimensions of local tensors increase exponentially, and then truncations are needed. To truncate in an optimized way, one should consider the "environment", a concept which appears in DMRG. In the truncation step of Levin's TRG, one only keeps the basis corresponding to the χ-largest singular values from the SVD in the contraction step, with χ called dimension cut-off. In other words, the environment of the truncation here is the tensor that is decomposed by SVD. Such a local environment only permits local optimizations of the truncations, which hinders the accuracy of Levin's TRG on the systems with long-range fluctuations.

Nevertheless, TRG is still one of the most important and computationally-cheap approaches for both classical (e.g., Ising and Potts models) and quantum (e.g., Heisenberg models) simulations in two and higher dimensions [447–465], several other TN contraction algorithms were proposed based on two aspects: more reasonable ways of contracting, and more optimized ways of truncating.

In 2004 Vidal proposed the time evolving block decimation (TEBD) [305–308]. The TEBD implements the TN contraction with the help of MPS in a linearized way [396]. Then, instead of using the singular values of local tensors, one uses the entanglement of the MPS to find the optimal truncation, meaning the environment is a (non-local) MPS, leading to a better precision than Levin's TRG. In this case, the MPS at the fixed point is the dominant eigenstate of the transfer matrix of the TN. Another group of RG algorithms, called corner transfer matrix renormalization group (CTMRG) was proposed [466]. They are based on the corner transfer matrix idea originally proposed by Baxter in 1978 [467], and developed by Nishino and Okunishi in 1996 [257]. In CTMRG, the contraction reduces the number of tensors in a polynomial way and the

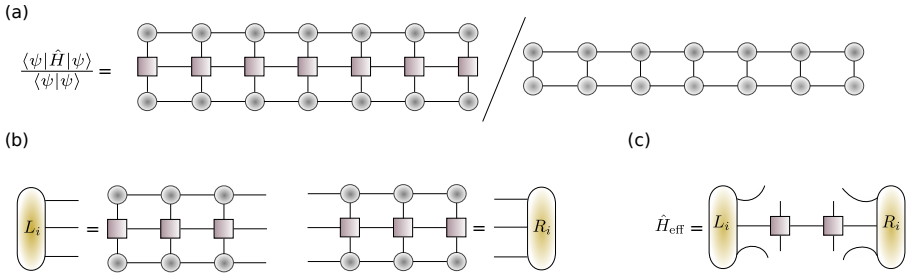

Figure 7.1: (a) Tensor network represented the quantity $\frac{\langle\psi|\hat{H}|\psi\rangle}{\langle\psi|\psi\rangle}$. (b) Graphical representation of environment left L and right R, where L contain the contracted left part while R contain the contracted right part of network. (c) Graphical representation of effective Hamiltonian $\hat{H}_{\text{eff}}$.

environment can be considered as a finite MPS defined on the boundary. CTMRG has a compatible accuracy compared with TEBD.

In this Chapter, firstly, we will discuss about the DMRG (sec. 7.1) and we will present a numerical approach named PT-DMRG that improves the accuracy of the conventional DMRG (sec. 7.2). Then we will demonstrate in Sec. 7.3 that many important physical problems can be transformed into 2D TN's, and the central tasks become to compute the corresponding TN contractions. From Sec. 7.4 to 7.7, we will then present several paradigm contraction algorithms of 2D TN's including TRG, TEBD, and CTMRG. Relations to other distinguished algorithms and the exactly contractible TN's will also be discussed.

7.1 Density matrix renormalization group

So far the most studied and successful of the algorithms in the field is DMRG. For clarity we will be restricting ourselves to finite DMRG, though there do exist thermodynamic variants.

In order to obtain the ground state $|\psi_0\rangle$, one needs to find the MPS that minimizes the following equation

$$E = \frac{\langle\psi|\hat{H}|\psi\rangle}{\langle\psi|\psi\rangle}. \tag{7.1}$$

Representing the Hamiltonian by an MPO, the eq. (7.1) is described in the Fig. 7.1 (a). The difficulty is that as we need the contraction of these MPS tensors; the overall objective function is highly non-linear, but it does however only depend quadratically on each individual tensor.

The most efficient way of doing this is in a variational approach by minimizing E over MPS family

$$\min_{|\psi\rangle\in MPS} \left\{ \langle\psi|\hat{H}|\psi\rangle - \lambda\langle\psi|\psi\rangle \right\}. \tag{7.2}$$

Ideally, the minimization should be done simultaneously over all the coefficients of all tensors. However, this is quite difficult and inefficient to implement. Following the original procedure, the strategy of DMRG that we use here is to minimize two tensors each time while keeping others fixed. Then, we move to another pair of tensors and repeat the procedure until convergence.

Starting from a MPS $|\psi\rangle$ described by three legs tensor $M^{\sigma_i}_{a_{i-1},a_i}$, we introduce the

vectors

$$|a_l\rangle_A = \sum_{\sigma_1 \ldots \sigma_l} (A^{\sigma_1} \ldots A^{\sigma_l})_{1,a_l} |\sigma_1 \ldots \sigma_l\rangle, \tag{7.3}$$

$$|a_l\rangle_B = \sum_{\sigma_{l+1} \ldots \sigma_L} (B^{\sigma_{l+1}} \ldots B^{\sigma_L})_{a_l,1} |\sigma_{l+1} \ldots \sigma_L\rangle, \tag{7.4}$$

where A and B are the right and left representation of MPS. Then the state $|\psi\rangle$ can be written as follows:

$$|\psi\rangle = \sum_{\sigma_l \sigma_{l+1} a_{l-1} a_{l+1}} D^{\sigma_l \sigma_{l+1}}_{a_{l-1},a_{l+1}} |a_{l-1}\rangle_A |\sigma_l \sigma_{l+1}\rangle |a_{l+1}\rangle_B. \tag{7.5}$$

Then the minimization is written as

$$\min_{|\psi\rangle \in MPS} \left\{ \langle\psi|\hat{H}|\psi\rangle - \lambda \langle\psi|\psi\rangle \right\} \to \min_D \left\{ D^\dagger \hat{H}_{eff} D - \lambda D^\dagger \hat{N} D \right\}. \tag{7.6}$$

$\hat{H}_{eff}$ and $\hat{N}$ correspond to $\langle\psi|\hat{H}|\psi\rangle$ and $\langle\psi|\psi\rangle$ without D and $D^\dagger$, respectively. The term $-\lambda\langle\psi|\psi\rangle$ is introduced to make all eigenvalues negative, so that MPS is generated to converge to the ground state. By considering D as a vector, the minimization becomes

$$\frac{\partial}{\partial D^\dagger} \left\{ D^\dagger \hat{H}_{eff} D - \lambda D^\dagger \hat{N} D \right\} = 0. \tag{7.7}$$

Furthermore, we define $L_0 = 1$ and $L_i = L_{i-1} A_i^\dagger W_i A_i$ with summation over all possible indices. Similarly the right environment $R_{L+1} = 1$ is defined by $R_i = B_i^\dagger W_i B_i R_{i+1}$. With these contractions it is possible to write:

$$\langle\psi|\hat{H}|\psi\rangle = L_{i-1} D^\dagger_{i,i+1} W_i W_{i+1} D_{i,i+1} R_{i+2}, \tag{7.8}$$

for any $i \in [0, L]$, where $D^{\sigma_i,\sigma_{i+1}} = \sum M^{\sigma_i} M^{\sigma_{i+1}}$. Therefore the optimization of the variational parameters of the MPS is implemented as a local update step. Local update step amounts to the solution of a generalized eigenvalue problem:

$$H_{eff} D - \lambda D = 0, \tag{7.9}$$

where $H_{eff} = L_{i-1} W_i W_{i+1} R_{i+1}$ is the effective Hamiltonian. The updated MPS is obtained from the singular value decomposition (SVD) of generalized eigenvector D

$$D^{\sigma_i \sigma_{i+1}}_{\alpha\beta} = \sum_\rho U_{\sigma_i \alpha,\rho} S_\rho V_{\rho,\sigma_{i+1}\beta}. \tag{7.10}$$

Take only the χ largest singular vectors in U as the new tensor $A^{\sigma_i}_{a_{i-1}\rho}$, i.e., $A^{\sigma_i}_{a_{i-1}\rho} = U_{\sigma_i a_{i-1},\rho}$ when sweeping from left to right, and take the χ largest singular vectors in V as the new tensor $A^{\sigma_{i+1}}_{\rho,a_{i+1}}$ when sweeping from right to left. In this way, the left and right orthogonal conditions of the MPS are automatically fulfilled.

Specifically speaking, a left-to-right (or right-to-left) sweep consists of the following steps:

- Start with a random initial MPS and transform it in the right orthogonal form, or alternatively start from a g.s found by iDMRG.
- Optimize the tensor $D^{\sigma_i \sigma_{i+1}}$: construct the environment L and R and solve the standard eigenvalue problem (7.9).
- Carry out an SVD of $D^{\sigma_i \sigma_{i+1}}$ and update the tensor A^{σ_i}.
- Repeat the same operations for every site until reaching the preset convergence:

$$\langle\psi|\hat{H}^2|\psi\rangle - \left(\langle\psi|\hat{H}|\psi\rangle\right)^2 \to 0. \tag{7.11}$$

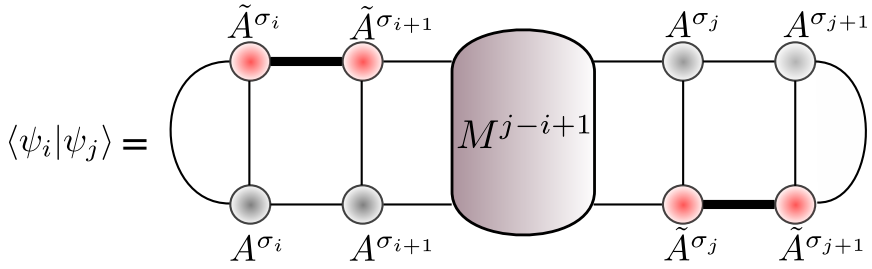

Figure 7.2: Graphical representation of the overlap $\langle\psi_i|\psi_j\rangle$ represented in the equation (7.12).

7.2 Perturbation theory DMRG

In the following, we develop a second-order perturbation theory for DMRG [62]. Note that from the orthogonality that the contribution of the first-order term is zero. This optimization permits the recovery of some of the lost information due to the truncation in the SVD of $D^{\sigma_i\sigma_{i+1}}$, and reach a better approximation of the ground state. In last section, we have shown how DMRG works and where its error comes from. To reduce the error, we define a new orthogonal basis $\{|\psi_i\rangle\}$, whose elements have the MPS form. We put an impurity bond in each $\{|\psi_i\rangle\}$ so that it is orthogonal to the ground state obtained by DMRG. To define this impurity bond (e.g. between the i-th and $(i+1)$-th sites), we consider the SVD of $D^{\sigma_i\sigma_{i+1}}$ and the tensor $\tilde{A}^{\sigma_i}$ as the second χ largest singular vectors. Thus, $\tilde{A}^{\sigma_i}$ is orthogonal to the tensor A^{σ_i} in the original MPS.

By introducing one impurity in different bonds of $|\psi_0\rangle$, we can define a new basis $\{|\psi_i\rangle\}$. Since both are in orthogonal form, one has

$$\langle\psi_i|\psi_j\rangle = \sum_{a_{i+1}a'_{i+1}a_{j-1}a'_{j-1}} A^{\sigma_i}_{a_{i-1},a_i}\tilde{A}^{\sigma_i\dagger}_{a_{i-1},a'_i}A^{\sigma_{i+1}}_{a_i,a_{i+1}}\tilde{A}^{\sigma_{i+1}\dagger}_{a'_i,a'_{i+1}} M^{j-i+1}_{a_{i+1}a'_{i+1},a_{j-1}a'_{j-1}}\tilde{A}^{\sigma_j}_{a_{j-1},a_j}A^{\sigma_j\dagger}_{a'_{j-1},a'_j}\tilde{A}^{\sigma_{j+1}}_{a'_j,a_{j+1}}A^{\sigma_{j+1}\dagger}_{a'_j,a_{j+1}}, \quad (7.12)$$

where M is the transfer matrix of the overlap $\langle\psi_i|\psi_j\rangle$ (see Fig. 7.2). Thus, $|\psi_i\rangle$ and $|\psi_j\rangle$ are orthogonal to each other for $i \neq j$.

Now one can define the perturbed Hamiltonian $\hat{\mathcal{H}}$ with $\{|\psi_i\rangle\}$ $(i = 0, 1, \cdots)$. Note that $|\psi_0\rangle$ is the ground state by the original DMRG. The matrix elements of $\hat{\mathcal{H}}$ are defined as

$$\mathcal{H}_{ij} = \langle\psi_i|\hat{\mathcal{H}}|\psi_j\rangle \quad (7.13)$$

and form the matrix $\mathcal{H}$. The ground state energy is calculated as

$$\tilde{E}_0 = \frac{\langle\tilde{\psi}_0|\hat{\mathcal{H}}|\tilde{\psi}_0\rangle}{\langle\tilde{\psi}_0|\tilde{\psi}_0\rangle} \quad (7.14)$$

where $|\tilde{\psi}_0\rangle$ is defined as the combination of $\{|\psi_i\rangle\}$

$$|\tilde{\psi}_0\rangle = \sum_j \Psi_j|\psi_j\rangle, \quad (7.15)$$

where Ψ_j are the coordinates of the dominant eigenvector of $\hat{\mathcal{H}}$. By using that the basis $\{|\psi_i\rangle\}$, the perturbed ground state energy is simply obtained as

$$\tilde{E}_0 = \sum_{ij} \Psi^\dagger_j \mathcal{H}_{ij}\Psi_j. \quad (7.16)$$

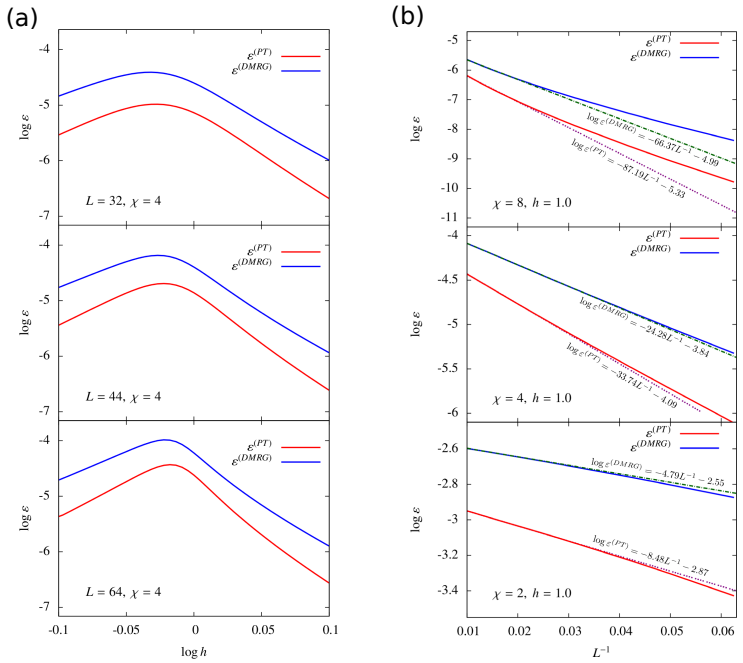

Figure 7.3: (a) The error ε of 1D Ising model on $32, 44, 64$ chain with open boundary condition as a function of h. The error of PT-DMRG method with bond dimension $\chi = 4$ is more than $O(10)$ time smaller compared with the error of standard DMRG. (b) The error ε of 1D Ising model as a function of length in the quantum phase transition $h = 1.0$, for different values of $\chi = 2, 4, 8$. We show that the error PT-DMRG is much smaller. The PT-DMRG gives a systematic improvement of accuracy.

Now we can explain how to implement the PT-DMRG in practice. Using the notation introduced above, the steps follow mostly the standard DMRG. In an outermost loop, the update sweeps over the system from left to right and right to left until the preset convergence is reached. The inner loop sweeps over the system, iterating over and updating the tensors on each site sequentially. Each local update during a left to right sweep consists of the following steps:

- Perform the standard DMRG to obtain the ground state MPS $|\psi_0\rangle$ (which is assumed in the right-orthogonal form).
- From left to right, calculate $D^{\sigma_i\sigma_{i+1}}$ and perform SVD for each i; Keep the second χ largest left and right singular vectors as $\tilde{A}^{\sigma_i}$ and $\tilde{A}^{\sigma_{i+1}}$, respectively.
- Construct the orthogonal basis $\{|\psi_i\rangle\}$ for by putting an impurity $\tilde{A}^{\sigma_i}$ in different bonds.
- Construct the perturbed Hamiltonian $\hat{\mathcal{H}}$ according to Eq. (7.13) and calculate its dominant eigenvector Ψ.
- Calculate the perturbed ground state of the systems as

$$|\tilde{\psi}_0\rangle = \sum_{i=1}^{N} \Psi_i |\psi_i\rangle. \tag{7.17}$$

As regards the computational cost, in addition, we need to consider the diagonalization of $\hat{\mathcal{H}}$ in the subspace. This cost is $O(N^3)$ where N is the number of the perturbed basis.

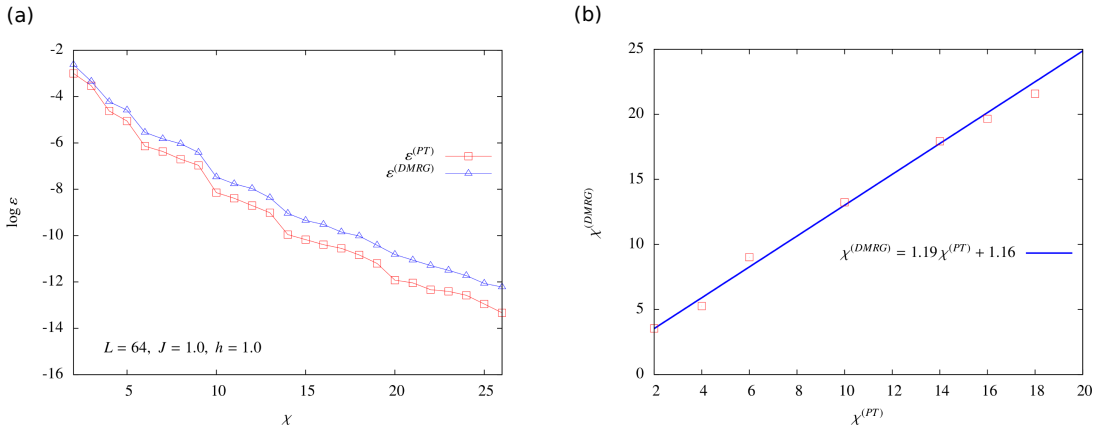

Figure 7.4: (a) The error ε of 1D Ising model versus of χ in the quantum phase transition $h = 1.0$ for $L = 64$. We show how the error of PT-DMRG decrease faster than the error of the standard DMRG. (b) The plot is the fit between $\chi^{(DMRG)}$ versus of $\chi^{(PT)}$ of 1D Ising model in the quantum phase transition $h = 1.0$ for $L = 64$. We show how the PT-DMRG needs smaller bond dimension χ than DMRG.

Therefore the full cost is $\chi^3 d\chi_W + O(\chi^2) + O(N^3)$, which makes it quite expensive. But the diagonal and first row/column of $\mathcal{H}$ can be obtained easily during the final DMRG sweep itself, which makes it much more practical.

To illustrate our method we study the 1D spin-half quantum Ising model in a transverse field, especially near the quantum phase transition. The Hamiltonian reads

$$\hat{H} = -J \sum_{i=1}^{L} \hat{\sigma}_i^x \hat{\sigma}_{i+1}^x + h \sum_{i=1}^{L} \hat{\sigma}_i^z. \tag{7.18}$$

In the infinite case, a quantum phase transition occurs at $h/J = 1$. The system for $h/J > 1.0$ is in a paramagnetic phase with an order parameter $\langle S^x \rangle \neq 0$, and in a ferromagnetic phase for $h/J < 1.0$ with an order parameter $\langle S^z \rangle \neq 0$. At the critical point, both order parameters go to zero. We set $J = 1$ as the energy scale.

In the numerical simulations, we considered a finite-size system with open boundary condition with the length $L = 16 \sim 128$. To benchmark PT-DMRG, we compute the ground state energies of DMRG and PT-DMRG with the same bond dimension χ, and compare with the (quasi-exact) result from the DMRG with sufficiently large $\chi = 100 \sim 400$ (note χ for quasi-exact calculations changes according with the length of the chain, in other words the entanglement). The error is defined as

$$\varepsilon = \frac{E_0 - \langle \psi | \hat{H} | \psi \rangle}{E_0}, \tag{7.19}$$

with E_0 the energy from the quasi-exact DMRG.

The Fig. 7.3 (a) shows the error with $L = 32, 44, 64$ versus magnetic field h. We compare the results of the conventional DMRG and PT-DMRG for $\chi = 2, 4, 8$. Near to the phase transition, the error of PT-DMRG is more than $O(10)$ times smaller compared with the error of the conventional DMRG with the same χ. Our simulations suggest that through PT-DMRG, we are able to retrieve the leading term of the lost information with the truncations in the SVD.

In Fig. 7.3 (b), we show the error against L^{-1} for $h = 1$ (critical point). The results show that the error increase both linearly with L^{-1} for DMRG and PT-DMRG,

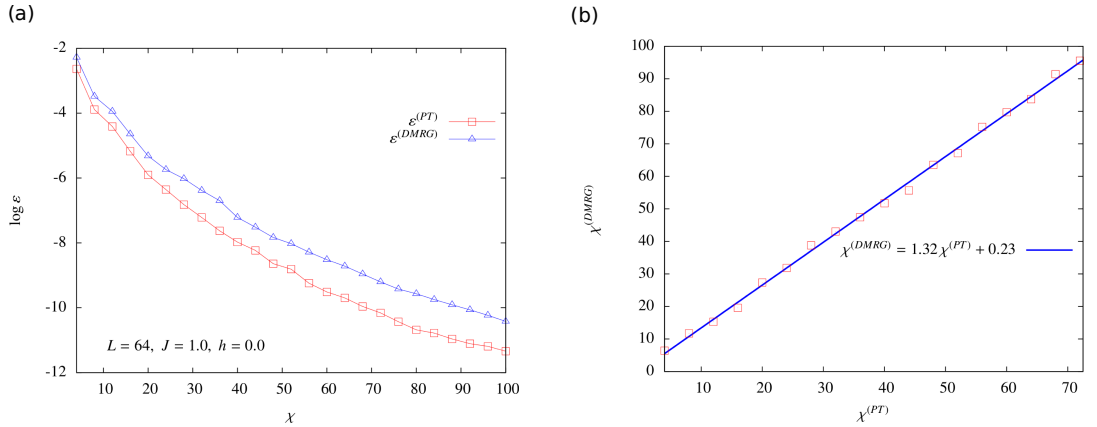

Figure 7.5: (a) The error ε of 1D Heisenberg model versus of χ in the quantum phase transition $h = 0.0$ for $L = 64$. We show how the error of PT-DMRG decrease faster than the error of the standard DMRG. (b) The plot is the fit between $\chi^{(DMRG)}$ versus of $\chi^{(PT)}$ of 1D Heisenberg model in the quantum phase transition $h = 0.0$ for $L = 64$. We show how the PT-DMRG needs smaller bond dimension χ than DMRG.

indicating a systematic improvement of the accuracy for moderate values of L. For the thermodynamic limit the error of PT-DMRG scales as $\sqrt{L^{-1}}$, for reasons explained below.

In Fig. 7.4 (a), we show the error against χ for $h = 1$ (phase transition) and for $L = 64$. The results show that the error decrease with bond dimension χ for DMRG and PT-DMRG. The error of PT-DMRG decreases faster than that of standard DMRG. This shows considerable improvement of the accuracy for any value of bond dimension χ near the phase transition.

To see more clearly the improvement of the efficiency of PT-DMRG, we study the correspondence between the bond dimension cut-off $\chi^{(DMRG)}$ of the standard DMRG and that of PT-DMRG $\chi^{(PT)}$. As shown in Fig. 7.4 (b), each pair of $\chi^{(DMRG)}$ and $\chi^{(PT)}$ given by the data points approximately have the same precision. In detail, to determine $\chi^{(DMRG)}$ for a given $\chi^{(PT)}$, we first find two χ's with DMRG, where the precision of one χ is higher than the precision of PT-DMRG with $\chi^{(PT)}$, and the other is lower. Then, we do a fit to find $\chi^{(DMRG)}$, which is an fraction between these two χ's.

We choose $h = 1$ and $L = 64$. The results show that with each $\chi^{(PT)}$ in PT-DMRG, we need a larger bond dimension cut-off (i.e. keep more states) in DMRG to reach the same precision. We also find a linear relation between $\chi^{(PT)}$ and $\chi^{(DMRG)}$ as

$$\chi^{(DMRG)} = 1.19\chi^{(PT)} + 1.16. \tag{7.20}$$

Since the computational cost an MPS takes scales as $\sim \chi^2$ (2 is the number of the virtual bond in each local tensor of MPS), such a linear relation suggests that the larger χ one uses, the more computational resource one can save by using PT-DMRG.

We study also the 1D spin-half quantum Heisenberg model, where the Hamiltonian reads

$$\hat{H} = -J \sum_{i=1}^{L} (\hat{\sigma}_i^x \hat{\sigma}_{i+1}^x + \hat{\sigma}_i^y \hat{\sigma}_{i+1}^y + \hat{\sigma}_i^z \hat{\sigma}_{i+1}^z). \tag{7.21}$$

We take $J = 1$ as energy scale.

In Fig. 7.5 (a), we show the error against χ for $L = 64$. The results show that the error decrease with bond dimension χ for DMRG and PT-DMRG. Amazingly, the error

of PT-DMRG decreases faster than that of standard DMRG. This shows considerable improvement of the accuracy for any value of bond dimension χ.

In Fig. 7.5 (b), we show the fit of $\chi^{(DMRG)}$ against $\chi^{(PT)}$ for $L = 64$. Again, a linear relation is found between $\chi^{(PT)}$ and $\chi^{(DMRG)}$ as

$$\chi^{(DMRG)} = 1.32\chi^{(PT)} + 0.23. \tag{7.22}$$

Especially, the slope is larger than that in the quantum Ising model, which implies a more significant improvement of efficiency when calculating Heisenberg chain with a large bond dimension cut-off.

Moeover, we explore a second order perturbation theory for DRMG in the thermodynamic limit. In the previous section we showed that the error scaling of PT-DMRG is linear in L^{-1} for moderate L. Now if L approach to infinity we have that the scaling law is $1/\sqrt{L}$.

We focus on the results first in the Fig. 7.3 (b). If we extend the results to larger L we can see a changing in behaviour for large L limit, the error in the energy per site becomes exactly equal to that of conventional DMRG.

We can understand that from looking at how the PT-DMRG approaches the thermodynamic limit. The off-diagonal matrix elements of effective Hamiltonian $\mathcal{H}_{ij}$ for $|i-j| > 1$ decay exponentially quickly, so it really only needs a few of them. For the Ising model $\mathcal{H}_{i,i+2}$ is already $O(10^{-6})$, so this gives no improvement over the old style of calculating just the diagonal part and the overlap with the ground state. In the large L limit, the effective Hamiltonian $\mathcal{H}_{ij}$ can be well-approximated by:

$$\mathcal{H} = \begin{bmatrix} a & b & b & b & b & \cdots \\ b & c & 0 & 0 & 0 & \cdots \\ b & 0 & c & 0 & 0 & \cdots \\ b & 0 & 0 & c & 0 & \cdots \\ \vdots & \vdots & \vdots & \vdots & \vdots & \ddots \end{bmatrix}, \tag{7.23}$$

where the non-zero elements are $a = E_0$ at the top-left (the energy of the original ground state), a series of L entries along the top row and left column which is $b = \langle\psi_i|H|\psi_0\rangle$ (assumed independent of i in the large L limit), and the diagonal entries $c = \langle\psi_i|H|\psi_i\rangle$ independent of i in the large L limit. a and c are extensive in the system size, but c has a constant offset because of the local perturbation. So we can set:

$$a = E_0 \times L \qquad c = E_0 \times L + q, \tag{7.24}$$

where q is the energy of the perturbation. It is possible to determine the eigenvalues of this matrix as a function of L, which is

$$E = (E_0 \times L + \frac{q}{2}) - \Delta, \tag{7.25}$$

where

$$\Delta^2 = \frac{q^2}{4} + b^2 L. \tag{7.26}$$

So we can see the origin now of the $1/\sqrt(L)$ behaviour. For large L the energy per site scales as

$$\frac{E}{L} = E_0 - \frac{|b|}{\sqrt{L}} + O(1/\sqrt{L}). \tag{7.27}$$

But in order to see the square root behaviour $b^2 L >> q^2/4$, which for the ising model, requires L > 650 (see Fig. 7.6). The plot in Fig. 7.6 is basically linearizing a square root in a region well away from the asymptotic large L behaviour.

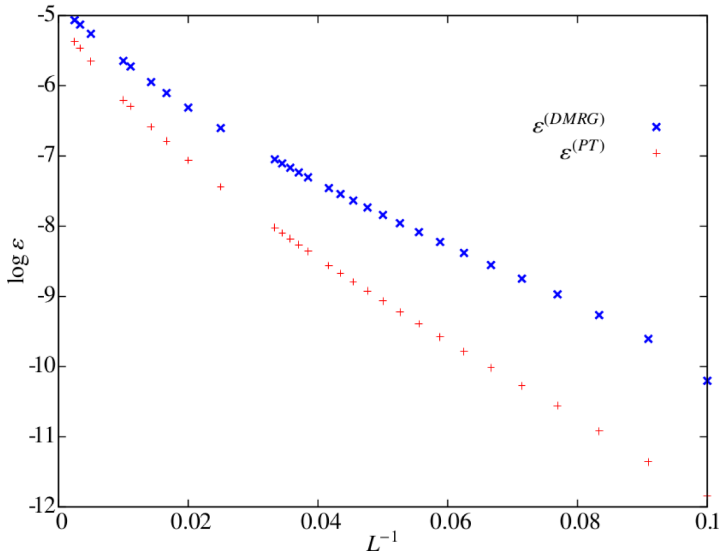

Figure 7.6: The error ε of 1D Ising model as a function of length in the quantum phase transition h = 1.0, for $\chi = 8$. We show that the error PT-DMRG In the large L limit doesn't give a systematic improvement of accuracy.

7.3 From physical problems to two-dimensional tensor networks

7.3.1 Classical partition functions

Partition function, which is a function of the variables of a thermodynamic state such as temperature, volume, and etc., contains the statistical information of a thermodynamic equilibrium system. From its derivatives of different orders, we can calculate the energy, free energy, entropy, and so on. Levin and Nave pointed out in Ref. [446] that the partition functions of statistical lattice models (such as Ising and Potts models) with local interactions can be written in the form of TN. Without losing generality, we take square lattice as an example.

Let us start from the simplest case: the classical Ising model on a single square with only four sites. The four Ising spins denoted by s_i $(i = 1, 2, 3, 4)$ locate on the four corners of the square, as shown in Fig.7.7 (a); each spin can be up or down, represented by $s_i = 0$ and 1, respectively. The classical Hamiltonian of such a system reads

$$H_{s_1 s_2 s_3 s_4} = J(s_1 s_2 + s_2 s_3 + s_3 s_4 + s_4 s_1) - h(s_1 + s_2 + s_3 + s_4) \tag{7.28}$$

with J the coupling constant and h the magnetic field.

When the model reaches the equilibrium at temperature T, the probability of each possible spin configuration is determined by the Maxwell-Boltzmann factor

$$T_{s_1 s_2 s_3 s_4} = e^{-\beta H_{s_1 s_2 s_3 s_4}}, \tag{7.29}$$

with the inverse temperature $\beta = 1/\mathrm{T}$ [1]. Obviously, Eq. (7.29) is a forth-order tensor T, where each element gives the probability of the corresponding configuration.

The partition function is defined as the summation of the probability of all configurations. In the language of tensor, it is obtained by simply summing over all indexes

[1] In this paper, we set Bolzmann constant $k_B = 1$ for convenience.

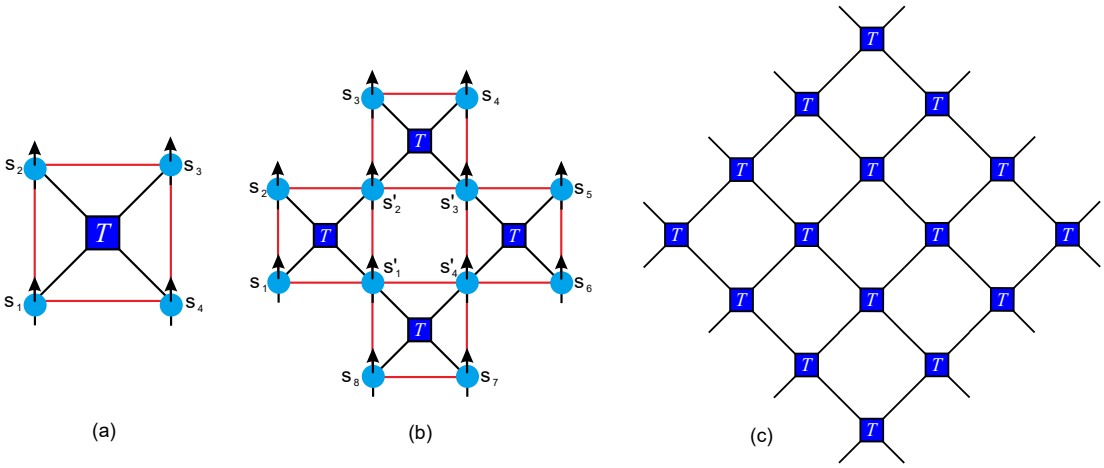

Figure 7.7: (a) Four Ising spins (blue balls with arrows) sitting on a single square, and the red lines represent the interactions. The blue block is the tensor T [Eq. (7.29)], with the black lines denoting the indexes of T. (b) The graphic representation of the TN on a larger lattice with more than one squares. (c) The TN construction of the partition function on infinite square lattice.

as

$$Z = \sum_{s_1 s_2 s_3 s_4} T_{s_1 s_2 s_3 s_4}. \tag{7.30}$$

Let us proceed a little bit further by considering four squares, whose partition function can be written in a TN with four tensors [Fig.7.7(b)] as

$$Z = \sum_{\{ss'\}} T_{s_1 s_2 s'_2 s'_1} T_{s'_2 s_3 s_4 s'_3} T_{s'_4 s'_3 s_5 s_6} T_{s_8 s'_1 s'_4 s_7}. \tag{7.31}$$

Each of the indexes $\{s'\}$ inside the TN is shared by two tensors, representing the spin that appears in both of the squares. The partition function is obtained by summing over all indexes.

For the infinite square lattice, the probability of a certain spin configuration $(s_1, s_2, \cdots)$ is given by the product of infinite number of tensor elements as

$$e^{-\beta H_{\{s\}}} = e^{-\beta H_{s_1 s_2 s_3 s_4}} e^{-\beta H_{s_4 s_5 s_6 s_7}} \cdots = T_{s_1 s_2 s_3 s_4} T_{s_4 s_5 s_6 s_7} \cdots \tag{7.32}$$

Then the partition function is given by the contraction of an infinite TN formed by the copies of T [Eq. (7.29)] as

$$Z = \sum_{\{s\}} \prod_n T_{s_1^n s_2^n s_3^n s_4^n}, \tag{7.33}$$

where two indexes satisfy $s_j^n = s_k^m$ if they refer to the same Ising spin. The graphic representation of Eq.7.33 is shown in Fig.7.7 (c). One can see that on square lattice, the TN still has the geometry of a square lattice. In fact, such a way will give a TN that has a geometry of the dual lattice of the system, and the dual of the square lattice is itself.

For the Q-state Potts model on square lattice, the partition function has the same TN representation as that of the Ising model, except that the elements of the tensor

are given by the Boltzmann wight of the Potts model and the dimension of each index is Q. Note that the Potts model with $q = 2$ is equivalent to the Ising model.

Another example is the eight-vertex model proposed by Baxter in 1971 [426]. It is one of the "ice-type" statistic lattice model, and can be considered as the classical correspondence of the Z_2 spin liquid state. The tensor that gives the TN of the partition function is also $(2 \times 2 \times 2 \times 2)$, whose non-zero elements are

$$T_{s_1,\cdots,s_N} = \begin{cases} 1, & s_1 + \cdots + s_N = even, \\ 0, & \text{otherwise.} \end{cases} \tag{7.34}$$

We shall remark that there are more than one ways to define the TN of the partition function of a classical system. For example, when there only exist nearest-neighbor couplings, one can define a matrix $M_{ss'} = e^{-\beta H_{ss'}}$ on each bond and put on each site a *super-digonal* tensor I (or called copy tensor) defined as

$$I_{s_1,\cdots,s_N} = \begin{cases} 1, & s_1 = \cdots = s_N; \\ 0, & \text{otherwise.} \end{cases} \tag{7.35}$$

Then the TN of the partition function is the contraction of copies of M and I, and possesses exactly the same geometry of the original lattice (instead of the dual one).

7.3.2 Quantum observables

With a TN state, the computations of quantum observables as $\langle\psi|\hat{O}|\psi\rangle$ and $\langle\psi|\psi\rangle$ is the contraction of a scalar TN, where $\hat{O}$ can be any operator. For a 1D MPS, this can be easily calculated, since one only needs to deal with a 1D TN stripe. For 2D PEPS, such calculations become contractions of 2D TN's. Taking $\langle\psi|\psi\rangle$ as an example, the TN of such an inner product is the contraction of the copies of the local tensor [Fig. 7.7 (c)] defined as

$$T_{a_1a_2a_3a_4} = \sum_s P^*_{s,a_1''a_2''a_3''a_4''} P_{s,a_1'a_2'a_3'a_4'}, \tag{7.36}$$

with P the tensor of the PEPS and $a_i = (a_i', a_i'')$. There are no open indexes left and the TN gives the scalar $\langle\psi|\psi\rangle$. The TN for computing the observable $\langle\hat{O}\rangle$ is similar. The only difference is that we should substitute some small number of $T_{a_1a_2a_3a_4}$ in original TN of $\langle\psi|\psi\rangle$ with "impurities" at the sites where the operators locate. Taking one-body operator as an example, the "impurity" tensor on this site can be defined as

$$\widetilde{T}^{[i]}_{a_1a_2a_3a_4} = \sum_{s,s'} P^*_{s,a_1''a_2''a_3''a_4''} \hat{O}^{[i]}_{s,s'} P_{s',a_1'a_2'a_3'a_4'}, \tag{7.37}$$

In such a case, the single-site observables can be represented by the TN contraction of

$$\frac{\langle\psi|\hat{O}^{[i]}|\psi\rangle}{\langle\psi|\psi\rangle} = \frac{\mathrm{tTr}\ \ \widetilde{T}^{[i]} \prod_{n\neq i} T}{\mathrm{tTr}\ \ \prod_{n=1}^{N} T}, \tag{7.38}$$

For some non-local observables, e.g., the correlation function, the contraction of $\langle\psi|\hat{O}^{[i]}\hat{O}^{[j]}|\psi\rangle$ is nothing but adding another "impurity" by

$$\langle\psi|\hat{O}^{[i]}\hat{O}^{[j]}|\psi\rangle = \mathrm{tTr}\ \ \widetilde{T}^{[i]}\widetilde{T}^{[j]} \prod_{n\neq i,j}^{N} T, \tag{7.39}$$

7.3.3 Ground-state and finite-temperature simulations

Ground-state simulations of 1D quantum models with short-range interactions can also be efficiently transferred to 2D TN contractions. When minimizing the energy

$$E = \frac{\langle\psi|\hat{H}|\psi\rangle}{\langle\psi|\psi\rangle}, \tag{7.40}$$

where we write $|\psi\rangle$ as an MPS. Generally speaking, there are two ways to solve the minimization problem: (i) simply treat all the tensor elements as variational parameters; (ii) simulate the imaginary-time evolution

$$|\psi_{gs}\rangle = \lim_{\beta\to\infty} \frac{e^{-\beta\hat{H}}|\psi\rangle}{\parallel e^{-\beta\hat{H}}|\psi\rangle \parallel}. \tag{7.41}$$

The first way can be realized by, e.g., Monte Carlo methods where one could randomly change or choose the value of each tensor element to locate the minimal of energy. One can also use the Newton method and solve the partial-derivative equations $\partial E/\partial x_n = 0$ with x_n standing for an arbitrary variational parameter. Anyway, it is inevitable to calculate E (i.e., $\langle\psi|\hat{H}|\psi\rangle$ and $\langle\psi|\psi\rangle$) for most cases, which is to contraction the corresponding TN's as explained above.

We shall stress that without TN, the dimension of the ground state (i.e., the number of variational parameters) increases exponentially with the system size, which makes the ground-state simulations impossible for large systems.

The second way of computing the ground state with imaginary-time evolution is more or less like an "annealing" process. One starts from an arbitrarily chosen initial state and acts the imaginary-time evolution operator on it. The "temperature" is lowered a little for each step, until the state reaches a fixed point. Mathematically speaking, by using Trotter-Suzuki decomposition, such an evolution is written in a TN defined on $(D+1)$-dimensional lattice, with D the dimension of the real space of the model.

Here, we take a 1D chain as an example. We assume that the Hamiltonian only contains at most nearest-neighbor couplings, which reads

$$\hat{H} = \sum_n \hat{h}_{n,n+1}, \tag{7.42}$$

with $\hat{h}_{n,n+1}$ containing the on-site and two-body interactions of the n-th and $n+1$-th sites. It is useful to divide $\hat{H}$ into two groups, $\hat{H} = \hat{H}^e + \hat{H}^o$ as

$$\hat{H}^e \equiv \sum_{even\ n} \hat{h}_{n,n+1}, \quad \hat{H}^o \equiv \sum_{odd\ n} \hat{h}_{n,n+1}. \tag{7.43}$$

By doing so, each two terms in $\hat{H}^e$ or $\hat{H}^o$ commute with each other. Then the evolution operator $\hat{U}(\tau)$ for infinitesimal imaginary time $\tau \to 0$ can be written as

$$\hat{U}(\tau) = e^{-\tau\hat{H}} = e^{-\tau\hat{H}^e} e^{-\tau\hat{H}^o} + O(\tau^2)[\hat{H}^e, \hat{H}^o] \tag{7.44}$$

If τ is small enough, the high-order terms are negligible, and the evolution operator becomes

$$\hat{U}(\tau) \simeq \prod_n \hat{U}(\tau)_{n,n+1}, \tag{7.45}$$

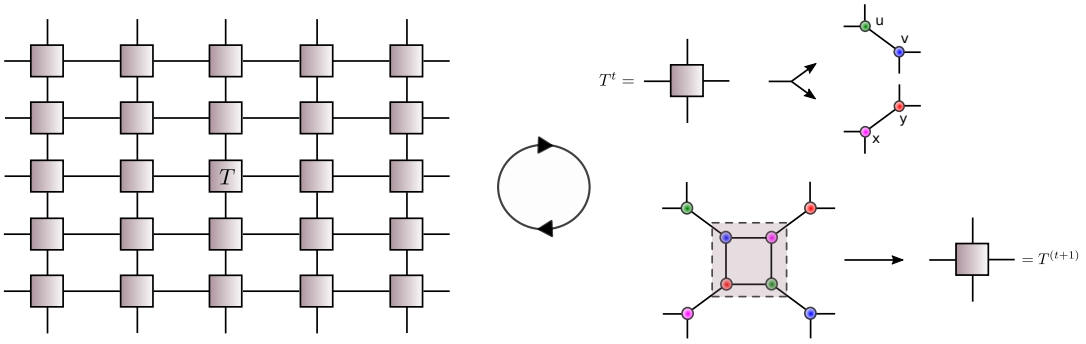

Figure 7.8: For an infinite square TN with translational invariance, the renormalization in the TRG algorithm is realized by two local operations of the local tensor. After each iteration, the bond dimensions of the tensor and the geometry of the network keep unchanged.

with the two-site evolution operator $\hat{U}(\tau)_{n,n+1} = e^{-\tau \hat{H}_{n,n+1}}$.

The above procedure is known as the first-order Trotter-Suzuki decomposition [468–470]. Note that higher-order decomposition can also be adopted. For example, one may use the second order Trotter-Suzuki decomposition that is written as

$$e^{-\tau \hat{H}} \simeq e^{-\frac{\tau}{2}\hat{H}^e} e^{-\tau \hat{H}^o} e^{-\frac{\tau}{2}\hat{H}^e}. \tag{7.46}$$

With Eq. (7.45), the time evolution can be transferred to a TN, where the local tensor is actually the coefficients of $\hat{U}(\tau)_{n,n+1}$, satisfying

$$T_{s_n s_{n+1} s'_n s'_{n+1}} = \langle s'_n s'_{n+1} | \hat{U}(\tau)_{n,n+1} | s_n s_{n+1} \rangle. \tag{7.47}$$

Such a TN is defined in a plain of two dimensions that corresponds to the spatial and (real or imaginary) time, respectively. The initial state is located at the bottom of the TN ($\beta = 0$) and its evolution is to do the TN contraction which can efficient solved by TN algorithms (presented later).

In addition, one can readily see that the evolution of a 2D state leads to the contraction of a 3D TN. Such a TN scheme provides a straightforward picture to understand the equivalence between a $(d+1)$-dimensional classical and a d-dimensional quantum theory. Similarly, the finite-temperature simulations of a quantum system can be transferred to TN contractions with Trotter-Suzuki decomposition. For the density operator $\hat{\rho}(\beta) = e^{-\beta \hat{H}}$, the TN is formed by the same tensor given by Eq. (7.47).

7.4 Tensor renormalization group

In 2007, Levin and Nave proposed TRG approach [446] to contract the TN of 2D classical lattice models. In 2008, Gu *et al* further developed TRG to handle 2D quantum topological phases [448]. TRG can be considered as a coarse-graining contraction algorithm. To introduce the TRG algorithm, let us consider a square TN formed by infinite number of copies of a forth-order tensor $T_{a_1 a_2 a_3 a_4}$ (see the left side of Fig. 7.8).

Contraction and truncation. The idea of TRG is to iteratively "coarse-grain" the TN without changing the bond dimensions, the geometry of the network, and the translational invariance. Such a process is realized by two local operations in each iteration. Let us denote the tensor in the t-th iteration as $T^{(t)}$ (we take $T^{(0)} = T$). For obtaining $T^{(t+1)}$, the first step is to decompose $T^{(t)}$ by SVD in two different ways [Fig.

7.8] as

$$T^{(t)}_{a_1a_2a_3a_4} = \sum_b U_{a_1a_2b} V_{a_3a_4b}, \tag{7.48}$$

$$T^{(t)}_{a_1a_2a_3a_4} = \sum_b X_{a_4a_1b} Y_{a_2a_3b}. \tag{7.49}$$

Note that the singular value spectrum can be handled by multiplying it with the tensor(s), and the dimension of the new index satisfies $dim(b) = \chi^2$ with χ the dimension of each bond of $T^{(t)}$.

The purpose of the first step is to deform the TN, so that in the second step, a new tensor $T^{(t+1)}$ can be obtained by contracting the four tensors that form a square [Fig. 7.8] as

$$T^{(t+1)}_{b_1b_2b_3b_4} \leftarrow \sum_{a_1a_2a_3a_4} V_{a_1a_2b_1} Y_{a_2a_3b_2} U_{a_3a_4b_3} X_{a_4a_1b_4}. \tag{7.50}$$

We use an arrow instead of the equal sign, because one may need to divide the tensor by a proper number to keep the value of the elements from being divergent. The arrows will be used in the same way below.

These two steps define the contraction strategy of TRG. By the first step, the number of tensors in the TN (i.e., the size of the TN) increases from N to $2N$, and by the second step, it decreases from $2N$ to $N/2$. Thus, after t times of each iterations, the number of tensors decreases to the $\frac{1}{2^t}$ of its original number. For this reason, TRG is an *exponential contraction algorithm.*

Error and environment. The dimension of the tensor at the t-th iteration becomes χ^{2^t}, if no truncations are implemented. that means that truncations of the bond dimensions are necessary. In its original proposal, the dimension is truncated by only keeping the singular vectors of the χ-largest singular values in Eq. (7.49). Then the new tensor $T^{(t+1)}$ obtained by Eq. (7.50) has exactly the same dimension as $T^{(t)}$.

Each truncation will absolutely introduce some error, which is called the *truncation error*. The truncation error is quantified by the discarded singular values λ as

$$\varepsilon = \frac{\sqrt{\sum_{b=\chi}^{\chi^2-1} \lambda_b^2}}{\sqrt{\sum_{b=0}^{\chi^2-1} \lambda_b^2}}. \tag{7.51}$$

According to the linear algebra, ε in fact gives the error of the SVD given in Eq. (7.49), meaning that such a truncation minimizes the error of reducing the rank of $T^{(t)}$, which reads

$$\varepsilon = |T^{(t)}_{a_1a_2a_3a_4} - \sum_{b=0}^{\chi-1} U_{a_1a_2b} V_{a_3a_4b}| \tag{7.52}$$

One may repeat the contraction-and-truncation process until $T^{(t)}$ converges. It usually only takes ~ 10 steps, after which one in fact contract a TN of 2^t tensors to a single tensor.

The truncation is optimized according to the SVD of $T^{(t)}$. Thus, $T^{(t)}$ is called the *environment*. In general, the tensor(s) that determines the truncations is called the environment. It is a key factor to the accuracy and efficiency of the algorithm. For those that use local environments, like TRG, the efficiency is relatively high since the truncations are easy to compute. But, the accuracy is bounded since the truncations are

only optimized according to some local information (like in TRG the local partitioning $T^{(t)}$).

One may choose other tensors or even the whole TN as the environment. In 2009, Xie *et al* proposed the second renormalization group (SRG) algorithm [471]. The idea is in each truncation step of TRG, they define the global environment that is a forth-order tensor $\mathcal{E}_{a_1^{\tilde{n}}a_2^{\tilde{n}}a_3^{\tilde{n}}a_4^{\tilde{n}}} = \sum_{\{a\}} \prod_{n\neq\tilde{n}} T^{(n,t)}_{a_1^n a_2^n a_3^n a_4^n}$ with $T^{(n,t)}$ the n-th tensor in the t-th step and $\tilde{n}$ the tensor to be truncated. $\mathcal{E}$ is the contraction of the whole TN after getting rid of $T^{(\tilde{n},t)}$, and is computed by TRG. Then the truncation is obtained not by the SVD of $T^{(\tilde{n},t)}$, but by the SVD of $\mathcal{E}$. The word "second" in the name of the algorithm comes from the fact that in each step of the original TRG, they use a second TRG to calculate the environment. SRG is obviously more consuming, but bears much higher accuracy than TRG. The balance between accuracy and efficiency, which can be controlled by the choice of environment, is one main factor top consider while developing or choosing the TN algorithms.

7.5 Time evolving block decimation

The TEBD algorithm by Vidal was developed originally for simulating the time evolution of 1D quantum models [305–307]. The (finite and infinite) TEBD algorithm has been widely applied to varieties of issues, such as criticality in quantum many body systems (e.g., [317,318,472]), the topological phases [330]. the many-body localization [473–475] and the thermodynamic property of quantum many-body systems [319,396, 476–480].

In the language of TN, TEBD solves the TN contraction problems in a linearized manner, and the truncation is calculated in the context of an MPS. In the following, let us explain the infinite TEBD (iTEBD) algorithm [307] (Fig. 7.9) by still taking the infinite square TN formed by the copies of a forth-order tensor T as an example. In each step, a row of tensors (which can be regarded as an MPO) are contracted to an MPS $|\psi\rangle$. Inevitably, the bond dimensions of the tensors in the MPS will increase exponentially as the contractions proceed. Therefore, truncations are necessary to prevent the bond dimensions diverging. The truncations are determined by minimizing the distance between the MPS's before and after the truncation. After the MPS $|\psi\rangle$ converges, the TN contraction becomes $\langle\psi|\psi\rangle$, which can be exactly and easily computed.

Contraction. We use is two-site translational invariant MPS, which is formed by the tensors A and B on the sites and the spectrum Λ and Γ on the bonds as

$$\sum_{\{a\}} \cdots \Lambda_{a_{n-1}} A_{s_{n-1},a_{n-1}a_n} \Gamma_{a_n} B_{s_n,a_n a_{n+1}} \Lambda_{a_{n+1}} \cdots . \tag{7.53}$$

In each step of iTEBD, the contraction is given by

$$A_{s,\tilde{a}\tilde{a}'} \leftarrow \sum_{s'} T_{sbs'b'} A_{s',aa'}, \quad B_{s,\tilde{a}\tilde{a}'} \leftarrow \sum_{s'} T_{sbs'b'} B_{s',aa'}, \tag{7.54}$$

where the new virtual bonds are entangled, satisfying $\tilde{a} = (b,a)$ and $\tilde{a}' = (b',a')$. Meanwhile, the spectrum are also updated as

$$\Lambda_{\tilde{a}} \leftarrow \Lambda_a \mathbf{1}_b, \quad \Gamma_{\tilde{a}'} \leftarrow \Gamma_{a'} \mathbf{1}_{b'}, \tag{7.55}$$

where $\mathbf{1}$ is a vector with $\mathbf{1}_b = 1$ for any b.

It is readily to see that the number of tensors in iTEBD will be reduced linearly as tN, with t the number of the contraction-and-truncation steps and $N \to \infty$ the number

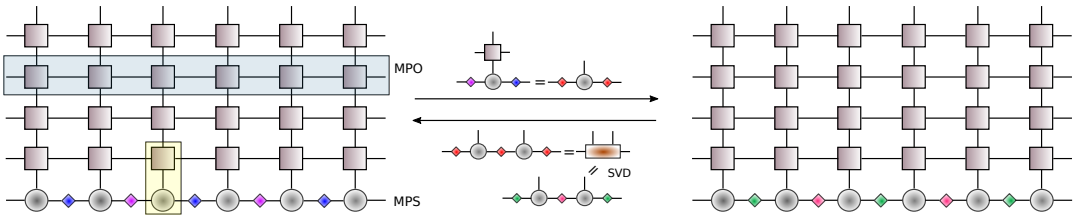

Figure 7.9: The illustration of the contraction and truncation of the iTEBD algorithm. In each iteration step, a row of tensors in the TN are contracted to the MPS, and truncations by SVD are implemented so that the bond dimensions of the MPS keep unchanged.

of the columns of the TN. Therefore, iTEBD (also finite TEBD) can be considered as a *linearized contraction algorithm*, in contrast to the exponential contraction algorithm like TRG.

Truncation. Truncations are needed when the dimensions of the virtual bonds exceed the preset dimension cut-off χ. In the original version of iTEBD [307], the truncations are done by local SVD's. To truncate the virtual bond $\tilde{a}$ for example, one defines a matrix by contracting the tensors and spectrum connected to the target bond as

$$M_{s_1\tilde{a}_1,s_2\tilde{a}_2} = \sum_{\tilde{a}} \Lambda_{\tilde{a}_1} A_{s_1,\tilde{a}_1\tilde{a}} \Gamma_{\tilde{a}} B_{s_2,\tilde{a}\tilde{a}_2} \Lambda_{\tilde{a}_2}. \tag{7.56}$$

Then, perform SVD on M, keeping only the χ-largest singular values and the corresponding basis as

$$M_{s_1\tilde{a}_1,s_2\tilde{a}_2} = \sum_{a=0}^{\chi-1} U_{s_1,\tilde{a}_1 a} \Gamma_a V_{s_2,a\tilde{a}_2}. \tag{7.57}$$

The spectrum Γ is updated by the singular values of the above SVD. The tensors A and B are also updated as

$$A_{s_1,\tilde{a}a} = (\Lambda_{\tilde{a}})^{-1} U_{s_1,\tilde{a}a}, \quad B_{s_2,a\tilde{a}} = V_{s_2,a\tilde{a}} (\Lambda_{\tilde{a}})^{-1}. \tag{7.58}$$

Till now, the truncation of the spectrum Γ and the corresponding virtual bond have been completed. Any spectra and virtual bonds can be truncated similarly.

Error and environment. Similar to TRG and SRG, the environment of the original iTEBD is M in Eq. (7.57), and the error is measured by the discarded singular values of M. Thus iTEBD seems to only use local information to optimize the truncations. What is amazing is that when the MPO is unitary or near unitary, the MPS converges to a so-called *canonical form* [52, 308]. The truncations are then optimal by taking the whole MPS as the environment. If the MPO is far from being unitary, Orús and Vidal proposed the *canonicalization* algorithm [308] to transform the MPS into the canonical form before truncating. We will talk about this issue in detail in the next section.

7.6 Corner transfer matrix renormalization group

In the 1960s, the corner transfer matrix (CTM) idea was developed originally by Baxter in Refs. [251, 467] and a book [481]. Such ideas and methods have been applied to various models, for example, the chiral Potts model [482–484], the 8-vertex model

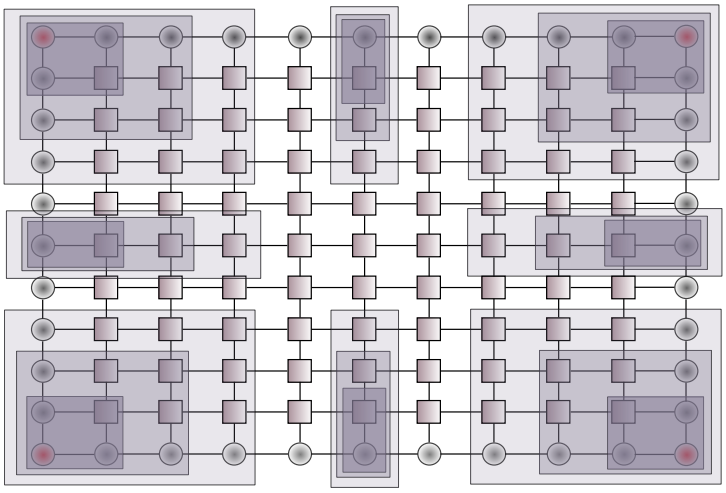

Figure 7.10: Overview of the CTMRG contraction scheme. The tensors in the TN are contracted to the variational tensors defined on the edges and corners.

[426,485,486], and to the 3D Ising model [487]. Combining CTM with DMRG, Nishino and Okunishi proposed the CTMRG [257] in 1996 and applied it to several models [257, 259–263, 488–492]. In 2009, Orús and Vidal further developed CTMRG to deal with TN's [466]. What they proposed to do is to put eight *variational tensors* to be optimized in the algorithm, which are four corner transfer matrices $C^{[1]}, C^{[2]}, C^{[3]}, C^{[4]}$ and four row (column) tensors $R^{[1]}, R^{[2]}, R^{[3]}, R^{[4]}$, on the boundary, and then to contract the tensors in the TN to these variational tensors in a specific order shown in Fig. 7.10. The TN contraction is considered to be solved with the variational tensors when they converge in this contraction process. Compared with the boundary-state methods in the last subsection, the tensors in CTMRG define the states on both the boundaries and corners.

Contraction. In each iteration step of CTMRG, one choses two corner matrices on the same side and the row tensor between them, e.g., $C^{[1]}$, $C^{[2]}$ and $R^{[2]}$. The update of these tensors (Fig.7.11) follows

$$\tilde{C}^{[1]}_{\tilde{b}_2 b'_1} \leftarrow \sum_{b_1} C^{[1]}_{b_1 b_2} R^{[1]}_{b_1 a_1 b'_1}, \tag{7.59}$$

$$\tilde{R}^{[2]}_{\tilde{b}_2 a_4 \tilde{b_3}} \leftarrow \sum_{a_2} R^{[2]}_{b_2 a_2 b_3} T_{a_1 a_2 a_3 a_4}, \tag{7.60}$$

$$\tilde{C}^{[2]}_{\tilde{b}_3 b'_4} \leftarrow \sum_{b_4} C^{[2]}_{b_3 b_4} R^{[3]}_{b_4 a_3 b'_4}, \tag{7.61}$$

where $\tilde{b}_2 = (b_2, a_1)$ and $\tilde{b}_3 = (b_3, a_1)$.

After the contraction given above, it can be considered that one column of the TN (as well as the corresponding row tensors $R^{[1]}$ and $R^{[3]}$) are contracted. Then one chooses other corner matrices and row tensors (such as $\tilde{C}^{[1]}$, $C^{[4]}$ and $R^{[1]}$) and implement similar contractions. By iteratively doing so, the TN is contracted in the way shown in Fig. 7.10.

Note that for a finite TN, the initial corner matrices and row tensors should be taken as the tensors locating on the boundary of the TN. For an infinite TN, they can be initialized randomly, and the contraction should be iterated until the preset

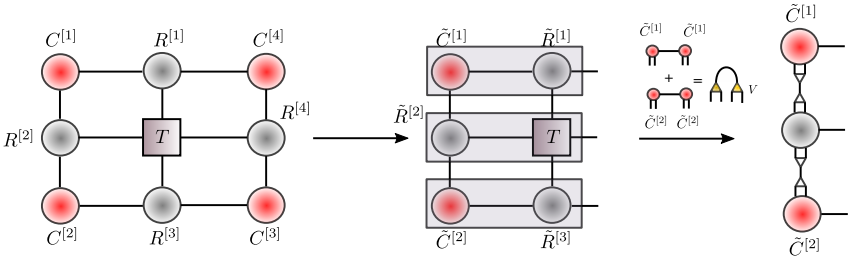

Figure 7.11: The first arrow shows absorbing tensors $R^{[1]}$, T, and $R^{[3]}$ to renew tensors $C^{[1]}$, $R^{[2]}$, and $C^{[2]}$ in left operation. The second arrow shows the truncation of the enlarged bond of $\tilde{C}^{[1]}$, $\tilde{R}^{[2]}$ and $\tilde{C}^{[2]}$. Inset is the acquisition of the truncation matrix Z.

convergence is reached. CTMRG can be regarded as a *polynomial contraction scheme*. One can see that the number of tensors that are contracted at each step is determined by the length of the boundary of the TN at each iteration time. When contracting a 2D TN defined on a $(L \times L)$ square lattice as an example, the length of each side is $L - 2t$ at the t-th step. The boundary length of the TN (i.e., the number of tensors contracted at the t-th step) bears a linear relation with t as $4(L - 2t) - 4$. For a 3D TN such as cubic TN, the boundary length scales as $6(L - 2t)^2 - 12(L - 2t) + 8$, thus the CTMRG for a 3D TN (if exists) gives a polynomial contraction.

Truncation. One can see that after the contraction in each iteration step, the bond dimensions of the variational tensors increase. Truncations are then in need to prevent the excessive growth of the bond dimensions. In Ref. [466], the truncation is obtained by inserting a pair of isometries V and $V^\dagger$ in the enlarged bonds. A reasonable (but not the only choice) of V for translational invariant TN is to consider the eigenvalue decomposition on the sum of corner transfer matrices as

$$\sum_b \tilde{C}^{[1]\dagger}_{\tilde{b}b} \tilde{C}^{[1]}_{\tilde{b}'b} + \sum_b \tilde{C}^{[2]\dagger}_{\tilde{b}b} \tilde{C}^{[1]}_{\tilde{b}'b} \simeq \sum_{b=0}^{\chi-1} V_{\tilde{b}b} \Lambda_b V^*_{\tilde{b}'b}. \tag{7.62}$$

Only the χ largest eigenvalues are preserved. Therefore, V is a matrix of the dimension $D\chi \times \chi$, where D is the bond dimension of T and χ is the dimension cut-off. We then truncate $\tilde{C}^{[1]}$, $\tilde{R}^{[2]}$, and $\tilde{C}^{[2]}$ using V as

$$C^{[1]}_{b'_1 b_2} = \sum_{\tilde{b}_2} \tilde{C}^{[1]}_{\tilde{b}_2 b'_1} V^*_{\tilde{b}_2 b_2}, \tag{7.63}$$

$$R^{[2]}_{b_2 a_4 b_3} = \sum_{\tilde{b}_2, \tilde{b}_3} \tilde{R}^{[2]}_{\tilde{b}_2 a_4 \tilde{b}_3} V_{\tilde{b}_2 b_2} V^*_{\tilde{b}_3 b_3}, \tag{7.64}$$

$$C^{[2]}_{b_3 b'_4} = \sum_{\tilde{b}_3} \tilde{C}^{[2]}_{\tilde{b}_3 b'_4} V_{\tilde{b}_3 b_3}. \tag{7.65}$$

Error and environment. Same as TRG or TEBD, the truncations are obtained by the matrix decompositions of certain tensors that define the environment. From Eq. (7.62), the environment in CTMRG is the loop formed by the corner matrices and row tensors. Note that symmetries might be considered to accelerate the computation. For example, one may take $C^{[1]} = C^{[2]} = C^{[3]} = C^{[4]}$ and $R^{[1]} = R^{[2]} = R^{[3]} = R^{[4]}$ when the TN has rotational and reflection symmetries ($T_{a_1 a_2 a_3 a_4} = T_{a'_1 a'_2 a'_3 a'_4}$ after any permutation of the indexes).

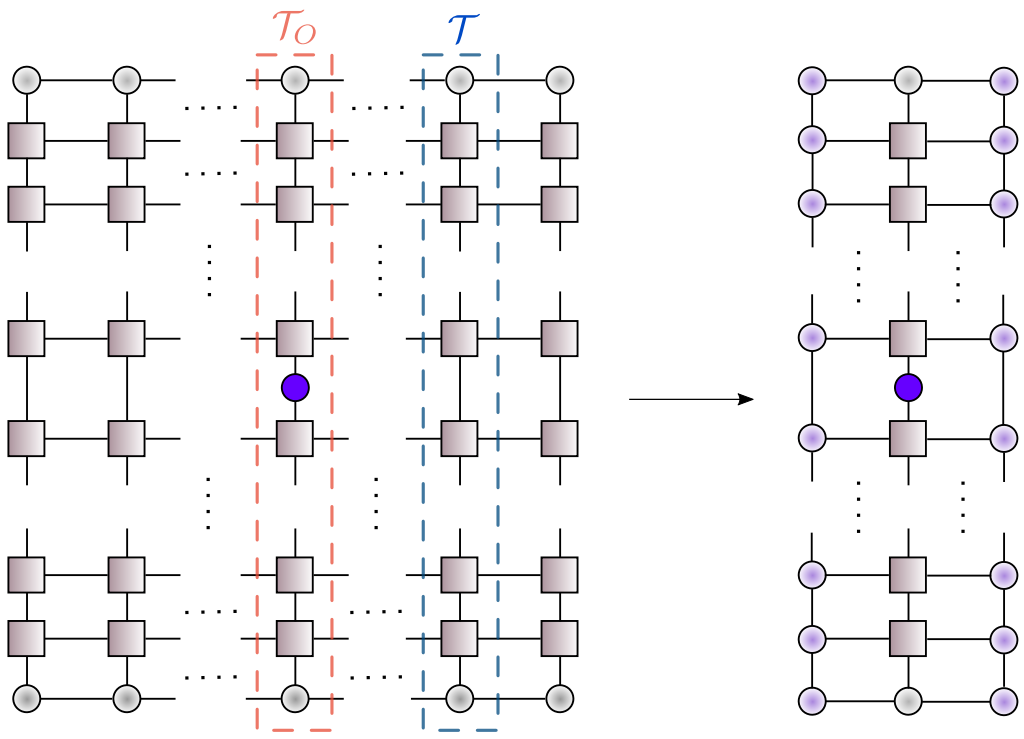

Figure 7.12: Transverse contraction of the TN for a local expectation value $\langle O(t)\rangle$.

7.7 Transverse contraction and folding tick

For the boundary-state methods introduced above, the boundary states are defined in the real space. Taking iTEBD for the real-time evolution as an example, the contraction is implemented along the time direction, which is to do the time evolution in an explicit way. It is quite natural to consider implementing the contraction along the other direction. In the following, we will introduce the transverse contraction and the folding trick proposed and investigated in Refs. [493–495]. The motivation of transverse contraction is to avoid the explicit simulation of the time-dependent state $|\psi(t)\rangle$ that might be difficult to capture due to the fast growth of its entanglement.

Transverse contraction. Let us consider to calculate the average of a one-body operator $o(t) = \langle\psi(t)|\hat{o}|\psi(t)\rangle$ with $|\psi(t)\rangle$ that is a quantum state of infinite size evolved to the time t. The TN representing $o(t)$ is given in the left part of Fig. 7.12, where the green squares give the initial MPS $|\psi(0)\rangle$ and its conjugate, the yellow diamond is $\hat{o}$, and the TN formed by the green circles represents the evolution operator $e^{it\hat{H}}$ and its conjugate (see how to define the TN in Sec. 7.3.3).

To perform the transverse contraction, we treat each column of the TN as an MPO $\hat{\mathcal{T}}$. Then as shown in the right part of Fig. 7.12, the main task of computing $o(t)$ becomes to solve the dominant eigenstate $|\phi\rangle$ (normalized) of $\hat{\mathcal{T}}$, which is an MPS illustrated by the purple squares. One may solve this eigenstate problems by any of the boundary-state methods (TEBD, DMRG, etc.). With $|\phi\rangle$, $o(t)$ can be exactly and efficiently calculated as

$$o(t) = \frac{\langle\psi(t)|\hat{o}|\psi(t)\rangle}{\langle\psi(t)|\psi(t)\rangle} = \frac{\langle\phi|\hat{\mathcal{T}}_o|\phi\rangle}{\langle\phi|\hat{\mathcal{T}}|\phi\rangle}, \tag{7.66}$$

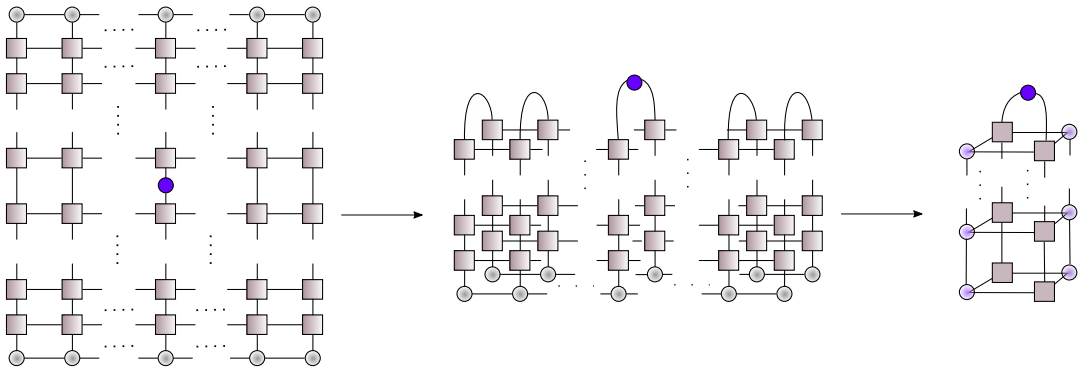

Figure 7.13: The illustration of the folding trick.

with $\hat{\mathcal{T}}_o$ is the column that contains the operator $\hat{o}$. Note that the length of $|\phi\rangle$ (i.e., the number of tensors in the MPS) is proportional to the time t, thus one should use the finite-size versions of the boundary-state methods. It should also be noted that $\hat{\mathcal{T}}$ may not be Hermitian. In this case, one should not use $|\phi\rangle$ and its conjugate, but compute the left and right eigenstates of $\hat{\mathcal{T}}$ instead.

Interestingly, similar ideas of the transverse contraction appeared long before the concept of TN emerged. For instance, transfer matrix renormalization group (TMRG) [269, 271, 272, 496] can be used to simulate the finite-temperature properties of a 1D system. The idea of TMRG is to utilize DMRG to calculate the dominant eigenstate of the transfer matrix (similar to $\mathcal{T}$). In correspondence with the TN terminology, it is to use DMRG to compute $|\phi\rangle$ from the TN that defines the imaginary-time evolution. We will skip of the details of TMRG since it is not directly related to TN. One may refer the related references if interested.

Folding trick. The main bottleneck of a boundary-state method concerns the entanglement of the boundary state. In other words, the methods will become inefficient when the entanglement of the boundary state grows too large. One example is the real-time simulation of a 1D chain, where the entanglement entropy increases linearly with time. Solely with the transverse contraction, it will not essentially solve this problem. Taking the imaginary-time evolution as an example, it has been shown that with the dual symmetry of space and time, the boundary states in the space and time directions possess the same entanglement [63, 495].

In Ref. [493], the folding trick was proposed. The idea is to "fold" the TN before the transverse contraction (Fig. 7.13). In the folded TN, each tensor is the tensor product of the original tensor and its conjugate. The length of the folded TN in the time direction is half of the original TN, and so is the length of the boundary state.

The previous work (Ref. [493]) on the dynamic simulations of 1D spin chains showed that the entanglement of the boundary state is in fact reduced compared with that of the boundary state without folding. This suggests that the folding trick provides a more efficient representation of the entanglement structure of the boundary state. The authors of Ref. [493] suggested an intuitive picture to understand the folding trick. Consider a product state as the initial state at $t - 0$ and a single localized excitation at the position x that propagates freely with velocity v. By evolving for a time t, only $(x \pm vt)$ sites will become entangled. With the folding trick, the evolutions (that are unitary) besides the $(x \pm vt)$ sites will not take effects since they are folded with the conjugates and become identities. Thus the spins outside $(x \pm vt)$ will remain product state and will not contribute entanglement to the boundary state. In short, one key

factor to consider here is the entanglement structure, i.e., the fact that the TN is formed by unitaries. The transverse contraction with the folding trick is a convincing example to show that the efficiency of contracting a TN can be improved by properly designing the contraction way according to the entanglement structure of the TN.

Chapter 8

Quantum filed theory with continuous MPS

In this Chapter, we focus on the continuous limit of a lattice model using tensor networks. Tensor networks allow to encode equilibrium states of many-body quantum systems described by local Hamiltonians with modest computational resources [53, 251, 257, 296, 305–309, 405, 466, 467, 497, 498]. They can be used to encode both quantum states, or to represent classical partition functions as a result of the well-known classical to quantum correspondence, based on the path-integral formulation of quantum mechanics.

The success of tensor networks started with White's DMRG algorithm that, as of today, is still the best numerical tool to characterize strongly-correlated systems in 1D [50,133,134,299,437]. They soon were extended to higher dimensions and connected with the theory of entanglement in many-body quantum systems that was being developed in parallel by the quantum information community [153, 260, 294, 317, 318, 332, 334, 407, 446–448, 499, 500].

In recent developments, tensor network have been used to study continuous quantum field theories (QFT). Rather than starting from a lattice model, one can indeed start from a continuous Hamiltoninan describing a QFT and formulate a variational calculation in order to express the vacuum of the QFT as tensor network [180,331,501–509].

Here we extract the matrix product state of a (1+1)D QFT vacuum by starting from a lattice model and constructing explicitly its continuous limit. The standard way for doing this is to reduce the lattice spacing while approaching a quantum critical point as customary in the context of building the continuous limit of lattice field theory [510]. This entails two limits, the lattice spacing a going to zero, and the correlation length ξ going to infinity as we approach the critical point. The two limits needs to be taken in parallel, by keeping their product $a\xi$ constant fixed to the desired physical value.

In the context of tensor networks, this procedure can be considerably simplified by observing that, in order to extract the ground state of a lattice system, we usually perform an imaginary time evolution. A D dimensional system thus actually becomes $D+1$ dimensional once we include the imaginary time. The evolution along the imaginary time is performed by first breaking it in small time steps. Each small step is then approximated by using a Suzuki-Trotter decomposition [469, 470]. The decomposition becomes more and more accurate as the small time steps tend to zero. Reducing the time steps, thus can be seen as analogous to taking the continuous limit along the time direction, something that Hastings had already observed in Ref. [495].

This observation can be exploited in order to extract a continuous MPS along the time direction that we call tMPS. The standard QFT vacuum to vacuum transition probabilities can thus be expressed as the norm of the tMPS state. Beside this fact, in general the tMPS encodes a different state from the ground state MPS of the discretized field theory that can be represented as a standard MPS by, e.g., performing the imaginary time evolution of a random initial MPS for very long times.

If the system possesses a Lorentz-invariant critical point, however, the tMPS and the standard ground state MPS, at the critical point, are related by a trivial non-universal re-scaling factor. In these specific cases, the tMPS thus encodes the continuum limit of the ground state of the discretized field theory, that is the tMPS represents the vacuum of the QFT.

Here we will check this statement. In particular we want to better characterize the regularized QFT described by the tMPS. The main advantage of encoding the vacuum of a QFT with a tensor network with finite bond dimension is indeed that the QFT is then automatically regularized. For example, the entanglement entropy of half of the vacuum is finite. The bond dimension of the tensor network thus acts as the UV regulator of the field theory, by limiting the number of degrees of freedom per unit length. This was first observed in [317, 331].

Despite the numerous studies that followed this initial observations [258, 320, 511–516] we still lack a full understanding of the role of the bond dimension as a regulator.

In particular, it is well known that, starting from a lattice model, the low-energy spectrum of the emerging field theory depends on both the critical exponents at the quantum critical point and the boundary conditions of the lattice system [517, 518]. This fact translates into well defined ratios for the masses of the low energy excitations only depending on the universality class of the quantum-phase transition. For example, by taking the continuous limit of the Ising model on a 2D torus, we obtain the Ising field theory whose low-energy excitations have masses fulfilling $m_2/m_1 = 4$ [520, 521, 524].

Since the tMPS transfer matrix propagates the dynamical correlations, one would naively expect to recover these ratios from appropriate functions of the eigenvalues of the tMPS transfer matrix. Our analysis of the tMPS for the Ising model show that this does not happen. Interestingly we find that the masses we extract from the tMPS correspond to those predicted by Zamolodchikov, $m_2/m_1 = 1.6$. These masses were obtained when characterizing the field theory emerging from the critical Ising model perturbed with a small parallel field [519, 521].

While this result could seem surprising, it can be easily understood by noticing that the finite bond dimension of a tMPS breaks the Z_2 symmetry in a similar way than the magnetic field does in the Zamolodchikov's scenario. The finite bond dimension thus acts as a relevant magnetic perturbation to the critical Hamiltonian, rather than as a thermal perturbation, and the spectrum is thus modified accordingly.

These results agree with what was discussed in [512]. There the authors compared the finite-size scaling implicit by taking a continuous limit of a discrete lattice model, and calculated the finite-entanglement scaling that we also use here to obtain the tMPS. They found that the two procedures generate different fixed point tensors. In performing the finite-size scaling with an MPS, indeed, we first fix the size of the system to a finite value N and increase the bond dimension χ until we accurately encode the ground state of the finite-size system. This procedure corresponds, in the MPS language, to taking first $\chi \to \infty$ and then $N \to \infty$.

The tMPS is obtained by inverting the order of the two limits, we first take $N \to \infty$ with fixed χ, and then $\chi \to \infty$. As observed in [512] the two limits do not commute.

At any finite size (either spatial or temporal) indeed the Z_2 symmetry is restored, while at any finite χ the Z_2 symmetry is broken.

In this paper we focus on the critical point of Ising model in a transverse field and derive these results by first showing that the tMPS is actually a continuous MPS [331]; it describes the same physics as the ground-state MPS up to a gauge transformation and some trivial rescaling factors. This allows us to analyze the low-energy spectrum of the field theory emerging from the tMPS and identify it with the one predicted by Zamolodchikov et al [519, 521].

8.1 Continuous MPS

The cMPS is a continuum analogue of the matrix product states (MPS) ansatz [331] a natural and effective form of parametrization of variational states for systems with limited entanglement due to short-range interactions. The MPS based algorithms are the arguably the most powerful numerical techniques to date for simulating quantum lattice systems in low dimensions. Although these algorithms have been tremendously successful, they are not ideal to be used on systems of dilute gases, as they were intrinsically tailored for lattice systems. For this reason, the cMPS has been developed to directly address 1D systems in a continuum, such as quantum gases and liquids where the positions of atoms are not restricted to discrete lattice sites. The cMPS has demonstrated its capability in predicting ground-state properties of 1D continuum systems of interacting bosons [331], Luttinger liquids [522, 523], relativistic fermions [501–503], as well as excitation properties of bosons [505]. In this section, we give an introduction to the cMPS with applications of it to an interacting 1D Bose gas and the quantum Ising model.

The cMPS suggests a systematic construction of variational many-body states with auxiliary matrices that capture essential correlations in one dimension. Since the system's energy can be expressed as a functional of the matrix elements, the ground state can thus be approximated using a proper minimization method. The advantage of cMPS is that the assumption of the variational state does not rely on the properties of the Hamiltonian, and therefore, one does not need to consider the integrability of the system as in the case of Bethe ansatz. It also works without any extension for systems having less symmetry, such as those with impurities or in a trapping potential.

A continuous matrix product state $|\chi\rangle$ for a ring of length L is characterized by the $D\times D$ matrices in the auxiliary space, $Q(x)$ and $R(x)$, where the variational parameters are stored. For a Bose gas in 1D, the cMPS has the form

$$|\chi\rangle = \mathrm{Tr}_{\mathrm{aux}}\left\{\mathcal{P}e^{\int_0^L dx\left[Q(x)\otimes I+R(x)\otimes\Psi^\dagger(x)\right]}\right\}|\Omega\rangle \tag{8.1}$$

where $\mathrm{Tr}_{\mathrm{aux}}$ is the trace over the auxiliary space, $\hat{I}$ is the identity operator on the Fock space, $\mathcal{P}$ is the path-ordered exponential, and $|\Omega\rangle$ is the Fock-space vacuum state. The bosonic particle creation and annihilation operators $\Psi(x)$ and $\Psi^\dagger(x)$ obey the commutation relation $[\Psi(x),\Psi^\dagger(x')]=\delta(x-x')$.

Let us expand $|\chi\rangle$ in terms of fields operators. Under the path-ordering the expan-

sion yields

$$|\chi\rangle = \sum_{n=0}^{\infty} \int dt_1 \cdots dt_n \mathrm{Tr}\left\{ \left(\mathcal{P} e^{\int_0^{x_1} dt Q(t)} \right) R(x_1) \left(\mathcal{P} e^{\int_{x_1}^{x_2} dt Q(t)} \right) R(x_2) \right\} \cdots \left(\mathcal{P} e^{\int_{x_n}^{x_{n-1}} dt Q(t)} \right) R(x_n) \left(\mathcal{P} e^{\int_{x_n}^{L} dt Q(t)} \right) \Psi^\dagger(x_1) \cdots \Psi^\dagger(x_n) |\Omega\rangle. \quad (8.2)$$

Defining the probability amplitude for any particular position eigenstate as

$$\phi = \mathrm{Tr}_{\mathrm{aux}} \left\{ u(0, x_1) R(x_1) u(x_1, x_2) R(x_2) \cdots R(x_n) \right\}, \quad (8.3)$$

the cMPS $|\chi\rangle$ can be expressed as

$$|\chi\rangle = \sum_{n=0}^{\infty} dx_1 \cdots dx_n \phi_n \Psi^\dagger(x_1) \cdots \Psi^\dagger(x_n) |\Omega\rangle \quad (8.4)$$

We thus can interpret $u(x, y) = \mathcal{P} \int_x^y dt Q(t)$ as a free propagation between points a and b. Furthermore the role of the $R(x)$ matrix is analogous to a scattering matrix at position x, that creates a field excitation (particle).

For translationally invariant states, one can assume spatially independent matrices $Q(x) = Q$ and $R(x) = R$. With this simplification, the expectation values for essential observables can be written down in simple closed forms as below, with the norm being $\langle \chi | \chi \rangle = \mathrm{Tr}\left[e^{TL} \right]$.

First we can write the cMPS in discretized form:

$$|\chi\rangle = \mathrm{Tr}_{\mathrm{aux}} \left[\mathcal{P} e^{\int_0^L dx \left[Q(x) + R(x) \Psi^\dagger(x) \right]} \right] |\chi\rangle = = \mathrm{Tr}\left\{ e^{\epsilon Q_0} e^{\epsilon R_0 \Psi_0^\dagger} e^{\epsilon Q_1} e^{\epsilon R_1 \Psi_1^\dagger} \cdots e^{\epsilon Q_{N-1}} e^{\epsilon R_{N-1} \Psi_{N-1}^\dagger} \right\} |\Omega\rangle, \quad (8.5)$$

with $\epsilon = L/N$. Using the eq. (8.5) and the property $\mathrm{Tr}\left[A\right] \mathrm{Tr}\left[B\right] = \mathrm{Tr}\left[A \otimes B\right]$ we obtain

$$\langle \chi | \chi \rangle = \mathrm{Tr}_{aux} \left(e^{\epsilon Q_0} \otimes e^{\epsilon \overline{Q}_0} \right) \langle 0_0 | e^{\epsilon \overline{R}_0 \Psi_0} \otimes e^{\epsilon R_0 \Psi_0^\dagger} | 0_0 \rangle \left(e^{\epsilon Q_1} \otimes e^{\epsilon \overline{Q}_1} \right) \langle 0_1 | e^{\epsilon \overline{R}_1 \Psi_1} \otimes e^{\epsilon R_1 \Psi_1^\dagger} | 0_1 \rangle \cdots \left(e^{\epsilon Q_{N-1}} \otimes e^{\epsilon \overline{Q}_{N-1}} \right) \langle 0_{N-1} | e^{\epsilon \overline{R}_{N-1} \Psi_{N-1}} \otimes e^{\epsilon R_{N-1} \Psi_{N-1}^\dagger} | 0_{N-1} \rangle, \quad (8.6)$$

where $|0_i\rangle$ is the vacuum state at $x = x_i$ such that $|\Omega\rangle = \otimes_{i=0}^{N-1} |0_i\rangle$. Furthermore

$$\langle 0_i | e^{\epsilon \overline{R}_i \Psi_i} \otimes e^{\epsilon R_i \Psi_i^\dagger} | 0_i \rangle \approx e^{\epsilon R \otimes \overline{R}}, \quad (8.7)$$

$$e^{\epsilon Q_j} \otimes e^{\epsilon \overline{Q}_j} \approx e^{\epsilon \left(Q_j \otimes I + I \otimes \overline{Q}_j \right)}. \quad (8.8)$$

Equations (8.6) and (8.7) give us:

$$\left(e^{\epsilon Q_j} \otimes e^{\epsilon \overline{Q}_j} \right) \langle 0_i | e^{\epsilon \overline{R}_i \Psi_i} \otimes e^{\epsilon R_i \Psi_i^\dagger} | 0_i \rangle = e^{\epsilon T_j}, \quad (8.9)$$

where $T_j = Q_j \otimes I + I \otimes \overline{Q}_j + R_j \otimes \overline{R}_j$. Therefore, we may write,

$$\langle \chi | \chi \rangle = \mathrm{Tr}\left[e^{\epsilon T_0} e^{\epsilon T_1} \cdots e^{\epsilon T_{N-1}} \right] = \mathrm{Tr}\left[\mathcal{P} e^{\int_0^L dx T(x)} \right]. \quad (8.10)$$

Now we can write the number density $\langle\Psi^\dagger(x)|\Psi(x)\rangle$. Starting with,

$$\Psi_j|\chi\rangle = \mathrm{Tr}_{aux}\left\{e^{\epsilon Q_1}e^{\epsilon R_1\Psi_1^\dagger}\cdots e^{\epsilon Q_N}e^{\epsilon R_N\Psi_N^\dagger}\right\} \tag{8.11}$$

the number density reads:

$$\langle\Psi^\dagger(x)|\Psi(x)\rangle = \mathrm{Tr}\left[\left(\mathcal{P}e^{\int_0^x dxT(x)}\right)\left(\overline{R}(x)\otimes R(x)\right)\left(\mathcal{P}e^{\int_x^L dxT(x)}\right)\right] \tag{8.12}$$

We have seen that the cMPS can be regarded as a superposition of the eigenstates, where the probability amplitudes for each of the eigenstates are traces of expressions that are functions of Q and R matrices. As the trace operation is invariant under arbitrary basis transformation, applying the transformations

$$Q \to P^{-1}QP \qquad R \to P^{-1}RP \tag{8.13}$$

would leave the state $|\chi\rangle$ invariant, where P is an arbitrary invertible matrix. One can show that for any arbitrary Q and R matrices, there exists a P, where one could apply the transformations (8.13) to satisfy the relation $Q+Q^\dagger+R^\dagger R=0$. For any given R, the most general form of Q which satisfies the relation is $Q=-\frac{1}{2}R^\dagger R+iH$, where H is a Hermitian matrix.

Let us next show how these continuous MPS can be understood as a limit of a family of MPS. For simplicity, we will consider a translational invariant system of bosons on a ring of length L; an identical construction works for the fermionic case. We define a family of translational invariant MPS of $N=L/\epsilon$ modes on a discretized lattice with lattice parameter ϵ with modes $\hat{a}_i$ that obey the commutation relation. Therefore we can write the $|\chi\rangle$ in the following way:

$$|\chi_\epsilon\rangle = \sum_{i_1\cdots i_N}\mathrm{Tr}\left[A^{i_1}\cdots A^{i_N}\right]\left(\Psi_1^\dagger\right)^{i_1}\cdots\left(\Psi_N^\dagger\right)^{i_N}|\Omega\rangle, \tag{8.14}$$

where the tensors A^i are defined as:

$$A^0 = I+\epsilon Q \qquad A^k=\frac{1}{k!}\epsilon^k R^k \qquad \psi_i=\frac{\hat{a}_i}{\sqrt{\epsilon}}. \tag{8.15}$$

Finally we have introduced a new family of states, the cMPS, for quantum field models in 1 spatial dimension. They correspond to the continuum limit of the MPS. We have shown how one can efficiently determine expectation values of different observables, so that they can be used to approximate ground state of such systems.

It would be interesting to explore new methods for finding the matrices Q and R variationally with high bond dimension, as well as to study nontranslationally invariant systems. Beyond that, it would also be interesting to substitute those matrices by operators acting on an infinite-dimensional Hilbert space as in order to capture critical phenomena and to study relativistic quantum field theories. Finally, the cMPS formalism allows to construct Hamiltonians whose exact ground states are known, which leads to new solvable field theories.

8.2 Emerging of cMPS in $2D$ tensor networks

We want to evaluate a 2D TN with the structure shown in Fig. 8.1 (a). The TN will be contracted to a scalar Z whose value could represent different physical quantities,

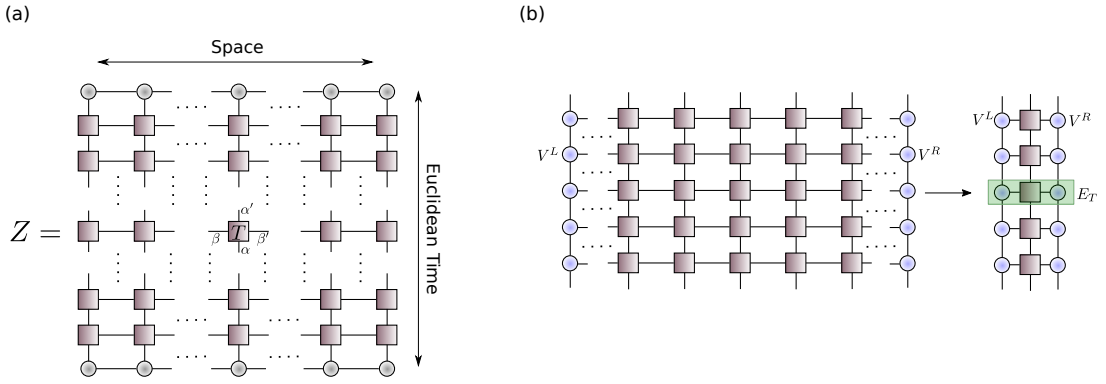

Figure 8.1: (a) Representation of 2D tensor network encoding the vacuum to vacuum transition probability corresponding to the norm of the ground state obtained by performing an imaginary time evolution of an initial matrix product state. Geometric shapes represent the elementary tensors, and the lines encode their contraction. (b) Temporal Matrix Product State (tMPS). The MPS fixed point obtained by contracting the 2D TN from left to right defines the tMPS. It describes a state along the Euclidean time direction and becomes a continuous MPS in the limit of the Trotter step going to zero.

depending on the content of the individual tensors. For example Z could encode the partition function of a $2D$ classical model, the norm of a 2D quantum state encoded in a PEPS, or the real or imaginary time evolution of a 1D quantum state. In our paper Z will encode the latter case, the imaginary time evolution of a 1D quantum state $|\psi\rangle$.

The $1D$ system is made by N constituents whose interaction is described by, for simplicity, a nearest neighbors Hamiltonian $\hat{H} = \sum_n \hat{H}^{[n,n+1]}$. $\hat{H}^{[n,n+1]}$ encodes the two-body interactions. If a system is translationally invariant, as in the cases we will consider here all the two body terms are the same, namely $\hat{H}^{[n,n+1]} = \hat{H}^{[2]}$.

The imaginary time evolution, performed for sufficiently large times, allows to approximate the ground state of $\hat{H}$ [1],

$$|\Omega\rangle = \lim_{\beta\to\infty} \frac{e^{-\frac{\beta}{2}\hat{H}}|\psi\rangle}{||e^{-\frac{\beta}{2}\hat{H}}|\psi\rangle||}. \tag{8.16}$$

Alternatively the ground state of $\hat{H}$ could be obtained variationally by minimizing the energy over the class of normalized MPS states with fixed bond dimension,

$$|\Omega\rangle = \arg\min_{|\psi\rangle} \left\{ \langle\psi|\hat{H}|\psi\rangle \right\}. \tag{8.17}$$

$|\psi\rangle$ is an MPS state fulfilling $\langle\psi|\psi\rangle = 1$.

At large fixed β in eq. (8.16) we need to divide the evolution in small steps by fixing M such that $\beta/2M = \tau \ll 1$. In this way we can approximate Eq. (8.16) step by step using a Suzuki-Trotter decomposition at the chosen order in τ.

When $|\psi\rangle$ is in an MPS form, each step $U(\tau)|\psi\rangle \equiv e^{-\tau\hat{H}}|\psi\rangle$ can be performed approximately by first contracting the TN and then truncating the MPS back to desired bond dimension D after normalizing the state. The fixed point of this procedure provides the MPS representation of $|\Omega\rangle$.

[1] We assume that $\langle\Omega|\psi| \neq\rangle 0$ as expected for a randomly chosen $|\psi\rangle$.

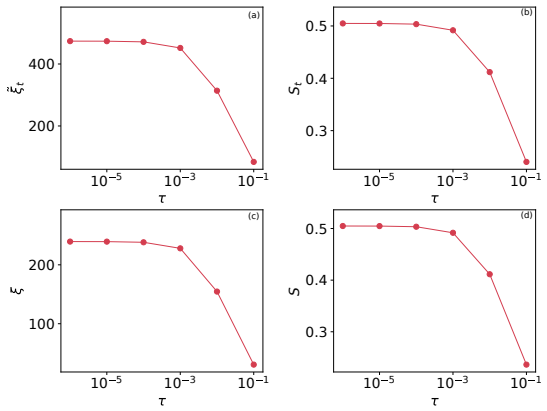

Figure 8.2: *Correlation time* **(a)**. The physical correlation time $\tilde{\xi}_t$ versus τ. We appreciate that $\tilde{\xi}_t$ stays finite when τ goes to zero. The system is at the critical point $h = J$ where we expect the correlation time to diverge. However, $\tilde{\xi}_t$ stays finite as a result of the finite bond dimension of the tMPS. *Entanglement entropy of the tMPS* **(b)**. The entanglement entropy of the tMPS only depends on the physical correlation time $\tilde{\xi}_t$ and stays finite when $\tilde{\xi}_t$ is finite. At the critical point the linear dispersion relation of the low-energy excitations implies an enhanced space-time symmetry. This can be checked by studying the correlation length in the ground state ξ **(c-d)**. Once more, it is finite as a result of the finite bond dimension χ. The entanglement entropy S of half of the ground state also stays finite, and weakly depends on τ as expected. We take the length of the unit cell $L = 2, 4$ and the bond dimension cut-off $\chi = 20$.

As a result, in the case of the imaginary time evolution, the individual tensors of the 2D TN represented in Fig. 8.1, are related to the small steps of time evolution $U(\tau)$.

The length of horizontal direction encodes the number of constituents N of the $1D$ quantum system, and we call it in the following spatial direction. The vertical length encodes the number of Trotter steps M and we call it Euclidean-temporal direction.

Looking at the $2D$ TN we can envisage a different contraction scheme (see Ref. [493, 495]). Rather than contracting the TN downwards, we can contract it from left to right as in (Fig. 8.1 (b)). Once again, if we enforce an MPS structure for the contraction (alternating contraction and truncation steps) we can define the tMPS as the fixed point of this contraction strategy,

$$|tMPS\rangle = \sum_{\{\beta\}} \cdots V_{\alpha_i\beta_i\beta_{i+1}} V_{\alpha_j\beta_j\beta_{j+1}} \cdots | \cdots \alpha_i\alpha_j \cdots \rangle. \tag{8.18}$$

The dots encode the fact that the tMPS is infinite (β and M diverge), and V denote its constituent tensors. Notice that the quantum sate is now defined as a state with fixed "auxiliary" position and one constituent per Trotter step, thus effectively encoding the time evolution of a single coarse-grained constituent. In the next sections, we characterize the tMPS through the conrner transfer matrix renormalization group algorithm (CTMRG) [257, 258]

8.3 The continuous tMPS

Besides very specific scenarios, the fixed points extracted after the contraction along the spatial and the temporal directions are different. The lattice spacing along the

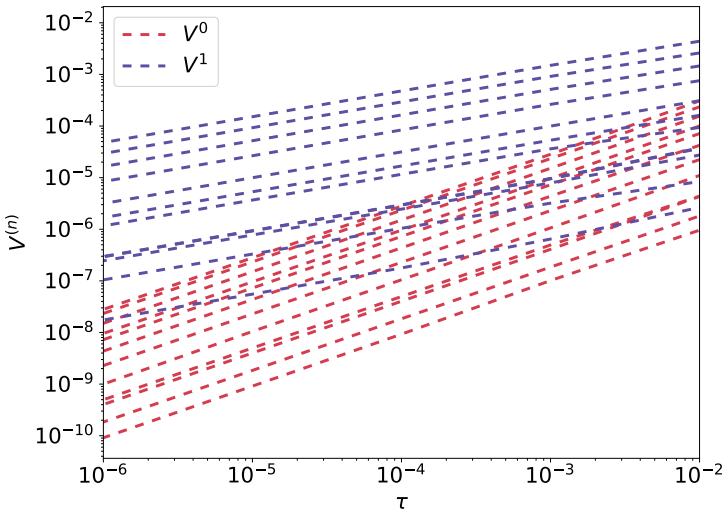

Figure 8.3: By plotting the elements of the tMPS tenors as a function of τ we can identify the elements whose extrapolation would produce V^0 and V^1 contribution in [Eqs. (8.22) and (8.23)]. They are distinguishable by the different slope of their τ dependence. We could thus reconstruct the V^0 and V^1 from a simple extrapolation of the finite τ data. These plots are a further confirmation that the tMPS converges to a continuous MPS.

horizontal direction is discrete, while, in the limit $M \to \infty$ it becomes continuous in the vertical direction. While the parallel MPS represents the ground state of $\hat{H}$ the tMPS sites encode the different instant of time of the evolution of a single coarse-grained constituent. Since in the limit $M \to \infty$ the time step goes to zero, the constituent continuously varies in time, and thus the tMPS encodes a continuous system [331].

When the $2D$ TN represents a classical isotropic model, the fixed points obtained by contracting the network along either the vertical or the horizontal directions should represent the same state. This equivalence has been tested on the TN that encodes the partition function of the $2D$ classical Ising model in [495]. This scenario can also occur in the quantum case in very special cases, where the original $\hat{H}$ possesses extra symmetries such as, e.g, the emerging Lorentz invariance we will consider in the following.

While the properties of the spatial MPS have been analyzed in several works, here we want to characterize the properties of the tMPS. This is a relatively unexplored area, and we only are aware of the results presented by Hasting and Mahajan [495].

We characterize the continuous nature of the tMPS by addressing the paradigmatic quantum Ising model defined by the Hamiltonian

$$H = J \sum_i S_i^x S_{i+1}^x - h \sum_i S_i^z, \tag{8.19}$$

with S^x and S^z are the Pauli matrices along the x and z directions. The model can be exactly solved [238, 525] . The system is in a paramagnetic phase for values of the couplings such that $h/J > 1.0$. In the thermodynamic limit the order parameter acquires a non vanishing expectation value $\langle S^z \rangle \neq 0$ in the paramagnetic phase. In the ferromagnetic phase, for $h/J < 1.0$ the order parameter goes to zero. The two phases are separated by a quantum phase transition at $h/J = 1.0$, where the low-energy physics of the system can be described by a conformal field theory with central charge $c = 0.5$ [526–528].

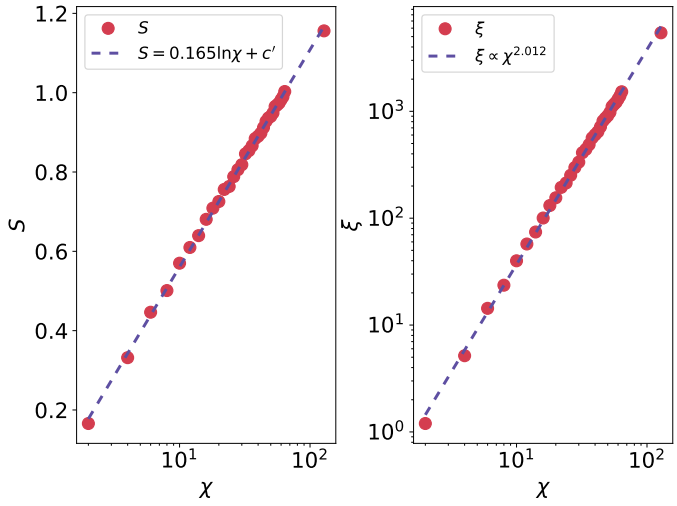

Figure 8.4: (Color online) |As a sanity check we reproduce the well known scaling of the correlation length ξ and entanglement entropy S versus the bond dimension cut-off χ of the spatial MPS. We take $h = 1$, and $\tau = 10^{-6}$.

The continuous nature of the tMPS emerges when taking the limit $M \to \infty$. If the system in the continuum has a finite correlation time $\tilde{\xi}_T$, we expect that the correlation time measured in terms of the lattice spacing ξ_T should diverge in the limit as $\xi_T = \tilde{\xi}_T/\tau$. This is the first check that we perform on our tMPS since the correlation time of a translationally invariant tMPS is encoded in the gap of its transfer matrix $E_T \equiv \sum_\alpha V_\alpha \bar{V}_\alpha$,

$$\xi_T = \frac{1}{\ln \eta_0 - \ln \eta_1}, \tag{8.20}$$

where η_n represents the n-th eigenvalue of E_T.

This property is analyzed in Fig. 8.2. The correlation time ξ_T obtained directly from the tMPS [Eq. (8.20)] diverges as expected as τ decreases. In panel (a) we show that, as expected, the physical correlation time $\tilde{\xi}_T$ converges rapidly when reducing τ. In panel (b) we check that a physical quantity, the entanglement entropy of half of the temporal chain S, only depends on $\tilde{\xi}_T$. S should indeed scale as $S \propto \log \tilde{\xi}_T$ [92].

Despite working at the critical point $h = J$ where the correlation time $\tilde{\xi}_T$ should diverge since $\hat{H}$ is gap-less, we observe a finite correlation time. This is a consequence of describing the system with a finite bond dimension χ, thus effectively cutting-off the correlations.

At the critical point, thanks to the linear dispersion relation of the low-energy excitations [238], we expect to observe an enhanced symmetry between space and time. Indeed, momentum plays the same role than energy, and we the theory becomes Lorentz invariant.

In panel (c) and (d) of Fig. 8.2 we thus characterize the spatial correlation length ξ and the entanglement entropy S of half of the ground state $|\Omega\rangle$. In this setting τ only controls the accuracy of the Trotter expansion, and we thus expect the results to converge to a finite value as τ decreases. Once more both S and ξ stay finite at the critical point as a result of the finite bond dimension χ. Our expectation are confirmed by the numerical results presented in panel (c) and (d) of Fig. 8.2.

In order to further verify that the tMPS is continuous we compare its structure

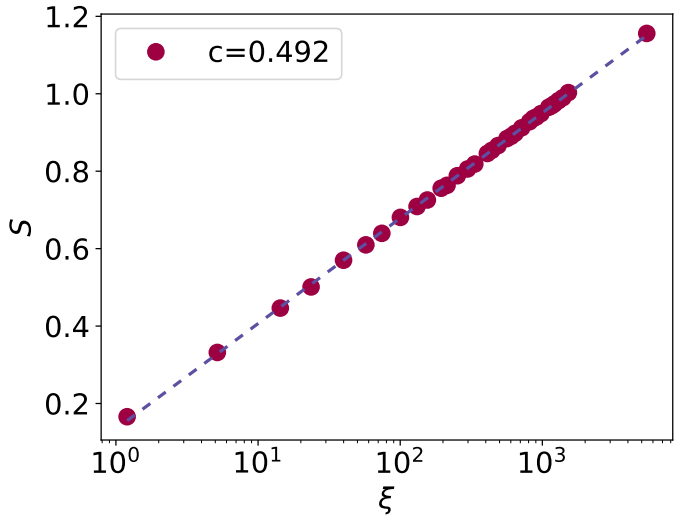

Figure 8.5: (Color online) The half chain entanglement entropy S as a function of the correlation length ξ at the critical point. Each point is obtained by choosing the bond dimension χ. A fit to the expected logarithmic scaling allows to extract $c = 0.5$ as expected.

with the one of a cMPS. The continuous limit of an MPS was discussed in the context of the Bethe ansatz [529, 530]. In the tensor network community, the cMPS was first proposed by Verstraete *et al* [331]. The cMPS can be used as the variational state for finding ground states of quantum field theories, as well as to describe real-time dynamical features.The cMPS describes the low-energy states of quantum field theories once appropriately regularized, in the same way as a normal MPS describes the low-energy states of quantum spin systems. The cMPS can be constructed as the continuous limit of a discrete MPS defined as (see [331]),

$$|\psi\rangle = \sum_{n_1 \cdots n_L} V^{n_1} \cdots V^{n_M} \left(\Psi_1^\dagger\right)^{\sigma_1} \cdots \left(\Psi_M^\dagger\right)^{n_M} |\Omega\rangle, \tag{8.21}$$

where the Vs satisfy

$$V^0 = I - \tau Q \tag{8.22}$$
$$V^1 = \tau R \tag{8.23}$$
$$V^n = \tau^n R^n \tag{8.24}$$
$$\Psi = \frac{\hat{a}_i}{\sqrt{\tau}}. \tag{8.25}$$

Both R and Q are independent from τ.

We can thus use in particular (8.22) and (8.23) to extract Q and R for the Ising field theory, defined by the tMPS. In Fig. 8.3 we show the components V^0 and V^1 as a function of τ. In the log-log plot we see that once we appropriately subtract the identity component to V_0, V_0 and V_1 scale differently as predicted by Eq. (8.22) and (8.23). This implies that by performing an appropriate scaling analysis, we can directly extract the R and Q for the tMPS of the Ising field theory. We only need to extrapolate the results at finite τ to the interesting $\tau \to 0$ limit, thus overcoming the difficulties that arise when trying to directly optimize the continuous MPS [331, 506, 513].

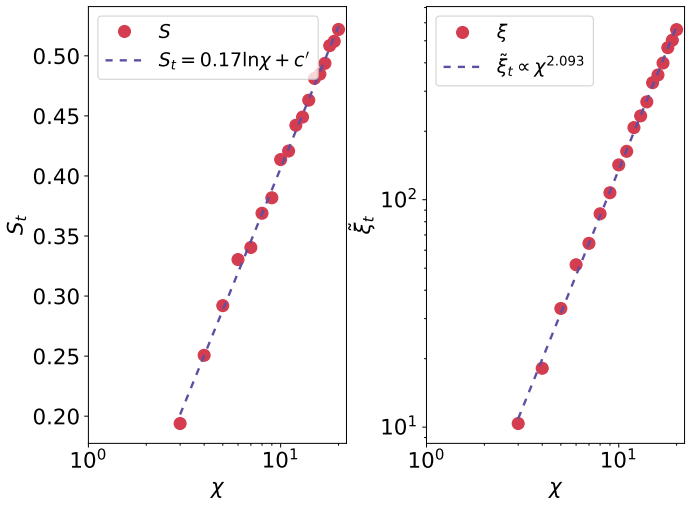

Figure 8.6: (Color online) The scaling of the correlation time $\tilde{\xi}_T$ and the temporal entanglement entropy S_T versus the bond dimension cut-off χ of the tMPS. We take $h = 0.5$, $L = 2$ and $\tau = 10^{-6}$.

8.4 Identifying the emerging quantum field theory

A finite χ MPS at criticality induces a finite correlation length [512, 513] scaling as

$$\xi \propto \chi^{\kappa}. \tag{8.26}$$

This implies that the entanglement entropy S scales as

$$S = \frac{c\kappa}{6} \ln \chi + c', \tag{8.27}$$

$$S = \frac{c}{6} \ln \xi + c'. \tag{8.28}$$

In order to characterize it, we use the CTMRG algorithm. Our results for the ground state MPS in Fig. 8.4 reproduce correctly Eq. (8.27).

In Fig. 8.5 we present the scaling of S against ξ of the spatial MPS with $L = 2$ and 4 that allow to extract the central charge, whose value turns out $c = 0.502(5)$ as expected where the error is obtained by fitting several subsets of data for different χ and L.

Close to the critical point, the system becomes not only scale invariant but also Lorentz invariant (this is equivalent to the Galileo invariance in Euclidean time), as a consequence of the linear dispersion relation for low-energy excitations. For this reason it is possible to rotate the system and invert the role of space and time. In this way we can think of the tMPS as a state along the infinite temporal direction, and we expect it to share some properties (e.g. the scaling exponents) with the matrix-product state defined along the spatial direction.

We now characterize the correlation time $\tilde{\xi}_T$ and the entanglement entropy S_T of the tMPS (that has been called temporal entanglement in Ref. [495]). As shown in Fig. 8.6 $\tilde{\xi}_T$ and S_T also satisfy Eqs. (8.26) and (8.27), respectively. From our best fit, we extract $\kappa = 2.026(4)$ and $c_T = 0.504(3)$ for the tMPS compatible with the ground state data.

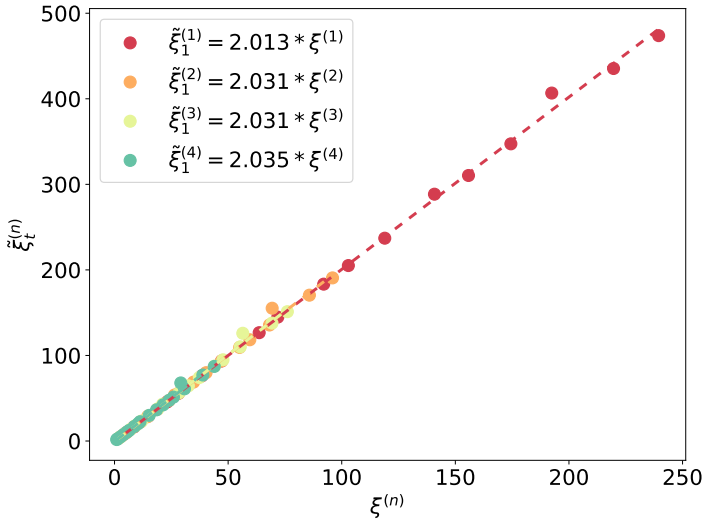

Figure 8.7: (Color online) Correlation length of the tMPS $\tilde{\xi}_T^{(n)}$ versus that of the spatial MPS $\xi^{(n)}$ for different bond dimensions χ and $\tau = 10^{-6}$. Our results show that $\tilde{\xi}_T^{(n)} = \nu\xi^{(n)}$ with $\nu = 2$.

The anisotropic continuous limit introduced in the Trotter expansion, that only involves the temporal direction, induces a non trivial dependence between the physical quantities extracted from the MPS and the those extracted from the tMPS. This can be understood to be the analogue of the well known physics of classical anisotropic models. They behave in the same way of their isotropic counterparts once non-universal rescaling factors are taken into account. For example the $2D$ anisotropic Ising model, where the coupling J_s and J_t along the two directions are different, possesses a line of critical points, all in the Ising universality class. They can be found from the equation $\sinh(2\beta J_t)\sinh(2\beta J_s) = 1$, where β is the inverse temperature (see, e.g. [531]).

The rescaling factor ν can be extracted from the ratio of the correlation lengths along the two directions

$$\xi = \nu^{-1}\tilde{\xi}_T. \tag{8.29}$$

We can extract ν from our data in Fig. 8.7 and find it to be roughly $\nu = 2$.

We verify that the same factor lives between all the gaps of the temporal transfer matrix with the corresponding ones of the space transfer matrix.

We define

$$\tilde{\xi}_T^{(n)} = \frac{1}{\tilde{\Delta}_n} = \left(\log\frac{\tilde{\eta}_0}{\tilde{\eta}_n}\right)^{-1}, \tag{8.30}$$

$$\xi^{(n)} = \frac{1}{\Delta_n} = \left(\log\frac{\eta_0}{\eta_n}\right)^{-1}, \tag{8.31}$$

where η and $\tilde{\eta}$ are the low-lying eigenvalues of the spatial and temporal transfer matrix. Note for $n = 1$, we have that $\tilde{\xi}_T^{(1)} = \tilde{\xi}_T$ and $\xi^{(1)} = \xi$.

In the same Fig. 8.7 we see that for all the χ we have considered, the gaps of the temporal transfer matrix are indeed proportional to the gaps of the spatial transfer matrix with the same proportionality constant $\nu = 2$. This fact confirms our interpretation of ν as a non-universal rescaling of the velocity of the excitations.

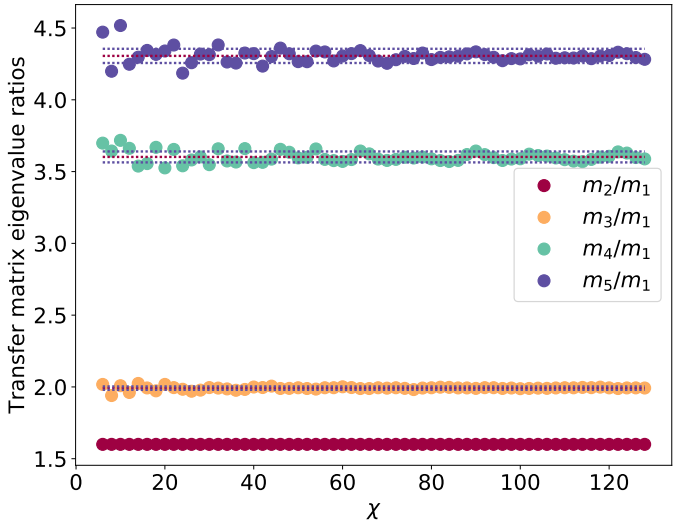

Figure 8.8: (Color online) The ratios of the eigenvalues of the temporal transfer matrix E_T versus χ at $\tau = 10^{-6}$. We use it in order to identify the field theory that the tMPS describes. The lightest mass is fixed so to produce a ratio $m_2/m_1 = 1.6$. All the other ratios are computed accordingly. The present results seem to reproduce those in Ref. [519], thus allowing to identify the field theory encoded in the tMPS with the one obtained by weakly perturbing an Ising model with a magnetic field.

The tMPS is continuous but its entropy is finite. The bond dimension of the tMPS indeed plays the role of an UV regulator, as already observed in [331]. As expected, thus the state emerging in the continuum limit is a massive state, where the masses should be dictated by the Ising fixed point.

We thus would like to check this expectation by trying to identify the field theory corresponding to the continuous limit of the anisotropic model. One way to do this, is by characterizing the masses of the low energy excitations m_1, m_2, m_3, m_4. They can be extracted by constructing the appropriate ratios of the tMPS transfer matrix eigenvalues, namely $m_n = 1/\tilde{\xi}_T^{(n)}$. The masses we extract are in good agreement with those reported elsewhere [513].

The first mass is generally fixed by the rescaling of the Hamiltonian that ensures that the tMPS is normalized. This is an arbitrary choice. A more physical choice is to fix it to the value of the lowest mass of the field theory we expect to reproduce. We thus adjust m_1 in such a way that $m_2/m_1 = 1.618$. This is the ratio first proposed by Zamolodchikov [519] in his analysis of the Ising model weakly perturbed by a parallel field. The results of our numerical analysis of the mass ratios are presented in Fig. 8.8. There we can see that once we fix $m_2/m_1 = 1.618$, m_3/m_1 turns out to be and $m_3/m_1 = 2.00(5)$. This value is very close to the value of the second mass ratio predicted by Zamolodchikov $m_3/m_1 = 1.989$ [519].

Our masses thus seems to suggest that the continuous limit of an Ising MPS with fixed bond dimension χ reproduces the field theory obtained by perturbing the Ising model close to the critical point with a small parallel field of [519]. The above result can be understood by noticing that the finite bond dimension χ opens a gap similarly to what happens with a finite system size or a finite temperature. However, differently from the finite size or the finite temperature, the finite bond dimension also breaks the Z_2 symmetry.

Surprisingly our $m_4/m_1 = 3.65(23)$ results is compatible with the value of the ratio $m_7/m_1 = 3.891$ in the predictions by Zamolodchikov and not with the lightest mass ratios as we would have expected. Our identification thus still leaves a puzzle about why m_4, m_5 and m_6 are absent in the tMPS spectrum. We leave the solution to this puzzle to further analysis. We indeed believe it can be solved by correctly keeping track of the symmetries of the low-lying excitations, something that can be done, but that goes beyond the scope of our present analysis.

We have explicitly constructed the ground state of a QFT obtained from the continuous limit of the Ising model as an MPS. We have done it by exploiting both Hastings's observation that the Euclidean time evolution generates a continuous MPS in imaginary time and the Lorentz invariance emerging at the critical point.

These two ingredients allow to characterize the QFT by studying the properties of the tMPS, a continuous MPS emerging, as a result of the Trotter expansion, along the temporal direction. As a result we have identified the QFT with the one first obtained by Zamolodchikov as the continuous limit of the Ising model perturbed with a weak magnetic field.

This result supports earlier claims [516] that the finite entanglement phenomenon is equivalent to perturbing the critical Hamiltonian with the lightest relevant field with the correct symmetry properties. In particular in our case, since the Z_2 symmetry of the Ising model is broken in the finite entanglement regime, we can identify the relevant perturbation corresponding to the finite entanglement phenomenon with a parallel magnetic field.

Our identification, however, opens a new puzzle, since in our transfer matrix some of the expected excitations are absent. We leave the solution of this puzzle to further studies.

Chapter 9

Conclusions

In this thesis, we addressed two main topics: (i) the quantum simulations of topological insulating phases in condensed matter and high-energy physics, (ii) the description of many-body systems through tensor network states and the development of tensor network-based algorithms.

As regards the first topic, in Chapter 2 we introduced basic concepts of symmetry topological phases of matter and we gave examples of non-interacting topological phases of matter including SSH model, Kitaev chain and ladder models.

In Chapter 3, we studied a paradigmatic model that hosts a topological insulator: the Creutz-Hubbard chain. In particular, we investigated the imbalanced Creutz-Hubbard model proposed in Ref. [59], providing a complete phase diagram found by combining DMRG simulations and analytical calculations.

In Chapter 4, we presented a detailed study of the use of the RG to obtain an effective relativistic QFT that provides a continuum long-wavelength description of correlated topological insulators. We showed that our description is valid for a variety of minimal models that serve as representatives of various topological insulators [13], and are related to self-interacting fermionic lattice field theories in various dimensions [104], which we refer to as topological Wilson-Hubbard matter.

Moreover, we showed that a Wilsonian RG provides a neat description of these correlated topological insulators. At the so-called tree level, and generic to various dimensions, the RG approach offers a neat qualitative connection between the topological invariants in the long-wavelength limit and the flat-band limit of topological insulators. This connection becomes quantitative by using the RG flows of the parameters in connection to the so-called topological Hamiltonian, which includes static self-energy corrections to characterize the many-body topological invariant of the correlated topological insulator.

Going beyond the tree level, we demonstrated that a loop expansion of the Wilsonian RG offers a quantitative route to understand the topological phase transitions that occur in Wilson-Hubbard matter, separating the correlated topological insulator from other non-topological phases. We have benchmarked the two-loop RG predictions for a particular 1D model, the imbalanced Creutz-Hubbard ladder, to quasi-exact numerical simulations based on matrix product states. This numerical comparison showed a very good agreement in the determination of the critical line determining the topological quantum phase transition, as well as various bi-partite correlations of the topological phase and the critical line. This benchmark may motivate the extension of the RG calculations to higher-dimensional correlated topological insulators in the future.

In Chapter 5, we described the existence of correlated symmetry-protected topological phases in a discretized version of the Gross-Neveu model. We have applied large-N techniques borrowed from high-energy physics, complemented with the study of topological invariants from condensed matter, to unveil a rich phase diagram that contains a wide region hosting a BDI topological insulator. This region extends to considerably strong interactions, and must thus correspond to a strongly-correlated symmetry-protected topological phase. We have shown that this phase, and the underlying topological invariant, can be understood in terms of the renormalization of Wilson masses due to interactions (i.e. dynamic mass generation due to a scalar fermionic condensate). This renormalization has been used to find a critical line at weak couplings that separates the topological insulator from a gapped phase that can be adiabatically deformed into a trivial product state (i.e. trivial band insulator). Moreover, we showed that for sufficiently-strong interactions, a gapped phase where parity symmetry is spontaneously broken (i.e. Aoki phase) is formed due to the appearance of a pseudoscalar fermion condensate. The large-N prediction has allowed us to find the critical line separating the topological insulator from the Aoki phase by studying the onset of the pseudoscalar condensate, and show that it terminates at a tri-critical point where all these three phases of matter coexist.

Motivated by the possibility of implementing a cold-atom quantum simulator of the Gross-Neveu-Wilson model for a single flavor $N = 1$, we have benchmarked these large-N predictions using quasi-exact numerical methods based on matrix product states. In particular, we have shown that the single-flavor model, corresponding to a discretized version of the massive Thirring model, can also be mapped into a condensed-matter Hamiltonian of spinless fermions hopping on a two-leg ladder, and interacting via Hubbard-type couplings. This connection has allowed us to identify the phases of the Gross-Neveu-Wilson model, discussed above, with condensed-matter counterparts that include orbital paramagnets and ferromagnets, as well as a chiral-unitary topological phase. In this way, the matrix-product-state simulations can readily access a variety of observables to determine the position of the critical lines, which show a remarkable qualitative agreement with the large-N predictions that becomes even quantitative in the region where the continuum Gross-Neveu QFT is expected to emerge (i.e. weak couplings). These numerical simulations also prove that the symmetry of the large-N phase diagram holds for $N = 1$, and should then be maintained at all orders $\mathcal{O}(1/N^{\alpha})$.

As regards the second topic, in Chapter 6, we introduced the basic concepts and definitions of tensor and tensor network states/operators, as well as, their graphic representations. Several frequently used architectures of TN states have been presented including matrix product state, tree tensor network state and project entangled pair state. Moreover, we explained the relation between tensor networks, entanglement entropy, and quantum circuit. Finally, we discussed the notion of the past causal cone to classify the tensor networks based on the complexity of computing their contractions, and we showed some examples of exactly contractible tensor networks.

In Chapter 7, we presented the density matrix renormalization group and a new numerical approach named PT-DMRG that improves the accuracy of the conventional DMRG. We showed that it gives a better approximation of the ground state of strong-correlated many-body systems by recovering the leading term of entanglement that is discarded in the truncations of DMRG. Moreover, we discussed several other contraction approaches for dealing with 2D TN's. Applying these algorithms, many challenging problems can be efficiently solved, including the ground-state and finite-temperature simulations of 1D quantum systems, and the simulations of 2D classical statistic mod-

els. Such algorithms consist of two key ingredients: contractions (local operations of tensors) and truncations. The local contraction determines how the TN is contracted step by step. Different (local or global) contractions may lead to different computational costs, consequently optimizing the contraction sequence is necessary in many cases. The truncation is the approximation to discard less important basis so that the computational costs are properly bounded. We showed that, one essential concept in the truncations is the "environment", which plays the role of the reference when determining the weights of the basis. Thus, the choice of the environment concerns the balance between the accuracy and efficiency of a TN algorithm.

In Chapter 8, we constructed the continuous Matrix Product State (MPS) representation of the vacuum of the field theory corresponding to the continuous limit of an Ising model. We did this by exploiting the observation made by Hastings and Mahajan in [495] that the Euclidean time evolution generates a continuous MPS along the time direction. We exploited this fact, together with the emerging Lorentz invariance at the critical point in order to identify the matrix product representation of the quantum field theory (QFT) vacuum with the continuous MPS in the time direction (tMPS). We explicitly constructed the tMPS and checked these statements by comparing the physical properties of the tMPS with those of the standard ground MPS. We furthermore identified the QFT that the tMPS encodes with the field theory emerging from taking the continuous limit of a weakly perturbed Ising model by a parallel field first analyzed by Zamolodchikov.

Appendix A

General properties of quadratic Hamiltonian

In this appendix we illustrate in detail a beautiful calculation allowing the computation of correlation functions and entanglement.

A.1 Reduced density matrices

In this section we describe a method to find a correlation matrix. Let us consider first a quadratic fermionic Hamiltonian

$$\hat{H} = \sum_{j,k}^{L} \hat{c}_j^\dagger H_{jk} \hat{c}_k, \tag{A.1}$$

with $\hat{H}$ hermitian and $\hat{c}_j$ a fermionic annihilation operator. For free theories the Wiek theorem holds and the physics of the system shall be given just by knowing the correlation matrix

$$C_{j,k} = \langle \hat{c}_j^\dagger \hat{c}_k \rangle \tag{A.2}$$

In particular, we are interesting in connecting to C the reduced density matrix of any subsystem A of the whole lattice.

Consider a subsystem A, we can assume the reduced density matrix of A to be of the form

$$\hat{\rho}_A = \frac{1}{Z_A} e^{h_a}, \tag{A.3}$$

where $h_A = \sum_{j=1}^{l} \hat{c}^\dagger h_{jk} \hat{c}_k$ and Z_A is the partition function.

To diagonalize h_a we introduce the following transformation

$$\hat{c}_j = \sum_{m=1}^{l} V_{j,m} \hat{d}_m, \tag{A.4}$$

being V a unitary matrix. By means of these new operators, h_A becomes

$$\hat{h}_A = \sum_{m,n=1}^{l} \hat{d}_m^\dagger \left(\sum_{j,k=1}^{l} V_{jm}^\star h_{jk} V_{km} \right) \hat{d}_n. \tag{A.5}$$

V can be chosen in order to diagonalize h_A, i.e.,

$$h_A = \sum_{m=1}^{l} \epsilon_m \hat{d}^\dagger \hat{d}_m. \tag{A.6}$$

From this form of h_a, it is immediate to see the reduced density matrix $\hat{\rho}$ becomes

$$\hat{\rho}_A = \otimes_{m=1}^{l} \frac{e^{-\epsilon_m \hat{d}_m^\dagger \hat{d}_m}}{Z_m}, \tag{A.7}$$

where $Z_m = 1 + e^{-\epsilon_m}$. Now our task is to find the expression of ϵ_m through the correlation matrix C. We compute ϵ_m, substituting the (A.7) in eq. (A.2) we obtain that:

$$C_{j,k} = \mathrm{Tr}\left[\hat{\rho}_A \hat{c}_j^\dagger \hat{c}_k\right] = \frac{1}{Z_A} \sum_{n,p=1}^{l} V_{j,n}^\star V_{k,p} \mathrm{Tr}\left[e^{-\sum_{m=1}^{l} \epsilon_m \hat{d}_m^\dagger \hat{d}_m} \hat{d}_n^\dagger \hat{d}_p\right]. \tag{A.8}$$

The second trace is zero if $n \neq p$, therefore we obtain that

$$\frac{1}{Z_A} \mathrm{Tr}_A \left[e^{-\sum_{m=1}^{l} \epsilon_m \hat{d}_m^\dagger \hat{d}_m} \hat{d}_n^\dagger \hat{d}_p\right] = \frac{\delta_{np}}{1 + e^{\epsilon_n}}. \tag{A.9}$$

Finally, the correlation matrix has the following expression:

$$C_{j,k} = \sum_{m=1}^{l} V_{j,n}^\star \frac{1}{1 + e^{\epsilon_n}} V_{kn}. \tag{A.10}$$

Beeing V unitary, the eigenvalues of C are $\zeta_m = (1 + e^{\epsilon_m})^{-1}$ and inverting the relation we obtain that:

$$\epsilon_m = \ln\left[\frac{1 - \zeta_m}{\zeta_m}\right]. \tag{A.11}$$

Therefore, diagonalizing C, one can immediately get ϵ_m and so the reduced density matrix $\hat{\rho}_A$.

A.2 General free theory

Consider the more general situation

$$\hat{H} = \sum_{j,k}^{L} \left\{ \hat{c}_j^\dagger H_{jk}^H \hat{c}_k + \frac{1}{2}\left(\hat{c}_j^\dagger H_{jk}^A \hat{c}_k^\dagger + H.C.\right)\right\}, \tag{A.12}$$

where H^H is hermitian and H^A is an anti-hermitian matrix. In this case we should be able to extract the reduced density matrix of any subsystem form the correlation matrices

$$C_{jk} = \langle \hat{c}_j^\dagger \hat{c}_k \rangle, \qquad F_{jk} = \langle \hat{c}_j \hat{c}_k \rangle. \tag{A.13}$$

The reduced density matrix of the subsystem A takes the form (A.7) with h_A defined as

$$h_A = \sum_{j,k=1}^{l} \left\{ \hat{c}_j^\dagger h_{jk}^H \hat{c}_k + \frac{1}{2}\left(\hat{c}_j^\dagger h_{jk}^A \hat{c}_k^\dagger + H.C.\right)\right\}, \tag{A.14}$$

with, again h^H and h^A anti-hermitian. Now we need to find operator $\hat{d}_m$ diagonlizing h_A. The solution of this problem was proposed by Lieb et. al. in [532], introducing the Bogolyubov transformation

$$\hat{d}_m = \sum_{j=1}^{l} \left\{ \frac{\phi_{mj} + \psi_{mj}}{2} \hat{c}_j + \frac{\phi_{mj} - \psi_{mj}}{2} \hat{c}_j^\dagger \right\}, \tag{A.15}$$

where ϕ_m and ψ_m satisfy the left eigenvalues equation

$$\begin{cases} \phi_m \left(A - B\right)\left(A + B\right) = \epsilon_m^2 \phi_m \\ \psi_m \left(A + B\right)\left(A - B\right) = \epsilon_m^2 \psi_m \end{cases} \tag{A.16}$$

and can be chosen to be real and orthonormal i.e.

$$\sum_{j=1}^{l} \phi_{mj}^\star \phi_{nj} = \sum_{j=1}^{l} \psi_{mj}^\star \psi_{nj} = \delta_{mn}. \tag{A.17}$$

To compute C and F, we invert the relation (A.15) obtaining:

$$\hat{c}_j = \sum_{m=1}^{l} \left(\frac{\phi_{mj} + \psi_{mj}}{2} \hat{d}_m + \frac{\phi_{mj} - \psi_{mj}}{2} \hat{d}_m^\dagger \right). \tag{A.18}$$

Putting the operators $\hat{c}_j^{(\dagger)}$ written as in (A.18) in the expression of C and F, we has to compute four traces. The two anomalous traces, i.e., $\mathrm{Tr}_A\left[\hat{\rho}_A \hat{d}_n^\dagger \hat{d}_m^\dagger\right]$ and $\mathrm{Tr}_A\left[\hat{\rho}_A \hat{d}_m \hat{d}_n\right]$ are of course of zero and the others are:

$$\mathrm{Tr}_A\left[\hat{\rho}_A \hat{d}_m^\dagger \hat{d}_n\right] = \frac{\delta_{mn}}{1 + e^{\epsilon_m}} \qquad \mathrm{Tr}_A\left[\hat{\rho}_A \hat{d}_m \hat{d}_n^\dagger\right] = \frac{\delta_{mn}}{1 + e^{-\epsilon_m}}. \tag{A.19}$$

Using the orthogonal conditions of ϕ and ψ, we obtain the following expression of C and F

$$C_{jk} = \frac{\delta_{jk}}{2} + \frac{1}{4} \sum_{m=1}^{l} \left(\phi_{mj}\psi_{mk} + \psi_{mj}\phi_{mk}\right) \tanh\left(\frac{\epsilon_m}{2}\right), \tag{A.20}$$

$$F_{jk} = \frac{1}{4} \sum_{m=1}^{l} \left(\phi_{mj}\psi_{mk} - \psi_{mj}\phi_{mk}\right) \tanh\left(\frac{\epsilon_m}{2}\right). \tag{A.21}$$

Therefore, neither C nor F is directly diagonalized, but we can diagonalize the combination:

$$\left[\left(C - \frac{I}{2} - F\right)\left(C - \frac{I}{2} + F\right)\right]_{jk} = \frac{1}{4} \sum_{m=1}^{l} \psi_{mj} \tanh^2\left(\frac{\epsilon_m}{2}\right) \psi_{mk} \tag{A.22}$$

and therefore the eigenvalues of $\left(C - \frac{I}{2} - F\right)\left(C - \frac{I}{2} + F\right)$ are

$$\zeta_m = \frac{1}{4} \tanh^2\left(\frac{\epsilon_m}{2}\right). \tag{A.23}$$

The inversion relation give us the ϵ_m

$$\epsilon_m = 2 \tanh^{-1}\left(2\sqrt{\zeta_m}\right). \tag{A.24}$$

Lets see now how to construct practically the matrices C and F. Lets write the Hamiltonian (A.12) in matrix form

$$\hat{H} = \begin{bmatrix} \overline{c}^\dagger & \overline{c} \end{bmatrix} \begin{bmatrix} \alpha & -\beta^\star \\ \beta & -\alpha^\star \end{bmatrix} \begin{bmatrix} \overline{c} \\ \overline{c}^\dagger \end{bmatrix}. \tag{A.25}$$

We write now the Bogolyubov transformation in the form (A.15) in the form:

$$\begin{bmatrix} \overline{d} \\ \overline{d}^\dagger \end{bmatrix} = T \begin{bmatrix} \overline{c} \\ \overline{c}^\dagger \end{bmatrix} = \begin{bmatrix} \gamma & \mu \\ \mu^\star & \gamma^\star \end{bmatrix} \begin{bmatrix} \overline{c} \\ \overline{c}^\dagger \end{bmatrix}, \tag{A.26}$$

where T is unitary in order to make the d's fermionic and,

$$\gamma = (\phi + \psi) \qquad \mu = (\phi - \psi). \tag{A.27}$$

In terms of new operators, the Hamiltonian becomes

$$\hat{H} = \begin{bmatrix} \overline{d}^\dagger & \overline{d} \end{bmatrix} \begin{bmatrix} \gamma & \mu \\ \mu^\star & \gamma^\star \end{bmatrix} \begin{bmatrix} \alpha & -\beta^\star \\ \beta & -\alpha^\star \end{bmatrix} \begin{bmatrix} \gamma^\dagger & \mu^t \\ \mu^\dagger & \gamma^t \end{bmatrix} \begin{bmatrix} \overline{d} \\ \overline{d}^\dagger \end{bmatrix}. \tag{A.28}$$

T is chosen in order to diagonalize $\hat{H}$. It contains as columns its eigenvectors. Being the ground state $|0\rangle$ annihilation by all the Bogolyubov annihilators $\hat{d}_m$, the correlation function C and F are

$$C_{jk} = \sum_{m=1}^{L} \left(\mu^\dagger\right)_{jm} \left(\mu^t\right)_{km}, \qquad F_{jk} = \sum_{m=1}^{L} \left(\gamma^\dagger\right)_{jm} \left(\mu^\dagger\right)_{km}. \tag{A.29}$$

A.3 Entanglemet entropies

In this section we show how to calculate the entanglement entropy from ϵ_m. Consider a subsystem A, the entanglement entropy is

$$S(A) = -\sum_{\lambda} \lambda \ln \lambda, \tag{A.30}$$

where λ are the eigenvalues of ρ_A.

To calculate λ we consider a set of 2^l elements, which are vectors that label all possible occupation configurations in subsystem $\mathcal{A}$

$$\mathcal{N} = \{(n_j, j = 1, \cdots l) \qquad n_j \in \{0, 1\}\}. \tag{A.31}$$

Starting from the eq. (A.7),we see that the density matrix has an operator representation with eigenvalues of the correlation matrix that depends on $\overline{n}$

$$\lambda(\overline{n}) = \prod_{m=1}^{l} \left(\frac{\epsilon_m}{1-\epsilon_m}\right)(1-\epsilon_m) = \prod_{m=1}^{l} \alpha_m. \tag{A.32}$$

The negative algorithm of this expression ready explicitly

$$S_A = -\sum_{n_1}\sum_{n_2}\cdots\sum_{n_l} \lambda(\overline{n}) \ln\left(\lambda(\overline{n})\right). \tag{A.33}$$

Let us evaluate just one of all l_A sums:

$$\sum_{n_j=0}^{1} \lambda(\overline{n}) \ln\left(\lambda(\overline{n})\right) = -\sum_{n_j=0}^{1} \left(\prod_{m=1}^{l} \alpha_m\right)\left(\prod_{n=1}^{l} \beta_n\right) =$$

$$= -\prod_{m\neq j} \alpha_m \left(\sum_{m\neq j} \beta_m + (1-\epsilon_j)\ln\left(1-\epsilon_j\right) + \epsilon_j \ln \epsilon_j\right). \quad \text{(A.34)}$$

Consequently, we are able to simplify all 2^{l_A} terms in the definition of the entropy to only $2l_A$ constituents

$$S(A) = -\sum_{m=1}^{l} \left((1-\epsilon_m)\ln\left(1-\epsilon_m\right) + \epsilon_m \ln \epsilon_m\right). \quad \text{(A.35)}$$

We have expressed analytically both the spectrum and the entropy in terms of eigenvalues of two-point correlation functions.

Appendix B

Numerical methods for Luttinger parameter estimations

In this appendix, we describe the two numerical independent methods that allowed us to make comparisons to the predictions of the method we developed. The first,called level spectroscopy, is very popular and reliable, while the second, the bipartite-fluctuations method, has been proposed very recently and a check of its working is by itself interesting.

B.1 Level Spectroscopy

An important result of Luttinger liquids physics links the system compressibility,defined by

$$\mathcal{K} = \frac{\partial n}{\partial \mu} \tag{B.1}$$

i.e., the density change with respect to a chemical potential change, and the bosonization parameters. Explicitly, one has

$$K = u\pi\mathcal{K} \tag{B.2}$$

and therefore, knowing u and $\mathcal{K}$, being u the sound velocity of the system, one can get K. Luckily, one can relate $\mathcal{K}$ (at size L) to the energy spectrum of the system by the so called level spectroscopy formula

$$\mathcal{K}_L = L\left[E_L(N-1) + E_L(N+1) - 2E_L(N)\right] \tag{B.3}$$

being $E_L(N)$ the energy of the ground state of a system of size L, at filling N/L. Of course one wants to estimate $\mathcal{K}$ in the $L \to \infty$ limit, and has therefore to take a finite-size scaling of his data to extrapolate the true $\mathcal{K}$. A step is still missing, i.e., a way to get u. The question is answered by the well-known CFT relation

$$e_{GS} = e_0 + \frac{f_\infty}{L} + \frac{uc\pi}{6\delta L^2} + O(L^{-2}) \tag{B.4}$$

where $\delta = 1/4$ for PBC/OBC, being e_{GS} the energy density for the ground state, e_0 its thermodynamic-limit value, f_{infty} the surface free energy, vanishing for PBC, and c the central charge of the CFT. Therefore, by this simple procedure, an estimate of K can be given.

B.2 The Bipartite-Fluctuations Method

Let us consider a $1D$ system, described by some quantum Hamiltonian having a $U(1)$ symmetry, implying, e.g., particle-number conservation for fermionic or bosonic system, or total-magnetization for spin systems. These quantities are constants of motion, but their fluctuations in a subsystem A are not. We introduce therefore the quantity

$$F_A = \langle \Big(\hat{N}_A - \langle \hat{N}_A \rangle \Big) \rangle \tag{B.5}$$

where N_A is the total-particle-number operator relative to subsystem A; for spin systems, it is replaced by the total magnetization relative to A. This quantity shares some interesting feature with the REE's. In particular, it is easily shown that $F_A = F_B$, where B is the complementary of A: therefore, some kind of area law should hold in gapped systems, possibly logarithmically violated in critical situations.

$$\pi^2 F(l, L) = \pi^2 F_A = g \ln \left(\frac{L}{\pi} \sin \left(\frac{\pi l}{L} \right) \right). \tag{B.6}$$

Such logarithmical violations actually arise, and the main difference with entanglement entropy resides in its pre-factor. It can be shown that, for generic CFT and a system, they take the form

$$g = \pi u \mathcal{K} \tag{B.7}$$

being u the sound velocity and $g = K$ the compressibility (see section 2.3). It is clear from relation (B.2) that, for Luttinger liquids, one has $g = K$, and therefore formula (B.6) provides a practical tool to detect K. This is what we used in Chap. 4. This technique for the detection of the Luttinger parameter, basing itself on REE's, is very powerful if the data is taken with DMRG, i.e., mostly in 1D. On the other hand, the bipartite-fluctuations method, taking into account fluctuations of observables, is in principle less accurate than ours when the data are obtained by DMRG, but more powerful in higher dimension, where computations are usually performed with quantum Monte Carlo algorithms, by which REE's are very difficult to get. Moreover, the present quantity has been conjectured to be easily experimentally accessible, differently from REE's.

Bibliography

[1] L. Landau. On the theory of phase transitions. *Zh. Eksp. Teor. Fiz.* **7,** 19 (1937).

[2] L. Landau and V. Ginzburg. On the theory of superconductivity. *Zh. Eksp. Teor. Fiz.* **20,** 1064 (1950).

[3] L. Landau and E. Lifshitz. Statistical Physics. *London: Pergamon*, (1938).

[4] P. W. Anderson. Basic Notions of Condensed Matter Physics. *Westview Press* Boulder, CO (1997).

[5] M. Z. Hasan and C. L. Kane. Colloquium: Topological insulators. *Rev. Mod. Phys.*, **82**, 3045 (2010).

[6] X.-L. Qi and S.-C. Zhang. Topological insulators and superconductors. *Rev. Mod. Phys.*, **83**, 1057 (2011).

[7] J. E. Moore. The birth of topological insulators. *Nature*, **464**, 194 (2010).

[8] K. V. Klitzing, G. Dorda, M. Pepper. New Method for High-Accuracy Determination of the Fine-Structure Constant Based on Quantized Hall Resistance. *Phys. Rev. Lett.* **45,** 494 (1980).

[9] K. V. Klitzing. The quantized Hall effect. *Rev. Mod. Phys.* **58,** 519 (1986).

[10] R. B. Laughlin. Quantized Hall conductivity in two dimensions. *Phys. Rev. B* **23,** 5632 (1981).

[11] D. J. Thouless, M. Kohmoto, M. P. Nightingale, and M. den Nijs. Quantized Hall Conductance in a Two-Dimensional Periodic Potential. *Phys. Rev. Lett.* **49,** 405 (1982).

[12] B. I. Halperin. Quantized Hall conductance, current-carrying edge states, and the existence of extended states in a two-dimensional disordered potential. *Phys. Rev. B* **25,** 2185 (1982).

[13] B. A. Bernevig and T. L. Hughes. Topological Insulators and Topologicalv Superconductors. *Princeton*, 2013.

[14] A. Bernevig and T. Neupert. Topological superconductors and category theory. Lecture Notes of the Les Houches Summer School: Topological Aspects of Condensed Matter Physics (2017).

[15] C.-K. Chiu, J. C. Y. Teo, A. P. Schnyder, and S. Ryu. Classification of topological quantum matter with symmetries. *Rev. Mod. Phys.* **88,** 035005 (2016).

[16] R. P. Feynman. Simulating physics with computers. *Int. J. Theor. Phys.* **21,** 467 (1982).

[17] S. Lloyd. Universal Quantum Simulators. *Science* **273,** 1073 (1996).

[18] M. Lewenstein, A. Sanpera, V. Ahufinger, B. Damski, A. Sen, and U. Sen. Ultracold atomic gases in optical lattices: mimicking condensed matter physics and beyond. *Adv. in Phys.* **56,** 243 (2007).

[19] I. Bloch, J. Dalibard, and S. Nascimbene. Quantum simulations with ultracold quantum gases. *Nat. Phys.* **8,** 267 (2012).

[20] I. Bloch, J. Dalibard, and W. Zwerger. Many-body physics with ultracold gases. *Rev. Mod. Phys.* **80,** 885 (2008).

[21] J. I. Cirac and P. Zoller. Quantum computations with cold trapped ions. *Phys. Rev. Lett.* **74,** 4091 (1995).

[22] Y. Makhlin, G. Schön, and A. Shnirman. Quantum-state engineering with Josephson junction devices. *Rev. Mod. Phys.* **73,** 357 (2001).

[23] A. Aspuru-Guzik and P. Walther. Photonic quantum simulators. *Nat. Phys.* **8,** 285 (2012).

[24] K. I. Petsas, A. B. Coates, and G. Grynberg. Crystallography of optical lattices. *Phys. Rev. A* **50,** 5173 (1994).

[25] D. Jaksch and P. Zoller. Creation of effective magnetic fields in optical lattices: the Hofstadter butterfly for cold neutral atoms. *New J. Phys.* **5,** 56 (2003).

[26] M. Greiner, I. Bloch, O. Mandel, T. Hänsch, and T. Esslinger. Coherence in a 2D Lattice of Bose-Einstein Condensates. *Phys. Rev. Lett.* **87,** 160405 (2001).

[27] J. Sebby-Strabley, M. Anderlini, P. S. Jessen, and J. V. Porto. Lattice of double wells for manipulating pairs of cold atoms. *Phys. Rev. A* **73,** 033605 (2006).

[28] S. Fölling, S. Trotzky, P. Cheinet, M. Feld, R. Saers, A. Widera, T. Müller, and I. Bloch. Direct observation of second-order atom tunnelling. *Nature* **448,** 1029 (2007).

[29] J. Hubbard. Electron correlations in narrow energy bands. *Proc. R. Soc. London A* **276,** 238 (1963).

[30] D. Jaksch, C. Bruder, J. I. Cirac, C. W. Gardiner, and P. Zoller. Cold Bosonic Atoms in Optical Lattices. *Phys. Rev. Lett.* **81,** 3108 (1998).

[31] D. Jaksch and P. Zoller. The cold atom Hubbard toolbox. *Ann. Phys.* **315,** 52 (2005).

[32] C. Chin, R. Grimm, P. Julienne, and E. Tiesinga. Feshbach resonances in ultracold gases. *Rev. Mod. Phys.* **82,** 1225 (2010).

[33] N. Goldman, G. Juzeliunas, P. Ohberg, and I. B. Spielman. Light-induced gauge fields for ultracold atoms. *Rep. Prog. Phys.* **77,** 126401 (2014).

[34] J. Dalibard, F. Gerbier, G. Juzelinas, and P. Ohberg. Colloquium: Artificial gauge potentials for neutral atoms. *Rev. Mod. Phys.* **83,** 1523 (2011).

[35] N. Cooper. Rapidly Rotating Atomic Gases. *Adv. Phys.* **57,** 539 (2008).

[36] V. Galitski and I.B. Spielman. Spin-orbit coupling in quantum gases. *Nature* **494,** 49 (2013).

[37] H. Zhai. Degenerate quantum gases with spin–orbit coupling: a review. *Rep. Prog. Phys.* **78,** 026001 (2015).

[38] D.-W. Zhang, Y.-Q. Zhu, Y. X. Zhao, H. Yan, S.-L. Zhu. Topological quantum matter with cold atoms. *Ad. Phys.* **67,** 253 (2018).

[39] M. Aidelsburger, M. Atala, S. Nascimbene, S. Trotzky, Y.-A. Chen, and I. Bloch. Experimental Realization of Strong Effective Magnetic Fields in an Optical Lattice. *Phys. Rev. Lett.* **107,** 255301 (2011).

[40] M. Aidelsburger, M. Atala, S. Nascimbene, S. Trotzky, Y.-A. Chen, and I. Bloch. Experimental realization of strong effective magnetic fields in optical superlattice potentials. *Appl. Phys. B* **113,** 1 (2013).

[41] H. Miyake, G. A. Siviloglou, C. J. Kennedy, W. C. Burton, and W. Ketterle. Realizing the Harper Hamiltonian with Laser-Assisted Tunneling in Optical Lattices. *Phys. Rev. Lett.* **111,** 185302 (2013).

[42] A. Eckardt. Colloquium: Atomic quantum gases in periodically driven optical lattices. *Rev. Mod. Phys.* **89,** 011004 (2017).

[43] C. L. Kane and E. J. Mele. Quantum Spin Hall Effect in Graphene. *Phys. Rev. Lett.* **95,** 226801 (2005).

[44] A. Bernevig and S.-C. Zhang. Quantum Spin Hall Effect. *Phys. Rev. Lett.* **96,** 106802 (2006).

[45] M. König, S. Wiedmann, C. Brüne, A. Roth, H. Buhmann, L. W. Molenkamp, X.-L. Qi, and S.-C. Zhang. Quantum Spin Hall Insulator State in HgTe Quantum Wells. *Science* **318,** 766 (2007).

[46] M. König, H. Buhmann, L. W. Molenkamp, T. Hughes, C.-X. Liu, X.-L. Qi, and S.-C. Zhang. The Quantum Spin Hall Effect: Theory and Experiment. *J. Phys. Soc. Jpn.* **77,** 031007 (2008).

[47] A. Roth, C. Brüne, H. Buhmann, L. W. Molenkamp, J. Maciejko, X.-L. Qi, and S.-C. Zhang. Nonlocal Transport in the Quantum Spin Hall State. *Science* **325,** 294 (2009).

[48] T. Senthil and Michael Levin. Integer quantum Hall effect for bosons: A physical realization. Phys. Rev. Lett. **110,** 046801 (2013).

[49] F. D. M. Haldane. Model for a Quantum Hall Effect without Landau Levels: Condensed-Matter Realization of the "Parity Anomaly". Phys. Rev. Lett. **61,** 2015 (1988).

[50] U. Schollwöck. The density-matrix renormalization group in the age of matrix product states. *Ann. of Phys.* **326,** 96 (2011).

[51] F. Verstraete, D. Porras, and J. I. Cirac. Density matrix renormalization group and periodic boundary conditions: A quantum information perspective. *Phys. Rev. Lett.* **93,** 227205 (2004).

[52] D. Pérez-García, F. Verstraete, M. M. Wolf, and J. I. Cirac. Matrix Product State Representations. *Quantum Inf. Comput.* **7**, 401 (2007).

[53] F. Verstraete, V. Murg, and J. I. Cirac. Matrix product states, projected entangled pair states, and variational renormalization group methods for quantum spin systems. *Adv. Phys.* **57,** 143 (2008).

[54] R. Orús. A Practical Introduction to Tensor Networks: Matrix Product States and Projected Entangled Pair States. *Ann. of Phys.* **349,** 117 (2014).

[55] S.-J. Ran, E. Tirrito, C. Peng, X. Chen, L. Tagliacozzo, G. Su, M. Lewenstein. Tensor Network Contractions. *Lecture notes in Physics*, Springer (2020).

[56] J. Eisert, M. Cramer, and M. B. Plenio. Colloquium: Area laws for the entanglement entropy. *Rev. Mod. Phys.* **82,** 277 (2010).

[57] M. B. Hastings. An area law for one-dimensional quantum systems. *J. Stat. Mech. Theor. Exp.*, **2007,** P08024 (2007).

[58] F. Verstraete, M. M. Wolf, D. Perez-Garcia, and J. I. Cirac. Criticality, the area law, and the computational power of projected entangled pair states. *Phys. Rev. Lett.* **96,** 220601 (2006).

[59] J. Jünemann, A. Piga, S.-J. Ran, M. Lewenstein, M. Rizzi, and A. Bermudez. Exploring Interacting Topological Insulators with Ultracold Atoms: The Synthetic Creutz-Hubbard Model. *Phys. Rev. X* **7,** 031057 (2017).

[60] E. Tirrito, M. Rizzi, G. Sierra, M. Lewenstein, and A. Bermudez. Renormalization group flows for Wilson-Hubbard matter and the topological Hamiltonian. *Phys. Rev. B* **99,** 125106 (2019).

[61] A. Bermudez, E. Tirrito, M. Rizzi, M. Lewenstein, and S. Hands. Gross-Neveu-Wilson model and correlated symmetry-protected topological phases. *Ann. of Phys.* **399,** 149 (2018).

[62] E. Tirrito, S.-J. Ran, A. J. Ferris, I. P. McCulloch, and M. Lewenstein. Efficient perturbation theory to improve the density matrix renormalization group. *Phys. Rev. B* **95**, 064110 (2017).

[63] E. Tirrito, L. Tagliacozzo, M. Lewenstein, and S.-J. Ran. Characterizing the quantum field theory vacuum using temporal matrix product states. *arXiv preprint arXiv:1810.08050*, 2018.

[64] L. Schubnikow and W.J. de Haas. Magnetic resistance increase in single crystals of bismuth at low temperatures. *Proc. Netherlands Roy. Acad. Sci.* , **33,** 130 (1930).

[65] W.J. de Haas and P. M. Van Alphen . The dependence of the susceptibility of diamagnetic metals upon the field. *Proc. Netherlands Roy. Acad. Sci.* , **33,** 1106 (1930).

[66] T. Ando, Y. Matsumoto, and Yasutada Uemura. Theory of Hall effect in a two-dimensional electron system. *J. Phys. Soc. Jpn.*, **39,** 279 (1975).

[67] D. R. Hofstadter. Energy levels and wave functions of Bloch electrons in rational and irrational magnetic fields. *Phys. Rev. B* **14,** 2239 (1976).

[68] J. B. Listing Vorstudien zur Topologie. *Vanderhoeck und Ruprecht* Göttingen (1848).

[69] M. Levin and X. G. Wen. Colloquium: Photons and electrons as emergent phenomena. *Rev. Mod. Phys.* **77,** 871 (2005).

[70] X. G. Wen. An introduction to quantum order, string-net condensation, and emergence of light and fermions. *Ann. Phys.* **316,** 1 (2005).

[71] A. Altland and M. R. Zirnbauer. Nonstandard symmetry classes in mesoscopic normal-superconducting hybrid structures. *Phys. Rev. B* **55,** 1142 (1997).

[72] W. P. Su, J. R. Schrieffer, and A. J. Heeger. Solitons in Polyacetylene. Phys. Rev. Lett. **42,** 1698 (1979).

[73] W. P. Su, J. R. Schrieffer, and A. J. Heeger. Soliton excitations in polyacetylene. Phys. Rev. B. **22,** 2099 (1980).

[74] J. Ruostekoski, G. V. Dunne, and J. Javanainen. Particle number fractionalization of an atomic fermi-dirac gas in an optical lattice. Phys. Rev. Lett. **88,** 180401 (2002).

[75] L. Li, Z. Xu, and S. Chen. Topological phases of generalized Su-Schrieffer-Heeger models. Phys. Rev. B **89,** 085111 (2014).

[76] R. E. Peierls. Quantum Theory of Solids. *Oxford University Press* 1955.

[77] M.J. Rice and E.J. Mele. Elementary Excitations of a Linearly Conjugated Diatomic Polymer. Phys. Rev. Lett. **49,** 1455 (1982).

[78] A. Y. Kitaev. Unpaired Majorana fermions in quantum wires. Physics-Uspekhi **44,** 131 (2001).

[79] M. Leijnse and K. Flensberg. Introduction to topological superconductivity and Majorana fermions. Semicond. Sci. Technol. **27,** 124003 (2012).

[80] G. C. Velasco and B. Paredes. Classification of topological ladder models. arXiv:1907.11460 (2019).

[81] C. L. Kane and E. J. Mele. Z_2 Topological Order and the Quantum Spin Hall Effect. *Phys. Rev. Lett.* **95,** 146802 (2005).

[82] Y. Aharonov and D. Bohm. Significance of Electromagnetic Potentials in the QuantumTheory. *Theory. Phys. Rev.*, **115,** 485 (1959).

[83] M. Creutz. End States, Ladder Compounds, and Domain-Wall Fermions. Phys. Rev. Lett. **83,** 2636 (1999).

[84] A. Bermudez, D. Patane, L. Amico, and M. A. Martin-Delgado. Topology-Induced Anomalous Defect Production by Crossing a Quantum Critical Point. *Phys. Rev. Lett.* **102,** 135702 (2009).

[85] D. Hügel and B. Paredes. Chiral ladders and the edges of quantum Hall insulators. *Phys. Rev. A* **89,** 023619 (2014).

[86] N. Sun and L.-K. Lim. Quantum charge pumps with topological phases in a Creutz ladder. *Phys. Rev. B* **96,** 035139 (2017).

[87] M. Bischoff, J. Jünemann, M. Polini, and M. Rizzi, Tuning the Drude weight of Dirac-Weyl fermions in one-dimensional ring traps. *Phys. Rev. B* **96,** 241112(R) (2017).

[88] M. Tovmasyan, E. P. L. van Nieuwenburg, and S. D. Huber. Geometry-induced pair condensation. *Phys. Rev. B*, **88,** 220510 (2013).

[89] S. Takayoshi, H. Katsura, N. Watanabe, and H. Aoki. Phase diagram and pair Tomonaga-Luttinger liquid in a Bose-Hubbard model with flat bands. *Phys. Rev. A*, **88,** 063613 (2013).

[90] M. Tovmasyan, S. Peotta, P. Törmä, and S. D. Huber. Effective theory and emergent $SU(2)$ symmetry in the flat bands of attractive Hubbard models. *Phys. Rev. B*, **94,** 245149 (2016).

[91] D. Sticlet, L. Seabra, F. Pollmann, and J. Cayssol. Topological superconductivity in the one-dimensional interacting Creutz model. *J. Phys. Conf. Ser.*, **592,** 012133 (2015).

[92] P. Calabrese and J. Cardy. Entanglement entropy and quantum field theory. *J. Stat. Mech.* **P06002,** (2004).

[93] X. L.- Qi, T. L. Hughes, and S.-C. Zhang. Topological field theory of time-reversal invariant insulators. *Phys. Rev. B*, **78**, 195424 (2008).

[94] S. Ryu, A. P. Schnyder, A. Furusaki, and A. W. W. Ludwig. Topological insulators and superconductors: tenfold way and dimensional hierarchy. *New J. Phys.* **12**, 065010 (2010).

[95] A. Bermudez, L. Mazza, M. Rizzi, N. Goldman, M. Lewenstein, and M. A. Martin-Delgado. Wilson Fermions and Axion Electrodynamics in Optical Lattices. *Phys. Rev. Lett.*, **105,**, 190404 (2010).

[96] L. Mazza, A. Bermudez, N. Goldman, M. Rizzi, M. A. Martin-Delgado, and M. Lewenstein. An optical-lattice-based quantum simulator for relativistic field theories and topological insulators. *New J. Phys.*, **14**, 015007 (2012).

[97] M. E. Peskin and D. V. Schroeder. An introduction to quantum field theory. *Adison Wesley*, Reading, 1995.

[98] P. Strange. Relativistic quantum mechanics. Cambridge University Press, Cambridge, 2005.

[99] A. P. Schnyder, S. Ryu, A. Furusaki, and A. W. W. Ludwig. Classification of topological insulators and superconductors in three spatial dimensions. *Phys. Rev. B* **78,** 195125 (2008).

[100] A. Y. Kitaev. Periodic table for topological insulators and superconductors. *AIP Conf. Proc.* **1134,** 22 (2009).

[101] E. Fradkin. Field Theories of Condensed Matter Physics. Cambridge University Press, Cambridge, (2013).

[102] J. Voit. One-dimensional Fermi liquids. *Prog. Phys.* **58,** 977 (1995).

[103] A. H. Castro Neto, F. Guinea, N. M. R. Peres, K. S. Novoselov, and A. K. Geim. The electronic properties of graphene. Rev. Mod. Phys. **81,** 109 (2009).

[104] C. Gattringer, and C. B. Lang, Quantum Chromodynamics on the Lattice: An Introductory Presentation. *Lect. Notes Phys.*,788, Springer, Berlin Heidelberg (2010).

[105] K. G. Wilson and J. B. Kogut. The renormalization group and the ϵ expansion. *Phys. Rep.* **12,** 75 (1974).

[106] H. B. Nielsen and M. Ninomiya. Absence of neutrinos on a lattice: (I). Proof by homotopy theory. *Phys. Rep.* **12,** 75 (1974).

[107] H. B. Nielsen and M. Ninomiya. Absence of neutrinos on a lattice: (II). Intuitive topological proof. *Nuc. Phys. B* **193,** 173 (1981).

[108] D. B. Kaplan. A method for simulating chiral fermions on the lattice. *Phys. Lett. B* **288,** 342 (1992).

[109] K. Jansen and M. Schmaltz. Critical momenta of lattice chiral fermions. *Phys. Lett. B* **296,** 374 (1992).

[110] K. Jansen. Chiral fermions and anomalies on a finite lattice. *Phys.Lett. B* **288,** 348 (1992).

[111] Y. Shamir. Chiral fermions from lattice boundaries. *Nucl. Phys. B* **406,** 90 (1993).

[112] M. Golterman, K. Jansen, and D. B. Kaplan. Chern-Simons Currents and Chiral Fermions on the Lattice. *Phys. Lett. B* **301,** 219 (1993).

[113] K. Wilson. New Phenomena in Subnuclear Physics.. *ed. A. Zichichi, Plenum*, New York, (1977).

[114] R. Jackiw and C. Rebbi. Solitons with fermion number 1/2. *Phys. Rev. D* **13,** 3398 (1976).

[115] D. Boyanovsky, E. Dagotto, and E. Fradkin. Anomalous currents, induced charge and bound states on a domain wall of a semiconductor. *Nucl. Phys. B* **285,** 340 (1987).

[116] A. W. W. Ludwig, M. P. A. Fisher, R. Shankar, and G. Grinstein. Integer quantum Hall transition: An alternative approach and exact results. *Phys. Rev. B* **50,** 7526 (1994).

[117] M. Hohenadler and F. F. Assaad. Correlation effects in two-dimensional topological insulators. *J. Phys.: Condens. Matter* **25,** 143201 (2013).

[118] S. A. Parameswaran, R. Roy, and S. L. Sondhi. Fractional quantum Hall physics in topological flat bands. *Compt. Rend. Phys.* **14,** 816 (2013).

[119] S. Rachel, Interacting topological insulators: a review. Rep. Prog. Phys. **81**, 116501 (2018).

[120] R. Shankar. Renormalization-group approach to interacting fermions. Rev. Mod. Phys. **66,** 129 (1994).

[121] T. J. Hollowod. Renormalization Group and Fixed Points in Quantum Field Theory. *Springer*, Heidelberg, (2013).

[122] Z. Wang and S.-C. Zhang. Simplified Topological Invariants for Interacting Insulators. *Phys. Rev. X* **2,** 031008 (2012).

[123] Z. Wang and S.-C. Zhang. Strongly correlated topological superconductors and topological phase transitions via Green's function. *Phys. Rev. B* **86,** 165116 (2012).

[124] Z. Wang and B. Yan. Topological Hamiltonian as an exact tool for topological invariants. *J. Phys.: Condens. Matter* **25,** 155601 (2013).

[125] J. C. Budich, B. Trauzettel, and G. Sangiovanni. Fluctuation-driven topological Hund insulators. *Phys. Rev. B* **87,** 235104 (2013).

[126] A. Amaricci, J. C. Budich, M. Capone, B. Trauzettel, G. Sangiovanni. Strong correlation effects on topological quantum phase transitions in three dimensions. *Phys. Rev. B* **93,** 235112 (2016).

[127] T. I. Vanhala, T. Siro, L. Liang, M. Troyer, A. Harju, and P. Törmä. Topological Phase Transitions in the Repulsively Interacting Haldane-Hubbard Model. *Phys. Rev. Lett.* **116,** 225305 (2016).

[128] P. Kumar, T. Mertz, and W. Hofstetter. Interaction-induced topological and magnetic phases in the Hofstadter-Hubbard model. *Phys. Rev. B* **94,** 115161 (2016).

[129] T. C. Lang, A. M. Essin, V. Gurarie, and S. Wessel. Z_2 topological invariants in two dimensions from quantum Monte Carlo. *Phys. Rev. B* **87,** 205101 (2013).

[130] H.-H. Hung, L. Wang, Z.-C. Gu, and G. A. Fiete. Topological phase transition in a generalized Kane-Mele-Hubbard model: A combined quantum Monte Carlo and Green's function study. *Phys. Rev. B* **87,** 121113 (2013).

[131] H.-H. Hung, V. Chua, L. Wang, and G. A. Fiete. Interaction effects on topological phase transitions via numerically exact quantum Monte Carlo calculations. *Phys. Rev. B* **89,** 235104 (2014).

[132] S. R. White and R. M. Noack. Real-space quantum renormalization groups. *Phys. Rev. Lett.* **68,** (1992).

[133] S. R. White. Density matrix formulation for quantum renormalization groups. *Phys. Rev. Lett.* **69,** 2863 (1992).

[134] S. R. White. Density-matrix algorithms for quantum renormalization groups. *Phys. Rev. B* **48,** 10345 (1993).

[135] J. Zak. Berry's phase for energy bands in solids. *Phys. Rev. Lett.* **62,** 2747 (1989).

[136] D. J. Gross and A. Neveu. Dynamical symmetry breaking in asymptotically free field theories. *Phys. Rev. D* **10,** 3235 (1974).

[137] D. J. Amit. Field Theory, The Renormalization Group, And Critical Phenomena. World Scientific Publishing, Singapore, 1984.

[138] M. B. Plenio and S. Virmani. An introduction to entanglement measures. *Quant. Inf. Comp.*. **7,** 1 (2007)

[139] L. Amico, R. Fazio, A. Osterloh, and V. Vedral. Entanglement in many-body systems. *Rev. Mod. Phys.* **80,** 517 (2008).

[140] N. Laflorencie. Quantum entanglement in condensed matter systems. *Phys. Rep.* **646,** 1 (2016).

[141] P. Calabrese and A. Lefevre. Entanglement spectrum in one-dimensional systems. Phys. Rev A **78,** 032329 (2008).

[142] H. Li and F.D.M. Haldane. Entanglement Spectrum as a Generalization of Entanglement Entropy: Identification of Topological Order in Non-Abelian Fractional Quantum Hall Effect States. *Phys. Rev. Lett.* **101,** 010504 (2008).

[143] M.-C. Chung and I. Peschel. Density-matrix spectra of solvable fermionic systems. *Phys. Rev. B* **64,** 064412 (2001).

[144] F. Pollmann, E. Berg, A. M. Turner, and M. Oshikawa. Entanglement spectrum of a topological phase in one dimension. *Phys. Rev. B* **81,** 064439 (2010).

[145] L. Fidkowski. Entanglement Spectrum of Topological Insulators and Superconductors. *Phys. Rev. Lett.* **104,** 130502 (2010).

[146] F. Pollmann, E. Berg, A. M. Turner, and M. Oshikawa. Symmetry protection of topological phases in one-dimensional quantum spin systems. *Phys. Rev. B* **85,** 075125 (2012).

[147] S.-A. Cheong and C. L. Henley. Many-body density matrices for free fermions. *Phys. Rev. B.* **69,** 075111 (2004).

[148] I. Peschel. Calculation of reduced density matrices from correlation functions. J. Phys. A: Math.Gen. **36,** L205 (2003).

[149] M. Dalmonte, B. Vermersch, and P. Zoller. Quantum simulation and spectroscopy of entanglement Hamiltonians. *Nat. Phys.* **14,** 827 (2018).

[150] G. Giudici, T. Mendes-Santos, P. Calabrese, and M. Dalmonte. Entanglement Hamiltonians of lattice models via the Bisognano-Wichmann theorem. *Phys. Rev. B* **98,** 134403 (2018).

[151] X. Turkeshi, T. Mendes-Santos, G. Giudici, and M. Dalmonte. Entanglement guided search for parent Hamiltonians. *Phys. Rev. Lett.* **122,** 150606 (2019).

[152] J. J. Bisignano and E. H. Wichmann. On the duality condition for quantum fields. *J. Math. Phys.* **17,** 303 (1976).

[153] G. Vidal, J. Latorre, E. Rico, and A. Kitaev. Entanglement in Quantum Critical Phenomena. *Phys. Rev. Lett.* **90,** 227902 (2003).

[154] P. Calabrese and J. Cardy. Entanglement entropy and conformal field theory *J. Phys. A* **42,** 504005 (2009).

[155] P. Di Francesco, P. Mathieu, and D. Sénéchal. Conformal Field Theory. *Springer verlag*, Berlin, 1997.

[156] N. Laflorencie, E. S. Sorensen, M.-S. Chang, and I. Affleck. Boundary Effects in the Critical Scaling of Entanglement Entropy in 1D Systems. *Phys. Rev. Lett.* **96,** 100603 (2006) .

[157] P. Calabrese, M. Campostrini, F. Essler, and B. Nienhuis. Parity Effects in the Scaling of Block Entanglement in Gapless Spin Chains. Phys. Rev. Lett. **104,** 095701 (2010).

[158] F. D. M. Haldane. "Luttinger liquid theory" of one-dimensional quantum fluids. I. Properties of the Luttinger model and their extension to the general 1D interacting spinless Fermi gas. *J. Phys. C: Solid State Physics* **14,** 2585 (1981).

[159] M. Dalmonte, E. Ercolessi, and L. Taddia. Estimating quasi-long-range order via Rényi entropies. *Phys. Rev. B* **84,** 085110 (2011).

[160] L. Taddia. Entanglement Entropies in One-Dimensional Systems. *arXiv:1309.4003* at Bologna University (2013).

[161] I. Klich and L. Levitov. Quantum Noise as an Entanglement Meter. *Phys. Rev. Lett.* **102,** 100502 (2009).

[162] H. Song, S. Rachel, C. Flindt, I. Klich, N. Laflorencie, and K. Le Hur. Bipartite fluctuations as a probe of many-body entanglement. *Phys. Rev. B* **85,** 035409 (2012).

[163] H. F. Song, S. Rachel, and K. Le Hur. General relation between entanglement and fluctuations in one dimension. *Phys. Rev. B* **82,** 012405 (2010).

[164] J. C. Xavier, F. C. Alcaraz, and G. Sierra. Equipartition of the entanglement entropy. *Phys. Rev. B* **98,** 041106(R) (2018).

[165] Y. Nambu and G. Jona-Lasinio. Dynamical Model of Elementary Particles Based on an Analogy with Superconductivity. I. *Phys. Rev.* **122,** 345 (1961).

[166] S. P. Klevansky. The Nambu—Jona-Lasinio model of quantum chromodynamics. *Rev. Mod. Phys.* **64,** 649 (1992).

[167] C. Yang and R. Mills. Conservation of Isotopic Spin and Isotopic Gauge Invariance. *Phys. Rev.* **96,** 191 (1954).

[168] D. J. Gross and F. Wilczek. Ultraviolet Behavior of Non-Abelian Gauge Theories. *Phys. Rev. Lett.* **30,**1343 (1973).

[169] H. D. Politzer. Reliable Perturbative Results for Strong Interactions?. *Phys. Rev. Lett.* **30,** 1346 (1973).

[170] C. Kopper, J. Magnen, and V. Rivasseau. Mass generation in the large N Gross-Neveu-Model. *Commun. Math. Phys.* **169,** 121 (1995).

[171] E. Pereira, and A. Procacci. Block Renormalization Group in a Formalism with Lattice Wavelets: Correlation Function Formulas for Interacting Fermions. *Ann. Phys.* **255,** 19 (1997).

[172] K. Gawędzki and A. Kupiainen. Gross-Neveu model through convergent perturbation expansions. Commun. Math. Phys. **102,** 1 (1985).

[173] L. Susskind. Lattice fermions. *Phys. Rev. D* **16,** 3031 (1977). Phys. Rev. D, **16,** 3031 (1977).

[174] B. I. Halperin. Quantized Hall conductance, current-carrying edge states, and the existence of extended states in a two-dimensional disordered potential. *Phys. Rev. B* **25,** 2185 (1982).

[175] A. Sekine, T. Z. Nakano, Y. Araki, and K. Nomura, Strong coupling expansion in a correlated three-dimensional topological insulator. *Phys. Rev. B* **87,** 165142 (2013).

[176] R. Resta. Theory of the electric polarization in crystals. *Ferroelectrics* **136,** 51 (1992).

[177] R. D. King-Smith and D. Vanderbilt, Theory of polarization of crystalline solids. *Phys. Rev. B* **47,** 1651 (1993).

[178] D. Xiao, M.-C. Chang, and Q. Niu. Berry phase effects on electronic properties. *Rev. Mod. Phys.* **82,** 1959 (2010).

[179] J. Kogut and L. Susskind. Hamiltonian formulation of Wilson's lattice gauge theories. *Phys. Rev. D* **11,** 395 (1975).

[180] A. Milsted, J. Haegeman, and T. J. Osborne. Matrix product states and variational methods applied to critical quantum field theory. *Phys. Rev. D* **88,** 085030 (2013).

[181] M. Bañuls, K. Cichy, J. I. Cirac, and K. Jansen. The mass spectrum of the Schwinger model with matrix product states. *J. High Energ. Phys.* **158,** (2013).

[182] B. Buyens, J. Haegeman, K. Van Acoleyen, H. Verschelde, and F. Verstraete. Matrix Product States for Gauge Field Theories. *Phys. Rev. Lett.* **113,** 091601 (2014).

[183] E. Rico, T. Pichler, M. Dalmonte, P. Zoller, and S. Montangero. Tensor Networks for Lattice Gauge Theories and Atomic Quantum Simulation. *Phys. Rev. Lett.* **112,** 201601 (2014). Phys. Rev. Lett. **112,** 201601 (2014);

[184] L. Tagliacozzo, A. Celi, and M. Lewenstein. Tensor Networks for Lattice Gauge Theories with Continuous Groups. *Phys. Rev. X* **4,** 041024 (2014).

[185] M. A. Cazalilla and A. M. Rey. Ultracold Fermi gases with emergent $SU(N)$ symmetry. *Rep. Prog. Phys.* **77,** 124401 (2014).

[186] W. Hofstetter, J. I. Cirac, P. Zoller, E. Demler, and M. D. Lukin. High-Temperature Superfluidity of Fermionic Atoms in Optical Lattices. *Phys. Rev. Lett.* **89,** 220407 (2002).

[187] A. Albus, F. Illuminati, and J. Eisert. Mixtures of bosonic and fermionic atoms in optical lattices. *Phys. Rev. A* **68,** 023606 (2003).

[188] M. Greiner, O. Mandel, T. Esslinger, T. W. Hänsch, and I. Bloch. Quantum phase transition from a superfluid to a Mott insulator in a gas of ultracold atoms. *Nature* **415,** 39 (2002).

[189] R. Jördens, N. Strohmaier, K. Günter, H. Moritz, and T. Esslinger. A Mott insulator of fermionic atoms in an optical lattice. *Nature* **455,** 204 (2008).

[190] U. Schneider, L. Hackermüller, S. Will, Th. Best, I. Bloch, T. A. Costi, R. W. Helmes, D. Rasch, and A. Rosch. Metallic and Insulating Phases of Repulsively Interacting Fermions in a 3D Optical Lattice. *Science* **322,** 1520 (2008).

[191] N. Goldman, A. Kubasiak, A. Bermudez, P. Gaspard, M. Lewenstein, and M. A. Martin-Delgado, Non-Abelian Optical Lattices: Anomalous Quantum Hall Effect and Dirac Fermions. *Phys. Rev. Lett.* **103,** 035301 (2009).

[192] A. Bermudez, N. Goldman, A. Kubasiak, M. Lewenstein, and M. A. Martin-Delgado, Topological phase transitions in the non-Abelian honeycomb lattice. *New J. Phys.* **12,** 033041 (2010).

[193] Z. Lan, N. Goldman, A. Bermudez, W. Lu, and P. Öhberg, Dirac-Weyl fermions with arbitrary spin in two-dimensional optical superlattices. *Phys. Rev. B* **84,** 165115 (2011).

[194] J. I. Cirac, P. Maraner, and J. K. Pachos, Cold Atom Simulation of Interacting Relativistic Quantum Field Theories. *Phys. Rev. Lett.* **105,** 190403 (2010).

[195] S. P. Jordan, K. S. Lee, and J. Preskill. Quantum Algorithms for Quantum Field Theories. *Science* **336,** 1130 (2012).

[196] S. P. Jordan, K. S. Lee, and J. Preskill. Quantum computation of scattering in scalar quantum field theories. *Quant. Inf. and Comp.* **14,** 1014 (2014).

[197] H. Zou, Y. Liu, C.-Y. Lai, J. Unmuth-Yockey, L.-P. Yang, A. Bazavov, Z. Y. Xie, T. Xiang, S. Chandrasekharan, S.-W. Tsai, and Y. Meurice. Progress towards quantum simulating the classical $O(2)$ model. *Phys. Rev. A* **90,** 063603 (2014).

[198] A. Bermudez, G. Aarts, and M. Müller. Quantum Sensors for the Generating Functional of Interacting Quantum Field Theories. *Phys. Rev. X* **7,** 041012 (2017).

[199] T. Byrnes and Y. Yamamoto. Simulating lattice gauge theories on a quantum computer. *Phys. Rev. A* **73,** 022328 (2006).

[200] H. P. Büchler, M. Hermele, S. D. Huber, M. P. A. Fisher, and P. Zoller. Atomic Quantum Simulator for Lattice Gauge Theories and Ring Exchange Models. *Phys. Rev. Lett.* **95,** 040402 (2005).

[201] H. Weimer, M. Müller, I. Lesanovsky, P. Zoller, and H. P. Büchler. A Rydberg quantum simulator. *Nat. Phys.* **6,** 382 (2010).

[202] L. Tagliacozzo, A. Celi, A. Zamora, and M. Lewenstein. Optical Abelian lattice gauge theories. *Ann. Phys.* **330,** 160 (2013).

[203] L.Tagliacozzo, A. Celi, P. Orland, M. W. Mitchell, and M. Lewenstein. Simulation of non-Abelian gauge theories with optical lattices. *Nat. Comm.* **4,** 2615 (2013).

[204] D. B. Kaplan and J. R. Stryker. Gauss's Law, Duality, and the Hamiltonian Formulation of U(1) Lattice Gauge Theory. *arXiv:1806.08797* (2018).

[205] K. Kasamatsu, I. Ichinose, and T. Matsui. Atomic Quantum Simulation of the Lattice Gauge-Higgs Model: Higgs Couplings and Emergence of Exact Local Gauge Symmetry. *Phys. Rev. Lett.* **111,** 115303 (2013).

[206] Y. Kuno, K. Kasamatsu, Y. Takahashi, I. Ichinose, and T. Matsui. Real-time dynamics and proposal for feasible experiments of lattice gauge–Higgs model simulated by cold atoms. *New J. Phys.* **17,** 063005 (2015).

[207] Y. Kuno, S. Sakane, K. Kasamatsu, I. Ichinose, and T. Matsui. Quantum simulation of $(1 + 1)$-dimensional $U(1)$ gauge-Higgs model on a lattice by cold Bose gases. *Phys. Rev. D* **95,** 094507 (2017).

[208] A. Bazavov, Y. Meurice, S.-W. Tsai, J. Unmuth-Yockey, and J. Zhang. Gauge-invariant implementation of the Abelian-Higgs model on optical lattices. *Phys. Rev. D* **92,** 076003 (2015).

[209] J. Zhang, J. Unmuth-Yockey, J. Zeiher, A. Bazavov, S. -W. Tsai, and Y. Meurice. Quantum simulation of the universal features of the Polyakov loop. *Phys. Rev. Lett.* **121,** 223201 (2018).

[210] E. Kapit and E. Mueller. Optical-lattice Hamiltonians for relativistic quantum electrodynamics. *Phys. Rev. A* **83,** 033625 (2011).

[211] E. Zohar and B. Reznik. Confinement and Lattice Quantum-Electrodynamic Electric Flux Tubes Simulated with Ultracold Atoms. *Phys. Rev. Lett.* **107,** 275301 (2011).

[212] E. Zohar, J. I. Cirac, and B. Reznik. Simulating Compact Quantum Electrodynamics with Ultracold Atoms: Probing Confinement and Nonperturbative Effects. *Phys. Rev. Lett.* **109,** 125302 (2012).

[213] D. Banerjee, M. Dalmonte, M. Müller, E. Rico, P. Stebler, U.-J. Wiese, and P. Zoller. Atomic Quantum Simulation of Dynamical Gauge Fields Coupled to Fermionic Matter: From String Breaking to Evolution after a Quench. *Phys. Rev. Lett.* **109,**175302 (2012).

[214] E. Zohar, J. I. Cirac, and B. Reznik. Simulating (2+1)-Dimensional Lattice QED with Dynamical Matter Using Ultracold Atoms. *Phys. Rev. Lett.* **110,** 055302 (2013).

[215] G. Magnifico, D. Vodola, E. Ercolessi, S. P. Kumar, M. Müller, and A. Bermudez. Symmetry-protected topological phases in lattice gauge theories: topological QED. *Phys. Rev. D* **99,** 014503 (2019).

[216] D. Banerjee, M. Bögli, M. Dalmonte, E. Rico, P. Stebler, U.-J. Wiese, and P. Zoller. Atomic Quantum Simulation of $U(N)$ and $SU(N)$ Non-Abelian Lattice Gauge Theories. *Phys. Rev. Lett.* **110,** 125303 (2013).

[217] E. Zohar, J. I. Cirac, and B. Reznik. Cold-Atom Quantum Simulator for SU(2) Yang-Mills Lattice Gauge Theory. *Phys. Rev. Lett.* **110,** 125304 (2013).

[218] Y. Kuno, I. Ichinose, and Y. Takahashi. Generalized lattice Wilson-Dirac fermions in $(1 + 1)$ dimensions for atomic quantum simulation and topological phases. Scientific Rep. **8,** 10699 (2018).

[219] T. V. Zache, F. Hebenstreit, F. Jendrzejewski, M. K. Oberthaler, J. Berges, and P. Hauke, Quantum simulation of lattice gauge theories using Wilson fermions. *Quantum Sci. Technol.* **3,** 034010 (2018).

[220] T. Eguchi and R. Nakayama, The Wilson lattice fermion and the recovery of chiral symmetry near the continuum limit. Phys. Lett. **126B** 89 (1983).

[221] S. Aoki and K. Higashijima. The Recovery of the Chiral Symmetry in Lattice Gross-Neveu Model. *Prog. Theor. Phys.* **76,** 521 (1986).

[222] S. Aoki. New phase structure for lattice QCD with Wilson fermions. *Phys. Rev. D* **30,** 2653 (1984).

[223] T. Izubuchi, J. Noaki, and A. Ukawa. Two-dimensional lattice Gross-Neveu model with Wilson fermion action at finite temperature and chemical potential. *Phys. Rev. D* **58,** 114507 (1998).

[224] Y. Araki and T. Kimura. Phase structure of two-dimensional topological insulators by lattice strong-coupling expansion. *Phys. Rev. B* **87,** 205440 (2013).

[225] F.W.J. Oliver, D. W. Lozier, R. F. Boisvert, and Charles W. Clark, NIST Handbook of Mathematical Functions. *Cambridge University Press*, Cambridge, 2010.

[226] T. DeGrand and C. DeTar. Lattice methods for quantum chromodynamics. *World Scientific*, New Jersey, 2006.

[227] P. Hasenfratz and F. Karsch. Chemical Potential on the Lattice. *Phys. Lett.* **125B ,** 308 (1983).

[228] I. Barbour, S. Hands, J. B. Kogut, M. P. Lombardo and S. Morrison. Chiral symmetry restoration and realisation of the Goldstone mechanism in the $U(1)$ Gross-Neveu model at non-zero chemical potential. *Nucl. Phys. B* **557,** 327 (1999).

[229] S. Hands, A. Kocic, and J. B. Kogut. The four-Fermi model in three dimensions at non-zero density and temperature. Nucl. Phys. B **390** 355 (1993).

[230] W. Thirring. A soluble relativistic field theory. Ann. Phys. **3,** 91 (1958).

[231] S. Coleman. Quantum sine-Gordon equation as the massive Thirring model. *Phys. Rev. D* **11,** 2088 (1975).

[232] N. Kawamoto, and J.Smit. Effective lagrangian and dynamical symmetry breaking in strongly coupled lattice QCD. *Nuc. Phys. B* **192,** 100 (1981).

[233] P. Fazekas. Lecture Notes on Electron Correlation and Magnetism. *World Scientific Pub.*, London, 2003.

[234] H. Li and F. D. M. Haldane, Entanglement Spectrum as a Generalization of Entanglement Entropy: Identification of Topological Order in Non-Abelian Fractional Quantum Hall Effect States. *Phys. Rev. Lett.* **101,** 010504 (2015).

[235] F. Pollmann, A. M. Turner, E. Berg, and M. Oshikawa, Entanglement spectrum of a topological phase in one dimension. *Phys. Rev. B* **81,** 064439 (2010).

[236] P.W. Anderson. New Approach to the Theory of Superexchange Interactions. *Phys. Rev.* **115,** 2 (1959).

[237] A. H. MacDonald, S. M. Girvin, and D. Yoshioka. $\frac{t}{U}$ expansion for the Hubbard model. Phys. Rev. B **37,** 9753 (1988).

[238] P. Pfeuty. The one-dimensional Ising model with a transverse field. *Ann. Phys.* **57,** 79 (1970).

[239] O. Boada, A. Celi, M. Lewenstein, and J. I. Latorre. Quantum Simulation of an Extra Dimension. *Phys. Rev. Lett.* **108,** 133001 (2012).

[240] A. Celi, P. Massignan, J. Ruseckas, N. Goldman, I.B. Spielman, G. Juzeliunas, and M. Lewenstein. Synthetic Gauge Fields in Synthetic Dimensions. *Phys. Rev. Lett.* **112,** 043001 (2014).

[241] M. B. Dahan, E. Peik, J. Reichel, Y. Castin, and C. Salomon. Bloch Oscillations of Atoms in an Optical Potential. *Phys. Rev. Lett.* **76,** 4508 (1996).

[242] A. Bermudez, T. Schaetz, and D. Porras. Synthetic Gauge Fields for Vibrational Excitations of Trapped Ions. Phys. Rev. Lett. **107,** 150501 (2011).

[243] A. Bermudez, T. Schaetz, and D. Porras. Photon-assisted-tunneling toolbox for quantum simulations in ion traps. *New J. Phys.* **14,** 053049 (2012).

[244] D. H. Dunlap and V. M. Kenkre. Dynamic localization of a charged particle moving under the influence of an electric field. *Phys. Rev. B* **34,** 3625 (1986).

[245] F. Grossman, T. Dittrich, P. Jung, and P. Hänggi. Coherent destruction of tunneling. *Phys. Rev. Lett.* **67,** 516 (1991).

[246] M. Holthaus, Collapse of minibands in far-infrared irradiated superlattices. *Phys. Rev. Lett.* **69,** 351 (1992).

[247] J. H. Kang, J. H. Han, and Y.-I. Shin, Realization of a cross-linked chiral ladder with neutral fermions in an optical lattice by orbital-momentum coupling. *Phys. Rev. Lett.* **121,** 150403 (2018).

[248] O. Dutta, M. Gajda, P. Hauke, M. Lewenstein, D.-S. Lühmann, B. A. Malomed, T. Sowiński, and J. Zakrzewski, Non-standard Hubbard models in optical lattices: a review. *Rep. Prog. Phys.* **78,** 066001 (2015).

[249] H. A. Kramers and G. H. Wannier. Statistics of the two-dimensional ferromagnet. part I. *Phys. Rev.*, **60,** 252 (1941).

[250] H. A. Kramers and G. H. Wannier. Statistics of the two-dimensional ferromagnet. part II. *Phys. Rev.*, **60,** 263 (1941).

[251] R. J. Baxter. Dimers on a rectangular lattice. *J. Math. Phys.* **9,** 650 (1968).

[252] M. P. Nightingale and H. W. J. Blöte. Gap of the linear spin-1 Heisenberg antiferromagnet: A Monte Carlo calculation. *Phys. Rev. B* **33,** 659 (1986).

[253] S. B. Kelland. Estimates of the critical exponent β for the Potts model using a variational approximation. *Can. J. Phys.* **54,** 1621 (1976).

[254] S. K. Tsang. Square lattice variational approximations applied to the Ising model. *J. Stat. Phys.* **20,** 95 (1979).

[255] B. Derrida and M. R. Evans. Exact correlation functions in an asymmetric exclusion model with open boundaries. *J. Phys. I* **3,** 311 (1993).

[256] B. Derrida, M. R. Evans, V. Hakim, and V. Pasquier. Exact solution of a 1D asymmetric exclusion model using a matrix formulation. *J. Phys. A Math. Gen.* **26,** 1493 (1993).

[257] T. Nishino and K. Okunishi. Corner transfer matrix renormalization group method. *J. Phys. Soc. Jpn.* **65,** 891 (1996).

[258] T. Nishino, K. Okunishi, and M. Kikuchi. Numerical renormalization group at criticality. *Phys. Lett. A* **213,** 69 (1996).

[259] T. Nishino, Y. Hieida, K. Okunishi, N. Maeshima, Y. Akutsu, and A. Gendiar. Two-dimensional tensor product variational formulation. *Prog. Theo. Phys.* **105,** 409 (2001).

[260] T. Nishino, K. Okunishi, Y. Hieida, N. Maeshima, and Y. Akutsu. Self-consistent tensor product variational approximation for 3D classical models. *Nucl. Phys. B* **575,** 504 (2000).

[261] T. Nishino and K. Okunishi. A density matrix algorithm for 3D classical models. *J. Phys. Soc. Jpn.* **67,** 3066 (1998).

[262] K. Okunishi and T. Nishino. Kramers-Wannier approximation for the 3D Ising model. *Prog. Theo. Phys.* **103,** 541 (2000).

[263] T. Nishino and K. Okunishi. Numerical latent heat observation of the $q = 5$ Potts model. *arXiv preprint cond-mat/9711214*, (1997).

[264] K. G. Willson. The renormalization group: Critical phenomena and the Kondo problem. *Rev. Mod. Phys.* **47,** 773 (1975).

[265] M. D. Kovarik. Numerical solution of large S=1/2 and S=1 Heisenberg antiferromagnetic spin chains using a truncated basis expansion. *Phys. Rev. B* **41,** 6889 (1990).

[266] T. Xiang and G. A. Gehring. Real space renormalisation group study of Heisenberg spin chain. *J. Magn. Magn. Mater.* **104,** 861 (1992).

[267] T. Xiang and G. A. Gehring. Numerical solution of S=1 antiferromagnetic spin chains using a truncated basis expansion. *Phys. Rev. B* **48,** 303 (1993).

[268] J. Kondo. Resistance minimum in dilute magnetic alloys. *Prog. Theor. Phys.* **32,** 37 (1964).

[269] R. J. Bursill, T. Xiang, and G. A. Gehring. The density matrix renormalization group for a quantum spin chain at non-zero temperature. *J. Phys. Cond. Matter* **8,** L583 (1996).

[270] S. Moukouri and L. G. Caron. Thermodynamic density matrix renormalization group study of the magnetic susceptibility of half-integer quantum spin chains. *Phys. Rev. Lett.* **77,** 4640 (1996).

[271] X.-Q. Wang and T. Xiang. Transfer-matrix density-matrix renormalization-group theory for thermodynamics of one-dimensional quantum systems. *Phys. Rev. B* **56,** 5061 (1997).

[272] N. Shibata. Thermodynamics of the anisotropic Heisenberg chain calculated by the density matrix renormalization group method. *J. Phys. Soc. Jpn.* **66,** 2221 (1997).

[273] K. A. Hallberg. Density-matrix algorithm for the calculation of dynamical properties of low-dimensional systems. *Phys. Rev. B* **52,** R9827 (1995).

[274] S. Ramasesha, S. K. Pati, H. R. Krishnamurthy, Z. Shuai, and J. L. Brédas. Low-lying electronic excitations and nonlinear optic properties of polymers via symmetrized density matrix renormalization group method. *Synthetic Met.* **85,** 1019 (1997).

[275] T. D. Kühner and S. R. White. Dynamical correlation functions using the density matrix renormalization group. *Phys. Rev. B* **60,** 335 (1999).

[276] E. Jeckelmann. Dynamical density-matrix renormalization-group method. *Phys. Rev. B* **66,** 045114 (2002).

[277] M. Fannes, B. Nachtergaele, and R. F. Werner. Ground states of VBS models on Cayley trees. *J. Stat. Phys.* **66,** 939 (1992).

[278] M. Fannes, B. Nachtergaele, and R. F. Werner. Finitely correlated states on quantum spin chains. *Comm. Math. Phys.* **144,** 443 (1992).

[279] A. Klumper, A. Schadschneider, and J. Zittartz. Equivalence and solution of anisotropic spin-1 models and generalized t-J fermion models in one dimension. *J. Phys. A Math. Gen.* **24,** L955 (1991).

[280] T. J. Osborne and M. A. Nielsen. Entanglement, quantum Phase transitions, and density matrix renormalization. *Quant. Inf. Proc.* **1,** 45 (2002).

[281] G. Vidal. Efficient classical simulation of slightly entangled quantum computations. *Phys. Rev. Lett.* **91,** 147902 (2003).

[282] G. Vidal. Efficient simulation of one-dimensional quantum many-body systems. *Phys. Rev. Lett.* **93,** 040502 (2004).

[283] C. H. Bennett and D. P. DiVincenzo. Quantum information and computation. *Nature* **404,** 247 (2000).

[284] M. A. Nielsen and I. Chuang. *Quantum computation and quantum communication.* Cambridge University Press, Cambridge, England, 2000.

[285] L. Amico, R. Fazio, A. Osterloh, and V. Vedral. Entanglement in many-body systems. *Rev. Mod. Phys.* **80,** 517 (2008).

[286] R. Horodecki, P. Horodecki, M. Horodecki, and K. Horodecki. Quantum entanglement. *Rev. Mod. Phys.* **81,** 865 (2009).

[287] M. B. Hastings. Locality in quantum and Markov dynamics on lattices and networks. *Phys. Rev. Lett.* **93,** 140402 (2004).

[288] M. B. Hastings. Lieb-Schultz-Mattis in higher dimensions. *Phys. Rev. B* **69,** 104431 (2004).

[289] Y.-C. Huang. *Classical simulation of quantum many-body systems.* University of California, Berkeley, 2015.

[290] J. D. Bekenstein. Black holes and entropy. *Phys. Rev. D* **7,** 2333 (1973).

[291] M. Srednicki. Entropy and area. *Phys. Rev. Lett.* **71,** 666 (1993).

[292] J. I. Latorre, E. Rico, and G. Vidal. Ground state entanglement in quantum spin chains. *Quant. Inf. Comp.* **4,** 48 (2004).

[293] M. B. Plenio, J. Eisert, J. Dreissig, and M. Cramer. Entropy, entanglement, and area: Analytical results for harmonic lattice systems. *Phys. Rev. Lett.* **94,** 060503 (2005).

[294] J. Eisert, M. Cramer, and M. B. Plenio. Colloquium: Area laws for the entanglement entropy. *Rev. Mod. Phys.* **82,** 277 (2010).

[295] F. Verstraete and J. I. Cirac. Matrix product states represent ground states faithfully. *Phys. Rev. B* **73,** 094423 (2006).

[296] S. Östlund and S. Rommer. Thermodynamic limit of density matrix renormalization. *Phys. Rev. Lett.* **75,** 3537 (1995).

[297] S. Rommer and S. Östlund. Class of ansatz wave functions for one-dimensional spin systems and their relation to the density matrix renormalization group. *Phys. Rev. B* **55,** 2164 (1997).

[298] J. Dukelsky, M. A. Martín-Delgado, T. Nishino, and G. Sierra. Equivalence of the variational matrix product method and the density matrix renormalization group applied to spin chains. *Europhys. Lett.* **43,** 457 (1998).

[299] I. P. McCulloch. From density-matrix renormalization group to matrix product states. *J. Stat. Mech. Theory Exp.* **10,** P10014 (2007).

[300] V. Alba, L.Tagliacozzo, and P. Calabrese. Entanglement entropy of two disjoint blocks in critical Ising models. *Phys. Rev. B*, **81,** 060411(R) (2010).

[301] V. Alba, L.Tagliacozzo, and P. Calabrese. Entanglement entropy of two disjoint intervals in $c = 1$ theories. *J. Stat. Mech.*, **1106,** P06012 (2011).

[302] P. Calabrese, L.Tagliacozzo, and E. Tonni. Entanglement negativity in the critical Ising chain. *J. Stat. Mech.*, **2013,** P05002 (2013).

[303] V. Alba, L.Tagliacozzo, and P. Calabrese. Perfect sampling with unitary tensor networks. *Phys. Rev. B*, **85,** 165146 (2012).

[304] F. Gliozzi and L.Tagliacozzo. Entanglement entropy and the complex plane of replicas. *J. Stat. Mech.*, **2010,** P01002 (2010).

[305] G. Vidal. Efficient classical simulation of slightly entangled quantum computations. *Phys. Rev. Lett.* **91,** 147902 (2003).

[306] G. Vidal. Efficient simulation of one-dimensional quantum many-body systems. *Phys. Rev. Lett.* **93,** 040502 (2004).

[307] G. Vidal. Classical simulation of infinite-size quantum lattice systems in one spatial dimension. *Phys. Rev. Lett.* **98,** 070201 (2007).

[308] R. Orús and G. Vidal. Infinite time-evolving block decimation algorithm beyond unitary evolution. *Phys. Rev. B* **78,** 155117 (2008).

[309] J. Haegeman, J. I. Cirac, T. J. Osborne, I. Pižorn, H. Verschelde, and F. Verstraete. Time-dependent variational principle for quantum lattices. *Phys. Rev. Lett.* **107,** 070601 (2011).

[310] E. Bartel, A. Schadschneider, and J. Zittartz. Excitations of anisotropic spin-1 chains with matrix product ground state. *Eur. Phys. J. B* **31,** 209 (2003).

[311] S.-G. Chung and L.-H. Wang. Entanglement perturbation theory for the elementary excitation in one dimension. *Phys. Lett. A* **373,** 2277 (2009).

[312] B. Pirvu, J. Haegeman, and F. Verstraete. Matrix product state based algorithm for determining dispersion relations of quantum spin chains with periodic boundary conditions. *Phys. Rev. B* **85,** 035130 (2012).

[313] J. Haegeman, B. Pirvu, D. J. Weir, J. I. Cirac, T. J. Osborne, H. Verschelde, and F. Verstraete. Variational matrix product ansatz for dispersion relations. *Phys. Rev. B* **85,** 100408 (2012).

[314] V. Zauner-Stauber, L. Vanderstraeten, J. Haegeman, I. P. McCulloch, and F. Verstraete. Topological nature of spinons and holons: Elementary excitations from matrix product states with conserved symmetries. *Phys. Rev. B* **97,** 235155 (2018).

[315] C. Holzhey, F. Larsen, and F. Wilczek. Geometric and renormalized entropy in conformal field theory. *Nucl. Phys. B* **424,** 443 (1994).

[316] G. Vidal, J. I. Latorre, E. Rico, and A. Kitaev. Entanglement in quantum critical phenomena. *Phys. Rev. Lett.* **90,** 227902 (2003).

[317] L. Tagliacozzo, T. de Oliveira, S. Iblisdir, and J. I. Latorre. Scaling of entanglement support for matrix product states. *Phys. Rev. B* **78,** 024410 (2008).

[318] F. Pollmann, S. Mukerjee, A. M. Turner, and J. E. Moore. Theory of finite-entanglement scaling at one-dimensional quantum critical points. *Phys. Rev. Lett.* **102,** 255701 (2009).

[319] F. Pollmann and J. E. Moore. Entanglement spectra of critical and near-critical systems in one dimension. *New J. Phys.* **12,** 025006 (2010).

[320] V. Stojevic, J. Haegeman, I. P. McCulloch, L. Tagliacozzo, and F. Verstraete. Conformal data from finite entanglement scaling. *Phys. Rev. B* **91,** 035120 (2015).

[321] S-J Ran, C. Peng, W. Li, M. Lewenstein, and G. Su. Criticality in two-dimensional quantum systems: Tensor network approach. *Phys. Rev. B* **95,** 155114 (2017).

[322] P. Hauke and L. Tagliacozzo. Spread of correlations in long-range interacting quantum systems. *Phys. Rev. Lett.* **111,** 207202 (2013).

[323] T. Koffel, M. Lewenstein, and L. Tagliacozzo. Entanglement entropy for the long-range Ising chain in a transverse field. *Phys. Rev. Lett.* **109,** 267203 (2012).

[324] I. Affleck, T. Kennedy, E. H. Lieb, and H. Tasaki. Rigorous results on valence-bond ground states in antiferromagnets. *Phys. Rev. Lett.* **59,** 799 (1987).

[325] I. Affleck, T. Kennedy, E. H. Lieb, and H. Tasaki. Valence bond ground states in isotropic quantum antiferromagnets. *Commun. Math. Phys.* **115,** 477 (1988).

[326] H. Niggemann, A. Klümper, and J. Zittartz. Quantum phase transition in spin-3/2 systems on the hexagonal lattice-optimum ground state approach. *Z. Phys. B* **104,** 103 (1997).

[327] H. Niggemann, A. Klümper, and J. Zittartz. Ground state phase diagram of a spin-2 antiferromagnet on the square lattice. *Eur. Phys. J. B* **13,** 15 (2000).

[328] F. Verstraete, M. A. Martin-Delgado, and J. I. Cirac. Diverging entanglement length in gapped quantum spin systems. *Phys. Rev. Lett.* **92,** 087201 (2004).

[329] V. Karimipour and L. Memarzadeh. Matrix product representations for all valence bond states. *Phys. Rev. B* **77,** 094416 (2008).

[330] F. Pollmann and Ari M. Turner. Detection of symmetry-protected topological phases in one dimension. *Phys. Rev. B* **86,** 125441 (2012).

[331] F. Verstraete and J. I. Cirac. Continuous matrix product states for quantum fields. *Phys. Rev. Lett.* **104,** 190405 (2010).

[332] T. Nishino, Y. Hieida, K. Okunishi, N. Maeshima, Y. Akutsu, and A. Gendiar. Two-dimensional tensor product variational formulation. *Prog. Theor. Phys.* **105,** 409 (2001).

[333] F. Verstraete and J. I. Cirac. Valence-bond states for quantum computation. *Phys. Rev. A* **70,** 060302 (2004).

[334] F. Verstraete and J. I. Cirac. Renormalization algorithms for quantum-many body systems in two and higher dimensions. *arXiv preprint cond-mat/0407066*, 2004.

[335] I. Affleck, T. Kennedy, E. H. Lieb, and H. Tasaki. Valence bond ground states in isotropic quantum antiferromagnets. *Comm. Math. Phys.* **115,** 477 (1988).

[336] D. Poilblanc, N. Schuch, D. Pérez-García, and J. I. Cirac. Topological and entanglement properties of resonating valence bond wave functions. *Phys. Rev. B* **86,** 014404 (2012).

[337] N. Schuch, D. Poilblanc, J. I. Cirac, and D. Pérez-García. Resonating valence bond states in the PEPS formalism. *Phys. Rev. B* **86,** 115108 (2012).

[338] L. Wang, D. Poilblanc, Z.-C. Gu, X.-G Wen, and F. Verstraete. Constructing a gapless spin-liquid state for the spin-1/2 j_1-j_2 Heisenberg model on a square lattice. *Phys. Rev. Lett.* **111,** 037202 (2013).

[339] D. Poilblanc, P. Corboz, N. Schuch, and J. I. Cirac. Resonating-valence-bond superconductors with fermionic projected entangled pair states. *Phys. Rev. B* **89,** 241106 (2014).

[340] P. W. Anderson. Resonating valence bonds: A new kind of insulator? *Mat. Res. Bull.* **8,** 153 (1973).

[341] P. W. Anderson. On the ground state properties of the anisotropic triangular antiferromagnet. *Philos. Mag.* **30,** 432 (1974).

[342] P. W. Anderson. The resonating valence bond state in La_2CuO_4 and superconductivity. *Science* **235,** 1196 (1987).

[343] G. Baskaran, Z. Zou, and P. W. Anderson. The resonating valence bond state and high-Tc superconductivity — A mean field theory. *Solid State Commun.* **63,** 973 (1987).

[344] P. W. Anderson, G. Baskaran, Z. Zou, and T. Hsu. Resonating-valence-bond theory of phase transitions and superconductivity in La_2CuO_4-based compounds. *Phys. Rev. Lett.* **58,** 2790 (1987).

[345] Z. C. Gu, M. Levin, B. Swingle, and X. G. Wen. Tensor-product representations for string-net condensed states. *Phys. Rev. B* **79,** 085118 (2009).

[346] O. Buerschaper, M. Aguado, and G. Vidal. Explicit tensor network representation for the ground states of string-net models. *Phys. Rev. B* **79,** 085119 (2009).

[347] X. Chen, B. Zeng, Z. C. Gu, I. L. Chuang, and X. G. Wen. Tensor product representation of a topological ordered phase: Necessary symmetry conditions. *Phys. Rev. B* **82,** 165119 (2010).

[348] X. G. Wen. Vacuum degeneracy of chiral spin states in compactified space. *Phys. Rev. B* **40,** 7387 (1989).

[349] X. G. Wen. Topological orders in rigid states. *Int. J. Mod. Phys. B* **4,** 239 (1990).

[350] X. G. Wen and Q. Niu. Ground-state degeneracy of the fractional quantum Hall states in the presence of a random potential and on high-genus Riemann surfaces. *Phys. Rev. B* **41,** 9377 (1990).

[351] X. G. Wen. Topological orders and edge excitations in fractional quantum Hall states. *Advanc. Phys.* **44,** 405 (1995).

[352] M. Levin and X. G. Wen. String-net condensation: A physical mechanism for topological phases. *Phys. Rev. B* **71,** 045110 (2005).

[353] N. Schuch, M. M. Wolf, F. Verstraete, and J. I. Cirac. Computational complexity of projected entangled pair states. *Phys. Rev. Lett.* **98,** 140506 (2007).

[354] A. García-Sáez and J. I. Latorre. An exact tensor network for the 3SAT problem. *arXiv preprint arXiv:1105.3201*, 2011.

[355] T. Hucklea, K. Waldherra, and T. Schulte-Herbrüggen. Computations in quantum tensor networks. *Linear Algebra Application* **438,** 750 (2013).

[356] Z.-Y. Xie, J. Chen, J.-F. Yu, X. Kong, B. Normand, and T. Xiang. Tensor renormalization of quantum many-body systems using projected entangled simplex states. *Phys. Rev. X* **4,** 011025 (2014).

[357] H.-J. Liao, Z.-Y. Xie, J. Chen, Z.-Y. Liu, H.-D. Xie, R.-Z. Huang, B. Normand, and T. Xiang. Gapless spin-liquid ground state in the $S = 1/2$ kagome antiferromagnet. *Phys. Rev. Lett.* **118,** 137202 (2017).

[358] B. Friedman. A density matrix renormalization group approach to interacting quantum systems on Cayley trees. *J. Phys.: Condens. Matter* **9,** 9021 (1997).

[359] M. Lepetit, M. Cousy, and G. M. Pastor. Density-matrix renormalization study of the Hubbard model on a Bethe lattice. *Eur. Phys. J. B* **13,** 421 (2000).

[360] M. A. Martin-Delgado, J. Rodriguez-Laguna, and G. Sierra. Density-matrix renormalization-group study of excitons in dendrimers. *Phys. Rev. B* **65,** 155116 (2002).

[361] Y.-Y. Shi, L. M. Duan, and G. Vidal. Classical simulation of quantum many-body systems with a tree tensor network. *Phys. Rev. A* **74,** 022320 (2006).

[362] D. Nagaj, E. Farhi, J. Goldstone, P. Shor, and I. Sylvester. Quantum transverse-field Ising model on an infinite tree from matrix product states. *Phys. Rev. B* **77,** 214431 (2008).

[363] L. Tagliacozzo, G. Evenbly, and G. Vidal. Simulation of two-dimensional quantum systems using a tree tensor network that exploits the entropic area law. *Phys. Rev. B* **80,** 235127 (2009).

[364] V. Murg, F. Verstraete, Ö. Legeza, and R. M. Noack. Simulating strongly correlated quantum systems with tree tensor networks. *Phys. Rev. B* **82,** 205105 (2010).

[365] W. Li, J. von Delft, and T. Xiang. Efficient simulation of infinite tree tensor network states on the Bethe lattice. *Phys. Rev. B* **86,** 195137 (2012).

[366] N. Nakatani and G. K. L. Chan. Efficient tree tensor network states (TTNS) for quantum chemistry: Generalizations of the density matrix renormalization group algorithm. *J. Chem. Phys.* **138,** 134113 (2013).

[367] I. Pižorn, F. Verstraete, and R. M. Konik. Tree tensor networks and entanglement spectra. *Phys. Rev. B* **88,** 195102 (2013).

[368] M. Gerster, P. Silvi, M. Rizzi, R. Fazio, T. Calarco, and S. Montangero. Unconstrained tree tensor network: An adaptive gauge picture for enhanced performance. *Phys. Rev. B* **90,** 125154 (2014).

[369] V. Murg, F. Verstraete, R. Schneider, P. R. Nagy, and Ö. Legeza. Tree tensor network state with variable tensor order: An efficient multireference method for strongly correlated systems. *J. Chem. Theory Comput.* **11,** 1027 (2015).

[370] G. Vidal. Entanglement renormalization. *Phys. Rev. Lett.* **99,** 220405 (2007).

[371] G. Vidal. Class of quantum many-body states that can be efficiently simulated. *Phys. Rev. Lett.* **101,** 110501 (2008).

[372] L. Cincio, J. Dziarmaga, and M. M. Rams. Multiscale entanglement renormalization ansatz in two dimensions: quantum Ising model. *Phys. Rev. Lett.* **100,** 240603 (2008).

[373] G. Evenbly and G. Vidal. Entanglement renormalization in two spatial dimensions. *Phys. Rev. Lett.* **102,** 180406 (2009).

[374] M. Aguado and G. Vidal. Entanglement renormalization and topological order. *Phys. Rev. Lett.* **100,** 070404 (2008).

[375] G. Evenbly and G. Vidal. Algorithms for entanglement renormalization. *Phys. Rev. B* **79,** 144108 (2009).

[376] P. Corboz and G. Vidal. Fermionic multiscale entanglement renormalization ansatz. *Phys. Rev. B* **80,** 165129 (2009).

[377] G. Evenbly and G. Vidal. Entanglement renormalization in free bosonic systems: real-space versus momentum-space renormalization group transforms. *New J. Phys.* **12,** 025007 (2010).

[378] G. Evenbly and G. Vidal. Entanglement renormalization in noninteracting fermionic systems. *Phys. Rev. B* **81,** 235102 (2010).

[379] R. N. C. Pfeifer, G. Evenbly, and G. Vidal. Entanglement renormalization, scale invariance, and quantum criticality. *Phys. Rev. A* **79,** 040301 (2009).

[380] S. Montangero, M. Rizzi, V. Giovannetti, and R. Fazio. Critical exponents with a multiscale entanglement renormalization Ansatz channel. *Phys. Rev. B* **80,** 113103 (2009).

[381] G. Evenbly, P. Corboz, and G. Vidal. Nonlocal scaling operators with entanglement renormalization. *Phys. Rev. B* **82,** 132411 (2010).

[382] P. Silvi, V. Giovannetti, P. Calabrese, G. E. Santoro, and R. Fazio. Entanglement renormalization and boundary critical phenomena. *J. Statist. Mechan.* **2010,** L03001 (2010).

[383] G. Evenbly and G. Vidal. *Quantum Criticality with the Multi-scale Entanglement Renormalization Ansatz.* Strongly Correlated Systems, Springer, p. 99-130, 2013.

[384] J. C. Bridgeman, A. O'Brien, S. D. Bartlett, and A. C. Doherty. Multiscale entanglement renormalization ansatz for spin chains with continuously varying criticality. *Phys. Rev. B* **91,** 165129 (2015).

[385] G. Evenbly and G. Vidal. Tensor Network States and Geometry. *J. Stat. Phys.* **145,** 891 (2011).

[386] B. Swingle. Entanglement renormalization and holography. *Phys. Rev. D* **86,** 065007 (2012).

[387] C. Beny. Causal structure of the entanglement renormalization ansatz. *New J. Phys.* **15,** 023020 (2013).

[388] X. L. Qi. Exact holographic mapping and emergent space-time geometry. *arXiv preprint arXiv:1309.6282.*

[389] M. Miyaji, T. Numasawa, N. Shiba, T. Takayanagi, and K. Watanabe. Continuous multiscale entanglement renormalization ansatz as holographic surface-state correspondence. *Phys. Rev. Lett.* **115,** 171602 (2015).

[390] N. Bao, C. J. Cao, S. M. Carroll, A. Chatwin-Davies, N. Hunter-Jones, J. Pollack, and G. N. Remmen. Consistency conditions for an AdS multiscale entanglement renormalization ansatz correspondence. *Phys. Rev. D* **91,** 125036 (2015).

[391] B. Czech, L. Lamprou, S. McCandlish, and J. Sully. Integral Geometry and Holography. *arXiv preprint arXiv:1505.05515.*

[392] M. Natsuume. *Ads/CFT duality user guide, lect. notes in phys. 903.* Springer, Tokyo, 2015.

[393] F. Verstraete, J. J. García-Ripoll, and J. I. Cirac. Matrix product density operators: Simulation of finite-temperature and dissipative systems. *Phys. Rev. Lett.* **93,** 207204 (2004).

[394] M. Zwolak and G. Vidal. Mixed-state dynamics in one-dimensional quantum lattice systems: A time-dependent superoperator renormalization algorithm. *Phys. Rev. Lett.* **93,** 207205 (2004).

[395] B. Pirvu, V. Murg, J. I. Cirac, and F. Verstraete. Matrix product operator representations. *New J. Phys.* **12,** 025012 (2010).

[396] W. Li, S. J. Ran, S. S. Gong, Y. Zhao, B. Xi, F. Ye, and G. Su. Linearized tensor renormalization group algorithm for the calculation of thermodynamic properties of quantum lattice models. *Phys. Rev. Lett.* **106,** 127202 (2011).

[397] L. Bonnes, D. Charrier, and A. M. Läuchli. Dynamical and steady-state properties of a bose-hubbard chain with bond dissipation: A study based on matrix product operators. *Phys. Rev. A* **90,** 033612 (2014).

[398] E. Mascarenhas, H. Flayac, and V. Savona. Matrix-product-operator approach to the nonequilibrium steady state of driven-dissipative quantum arrays. *Phys. Rev. A* **92,** 022116 (2015).

[399] J. Cui, J. I. Cirac, and M. C. Bañuls. Variational matrix product operators for the steady state of dissipative quantum systems. *Phys. Rev. Lett.* **114,** 220601 (2015).

[400] J. Becker, T. Köhler, A. C. Tiegel, S. R. Manmana, S. Wessel, and A. Honecker. Finite-temperature dynamics and thermal intraband magnon scattering in Haldane spin-one chains. *Phys. Rev. B* **96,** 060403 (2017).

[401] A. A. Gangat, I. Te, and Y.-J. Kao. Steady states of infinite-size dissipative quantum chains via imaginary time evolution. *Phys. Rev. Lett.* **119,** 010501 (2017).

[402] J. Haegeman and F. Verstraete. Diagonalizing transfer matrices and matrix product operators: A medley of exact and computational methods. *Ann. Rev. Condens. Matter Phys.* **8,** 355 (2017).

[403] J.I. Cirac, D. Pérez-García, N. Schuch, and F. Verstraete. Matrix product density operators: Renormalization fixed points and boundary theories. *Ann. Phys.* **378,** 100 (2017).

[404] F. Fröwis, V. Nebendahl, and W. Dür. Tensor operators: Constructions and applications for long-range interaction systems. *Phys. Rev. A* **81,** 062337 (2010).

[405] R. Orús. Exploring corner transfer matrices and corner tensors for the classical simulation of quantum lattice systems. *Phys. Rev. B* **85,** 205117 (2012).

[406] S. J. Ran, W. Li, B. Xi, Z. Zhang, and G. Su. Optimized decimation of tensor networks with super-orthogonalization for two-dimensional quantum lattice models. *Phys. Rev. B* **86,** 134429 (2012).

[407] P. Czarnik, L. Cincio, and J. Dziarmaga. Projected entangled pair states at finite temperature: Imaginary time evolution with ancillas. *Phys. Rev. B* **86,** 245101 (2012).

[408] S. J. Ran, B. Xi, T. Liu, and G. Su. Theory of network contractor dynamics for exploring thermodynamic properties of two-dimensional quantum lattice models. *Phys. Rev. B* **88,** 064407 (2013).

[409] P. Czarnik and J. Dziarmaga. Variational approach to projected entangled pair states at finite temperature. *Phys. Rev. B* **92,** 035152 (2015).

[410] P. Czarnik and J. Dziarmaga. Projected entangled pair states at finite temperature: Iterative self-consistent bond renormalization for exact imaginary time evolution. *Phys. Rev. B* **92,** 035120 (2015).

[411] P. Czarnik, J. Dziarmaga, and A. M. Oleś. Variational tensor network renormalization in imaginary time: Two-dimensional quantum compass model at finite temperature. *Phys. Rev. B* **93,** 184410 (2016).

[412] P. Czarnik, M. M. Rams, and J. Dziarmaga. Variational tensor network renormalization in imaginary time: Benchmark results in the Hubbard model at finite temperature. *Phys. Rev. B* **94,** 235142 (2016).

[413] Y.-W. Dai, Q.-Q. Shi, S.-Y.. Cho, M. T. Batchelor, and H.-Q. Zhou. Finite-temperature fidelity and von Neumann entropy in the honeycomb spin lattice with quantum Ising interaction. *Phys. Rev. B* **95,** 214409 (2017).

[414] P. Czarnik, J. Dziarmaga, and A. M. Oleś. Overcoming the sign problem at finite temperature: Quantum tensor network for the orbital e_g model on an infinite square lattice. *Phys. Rev. B* **96,** 014420 (2017).

[415] A. Kshetrimayum, M. Rizzi, J. Eisert, and R. Orús. A tensor network annealing algorithm for two-dimensional thermal states. *arXiv preprint arXiv:1809.08258*, 2018.

[416] P. Czarnik, J. Dziarmaga, and P. Corboz. Time evolution of an infinite projected entangled pair state: An efficient algorithm. *Phys. Rev. B* **99,** 035115 (2019).

[417] H. Matsueda, M. Ishihara, and Y. Hashizume. Tensor network and a black hole. *Phys. Rev. D* **87,** 066002 (2013).

[418] A. Mollabashi, M. Naozaki, S. Ryu, and T. Takayanagi. Holographic geometry of cMERA for quantum quenches and finite temperature. *J. High Energy Phys.* **2014,** 98 (2014).

[419] W.-C. Gan, F.-W. Shu, and M.-H. Wu. Thermal geometry from CFT at finite temperature. *Phys. Lett. B* **760,** 796 (2016).

[420] I. V. Oseledets. Tensor-train decomposition. *SIAM J. Sci. Comput.* **33,** 2295 (2011).

[421] J. J. de Swart. The octet model and its Clebsch-Gordan coefficients. *Rev. Mod. Phys.* **35,** 916 (1963).

[422] L. Balents. Spin liquids in frustrated magnets. *Nature* **464,** 199 (2010).

[423] S.T. Bramwell and M. J. P. Gingras. Spin Ice State in Frustrated Magnetic Pyrochlore Materials. *Science* **5546,** 1495 (2017).

[424] J. D. Bernal and R. H. Fowler. A Theory of Water and Ionic Solution, with Particular Reference to Hydrogen and Hydroxyl Ions. *J. of Chem. Phys.* **8,** 515 (1933).

[425] T. Fennell, P. P. Deen, A. R. Wildes, K. Schmalzl, D. Prabhakaran, A. T. Boothroyd, R. J. Aldus, D. F. McMorrow, and S. T. Bramwell. Magnetic Coulomb Phase in the Spin Ice $Ho_2Ti_2O_7$. *Science* **5951,** 415 (2009).

[426] R. J. Baxter. Eight-vertex model in lattice statistics. *Phys. Rev. Lett.* **26,** 832 (1971).

[427] G. M. Crosswhite and D. Bacon. Finite automata for caching in matrix product algorithms. *Phys. Rev. A* **78,** 012356 (2008).

[428] G. M. Crosswhite, A. C. Doherty, and G. Vidal. Applying matrix product operators to model systems with long-range interactions. *Phys. Rev. B* **78,** 035116 (2008).

[429] W. Kohn. Nobel lecture: electronic structure of matter: wave functions and density functionals. *Rev. Mod. Phys.* **71,** 1253 (1999).

[430] M. Troyer and U. J. Wiese. Computational complexity and fundamental limitations to fermionic quantum Monte Carlo simulations. *Phys. Rev. Lett.* **94,** 170201 (2005).

[431] I. Peschel, M. Kaulke, and Ö. Legeza. Density-matrix spectra for integrable models. *Annalen der Physik* **8,** 153 (1999).

[432] G. Vitagliano, A. Riera, and J. I. Latorre. Volume-law scaling for the entanglement entropy in spin-1/2 chains. *New J. Phys.* **12,** 113049 (2010).

[433] R. Movassagh and P. W. Shor. Supercritical entanglement in local systems: Counterexample to the area law for quantum matter. *Proceedings of the National Academy of Sciences* **113,** 13278 (2016).

[434] I. L. Markov and Y.-Y. Shi. Simulating quantum computation by contracting tensor networks. *SIAM J. Comput.* **38,** 963 (2008).

[435] R. Jozsa and N. Linden. On the role of entanglement in quantum-computational speed-up. *Proceedings of the Royal Society of London. Series A: Mathematical, Physical and Engineering Sciences* **459,** 2036 (2003).

[436] C. Schön, E. Solano, F. Verstraete, J. I. Cirac, and M. M. Wolf. Sequential generation of entangled multiqubit states. *Phys. Rev. Lett.*, **95,** 110503 (2005).

[437] I. P. McCulloch. Infinite size density matrix renormalization group, revisited. *arXiv preprint arXiv:0804.2509*, 2008.

[438] P. Silvi, V. Giovannetti, S. Montangero, M. Rizzi, J. I. Cirac, and R. Fazio. Homogeneous binary trees as ground states of quantum critical Hamiltonians. *Phys. Rev. A* **81,** 062335 (2010).

[439] V. Bapst, L. Foini, F. Krzakala, G. Semerjian, and F. Zamponi. The quantum adiabatic algorithm applied to random optimization problems: The quantum spin glass perspective. *Phys. Rep.* **523,** 127 (2013).

[440] G. Vidal. Entanglement renormalization: an introduction. *arXiv preprint arXiv:0912.1651*, 2009.

[441] L. Tagliacozzo and G. Vidal. Entanglement renormalization and gauge symmetry. *Phys. Rev. B* **83,** 115127 (2011).

[442] M.-C. Bañuls, D. Pérez-García, M. M. Wolf, F. Verstraete, and J. I. Cirac. Sequentially generated states for the study of two-dimensional systems. *Phys. Rev. A* **77,** 052306 (2008).

[443] Y. Nishino, N. Maeshima, A. Gendiar, and T. Nishino. Tensor product variational formulation for quantum systems. *arXiv preprint cond-mat/0401115*, 2004.

[444] M. P. Zaletel and F. Pollmann. Isometric Tensor Network States in Two Dimensions. *arXiv preprint arXiv:1902.05100*, 2019.

[445] R. Haghshenas, M. J. O'Rourke, and G. K. Chan. Canonicalization of projected entangled pair states. *arXiv preprint arXiv:1903.03843*, 2019.

[446] M. Levin and C. P. Nave. Tensor renormalization group approach to two-dimensional classical lattice models. *Phys. Rev. Lett.* **99,** 120601 (2007).

[447] H. C. Jiang, Z. Y. Weng, and T. Xiang. Accurate determination of tensor network state of quantum lattice models in two dimensions. *Phys. Rev. Lett.* **101,** 090603 (2008).

[448] Z. C. Gu, M. Levin, and X. G. Wen. Tensor-entanglement renormalization group approach as a unified method for symmetry breaking and topological phase transitions. *Phys. Rev. B* **78,** 205116 (2008).

[449] Z. C. Gu and X. G. Wen. Tensor-entanglement-filtering renormalization approach and symmetry protected topological order. *Phys. Rev. B* **80,** 155131 (2009).

[450] M.-C. Chang and M.-F. Yang. Magnetization plateau of the classical Ising model on the shastry-sutherland lattice: A tensor renormalization-group approach. *Phys. Rev. B* **79,** 104411 (2009).

[451] R. König, B. W. Reichardt, and G. Vidal. Exact entanglement renormalization for string-net models. *Phys. Rev. B* **79,** 195123 (2009).

[452] H.-H. Zhao, Z.-Y. Xie, Q.-N. Chen, Z.-C. Wei, J.-W. Cai, and T. Xiang. Renormalization of tensor-network states. *Phys. Rev. B* **81,** 174411 (2010).

[453] C.-Y. Huang and F.-L. Lin. Multipartite entanglement measures and quantum criticality from matrix and tensor product states. *Phys. Rev. A* **81,** 032304 (2010).

[454] W. Li, S.-S. Gong, Y. Zhao, and G. Su. Quantum phase transition, O(3) universality class, and phase diagram of the spin-$\frac{1}{2}$ Heisenberg antiferromagnet on a distorted honeycomb lattice: A tensor renormalization-group study. *Phys. Rev. B* **81,** 184427 (2010).

[455] C. Güven and M. Hinczewski. The tensor renormalization group for pure and disordered two-dimensional lattice systems. *Phys. A: Stat. Mech. Applications* **389,** 2915 (2010).

[456] C Güven, M. Hinczewski, and A. Nihat Berker. Tensor renormalization group: Local magnetizations, correlation functions, and phase diagrams of systems with quenched randomness. *Phys. Rev. E* **82,** 051110 (2010).

[457] L. Wang, Y.-J. Kao, and A. W. Sandvik. Plaquette renormalization scheme for tensor network states. *Phys. Rev. E* **83,** 056703 (2011).

[458] Q. N. Chen, M. P. Qin, J. Chen, Z. C. Wei, H. H. Zhao, B. Normand, and T. Xiang. Partial order and finite-temperature phase transitions in Potts models on irregular lattices. *Phys. Rev. Lett.* **107,** 165701 (2011).

[459] Z.-Y. Xie, J. Chen, M.-P. Qin, J.-W. Zhu, L.-P. Yang, and T. Xiang. Coarse-graining renormalization by higher-order singular value decomposition. *Phys. Rev. B* **86,** 045139 (2012).

[460] Y. SHIMIZU. Tensor renormalization group approach to a lattice boson model. *Modern Phys. Lett. A* **27,** 1250035 (2012).

[461] A. García-Sáez and J. I. Latorre. Renormalization group contraction of tensor networks in three dimensions. *Phys. Rev. B* **87,** 085130 (2013).

[462] M. P. Qin, Q. N. Chen, Z. Y. Xie, J. Chen, J. F. Yu, H. H. Zhao, B. Normand, and T. Xiang. Partial long-range order in antiferromagnetic Potts models. *Phys. Rev. B* **90,** 144424 (2014).

[463] Wang S., Xie Z.-Y., Chen J., B. Normand, and Xiang T.. Phase transitions of terromagnetic Potts models on the simple cubic lattice. *Chn. Physm Lett.* **31,** 070503 (2014).

[464] K. Roychowdhury and C.-Y. Huang. Tensor renormalization group approach to classical dimer models. *Phys. Rev. B* **91,** 205418 (2015).

[465] H.-H. Zhao, Z.-Y. Xie, T. Xiang, and M. Imada. Tensor network algorithm by coarse-graining tensor renormalization on finite periodic lattices. *Phys. Rev. B* **93,** 125115 (2016).

[466] R. Orús and G. Vidal. Simulation of two-dimensional quantum systems on an infinite lattice revisited: Corner transfer matrix for tensor contraction. *Phys. Rev. B* **80,** 094403 (2009).

[467] R. J. Baxter. Variational approximations for square lattice models in statistical mechanics. *J. Stat. Phys.* **19,** 461 (1978).

[468] H. F. Trotter. On the product of semi-groups of operators. *Proceedings of the American Mathematical Society* **10,** 545 (1959).

[469] M. Suzuki and M. Inoue. The ST-transformation approach to analytic solutions of quantum systems. I general formulations and basic limit theorems. *Prog. Theor. Phys.* **78,** 787 (1987).

[470] M. Inoue and M. Suzuki. The ST-transformation approach to analytic solutions of quantum systems. II: Transfer-matrix and Pfaffian methods. *Prog. Theor. Phys.* **79,** 645 (1988).

[471] Z. Y. Xie, H. C. Jiang, Q. N. Chen, Z. Y. Weng, and T. Xiang. Second renormalization of tensor-network states. *Phys. Rev. Lett.* **103,** 160601 (2009).

[472] F. Pollmann and J. E. Moore. Entanglement spectra of critical and near-critical systems in one dimension. *New J. Phys.* **12,** 025006 (2010).

[473] D. Delande, K. Sacha, M. Płodzień, S. K. Avazbaev, and J. Zakrzewski. Many-body Anderson localization in one-dimensional systems. *New J. Phys.* **15,** 045021 (2013).

[474] J. H. Bardarson, F. Pollmann, and J. E. Moore. Unbounded growth of entanglement in models of many-body localization. *Phys. Rev. Lett.* **109,** 017202 (2012).

[475] P. Ponte, Z. Papić, F. Huveneers, and D. A. Abanin. Many-body localization in periodically driven systems. *Phys. Rev. Lett.* **114,** 140401 (2015).

[476] B. Pozsgay, M. Mestyán, M. A. Werner, M. Kormos, G. Zaránd, and G. Takács. Correlations after Quantum Quenches in the X X Z Spin Chain: Failure of the Generalized Gibbs Ensemble. *Phys. Rev. Lett.* **113,** 117203 (2014).

[477] P. Barmettler, M. Punk, V. Gritsev, E. Demler, and E. Altman. Relaxation of antiferromagnetic order in spin-1/2 chains following a quantum quench. *Phys. Rev. Lett.* **102,** 130603 (2009).

[478] M. Fagotti, M. Collura, F. H. L. Essler, and P. Calabrese. Relaxation after quantum quenches in the spin-1 2 Heisenberg XXZ chain. *Phys. Rev. B* **89,** 125101 (2014).

[479] P. Barmettler, M. Punk, V. Gritsev, E. Demler, and E. Altman. Quantum quenches in the anisotropic spin-Heisenberg chain: different approaches to many-body dynamics far from equilibrium. *New J. Phys.* **12,** 055017 (2010).

[480] F. H. L. Essler and M. Fagotti. Quench dynamics and relaxation in isolated integrable quantum spin chains. *J. Stat. Mech.: Theo. Exp.* **2016,** 064002 (2016).

[481] R. J. Baxter. *Exactly solved models in statistical mechanics.* Elsevier, 2016.

[482] R. J. Baxter. Corner transfer matrices of the chiral Potts model. *J. Stat. Phys.* **63,** 433 (1991).

[483] R. J. Baxter. Chiral Potts model: corner transfer matrices and parametrizations. *Int. J. Mod. Phys. B* **7,** 3489 (1993).

[484] R. J. Baxter. Corner transfer matrices of the chiral Potts model. II. The triangular lattice. *J. Stat. Phys.* **70,** 535 (1993).

[485] R. J. Baxter. Corner transfer matrices of the eight-vertex model. I. Low-temperature expansions and conjectured properties. *J. Stat. Phys.* **15,** 485 (1976).

[486] R. J. Baxter. Corner transfer matrices of the eight-vertex model. II. The Ising model case. *J. Stat. Phys.* **17,** 1 (1977).

[487] R. J. Baxter and P. J. Forrester. A variational approximation for cubic lattice models in statistical mechanics. *J. Phys. A: Math. Gen.* **17,** 2675 (1984).

[488] T. Nishino and K. Okunishi. Corner transfer matrix algorithm for classical renormalization group. *J. Phys. Soc. Jpn.* **66,** 3040 (1997).

[489] N. Tsushima and T. Horiguchi. Phase diagrams of spin-3/2 Ising model on a square lattice in terms of corner transfer matrix renormalization group method. *J. Phys. Soc. Jpn.* **67,** 1574 (1998).

[490] K. Okunishi, Y. Hieida, and Y. Akutsu. Universal asymptotic eigenvalue distribution of density matrices and corner transfer matrices in the thermodynamic limit. *Phys. Rev. E* **59,** 6 (1999).

[491] Z. B. Li, Z. Shuai, Q. Wang, H. J. Luo, and L. Schülke. Critical exponents of the two-layer Ising model. *J. Phys. A: Math. Gen.* **34,** 6069 (2001).

[492] A. Gendiar and T. Nishino. Latent heat calculation of the three-dimensional q= 3, 4, and 5 Potts models by the tensor product variational approach. *Phys. Rev. E* **65,** 046702 (2002).

[493] M. C. Bañuls, M. B. Hastings, F. Verstraete, and J. I. Cirac. Matrix Product States for Dynamical Simulation of Infinite Chains. *Phys. Rev. Lett.* **102,** 240603 (2009).

[494] A. Müller-Hermes, J. I. Cirac, and M.-C. Bañuls. Tensor network techniques for the computation of dynamical observables in one-dimensional quantum spin systems. *New J. Phys.* **14,** 075003 (2012).

[495] M. B. Hastings and R. Mahajan. Connecting entanglement in time and space: Improving the folding algorithm. *Phys. Rev. A* **91,** 032306 (2015).

[496] T. Nishino. Density matrix renormalization group method for 2d classical models. *J. Phys. Soc. Jpn.* **64,** 3598 (1995).

[497] A. J. Daley, C. Kollath, U. Schollwöck, and G. Vidal. Time-dependent density-matrix renormalization-group using adaptive effective Hilbert spaces. *J. Stat. Mech.: Theor. Exp.* **2004,** P04005 (2004).

[498] J. Jordan, R. Orús, G. Vidal, F. Verstraete, and J. I. Cirac. Classical Simulation of Infinite-Size Quantum Lattice Systems in Two Spatial Dimensions. Phys. Rev. Lett. **101,** 250602 (2008).

[499] E. M. Stoudenmire and S. R. White. Studying Two-Dimensional Systems with the Density Matrix Renormalization Group. *Ann. Rev. Cond. Matter Phys.* **3,** 111 (2012).

[500] H. N. Phien, J. A. Bengua, H. D. Tuan, P. Corboz, and R. Orús. Infinite projected entangled pair states algorithm improved: Fast full update and gauge fixing. *Phys. Rev. B* **92** 035142 (2015).

[501] J. Haegeman, J. I. Cirac, T. Osborne, and F. Verstraete. Calculus of continuous matrix product states. *Phys. Rev. B* **88**, 085118 (2013).

[502] J. Haegeman, T. J. Osborne, H. Verschelde, and F. Verstraete. Entanglement renormalization for quantum fields in real space. *Phys. Rev. Lett.* **110**, 100402 (2013).

[503] D. Jennings, C. Brockt, J. Haegeman, T. Osborne, and F. Verstraete. Continuum tensor network field states, path integral representations and spatial symmetries. *New J. Phys.* **17**, 063039 (2015).

[504] B. Buyens ,J. Haegeman, H. Verschelde, F. Verstraete, and K. Van Acoleyen. Confinement and String Breaking for QED_2 in the Hamiltonian Picture. *Phys. Rev. X* **6**, 041040 (2016).

[505] D. Draxler ,J. Haegeman, F. Verstraete, and M. Rizzi. Continuous matrix product states with periodic boundary conditions and an application to atomtronics. *Phys. Rev. B* **95**, 045145 (2017).

[506] M. Ganahl, J. Rincón, and G. Vidal. Continuous Matrix Product States for Quantum Fields: An Energy Minimization Algorithm. *Phys. Rev. Lett.* **118**(22), 220402 (2017).

[507] M. Ganahl and G. Vidal. Continuous matrix product states for non-relativistic quantum fields: a lattice algorithm for inhomogeneous systems. *Phys. Rev. B* **98,** 195105 (2018).

[508] A. Tilloy and J. I. Cirac. Continuous Tensor Network States for Quantum Fields. *Phys. Rev. X* **9,** 021040 (2019).

[509] Q. Hu, A. Franco-Rubio, and G. Vidal. Continuous tensor network renormalization for quantum fields. *arXiv preprint arXiv:1809.05176* (2018).

[510] I. Montvay and G. Münster. *Quantum Phase Transitions, 2nd ed.*. Cambridge University Press, Cambridge, 1997.

[511] J. A. Kjäll, F. Pollmann, and J. E. Moore. Bound states and E_8 symmetry effects in perturbed quantum Ising chains. *Phys. Rev. B* **83**, 020407 (2011).

[512] B. Pirvu, G. Vidal, F. Verstraete, and L. Tagliacozzo. Matrix product states for critical spin chains: finite size scaling versus finite entanglement scaling. *Phys. Rev. B* **86**, 075117 (2012).

[513] V. Stojevic, J. Haegeman, I. P. McCulloch, L. Tagliacozzo, and F. Verstraete. Conformal data from finite entanglement scaling. *Phys. Rev. B* **91**, 035120 (2015).

[514] Y. Zou, A. Milsted, and G. Vidal. Conformal data and renormalization group flow in critical quantum spin chains using periodic uniform matrix product states. arXiv preprint arXiv:1710.05397 (2017).

[515] P. Corboz, P. Czarnik, G. Kapteijns, and L. Tagliacozzo. Finite correlation length scaling with infinite projected entangled-pair states. *Phys. Rev. X* **8,** 031031, (2018).

[516] M. Rader and A. M. Läuchli. Finite Correlation Length Scaling in Lorentz-Invariant Gapless iPEPS Wave Functions. Phys. Rev. X **8,** 031030 (2018).

[517] J. L. Cardy. Operator content of two-dimensional conformally invariant theories. *Nucl. Phys. B* **270**, 186–204 (1986).

[518] J. L. Cardy. Effect of boundary conditions on the operator content of two-dimensional conformally invariant theories. *Nucl. Phys. B* **275**, 200 (1986).

[519] A. B. Zamolodchikov. Integrals Of Motion and S-Matrix of the (scaled) T = Tc Ising Model with magnetic field. *Int. J. Mod. Phys. A* **4,** 4235 (1989).

[520] M. Henkel. Finite-size scaling and universality in the spectrum of the quantum ising chain. I. Periodic and antiperiodic boundary condition. *J. Phys. A: Mathematical and General* **20**, 995 (1987).

[521] M. Henkel and H. Saleur. The two-dimensional Ising model in the magnetic field: a numerical check of Zamolodchikov's conjecture. *J. Phys. A Mathematical and General* **22**, L513 (1989).

[522] F. Quijandría, J. J. García-Ripoll, and D. Zueco. Continuous matrix product states for coupled fields: application to luttinger liquids and quantum simulators. *Phys. Rev. B* **90,** 235142 (2014).

[523] F. Quijandría and D. Zueco. Continuous-matrix-product-state solution for the mixingdemixing transition in one-dimensional quantum fields. *Phys. Rev. A* **92,** 043629 (2015).

[524] G. Evenbly, R. N. C. Pfeifer, V. Pico, S. Iblisdir, L. Tagliacozzo, I. P. McCulloch, and G. Vidal. Boundary quantum critical phenomena with entanglement renormalization. *Phys. Rev. B* **82**, 161107 (2010).

[525] T. D. Schultz, D. C. Mattis, and E. H. Lieb. Two-dimensional Ising model as a soluble problem of many fermions. *Rev. Mod. Phys.* **36,** 856 (1964).

[526] A. A. Belavin, A. M. Polyakov, and A. B. Zamolodchikov. Infinite conformal symmetry of critical fluctuations in two dimensions. *J. Stat.* **34** 5-6 (1984).

[527] J. Cardy. *Scaling and renormalization in statistical physics*. Cambridge university press (1996).

[528] P. Ginsparg. Applied conformal field theory. arXiv preprint arXiv:hep-th/9108028 (1998)

[529] H. Katsura and I. Maruyama. Derivation of the matrix product ansatz for the Heisenberg chain from the algebraic Bethe ansatz. *J. Phys. A: Mathematical and Theoretical* **43**, 175003 (2010).

[530] I. Maruyama and H. Katsura. Continuous matrix product ansatz for the one-dimensional Bose gas with point interaction. *J. Phys. Soc. of Japan* **79**, 073002 (2010).

[531] J. B. Kogut. An introduction to lattice gauge theory and spin systems. Rev. Mod. Phys. **51**, 659 (1979).

[532] Lieb, Elliott, Theodore Schultz, and Daniel Mattis. Two soluble models of an antiferromagnetic chain. *An. of Phys.* **16,** 407 (1961).